

Nanoparticle-nanoparticle interactions and light-matter interaction studied by simulated
absorption spectroscopy

by

Zhen Liu

B.S., Dalian University, 2016

AN ABSTRACT OF A DISSERTATION

submitted in partial fulfillment of the requirements for the degree

DOCTOR OF PHILOSOPHY

Department of Chemistry
College of Arts and Sciences

KANSAS STATE UNIVERSITY
Manhattan, Kansas

2023

Abstract

Plasmonics is one of the most important features of nanoparticles and other materials. Understanding plasmon interactions, plasmon-induced excitation energy transfer, and excited state dynamics of molecular plasmons are goals of this thesis. Utilizing efficient tight-binding calculations, the absorption spectra of homodimer and heterodimer nanoparticles are explored. Then, plasmon-induced excitation energy transfer is simulated with an attosecond time step up to investigate processes occurring on the picosecond dynamics time scale. Third, the naphthalene molecule, which has a molecular plasmon, is studied by simulated transient absorption spectroscopy using real-time time-dependent density functional theory calculations. Finally, nanoclusters Au_{25} and Au_{38} are also studied by ab initio transient absorption spectroscopy calculations. This dissertation represents the first time that atomically precise nanoclusters are explored by simulated ultrafast spectroscopy.

In this thesis, we systematically study the nanoparticle homodimer and heterodimer interaction and analyze the peak shifting observed in absorption spectroscopy. As the interparticle distance decreases, the red shifting peaks originate from excitations with transition dipole moments along the z-axis with nondegenerate features. Conversely, the blue shifting peaks arise from excitations with transition dipole moments in the x and y direction with double degeneracy.

The energy transfer between two nanoparticles has also been studied. Different energy transfer patterns as a function of different interparticle distances are explored. At relatively long distances, the energy transfer from one nanoparticle to another becomes more efficient as the interparticle distance decreases. However, at short distance, back-transfers of energy are observed, which reduces the dimer's ability to accept energy from the electric field. The back-transfers also reduce energy transfer between nanoparticle dimer.

Simulated transient absorption spectroscopy is performed to study naphthalene in order to explore the electron dynamics that occur after the plasmon peak is excited. With the help of electronic structure analysis, transient absorption signals below 3.5 eV are explored.

Finally, we present a study of excited state dynamics of Au₂₅ and Au₃₈ by simulated transient absorption spectroscopy. With the help of orbital symmetry from ground state calculations, the electron and hole excitations in the simulated pump-probe experiment can be distinguished. Because of the nanorod-like shape of Au₃₈, different energies and directions of the pump laser are applied to Au₃₈ to induce absorptions polarized in different directions. This work provides an opportunity to compare isotropic nanoclusters such as Au₂₅ with anisotropic ones such as Au₃₈.

Nanoparticle-nanoparticle interactions and light-matter interaction studied by simulated
absorption spectroscopy

by

Zhen Liu

B.S., Dalian University, 2016

A DISSERTATION

submitted in partial fulfillment of the requirements for the degree

DOCTOR OF PHILOSOPHY

Department of Chemistry
College of Arts and Sciences

KANSAS STATE UNIVERSITY
Manhattan, Kansas

2023

Approved by:

Major Professor
Christine M. Aikens

Copyright

© Zhen Liu 2023.

Abstract

Plasmonics is one of the most important features of nanoparticles and other materials. Understanding plasmon interactions, plasmon-induced excitation energy transfer, and excited state dynamics of molecular plasmons are goals of this thesis. Utilizing efficient tight-binding calculations, the absorption spectra of homodimer and heterodimer nanoparticles are explored. Then, plasmon-induced excitation energy transfer is simulated with an attosecond time step up to investigate processes occurring on the picosecond dynamics time scale. Third, the naphthalene molecule, which has a molecular plasmon, is studied by simulated transient absorption spectroscopy using real-time time-dependent density functional theory calculations. Finally, nanoclusters Au_{25} and Au_{38} are also studied by ab initio transient absorption spectroscopy calculations. This dissertation represents the first time that atomically precise nanoclusters are explored by simulated ultrafast spectroscopy.

In this thesis, we systematically study the nanoparticle homodimer and heterodimer interaction and analyze the peak shifting observed in absorption spectroscopy. As the interparticle distance decreases, the red shifting peaks originate from excitations with transition dipole moments along the z-axis with nondegenerate features. Conversely, the blue shifting peaks arise from excitations with transition dipole moments in the x and y direction with double degeneracy.

The energy transfer between two nanoparticles has also been studied. Different energy transfer patterns as a function of different interparticle distances are explored. At relatively long distances, the energy transfer from one nanoparticle to another becomes more efficient as the interparticle distance decreases. However, at short distance, back-transfers of energy are observed, which reduces the dimer's ability to accept energy from the electric field. The back-transfers also reduce energy transfer between nanoparticle dimer.

Simulated transient absorption spectroscopy is performed to study naphthalene in order to explore the electron dynamics that occur after the plasmon peak is excited. With the help of electronic structure analysis, transient absorption signals below 3.5 eV are explored.

Finally, we present a study of excited state dynamics of Au₂₅ and Au₃₈ by simulated transient absorption spectroscopy. With the help of orbital symmetry from ground state calculations, the electron and hole excitations in the simulated pump-probe experiment can be distinguished. Because of the nanorod-like shape of Au₃₈, different energies and directions of the pump laser are applied to Au₃₈ to induce absorptions polarized in different directions. This work provides an opportunity to compare isotropic nanoclusters such as Au₂₅ with anisotropic ones such as Au₃₈.

Table of Contents

List of Figures	xi
List of Tables	xvii
Acknowledgements.....	xviii
Chapter 1 - Introduction.....	1
1.1 Plasmon resonance	1
1.2 Molecular plasmons	2
1.3 Nanoparticle dimers	3
1.4 Thiolate protected nanoparticles	5
1.4.1 Ultrafast electron dynamics in thiolate-protected nanoparticles.....	10
1.5 Objectives and Outlook.....	11
1.6 References.....	13
Chapter 2 - Theoretical methods.....	22
2.1 Fundamentals of Electronic Structure Theory	22
2.2 Density functional theory.....	24
2.3 Density functional tight binding	26
2.4 Time-dependent density functional theory	28
2.4.1 Linear response density functional theory	29
2.4.2 Real-time density functional theory	29
2.5 Time-dependent density functional tight binding.....	30
2.6 Transient absorption spectroscopy simulation	32
2.7 References.....	35
Chapter 3 - TD-DFTB Study of Optical Properties of Silver Nanoparticle Homodimers and Heterodimers.....	38
3.1 Abstract.....	38
3.2 Introduction.....	39
3.3 Computational Details	41
3.4 Result and Discussion	45
3.4.1 Absorption spectra of monomers of FCC-structured silver nanoparticles.....	45
3.4.2 Absorption spectra of silver nanoparticle homodimers	47

3.4.3 Absorption spectra of heterodimer FCC structure silver nanoparticles	56
3.5 Conclusion	60
3.6 Acknowledgement	61
3.7 References.....	62
Chapter 4 - Plasmon induced excitation energy transfer in silver nanoparticle dimers: A real-time TDDFTB investigation	68
4.1 Abstract.....	68
4.2 Introduction.....	69
4.3 Computational Methods.....	71
4.4 Results and Discussion	74
4.4.1 Short-time dynamics	74
4.4.2 Long-time dynamics	75
4.5 Conclusions	91
4.6 Acknowledgement	92
4.7 Reference	93
Chapter 5 - Electronic Excited State Dynamics of Naphthalene Studied by Simulated Transient Absorption Spectroscopy.....	99
5.1 Abstract.....	99
5.2 Introduction.....	99
5.3 Result and Discussion	101
5.4 Computational Methods.....	108
5.5 Acknowledgement	109
5.6 Reference	110
Chapter 6 - Electronic Excited State Dynamics of Au ₂₅ and Au ₃₈ Studied by Simulated Transient Absorption Spectroscopy.....	113
6.1 Abstract.....	114
6.2 Introduction.....	115
6.3 Computational Methods.....	117
6.4 Results and Discussion	119
6.4.1 Au ₂₅	119
6.4.1.1 Pump energy of 1.40 eV	121

6.4.1.2 Pump energy of 1.92 eV and 2.06 eV.....	122
6.4.1.3 Pump energy of 2.40 eV	124
6.4.2 Au ₃₈	126
6.4.2.1 Pump energy of 1.04 eV	129
6.4.2.2 Pump energy of 1.37 eV	130
6.4.2.3 Pump energy of 1.62 eV	132
6.4.2.4 Pump energy of 1.93 eV	133
6.4.3 Comparison of Au ₂₅ and Au ₃₈	134
6.5 Conclusions.....	136
6.6 Acknowledgement	138
6.6 Reference	139
Chapter 7 - Conclusion	142
Appendix A - Supporting Information for “TD-DFTB Study of Optical Properties of Silver Nanoparticle Homodimers and Heterodimers”	144
Appendix B - Supporting Information for “Electronic Excited State Dynamics of Naphthalene Studied by Simulated Transient Absorption Spectroscopy”	180
Appendix C - Supporting Information for “Electronic Excited State Dynamics of Au ₂₅ and Au ₃₈ Studied by Simulated Transient Absorption Spectroscopy”	186

List of Figures

Figure 1.1 Plasmon resonance in spherical nanoparticles. Reprinted from Ref.8 with permission from The Royal Society of Chemistry	2
Figure 1.2 Transition densities for the α - and β -peaks of naphthalene. Reprinted with permission from Ref. 22. Copyright 2013 American Chemical Society	3
Figure 1.3 Plasmon interaction diagram that causes a red-shift in the absorption peak upon decreasing the distance between monomers. Reprinted from Ref. 32, with the permission of AIP Publishing	4
Figure 1.4 Plasmon interaction diagram that causes a blue-shift in the absorption peak upon decreasing the distance between monomers Reprinted from Ref.32, with the permission of AIP Publishing	5
Figure 1.5 X-ray crystal structure determination of the $\text{Au}_{102}(\text{p-MBA})_{44}$ nanoparticle. From Ref. 33. Reprinted with permission from AAAS.	6
Figure 1.6 Crystal structure of an $\text{Au}_{25}(\text{SR})_{18}$ cluster. (A) the icosahedral Au_{13} core; (B) the Au_{13} core plus the exterior 12 Au atoms; (C) the whole Au_{25} cluster protected by 18 thiolate ligands. Reprinted with permission from Ref. 34. Copyright 2008 American Chemical Society.....	7
Figure 1.7 (A) Kohn–Sham orbital energy level diagram for a model compound $\text{Au}_{25}(\text{SH})_{18}^-$. (B) The theoretical absorption spectrum of $\text{Au}_{25}(\text{SH})_{18}^-$. Reprinted with permission from Ref. 34. Copyright 2008 American Chemical Society.	8
Figure 1.8 (a) Au_{23} core with the labeling of the surface Au atoms involved in determining the symmetry of the ligand layer. (b) Chiral D_3 arrangement of the Au–S atoms. (c) C_{3h} arrangement of the Au–S atoms. (d) Optimal SCH_3 distribution. Reprinted with permission from Ref. 47. Copyright 2010 American Chemical Society.	9
Figure 2.1 Electronic transition of a transient absorption experiment	33
Figure 2.2 Simulation process of a transient absorption experiment	34
Figure 3.1 Structures for FCC homodimer nanoparticles.	42
Figure 3.2 Structures for FCC heterodimer nanoparticles.	43
Figure 3.3 Calculated absorption spectra for FCC silver nanoparticle monomers. (a) Ag_{14} , (b) Ag_{92} , (c) Ag_{116} , (d) Ag_{164}	46

Figure 3.4	Calculated absorption spectra for FCC silver nanoparticle dimers.	48
Figure 3.5	Distance dependence of the absorption energy from the highest intensity excitation of the Ag ₁₁₆ dimer and the predicted distance dependence of this absorption energy in the form of $E=AR^{-b}$, where the best-fit curve corresponds to $A=-0.8968$, $b=1.7331$	51
Figure 3.6	Distance dependence of the absorption energy from the second highest intensity excitation of the Ag ₁₁₆ dimer and the predicted distance dependence of this absorption energy in the form of $E = AR^{-b}$, with $A=0.0545$, $b=1.3521$	51
Figure 3.7	Distance dependence of the absorption energy from the third highest intensity excitation of the Ag ₁₁₆ dimer and the predicted distance dependence of this absorption energy in the form of $E = AR^{-b}$, with $A=0.0696$, $b=1.5119$	52
Figure 3.8	Distance dependence of absorption energy from the fourth highest energy excitation of the Ag ₁₁₆ dimer and the predicted distance dependence of this absorption energy in the form of $E = AR^{-b}$, with $A=0.1500$, $b=1.8516$	52
Figure 3.9	Calculated absorption spectra for FCC silver nanoparticle heterodimers. (a) Ag ₁₄ and Ag ₉₂ , (b) Ag ₁₄ and Ag ₁₁₆ , (c) Ag ₁₄ and Ag ₁₆₄ , (d) Ag ₉₂ and Ag ₁₁₆ , (e) Ag ₉₂ and Ag ₁₆₄ , (f) Ag ₁₁₆ and Ag ₁₆₄	58
Figure 4.1	Interparticle distances between two identical Ag ₁₄ clusters.	73
Figure 4.2	Short-time electron dynamics in our RT-TDDFTB simulation with an interparticle distance of 25 Å. The dipole moment of NP1 fluctuates under the external field, and the induced dipole moment of NP2 arises from the excitation of NP1.	75
Figure 4.3	(a) Total dipole moment, (b) dipole moment of NP1, and (c) induced dipole moment of NP2 for a nanoparticle dimer with a 50 Å interparticle separation.	77
Figure 4.4	(a) Total dipole moment, (b) dipole moment of NP1, and (c) induced dipole moment of NP2 for a nanoparticle dimer with a 40 Å interparticle separation.	78
Figure 4.5	(a) Total dipole moment, (b) dipole moment of NP1, and (c) induced dipole moment of NP2 for a nanoparticle dimer with a 30 Å interparticle separation.	80
Figure 4.6	(a) Total dipole moment, (b) dipole moment of NP1, and (c) induced dipole moment of NP2 for a nanoparticle dimer with a 25 Å interparticle separation.	81
Figure 4.7	(a) Total dipole moment, (b) dipole moment of NP1, and (c) induced dipole moment of NP2 for a nanoparticle dimer with a 20 Å interparticle separation.	83

Figure 4.8 (a) Total dipole moment, (b) dipole moment of NP1, and (c) induced dipole moment of NP2 for a nanoparticle dimer with a 15 Å interparticle separation.	85
Figure 4.9 (a) Total dipole moment, (b) dipole moment of NP1, and (c) induced dipole moment of NP2 for a nanoparticle dimer with a 12 Å interparticle separation.	87
Figure 4.10 (a) Total dipole moment, (b) dipole moment of NP1, and (c) induced dipole moment of NP2 for a nanoparticle dimer with a 10 Å interparticle separation.	88
Figure 4.11 (a) Total dipole moment, (b) dipole moment of NP1, and (c) induced dipole moment of NP2 for a nanoparticle dimer with a 9 Å interparticle separation.	89
Figure 4.12 (a) Total dipole moment, (b) dipole moment of NP1, and (c) induced dipole moment of NP2 for a nanoparticle dimer with an 8 Å interparticle separation.	90
Figure 5.1 (a) Ground state absorption spectrum of naphthalene calculated from LR-TDDFT and RT-TDDFT showing the plasmonic β peak at 5.74 eV with polarization in the x direction. (b) Orientation of naphthalene. (c) Electronic energy levels and the primary orbital transitions involved in the plasmonic β peak, as determined by LR-TDDFT. Note that all apparent degeneracies are accidental degeneracies; naphthalene belongs to the D_{2h} point group which has irreducible representations with dimension 1.	101
Figure 5.2 Transient absorption spectrum of naphthalene with x-polarized probe after excitation of the plasmonic β peak. Orbital transitions excited with the 5.74 eV pump are shown in black; the orbital transitions determined to be responsible for the indicated excited state absorptions are shown with blue dotted arrows. A transient absorption spectrum covering the range of 0 to 5 eV is shown in Figure B5.2.	104
Figure 5.3 Transient absorption spectrum of naphthalene with y-polarized probe after excitation of the plasmonic β peak. Orbital transitions excited with the 5.74 eV pump are shown in black; the orbital transitions determined to be responsible for the indicated excited state absorptions are shown with blue dotted arrows.	106
Figure 5.4 Transient absorption spectrum of naphthalene with y-polarized probe after excitation of y-polarized pump at 4.1 eV. The orbitals shown are involved in the excited state absorption polarized in the y direction. Orbital transitions excited with the pump are shown in black; the orbital transitions determined to be responsible for the indicated excited state absorptions are shown with blue dotted arrows.	107
Figure 6.1 Kohn–Sham energy level and orbital diagram for Au ₂₅	120

Figure 6.2 Ground state absorption of Au ₂₅ from LR-TDDFT and RT-TDDFT.....	121
Figure 6.3 Transient absorption spectrum of Au ₂₅ with pump energy of 1.40 eV	122
Figure 6.4 (a) Transient absorption spectrum of Au ₂₅ with pump energy of 1.92 eV and (b) Transient absorption spectrum of Au ₂₅ with pump energy of 2.06 eV.....	123
Figure 6.5 Transient absorption spectrum of Au ₂₅ with pump energy of 2.40 eV	125
Figure 6.6 (a) Ground state absorption of Au ₃₈ from LR-TDDFT and RT-TDDFT, (b) Calculated RT-TDDFT absorption spectrum of Au ₃₈ with contributions from x, y, and z polarization directions.....	127
Figure 6.7 Kohn–Sham energy levels and orbital diagram for Au ₃₈	128
Figure 6.8 Transient absorption spectrum of Au ₃₈ with pump energy of 1.04 eV polarized in the z direction	130
Figure 6.9 Transient absorption spectrum of Au ₃₈ with pump energy of 1.37 eV polarized in the x direction	132
Figure 6.10 Transient absorption spectrum of Au ₃₈ with pump energy of 1.62 eV polarized in the z direction and probe in x direction	133
Figure 6.11 Transient absorption spectrum of Au ₃₈ with pump energy of 1.93 eV polarized in the z direction.....	134
Figure 6.12 Dipole fluctuation of Au ₂₅ with pump energy of 2.40 eV.....	135
Figure 6.13 Dipole fluctuation of Au ₃₈ with pump energy of 1.93 eV polarized in z direction.	136
Figure A.1 Calculated absorption spectra for FCC silver nanoparticle dimers at 50 Å.	151
Figure A.2 Energy of highest peak (Peak 1) for different interparticle distance of dimer Ag ₁₄ , A = -1.5030, b = 2.0440	152
Figure A.3 Energy of second highest peak (Peak2) for different interparticle distance of dimer Ag ₁₄ , A = 1.7394, b = 2.2949	152
Figure A.4 Energy of highest peak (Peak 1) for different interparticle distance of dimer Ag ₉₂ , A = -0.3172, b = 1.6486	153
Figure A.5 Energy of second highest peak (Peak 2) for different interparticle distance of dimer Ag ₉₂ , A = 0.1942, b = 1.7809	153
Figure A.6 Energy of third highest peak (Peak 3) for different interparticle distance of dimer Ag ₉₂ , A = -0.9710, b = 2.1528.....	154

Figure A.7 Energy of highest peak (Peak 1) for different interparticle distance of dimer Ag_{164} , $A = -0.1228$, $b = 1.4550$	154
Figure A.8 Energy of second highest peak (Peak 2) for different interparticle distance of dimer Ag_{164} , $A = 0.0487$, $b = 1.3679$	155
Figure A.9 Energy of highest peak (Peak 1) for different interparticle distance of heterodimer Ag_{14} , $A = -0.2276$, $b = 2.5947$	155
Figure A.10 Energy of second highest peak (Peak 2) for different interparticle distance of heterodimer $Ag_{14} Ag_{92}$, $A = 0.1069$, $b = 3.1307$	156
Figure A.11 Energy of highest peak (Peak 1) for different interparticle distance of heterodimer $Ag_{14} Ag_{116}$, $A = -0.3429$, $b = 2.6619$	156
Figure A.12 Energy of second highest peak (Peak 2) for different interparticle distance of heterodimer $Ag_{14} Ag_{116}$, $A = 0.1467$, $b = 3.3415$	157
Figure A.13 Energy of highest peak (Peak 1) for different interparticle distance of heterodimer $Ag_{14} Ag_{164}$, $A = -0.2276$, $b = 2.5947$	157
Figure A.14 Energy of second highest peak (Peak 2) for different interparticle distance of heterodimer $Ag_{14} Ag_{164}$, $A = -0.0278$, $b = 2.3269$	158
Figure A.15 Energy of highest peak (Peak 1) for different interparticle distance of heterodimer $Ag_{92} Ag_{116}$, $A = -0.8416$, $b = 2.3968$	158
Figure A.16 Energy of second highest peak (Peak 2) for different interparticle distance of heterodimer $Ag_{92} Ag_{116}$, $A = 0.0043$, $b = 2.1439$	159
Figure A.17 Energy of third highest peak (Peak 3) for different interparticle distance of heterodimer $Ag_{92} Ag_{116}$, $A = -0.3142$, $b = 2.4084$	159
Figure A.18 Energy of highest peak (Peak 1) for different interparticle distance of heterodimer $Ag_{92} Ag_{164}$, $A = -1.5342$, $b = 2.4044$	160
Figure A.19 Energy of second highest peak (Peak 2) for different interparticle distance of heterodimer $Ag_{92} Ag_{164}$, $A = 0.0249$, $b = 1.4583$	160
Figure A.20 Energy of third highest peak (Peak 3) for different interparticle distance of heterodimer $Ag_{92} Ag_{164}$, $A = 0.0789$, $b = 1.9251$	161
Figure A.21 Energy of highest peak (Peak 1) for different interparticle distance of heterodimer $Ag_{116} Ag_{164}$, $A = -0.8416$, $b = 2.3968$	161

Figure A.22 Energy of second highest peak (Peak 2) for different interparticle distance of heterodimer $\text{Ag}_{116}\text{Ag}_{164}$, $A = 0.0149$, $b = 0.9688$	162
Figure A.23 Energy of third highest peak (Peak 3) for different interparticle distance of heterodimer $\text{Ag}_{116}\text{Ag}_{164}$, $A = -0.3142$, $b = 2.4084$	162
Figure A.24 Plasmon interaction diagram that causes a red-shift in the absorption peak upon decreasing the distance between monomers.	163
Figure A.25 Plasmon interaction diagram that causes a blue-shift in the absorption peak upon decreasing the distance between monomers.	164
Figure B.1 Energy transfer from the electric field to the system Figure B.2. Transient absorption spectrum of naphthalene with x-polarized probe after excitation of the plasmonic β peak	184
Figure B.2 Transient absorption spectrum of naphthalene with x-polarized probe after excitation of the plasmonic β peak	185
Figure C.1 Dipole fluctuation of Au_{25} with pump energy of 1.40 eV	189
Figure C.2 Dipole fluctuation of Au_{25} with pump energy of 1.92 eV	190
Figure C.3 Dipole fluctuation of Au_{25} with pump energy of 2.99 eV	190
Figure C.4 Dipole fluctuation of Au_{38} with pump energy of 1.04 eV polarized in z direction ..	191
Figure C.5 Dipole fluctuation of Au_{38} with pump energy of 1.37 eV polarized in x direction.	191
Figure C.6 Dipole fluctuation of Au_{38} with pump energy of 1.62 eV polarized in z direction.	192

List of Tables

Table A.1 Calculated absorption spectra for FCC silver nanoparticle dimers at 50 Å.....	144
Table A.2 Comparison of Energy of Second Highest Peak (Peak 2) for Ag ₁₁₆ , A = 0.0545, b = 1.3521.....	145
Table A.3 Comparison of Energy of Third Highest Peak (Peak 3) for Ag ₁₁₆ , A = 0.0696, b = 1.5119.....	146
Table A.4 Comparison of Energy of Fourth Highest Peak (Peak 4) for Ag ₁₁₆ , A = 0.1500, b = 1.8516.....	147
Table B.1 The first ten excited states calculated by LR-TDDFT	180
Table B.2 Frontier orbitals with their orbital energy and symmetry representation	181
Table B.3 Possible excited state absorptions induced by the probe pulse due to electronic excitation out of the newly occupied LUMO with b_{2g} symmetry and LUMO+1 with b_{3g} symmetry. The states with B_{3u} symmetry (x-polarized) would be bright state transitions from LUMO and LUMO+1. The states with green font with B_{2u} symmetry (green font) are the y-polarized bright state transitions from LUMO and LUMO+1. The states with B_{1u} symmetry (blue font) are the bright state transitions from LUMO and LUMO+1 polarized in the z direction.....	183
Table B.4 Possible hole excited state absorptions induced by the probe that involve the HOMO with a_u symmetry and HOMO-1 with b_{1u} symmetry. The B_{3u} states (red font) are the x-polarized bright state transitions from HOMO and HOMO-1. The green font with B_{2u} symmetry states (green font) are the y-polarized bright state transitions from HOMO and HOMO-1. The B_{1u} states (blue font) are the z-polarized bright state transitions from HOMO and HOMO-1.....	184
Table C.1 Frontier orbitals with their orbital energy and symmetry representation	186

Acknowledgements

I would like to express my sincere gratitude to my advisor, Christine Aikens for all the guidance, teaching, patient and support through my entire Ph.D. program. She always shows us how to be a good teacher, a good researcher and good professor by example.

I would also like to thank Prof. Jun Li, Prof. Bin Liu and Prof. Loren Greenman for serving as my committee members with their support and time.

I am grateful to the former and current group members of the Aikens group: Dr. Fahri Alkan, Dr. Gowri Udayangani, Dr. Pratima Pandeya, Dr. Olivia Hull, Dr. Shana Havenridge, Yuchen Wang, and Sulalith Samarasinghe.

I would also thank Prof. Bin Liu and his group members Jiayi Xu, Narges Manavi, and Hao Deng for the joint research group meetings and discussion. I would thank our collaborators Prof. Di Sun, Prof. Ken Knappenberger, William Jeffries, Prof. Caterina Cocchi, Jannis Krumland, Prof. Bryan Wong, and Dr. M. Belen Oviedo.

I would also thank my undergraduate advisor Prof. Shenmin Li and Prof. Xin Zhou who brought me to the wonderful computational chemistry field.

Last but not least, I would like to thank my family, especially my beloved wife, Fengqing Di, for all the support. I would like to express my appreciation to my parents Hongzhang Liu and Luyan Zhang for highly valuing education for me and my younger brother, Tuo Liu.

Chapter 1 - Introduction

1.1 Plasmon resonance

The earliest plasmonic feature can be found in the Lycurgus cup which was created in the 4th century.¹ The Lycurgus cup will show different colors under different light sources. However, the explanation for this effect, which arises as a result of plasmonic features, was not recognized then. In 1908, Gustav Mie solved Maxwell's equations for the absorption and scattering cross section for spherical colloidal nanoparticles.² The plasmons of spherical metallic nanoparticles ranging from 100 nm to 10 nm are well described through Mie theory.^{3,4} With recent developments in nanoparticle synthesis and separation, smaller sized (less than 2 nm) and differently shaped nanoparticles have been synthesized, and the properties of these systems are of great interest.⁵⁻⁷ However, the small sizes and complicated shapes cannot be calculated through Mie theory.^{3,4} Since the plasmon resonance is an electronic effect, quantum mechanics methods can be used to fully reveal its origin.

The surface plasmon resonance (SPR) has been one of the most important features of nanoparticles. Plasmons are defined as collective electronic oscillations under the external field, as shown in Figure 1.1.⁸ In optical absorption spectroscopy, a strong absorption peak can be found that corresponds to the collective oscillation of electrons from one side of the nanoparticle to the other.⁸ The plasmon in nanoparticles is of great research interest for both fundamental science in examining the collective electron effect^{9,10} and for applications such as photocatalysis¹¹⁻¹³ and bioimaging.^{14,15}

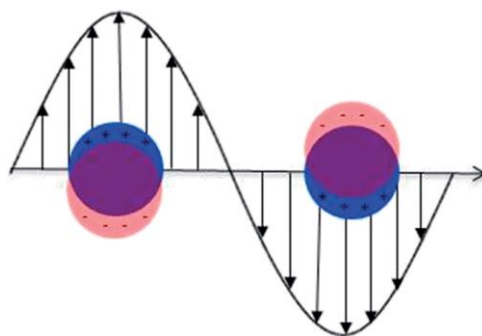


Figure 1.1 Plasmon resonance in spherical nanoparticles. Reprinted from Ref.8 with permission from The Royal Society of Chemistry

1.2 Molecular plasmons

Graphene has been the first and the most studied two-dimensional material since it was isolated by Geim and Novoselov.¹⁶ Due to its unique electronic structure, graphene has been used in photodetectors,¹⁷ optical modulators,¹⁸ and photovoltaic devices.¹⁹ Fully understanding the graphene and light interaction is key to further exploring its application. The existence of surface plasmons in graphene results in strong light confinement, which make it a great material for plasmonic biosensors.²⁰ Polycyclic aromatic hydrocarbons (PAHs) are regarded as a building block of graphene.²¹ The constructive interaction between two or more single particle transitions in PAHs is known as a molecular plasmon.^{8,22,23}

Naphthalene is the simplest molecule with plasmon-like character, which makes it an ideal platform for understanding the origin of plasmon resonances. As shown in Figure 1.2, the strong β peak in the absorption spectrum of naphthalene corresponds to electron density moving from one side to other side.²² This transition can be constructed by two single-particle transitions.²²

Transition densities

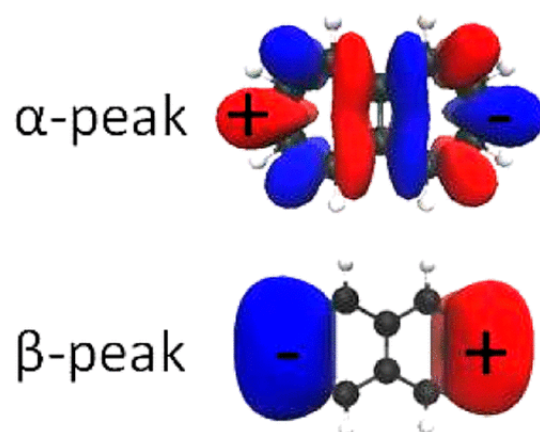


Figure 1.2 Transition densities for the α - and β -peaks of naphthalene. Reprinted with permission from Ref. 22. Copyright 2013 American Chemical Society.

1.3 Nanoparticle dimers

Due to strong plasmonic coupling, the electronic structure and optical properties of nanoparticles are highly affected by the presence of neighboring nanoparticles.²⁴⁻²⁹ A nanoparticle dimer is the simplest model to study nanoparticle interactions, which can provide a model for the systematic study of nanoparticle plasmonic interactions and can pave the way for further understanding of hybridized plasmons^{24,30,31} in more complex systems. When the surface plasmons are excited, the nanoparticle junction can experience a large electromagnetic field enhancement.²⁹ Studying the interaction of nanoparticles dimers can also provide more understanding regarding the resulting electromagnetic field enhancements.²⁹

In this dissertation, the optical properties of face-centered cubic (FCC) Ag₁₄, Ag₉₂, Ag₁₁₆, and Ag₁₆₄ are studied through calculated absorption spectra. The absorption spectra peak shifting is dependent on the polarization direction of the transition dipole moment. When the absorption peak of the dimer is polarized in the z direction (i.e. the nanoparticle interaction axis), absorption

peak red shifting can be observed as the distance decreases as shown in Figure 1.3. Conversely, while the absorption peak of the dimer is polarized in the x-y plane (i.e. perpendicular to the nanoparticle interaction axis), the absorption peak blue shifts as the distance decreases as shown in Figure 1.4.

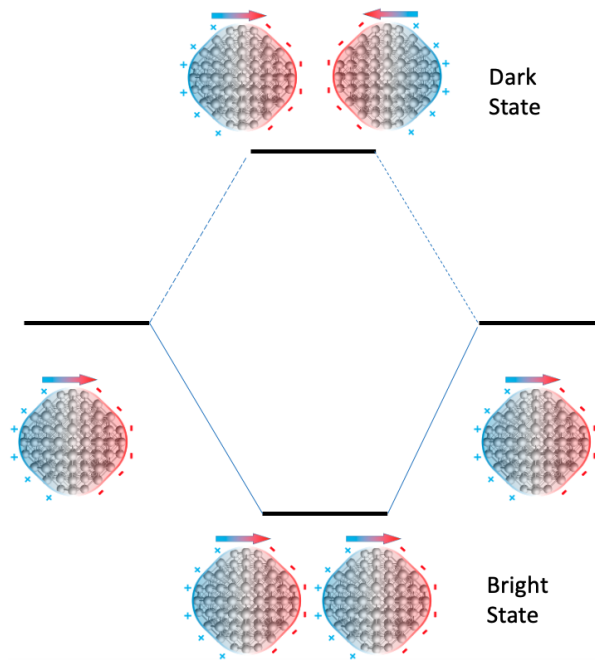


Figure 1.3 Plasmon interaction diagram that causes a red-shift in the absorption peak upon decreasing the distance between monomers. Reprinted from Ref. 32, with the permission of AIP Publishing.

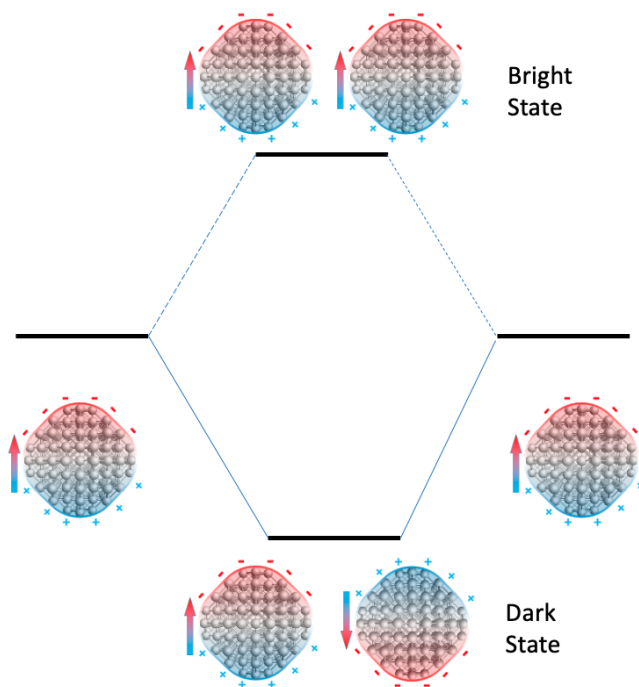


Figure 1.4 Plasmon interaction diagram that causes a blue-shift in the absorption peak upon decreasing the distance between monomers Reprinted from Ref.32, with the permission of AIP Publishing.

1.4 Thiolate protected nanoparticles

In 2007, the ligand-protected noble metal nanoparticle community saw dramatic change with the advent of atomically precise structural determination. The first X-ray crystal structure, of the $\text{Au}_{102}(\text{p-MBA})_{44}$ nanoparticle (Figure 1.5), opened the door for exploring fully space-resolved nanoclusters.³³

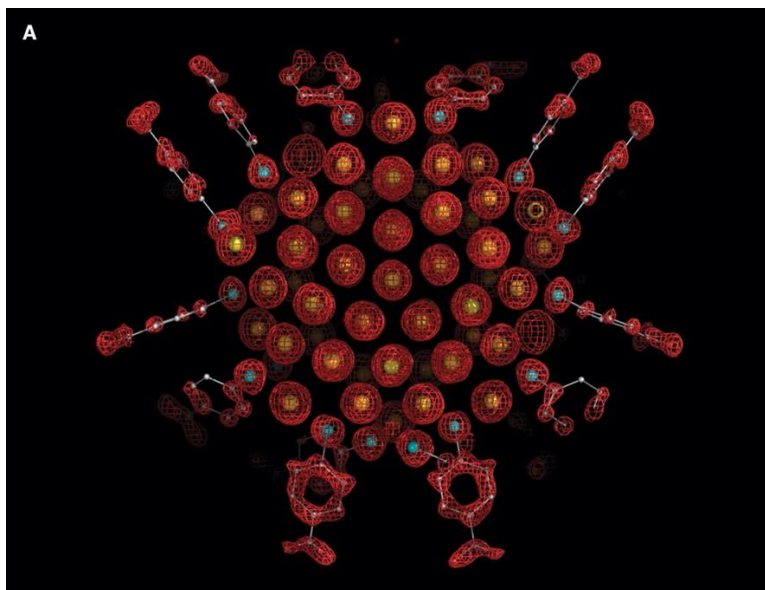


Figure 1.5 X-ray crystal structure determination of the Au₁₀₂(p-MBA)₄₄ nanoparticle. From Ref. 33. Reprinted with permission from AAAS.

By 2008, another nanocluster Au₂₅(SR)₁₈⁻ had been synthesized. With X-ray crystallographic analysis and TDDFT calculations, the nanocluster Au₂₅(SR)₁₈⁻ had not only been resolved in space with atomically precise structural determination (Figure 1.6), but also fully resolved in the energy regime with precise determination of the absorption peaks in its optical absorption spectra as shown in Figure 1.7.³⁴ Up to date, Au₂₅(SR)₁₈⁻ has been the most extensively studied thiolate protected nanocluster.³⁵ The role of ligand,^{36–38} effect of doping,^{39–41} luminescence^{42–44} and solvent effect^{36,45,46} has been studied.

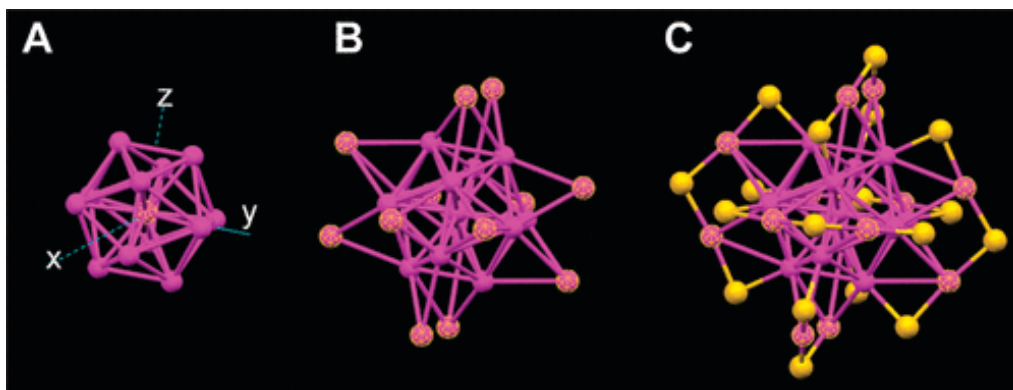


Figure 1.6 Crystal structure of an Au₂₅(SR)₁₈ cluster. (A) the icosahedral Au₁₃ core; (B) the Au₁₃ core plus the exterior 12 Au atoms; (C) the whole Au₂₅ cluster protected by 18 thiolate ligands. Reprinted with permission from Ref. 34. Copyright 2008 American Chemical Society.

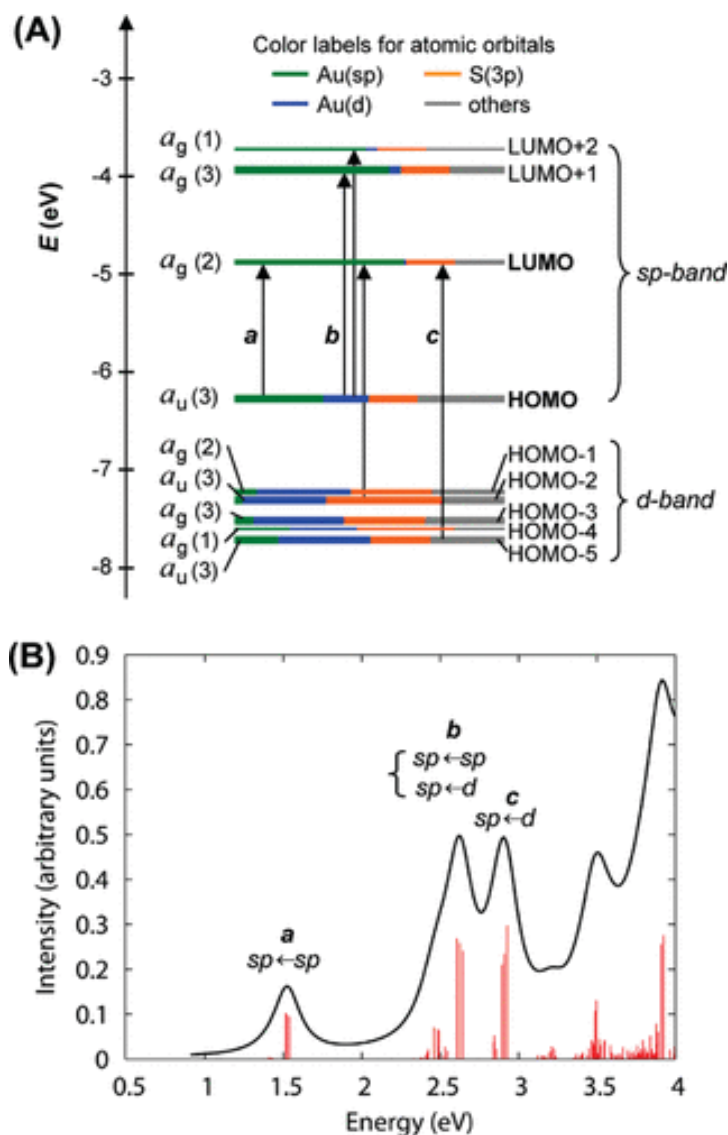


Figure 1.7 (A) Kohn–Sham orbital energy level diagram for a model compound $\text{Au}_{25}(\text{SH})_{18}^-$. (B) The theoretical absorption spectrum of $\text{Au}_{25}(\text{SH})_{18}^-$. Reprinted with permission from Ref. 34. Copyright 2008 American Chemical Society.

The structure of $\text{Au}_{38}(\text{SR})_{24}$ predicted theoretically by Zeng and Aikens groups^{47,48} was independently synthesized and verified experimentally by the Jin group.⁴⁹ As shown in Figure 1.8, $\text{Au}_{38}(\text{SR})_{24}$ consists of a bi-icosahedral core surrounded by three short and six long motifs. The elongated nanorod-shaped $\text{Au}_{38}(\text{SR})_{24}$ has a unique electronic structure compared to a spherical nanoparticle. In Chapter 6, the simulated pump-probe experiments are performed to study $\text{Au}_{25}(\text{SR})_{18}^-$ and $\text{Au}_{38}(\text{SR})_{24}$. The nanorod-shaped $\text{Au}_{38}(\text{SR})_{24}$ will confine the dipole oscillation in

the pump direction, while spherical nanocluster $\text{Au}_{25}(\text{SR})_{18}^-$ transfers the energy from the pump direction to the other two directions.

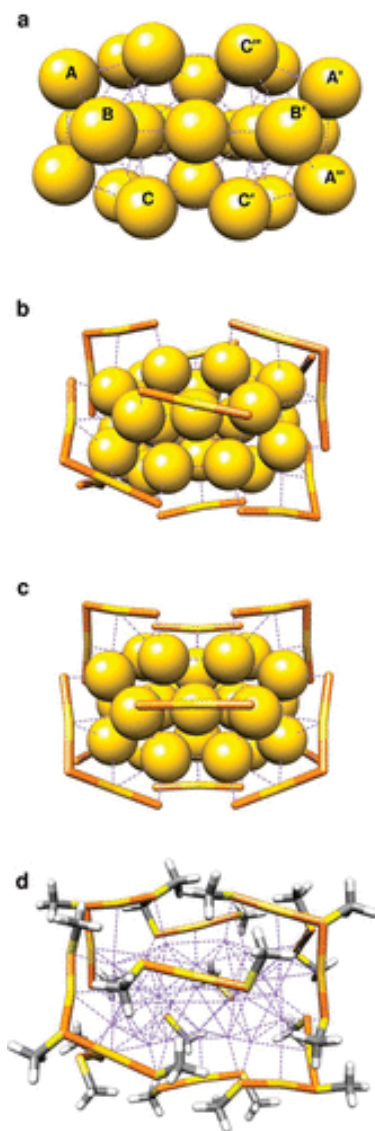


Figure 1.8 (a) Au_{23} core with the labeling of the surface Au atoms involved in determining the symmetry of the ligand layer. (b) Chiral D_3 arrangement of the Au-S atoms. (c) C_{3h} arrangement of the Au-S atoms. (d) Optimal SCH_3 distribution. Reprinted with permission from Ref. 47. Copyright 2010 American Chemical Society.

1.4.1 Ultrafast electron dynamics in thiolate-protected nanoparticles

Transient absorption spectroscopy is one kind of time-resolved spectroscopy that is a powerful tool for monitoring the excited state dynamics.^{50,51} The first transient absorption spectroscopy experiment on smaller nanoparticles (i.e., diameters less than 2 nm) was performed in 2002, even before the structure of the nanoparticle had been fully resolved.⁵² In the study, $\text{Au}_{25}(\text{SG})_{18}^-$ shows a biexponential decay with a fast sub-picosecond and a much slower nanosecond decay.⁵² One year after the fully resolved coordinates of Au_{25} were achieved, Moran and coworkers studied the ultrafast dynamics of Au_{25} by exciting the Au_{13} core in Au_{25} . In the pump-probe experiment, a sub 200 fs internal conversion process between the multilevel electronic structure was found. The experimentally observed process in the picosecond range was later identified to arise from core-to-core transitions rather than from a core-to-semiring transition.^{53,54} In 2016, Knappenberger and coworkers performed the first femtosecond two-dimensional spectroscopy experiments to study Au_{25} . In their experiment, a 200 ± 15 fs timescale of hot electron relaxation was distinguished from the manifold of superatom D states from 290 ± 200 fs hot hole relaxation with the superatom P states.⁵⁵ Zhou and coworkers observed a two-state relaxation in both Au_{38} isomers despite the significant differences in their geometrical structure.⁵⁶ Knappenberger and coworkers performed both femtosecond transient absorption and two-dimensional electronic spectroscopy to study the electronic charge carrier relaxation dynamics of $\text{Au}_{38}(\text{SC}_6\text{H}_{13})_{24}$. They found a rapid 120 ± 20 fs and a slower 905 ± 115 fs decay, and the off-diagonal cross peaks indicated a sub 100 fs state-to-state dynamics.⁵⁷

Transient absorption spectroscopy is one of the most powerful tools for characterizing and probing the excited state dynamics in atomically precise nanoclusters. It can both provide physical

insight into the dynamics process and advance the application in energy harvesting. The details of simulated transient absorption spectroscopy are discussed in Chapter 2. Prior to the work described in this dissertation, the ultrafast excited state dynamics of nanoparticles had been studied after the excitation with femtosecond laser pulses, even before the geometries of nanoparticles had been fully determined. The atomically precise nanoclusters Au_{25} and Au_{38} had also been fully resolved in space and in energy. With the help of theoretical transient absorption spectroscopy, ultrafast electron dynamics in Au_{25} and Au_{38} are being resolved with femtosecond time-resolution through ab initio calculations.

1.5 Objectives and Outlook

This thesis focuses on providing a systematic study of nanoparticle-nanoparticle interactions and light-matter interactions in nanoparticles and related systems. Chapter 2 provides the computational details used in this thesis, including density functional theory and the density functional theory tight-binding approach. Chapter 3 describes the optical properties of silver nanoparticle homodimers and heterodimers. Using the computational efficiency of the tight-binding formalism, different interparticle distances in silver nanoparticle homodimers and heterodimers were calculated and thoroughly analyzed. We found that the peak shifting is related to the transition dipole moment direction. Chapter 4 presents a simulation of energy transfer between nanoparticles. The total dipole moment increases as the interparticle distance decrease in large distance. At a short distance, back-transfer effects were observed, which reduced the ability of the dimer to accept energy from the incident electric field. The plasmon-induced excitation energy transformations in silver nanoparticles also benefitted from the tight-binding method. The electron dynamics in ab initio calculation reaches the picosecond time regime with an attosecond

time step so that time scales varying over six orders of magnitude were achieved. Then, the plasmonic molecule, naphthalene, and atomically precise nanoclusters, Au₂₅ and Au₃₈, were studied by simulated transient absorption spectroscopy. Chapter 5 provides the simulated transient absorption spectra of naphthalene. By selectively exciting the plasmon peak or single particle transitions, we observed different transient absorption signals. Chapter 6 provides the work of simulated transient absorption spectroscopy for atomically precise nanoclusters, Au₂₅ and Au₃₈.

1.6 References

- (1) Freestone, I.; Meeks, N.; Sax, M.; Higgitt, C. The Lycurgus Cup — A Roman Nanotechnology. *Gold Bull* 2007, 40 (4), 270–277. <https://doi.org/10.1007/BF03215599>.
- (2) Mie, G. Beiträge zur Optik trüber Medien, speziell kolloidaler Metallösungen. *Ann. Phys.* 1908, 330 (3), 377–445. <https://doi.org/10.1002/andp.19083300302>.
- (3) Kelly, K. L.; Coronado, E.; Zhao, L. L.; Schatz, G. C. The Optical Properties of Metal Nanoparticles: The Influence of Size, Shape, and Dielectric Environment. *J. Phys. Chem. B* 2003, 107, 668.
- (4) Jain, P. K.; Lee, K. S.; El-Sayed, I. H.; El-Sayed, M. A. Calculated Absorption and Scattering Properties of Gold Nanoparticles of Different Size, Shape, and Composition: Applications in Biological Imaging and Biomedicine. *J. Phys. Chem. B* 2006, 110, 7238.
- (5) Chen, S.; Ingram, R. S.; Hostetler, M. J.; Pietron, J. J.; Murray, R. W.; Schaaff, T. G.; Khoury, J. T.; Alvarez, M. M.; Whetten, R. L. Gold Nanoelectrodes of Varied Size: Transition to Molecule-Like Charging. *Science* 1998, 280 (5372), 2098–2101. <https://doi.org/10.1126/science.280.5372.2098>.
- (6) Sardar, R.; Funston, A. M.; Mulvaney, P.; Murray, R. W. Gold Nanoparticles: Past, Present, and Future. *Langmuir* 2009, 25 (24), 13840–13851. <https://doi.org/10.1021/la9019475>.
- (7) Whetten, R. L.; Khoury, J. T.; Alvarez, M. M.; Murthy, S.; Vezmar, I.; Wang, Z. L.; Stephens, P. W.; Cleveland, C. L.; Luedtke, W. D.; Landman, U. Nanocrystal Gold Molecules. *Adv. Mater.* 1996, 8 (5), 428–433. <https://doi.org/10.1002/adma.19960080513>.

- (8) Guidez, E. B.; Aikens, C. M. Quantum Mechanical Origin of the Plasmon: From Molecular Systems to Nanoparticles. *Nanoscale* 2014, 6 (20), 11512–11527. <https://doi.org/10.1039/C4NR02225D>.
- (9) El-Sayed, I. H.; Huang, X. H.; El-Sayed, M. A. Surface Plasmon Resonance Scattering and Absorption of Anti-EGFR Antibody Conjugated Gold Nanoparticles in Cancer Diagnostics: Applications in Oral Cancer. *Nano Lett.* 2005, 5, 829.
- (10) Link, S.; El-Sayed, M. A. Spectral Properties and Relaxation Dynamics of Surface Plasmon Electronic Oscillations in Gold and Silver Nanodots and Nanorods. *J. Phys. Chem. B* 1999, 103 (40), 8410–8426. <https://doi.org/10.1021/jp9917648>.
- (11) Sanchez, A.; Abbet, S.; Heiz, U.; Schneider, W.-D.; Häkkinen, H.; Barnett, R. N.; Landman, U. When Gold Is Not Noble: Nanoscale Gold Catalysts. *J. Phys. Chem. A* 1999, 103 (48), 9573–9578. <https://doi.org/10.1021/jp9935992>.
- (12) Gao, Y.; Shao, N.; Pei, Y.; Chen, Z.; Zeng, X. C. Catalytic Activities of Subnanometer Gold Clusters (Au_{16} – Au_{18} , Au_{20} , and Au_{27} – Au_{35}) for CO Oxidation. *ACS Nano* 2011, 5 (10), 7818–7829. <https://doi.org/10.1021/nn201817b>.
- (13) Wallace, W. T.; Whetten, R. L. Coadsorption of CO and O₂ on Selected Gold Clusters: Evidence for Efficient Room-Temperature CO₂ Generation. *J. Am. Chem. Soc.* 2002, 124 (25), 7499–7505. <https://doi.org/10.1021/ja0175439>.
- (14) Liu, J.; Yu, M.; Zhou, C.; Yang, S.; Ning, X.; Zheng, J. Passive Tumor Targeting of Renal-Clearable Luminescent Gold Nanoparticles: Long Tumor Retention and Fast Normal

Tissue Clearance. *J. Am. Chem. Soc.* 2013, 135 (13), 4978–4981.

<https://doi.org/10.1021/ja401612x>.

(15) Liu, J.; Yu, M.; Ning, X.; Zhou, C.; Yang, S.; Zheng, J. PEGylation and Zwitterionization: Pros and Cons in the Renal Clearance and Tumor Targeting of Near-IR-Emitting Gold Nanoparticles. *Angew. Chem. Int. Ed.* 2013, 52 (48), 12572–12576.

<https://doi.org/10.1002/anie.201304465>.

(16) Novoselov, K. S.; Geim, A. K.; Morozov, S. V.; Jiang, D.; Zhang, Y.; Dubonos, S. V.; Grigorieva, I. V.; Firsov, A. A. Electric Field Effect in Atomically Thin Carbon Films. *Science* 2004, 306 (5696), 666–669. <https://doi.org/10.1126/science.1102896>.

(17) Xia, F.; Mueller, T.; Lin, Y.; Valdes-Garcia, A.; Avouris, P. Ultrafast Graphene Photodetector. *Nature Nanotech* 2009, 4 (12), 839–843. <https://doi.org/10.1038/nnano.2009.292>.

(18) Liu, M.; Yin, X.; Ulin-Avila, E.; Geng, B.; Zentgraf, T.; Ju, L.; Wang, F.; Zhang, X. A Graphene-Based Broadband Optical Modulator. *Nature* 2011, 474 (7349), 64–67.

<https://doi.org/10.1038/nature10067>.

(19) Bonaccorso, F.; Sun, Z.; Hasan, T.; Ferrari, A. C. Graphene Photonics and Optoelectronics. *Nature Photon* 2010, 4 (9), 611–622. <https://doi.org/10.1038/nphoton.2010.186>.

(20) Rodrigo, D.; Limaj, O.; Janner, D.; Etezadi, D.; García de Abajo, F. J.; Pruneri, V.; Altug, H. Mid-Infrared Plasmonic Biosensing with Graphene. *Science* 2015, 349 (6244), 165–168. <https://doi.org/10.1126/science.aab2051>.

- (21) Chen, L.; Hernandez, Y.; Feng, X.; Müllen, K. From Nanographene and Graphene Nanoribbons to Graphene Sheets: Chemical Synthesis. *Angew. Chem. Int. Ed.* 2012, 51 (31), 7640–7654. <https://doi.org/10.1002/anie.201201084>.
- (22) Guidez, E. B.; Aikens, C. M. Origin and TDDFT Benchmarking of the Plasmon Resonance in Acenes. *J. Phys. Chem. C* 2013, 117 (41), 21466–21475. <https://doi.org/10.1021/jp4059033>.
- (23) Chapkin, K. D.; Bursi, L.; Stec, G. J.; Lauchner, A.; Hogan, N. J.; Cui, Y.; Nordlander, P.; Halas, N. J. Lifetime Dynamics of Plasmons in the Few-Atom Limit. *Proc. Natl. Acad. Sci. U.S.A.* 2018, 115 (37), 9134–9139. <https://doi.org/10.1073/pnas.1805357115>.
- (24) Nordlander, P.; Oubre, C.; Prodan, E.; Li, K.; Stockman, M. I. Plasmon Hybridization in Nanoparticle Dimers. *Nano Lett.* 2004, 4, 899.
- (25) Aćimović, S. S.; Kreuzer, M. P.; González, M. U.; Quidant, R. Plasmon Near-Field Coupling in Metal Dimers as a Step toward Single-Molecule Sensing. *ACS Nano* 2009, 3, 1231.
- (26) Alkan, F.; Aikens, C. M. TD-DFT and TD-DFTB Investigation of the Optical Properties and Electronic Structure of Silver Nanorods and Nanorod Dimers. *J. Phys. Chem. C* 2018, 122 (41), 23639–23650. <https://doi.org/10.1021/acs.jpcc.8b05196>.
- (27) Alkan, F.; Aikens, C. M. Understanding Plasmon Coupling in Nanoparticle Dimers Using Molecular Orbitals and Configuration Interaction. *Phys. Chem. Chem. Phys.* 2019, 21 (41), 23065–23075. <https://doi.org/10.1039/C9CP03890F>.

- (28) Bae, G. T.; Aikens, C. M. Time-Dependent Density Functional Theory Studies of Optical Properties of Ag Nanoparticles: Octahedra, Truncated Octahedra, and Icosahedra. *J. Phys. Chem. C* 2012, 116, 10356.
- (29) Marinica, D. C.; Kazansky, A. K.; Nordlander, P.; Aizpurua, J.; Borisov, A. G. Quantum Plasmonics: Nonlinear Effects in the Field Enhancement of a Plasmonic Nanoparticle Dimer. *Nano Lett.* 2012, 12, 1333.
- (30) Prodan, E.; Nordlander, P. Structural Tunability of the Plasmon Resonances in Metallic Nanoshells. *Nano Lett.* 2003, 3, 543.
- (31) Willingham, B.; Brandl, D. W.; Nordlander, P. Plasmon Hybridization in Nanorod Dimers. *Appl. Phys. B* 2008, 93, 209.
- (32) Liu, Z.; Alkan, F.; Aikens, C. M. TD-DFTB Study of Optical Properties of Silver Nanoparticle Homodimers and Heterodimers. *J. Chem. Phys.* 2020, 153 (14), 144711. <https://doi.org/10.1063/5.0025672>.
- (33) Jadzinsky, P. D.; Calero, G.; Ackerson, C. J.; Bushnell, D. A.; Kornberg, R. D. Structure of a Thiol Monolayer-Protected Gold Nanoparticle at 1.1 Å Resolution. *Science* 2007, 318 (5849), 430–433. <https://doi.org/10.1126/science.1148624>.
- (34) Zhu, M.; Aikens, C. M.; Hollander, F. J.; Schatz, G. C.; Jin, R. Correlating the Crystal Structure of A Thiol-Protected Au₂₅ Cluster and Optical Properties. *J. Am. Chem. Soc.* 2008, 130 (18), 5883–5885. <https://doi.org/10.1021/ja801173r>.
- (35) Kang, X.; Chong, H.; Zhu, M. Au₂₅(SR)₁₈: The Captain of the Great Nanocluster Ship. *Nanoscale* 2018, 10 (23), 10758–10834. <https://doi.org/10.1039/C8NR02973C>.

- (36) Aikens, C. M. Effects of Core Distances, Solvent, Ligand, and Level of Theory on the TDDFT Optical Absorption Spectrum of the Thiolate-Protected Au₂₅ Nanoparticle. *J. Phys. Chem. A* 2009, 113 (40), 10811–10817. <https://doi.org/10.1021/jp9051853>.
- (37) Fernando, A.; Aikens, C. M. Ligand Exchange Mechanism on Thiolate Monolayer Protected Au₂₅(SR)₁₈ Nanoclusters. *J. Phys. Chem. C* 2015, 119 (34), 20179–20187. <https://doi.org/10.1021/acs.jpcc.5b06833>.
- (38) Parker, J. F.; Weaver, J. E. F.; McCallum, F.; Fields-Zinna, C. A.; Murray, R. W. Synthesis of Monodisperse [Oct₄N⁺][Au₂₅(SR)₁₈⁻] Nanoparticles, with Some Mechanistic Observations. *Langmuir* 2010, 26 (16), 13650–13654. <https://doi.org/10.1021/la1020466>.
- (39) Guidez, E. B.; Mäkinen, V.; Häkkinen, H.; Aikens, C. M. Effects of Silver Doping on the Geometric and Electronic Structure and Optical Absorption Spectra of the Au_{25-n}Ag_n(SH)₁₈⁻ (n = 1, 2, 4, 6, 8, 10, 12) Bimetallic Nanoclusters. *J. Phys. Chem. C* 2012, 116 (38), 20617–20624. <https://doi.org/10.1021/jp306885u>.
- (40) Wang, S.; Song, Y.; Jin, S.; Liu, X.; Zhang, J.; Pei, Y.; Meng, X.; Chen, M.; Li, P.; Zhu, M. Metal Exchange Method Using Au₂₅ Nanoclusters as Templates for Alloy Nanoclusters with Atomic Precision. *J. Am. Chem. Soc.* 2015, 137 (12), 4018–4021. <https://doi.org/10.1021/ja511635g>.
- (41) Negishi, Y.; Iwai, T.; Ide, M. Continuous Modulation of Electronic Structure of Stable Thiolate-Protected Au₂₅ Cluster by Ag Doping. *Chem. Commun.* 2010, 46 (26), 4713. <https://doi.org/10.1039/c0cc01021a>.

- (42) Weerawardene, K. L. D. M.; Aikens, C. M. Theoretical Insights into the Origin of Photoluminescence of $\text{Au}_{25}(\text{SR})_{18}^-$ Nanoparticles. *J. Am. Chem. Soc.* 2016, 138 (35), 11202–11210. <https://doi.org/10.1021/jacs.6b05293>.
- (43) Tao, Y.; Li, M.; Ren, J.; Qu, X. Metal Nanoclusters: Novel Probes for Diagnostic and Therapeutic Applications. *Chem. Soc. Rev.* 2015, 44 (23), 8636–8663. <https://doi.org/10.1039/C5CS00607D>.
- (44) Wang, S.; Zhu, X.; Cao, T.; Zhu, M. A Simple Model for Understanding the Fluorescence Behavior of Au_{25} Nanoclusters. *Nanoscale* 2014, 6 (11), 5777. <https://doi.org/10.1039/c3nr06722j>.
- (45) Raut, S.; Chib, R.; Rich, R.; Shumilov, D.; Gryczynski, Z.; Gryczynski, I. Polarization Properties of Fluorescent BSA Protected Au_{25} Nanoclusters. *Nanoscale* 2013, 5 (8), 3441. <https://doi.org/10.1039/c3nr34152f>.
- (46) Collins, C. B.; Tofanelli, M. A.; Crook, M. F.; Phillips, B. D.; Ackerson, C. J. Practical Stability of $\text{Au}_{25}(\text{SR})_{18}^{-1/0/+1}$. *RSC Adv.* 2017, 7 (71), 45061–45065. <https://doi.org/10.1039/C7RA07511A>.
- (47) Lopez-Acevedo, O.; Tsunoyama, H.; Tsukuda, T.; Häkkinen, H.; Aikens, C. M. Chirality and Electronic Structure of the Thiolate-Protected Au_{38} Nanocluster. *J. Am. Chem. Soc.* 2010, 132 (23), 8210–8218. <https://doi.org/10.1021/ja102934q>.
- (48) Pei, Y.; Gao, Y.; Zeng, X. C. Structural Prediction of Thiolate-Protected Au_{38} : A Face-Fused Bi-Icosahedral Au Core. *J. Am. Chem. Soc.* 2008, 130 (25), 7830–7832. <https://doi.org/10.1021/ja802975b>.

- (49) Qian, H.; Eckenhoff, W. T.; Zhu, Y.; Pintauer, T.; Jin, R. Total Structure Determination of Thiolate-Protected Au₃₈ Nanoparticles. *J. Am. Chem. Soc.* 2010, 132 (24), 8280–8281. <https://doi.org/10.1021/ja103592z>.
- (50) Hollas, J. M. *Modern Spectroscopy*, 4th ed.; J. Wiley: Chichester ; Hoboken, NJ, 2004.
- (51) McHale, J. L. *Molecular Spectroscopy*, Second edition.; CRC Press, Taylor & Francis Group: Boca Raton, 2017.
- (52) Link, S.; El-Sayed, M. A.; Gregory Schaaff, T.; Whetten, R. L. Transition from Nanoparticle to Molecular Behavior: A Femtosecond Transient Absorption Study of a Size-Selected 28 Atom Gold Cluster. *Chemical Physics Letters* 2002, 356 (3), 240–246. [https://doi.org/10.1016/S0009-2614\(02\)00306-8](https://doi.org/10.1016/S0009-2614(02)00306-8).
- (53) Miller, S. A.; Womick, J. M.; Parker, J. F.; Murray, R. W.; Moran, A. M. Femtosecond Relaxation Dynamics of Au₂₅L₁₈⁻ Monolayer-Protected Clusters. *J. Phys. Chem. C* 2009, 113 (22), 9440–9444. <https://doi.org/10.1021/jp9025046>.
- (54) Senanayake, R. D.; Guidez, E. B.; Neukirch, A. J.; Prezhdo, O. V.; Aikens, C. M. Theoretical Investigation of Relaxation Dynamics in Au₃₈(SH)₂₄ Thiolate-Protected Gold Nanoclusters. *J. Phys. Chem. C* 2018, 122 (28), 16380–16388. <https://doi.org/10.1021/acs.jpcc.8b03595>.
- (55) Stoll, T.; Sgrò, E.; Jarrett, J. W.; Réhault, J.; Oriana, A.; Sala, L.; Branchi, F.; Cerullo, G.; Knappenberger, K. L. Superatom State-Resolved Dynamics of the Au₂₅(SC₈H₉)₁₈⁻ Cluster from Two-Dimensional Electronic Spectroscopy. *J. Am. Chem. Soc.* 2016, 138 (6), 1788–1791. <https://doi.org/10.1021/jacs.5b12621>.

(56) Zhou, M.; Tian, S.; Zeng, C.; Sfeir, M. Y.; Wu, Z.; Jin, R. Ultrafast Relaxation Dynamics of Au₃₈(SC₂H₄Ph)₂₄ Nanoclusters and Effects of Structural Isomerism. *J. Phys. Chem. C* 2017, 121 (20), 10686–10693. <https://doi.org/10.1021/acs.jpcc.6b10360>.

(57) Jeffries, W. R.; Wallace, J. L.; Knappenberger, K. L. Ultrafast Relaxation Dynamics of Au₃₈(SC₆H₁₃)₂₄ Monolayer-Protected Clusters Resolved by Two-Dimensional Electronic Spectroscopy. *J. Chem. Phys.* 2021, 155 (12), 124303. <https://doi.org/10.1063/5.0056832>.

Chapter 2 - Theoretical methods

2.1 Fundamentals of Electronic Structure Theory

Electronic structure determines the chemical, optical and electrical properties of a molecule. The electronic structure of a given molecule is obtained by solving the Schrödinger Equation, which is the central goal of quantum chemistry.¹⁻³ The Schrödinger Equation is a key result and significant landmark in quantum mechanics.⁴ The most general form is the time-dependent Schrödinger equation⁴

$$i\hbar \frac{\partial}{\partial t} \Psi(\vec{r}, t) = \hat{\mathcal{H}}(\vec{r}, t) \Psi(\vec{r}, t) \quad (2.1)$$

$$\hat{\mathcal{H}}(\vec{r}, t) = \hat{T}(\vec{r}, t) + V(\vec{r}, t) \quad (2.2)$$

$$\hat{T}(\vec{r}, t) = -\frac{\hbar^2}{2m} \nabla^2 \quad (2.3)$$

where $\Psi(\vec{r}, t)$ is the wavefunction, which includes all the information about the particle. The wave function Ψ depends on position \vec{r} and time t . \hbar is $h/2\pi$, where h is the Planck constant. The $\hat{\mathcal{H}}$ includes a kinetic part and a potential part. For a bound system, the potential energy and kinetic energy are time-independent. The Hamiltonian operator that yields total energy for a stationary state should also be time-independent.

$$\hat{\mathcal{H}}(\vec{r}, t) = \hat{\mathcal{H}}(\vec{r}) = \hat{T}(\vec{r}) + V(\vec{r}) \quad (2.4)$$

$$\hat{\mathcal{H}}(\vec{r}) \Psi(\vec{r}, t) = E(\vec{r}) \Psi(\vec{r}, t) \quad (2.5)$$

In this case, the wave function can be separated as a phase factor multiplied by the spatial wave function.

$$\Psi(\vec{r}, t) = \Psi(\vec{r}) e^{-iEt} \quad (2.6)$$

For the time-independent case, the phase factor can be neglected. The time-independent Schrödinger Equation is represented as:

$$\hat{\mathcal{H}}|\Phi\rangle = E|\Phi\rangle \quad (2.7)$$

$$\begin{aligned} \hat{\mathcal{H}} &= -\sum_{i=1}^N \frac{1}{2} \nabla_i^2 - \sum_{A=1}^M \frac{1}{2M_A} \nabla_A^2 - \sum_{i=1}^N \sum_{A=1}^M \frac{Z_A}{r_{iA}} + \sum_{i=1}^N \sum_{j>i}^N \frac{1}{r_{ij}} + \sum_{A=1}^M \sum_{B>A}^M \frac{Z_A Z_B}{R_{AB}} \\ &= \hat{T}_e + \hat{T}_n + \hat{V}_{e-n} + \hat{V}_{e-e} + \hat{V}_{n-n} \end{aligned} \quad (2.8)$$

Since the mass of the electron is far smaller than the nuclear mass, and the electron motion is far faster than nuclear motion, the Born-Oppenheimer (BO) approximation^{1,5} is valid for most cases in quantum chemistry calculations. Under the BO approximation, the kinetic energy of the nuclei (\hat{T}_n) is neglected, and the nuclear-nuclear potential (\hat{V}_{n-n}) is held as a constant. The electronic Hamiltonian is made of the kinetic energy of the electrons (\hat{T}_e), electron-nuclear interaction energy (\hat{V}_{e-n}), and electron-electron interaction energy (\hat{V}_{e-e}).

In the electronic structure calculation, each molecular orbital (MO) can be expressed as a linear combination of atomic orbitals (LCAO).¹⁻³ The most used atomic basis functions in electronic structure calculation are Slater Type Orbitals (STO) and Gaussian Type Orbitals (GTO).¹⁻³ Slater Type Orbitals have the form⁶

$$\chi_{\zeta,n,l,m}(r, \theta, \varphi) = N Y_{l,m}(\theta, \varphi) r^{n-1} e^{-\zeta r} \quad (2.9)$$

Gaussian Type Orbitals have the form⁷

$$\chi_{\zeta,n,l,m}(r, \theta, \varphi) = N Y_{l,m}(\theta, \varphi) r^{2n-2-l} e^{-\zeta r^2} \quad (2.10)$$

where r is the distance of the electron from the atomic nucleus; n , l , and m are the quantum numbers. N is a normalization constant, and $Y_{l,m}(\theta, \varphi)$ is a spherical function. ζ is an orbital exponent.

The main difference between STO and GTO is the exponential part $e^{-\zeta r}$ and $e^{-\zeta r^2}$. The Kato's cusp⁸ near the nucleus and the exponential decay at long range are the main advantages of STO. The desired cusp is important for a good representation of AOs around nuclei. The exponential decay also correctly describes the electron far from the nucleus. In this thesis, ADF^{9,10} calculations use STO.

The main advantage of GTO is their computational efficiency. Through optimal contraction coefficient and exponents, the Slater Type Orbitals can be approximated by a linear combination of GTO, denoted as STO-NG, where N is the number of primitive Gaussian functions. STO and GTO are the commonly used atomic orbitals in quantum chemistry calculations.

One alternative to the atomic-orbitals basis set is using a grid to directly represent the field in real-space. In 1989, Becke presented the first fully numerical, non-basis-set molecular orbital calculation on a polyatomic system using a radial grid around each atom.¹¹ The uniform grid was first introduced by Chelikowsky, Troullier and Saad.¹² The Kohn-Sham (KS) equations are solved by pseudo-potentials on a uniform grid space.

2.2 Density functional theory

The electronic wave function of N electrons in a molecule depends on $3N$ spatial and N spin coordinates. In 1964, Hohenberg and Kohn proved that ground state energy, and all other molecular electronic properties, could be determined by the ground state electron density, which

is a function of three spatial variables (x, y, and z) and one spin variable.¹³ According to Hohenberg-Kohn theorems, the total energy is uniquely determined by electron density. Due to its computational efficiency and rigorously established theorems, density functional theory (DFT), which had been widely used in solid-state physics, was gaining attention in the chemistry community.

The popularity of DFT methods in computational chemistry was initiated with the introduction of orbitals by Kohn and Sham.¹⁴ The key to Kohn-Sham theory is calculating the non-interacting electrons and adding the corrections due to the interactions of electrons. The energy functional can be written as:

$$E[\rho(\mathbf{r})] = T_{\text{ni}}[\rho(\mathbf{r})] + V_{\text{ne}}[\rho(\mathbf{r})] + V_{\text{ee}}[\rho(\mathbf{r})] + \Delta T[\rho(\mathbf{r})] + \Delta V_{\text{ee}}[\rho(\mathbf{r})] \quad (2.11)$$

where $T_{\text{ni}}[\rho(\mathbf{r})]$ is the kinetic energy of the non-interacting electrons, $V_{\text{ne}}[\rho(\mathbf{r})]$ is nuclear-electron interaction energy, $V_{\text{ee}}[\rho(\mathbf{r})]$ is electron-electron interaction energy, $\Delta T[\rho(\mathbf{r})]$ is the correction due to interacting nature of electron, and $\Delta V_{\text{ee}}[\rho(\mathbf{r})]$ is the correction due to all non-classical corrections to the electron-electron repulsion energy.

Within an orbital expression, the energy functional can be expressed as:

$$E[\rho(\mathbf{r})] = \sum_i^N \left(\left\langle \chi_i \left| -\frac{1}{2} \nabla_i^2 \right| \chi_i \right\rangle - \left\langle \chi_i \left| \sum_k^n \frac{Z_k}{|\mathbf{r}_i - \mathbf{r}_k|} \right| \chi_i \right\rangle \right) + \sum_i^N \left\langle \chi_i \left| \frac{1}{2} \int \frac{\rho(\mathbf{r}')}{|\mathbf{r}_i - \mathbf{r}'|} d\mathbf{r}' \right| \chi_i \right\rangle + E_{\text{xc}}[\rho(\mathbf{r})] \quad (2.12)$$

All the terms in functional have a known form except for the exchange-correlation functional $E_{\text{xc}}[\rho(\mathbf{r})]$. Therefore, the approximation of $E_{\text{xc}}[\rho(\mathbf{r})]$ is key to the accuracy of DFT.

In the Local Density Approximation (LDA),¹⁵ the density can be treated as a uniform electron gas locally. When electron density varies slowly with position, the LDA works well.

An improvement over the LDA has to be considered for non-uniform electron gas. The Generalized Gradient Approximation (GGA)^{16–18} considers not only the electron density but also the density gradient. The transient absorption spectra of Au₂₅ and Au₃₈ in this thesis use the PBE¹⁹ GGA functional due to previous good performance of GGA in absorption spectra calculation.^{38,39}

2.3 Density functional tight binding

The density functional tight-binding (DFTB) method^{20,21} is an approximated density functional theory (DFT) method by applying the tight-binding (TB) formalism to parameterize full DFT. In the DFTB formalism,^{1,20} the Hamiltonian is replaced by a pre-computed reference Hamiltonian H^0 , and parameterized matrix elements. The fluctuations of the electron density, $\rho(r) = \rho_0(r) + \delta\rho(r)$, around a reference density, $\rho_0(r)$, of neutral atomic species are considered.

The DFTB formalism originates from the Kohn-Sham expression of total energy,

$$E_{\text{KS}} = \sum_i^{\text{occ}} \left\langle \psi_i \left| \left(-\frac{1}{2} \nabla_i^2 + V_{\text{ext}} \right) \right| \psi_i \right\rangle + E_{\text{H}} + E_{\text{xc}} + E_{\text{II}} \quad (2.13)$$

where ψ_i are the Kohn–Sham orbitals, V_{ext} is the external interaction, E_{H} is the Hartree energy, E_{xc} is the exchange–correlation energy, and E_{II} is the ion–ion interaction energy.

The DFTB energy is parameterized in terms of a reference density and a small correction $\rho_0 + \delta\rho$ from the Kohn-Sham total energy as

$$E_{\text{DFTB}} = \sum_i^{\text{oc}} \left\langle \varphi_i \left| \hat{H}_0 \right| \varphi_i \right\rangle + \frac{1}{2} \sum_{\text{AB}}^{\text{M}} \gamma_{\text{AB}} \Delta q_{\text{A}} \Delta q_{\text{B}} + E_{\text{rep}} \quad (2.14)$$

The first term corresponds to the Kohn-Sham Hamiltonian H^0 , which is evaluated at the reference density, $\rho_0(\mathbf{r})$, and approximated in the DFTB framework as

$$\hat{H} \approx \left\langle \varphi_\mu \left| -\frac{1}{2} \nabla^2 + v_{\text{eff}}[\rho_A^0 + \rho_B^0] \right| \varphi_\nu \right\rangle, \mu \in A, \nu \in B \quad (2.15)$$

where φ_μ forms a minimal Slater-type orbital basis centered on the atomic sites, ρ_A^0 is the reference density of the neutral atom A, and v_{eff} is the effective Kohn–Sham potential. In the DFTB formalism, only two-center Hamiltonian matrix elements and two-center elements of the overlap matrix are explicitly calculated using analytical functions as LCAO formalism.

The pre-computed matrix elements work as a function of the distance between atomic pairs, which significantly improves computational efficiency. The second term in the total energy of the DFTB formalism came from charge fluctuations. It is parameterized analytically as a function of orbital charges and γ_{AB} , which is a function of inter-atomic separation and the Hubbard parameter (U). The quantity $\Delta q_A = q_A - q_A^0$ is the difference between the charge of the isolated atom q_A^0 and the charge q_A . E_{rep} is the distance-dependent diatomic repulsive potential and contains the core electron effects, ion–ion repulsion terms, as well as some exchange–correlation effects. E_{rep} can be considered a practical equivalent to an xc-functional in DFT as it approximates the many-body correlation interactions with simple functions. ρ_0 is spherically symmetric; hence, the ion–ion repulsion can be approximated to depend only on the elements and their distance. Contributions of three and more centers are rather small and can be neglected. These pair-wise repulsive functions are obtained by fitting to DFT calculations using a suitable reference structure. With this assumption of tightly bound electrons and a minimal local basis (only one radial function for each angular momentum state), the DFTB Hamiltonian is given by

$$\hat{H}_{\text{DFTB}} = \langle \varphi_\mu | \hat{H}_0 | \varphi_\nu \rangle + \frac{1}{2} \hat{S}_{\mu\nu} \sum_X (\gamma_{\text{AX}} + \gamma_{\text{BX}}) \Delta q_X \quad (2.16)$$

where the Hamiltonian matrix elements and the overlap matrix elements are precalculated as discussed above. Since the DFTB Hamiltonian depends explicitly on the atomic charge, a self-consistent charge (SCC) procedure is used in the SCC-DFTB approach to self-consistently solve the DFTB Hamiltonian.²⁰ Once the initial electronic ground state is calculated using the above procedure, it is used as an initial input condition in the real-time quantum dynamics calculations.

2.4 Time-dependent density functional theory

Density functional theory is a great analogy to wave function methods to calculate ground state properties. The time-dependent density functional theory (TDDFT)²² is an extension of DFT. The foundation of TDDFT originates from the Runge-Gross theorem,²² which states that there is a one-to-one mapping between the time-dependent external potential and the time-dependent electron density for any fixed initial many-body state.

Linear response (LR-TDDFT) and real-time (RT-TDDFT) are the TDDFT methods used in this thesis to calculate the excitation energies and oscillator strengths.

2.4.1 Linear response density functional theory

The most important application of TDDFT under a weak perturbation regime is the calculation of excitation energies.²³ The solution of the time-dependent Kohn-Sham equations in linear response has been proposed by Mark Casida:²⁴

$$\begin{bmatrix} A & B \\ B^* & A^* \end{bmatrix} \begin{bmatrix} X \\ Y \end{bmatrix} = \omega \begin{bmatrix} 1 & 0 \\ 0 & -1 \end{bmatrix} \begin{bmatrix} X \\ Y \end{bmatrix} \quad (2.17)$$

$$\text{where } A_{ia,jb} = \delta_{ab} \delta_{ij} (\varepsilon_a - \varepsilon_i) + (ia|jb) - c_{HF} (ij|ab) + \\ (1 - c_{HF})(ia|f_{xc} |jb),$$

$$B_{ia,jb} = (ia|bj) - c_{HF}(ib|aj) + (1 - c_{HF})(ia|f_{xc} |bj),$$

where i, j denote the occupied orbitals and a, b denote the unoccupied orbitals. ε is the orbital energy. c_{HF} is the amount of Hartree Fock exchange included and f_{xc} is the exchange-correlation functional. ω is the excitation energy. The oscillator strength can be calculated as

$$f_n = \frac{2}{3} \omega |\langle \Phi_0 | \vec{r} | \Phi_n \rangle|^2 \quad (2.18)$$

2.4.2 Real-time density functional theory

In 1996, Bertsch and Yabana introduced the first use of Real-Time Density Functional Theory (RT-TDDFT) for studying the dipole responses of atomic clusters.²⁵ Octopus is one of the pioneer programs that combined the real-space density functional theory with explicitly time-dependent electronic structure theory. Within the RT-TDDFT framework,²⁶ the electron density is calculated through time propagation.²⁷

Starting from the time-dependent Schrödinger equation (2.1), the orbitals are obtained from a ground state calculation.

$$\Psi(t = 0) = \Psi^{(0)} \quad (2.19)$$

The time evolution operator acting on initial orbitals will obtain the solution at time T:

$$\Psi(T) = U(T, 0)\Psi^{(0)} \quad (2.20)$$

For a Hermitian Hamiltonian, the exact expression for the time-evolution operator is

$$U(T, 0) = T \exp\left(-i \int_0^T d\tau H(\tau)\right) \quad (2.21)$$

Under the time-reversal symmetry, propagating backward from $t + \Delta t$ to $t + \Delta t / 2$ is equal to propagating forward from t to $t + \Delta t / 2$, which is also called enforced time-reversal symmetry (ETRS)²⁷ with the expression

$$U_{\text{ETRS}}(t + \Delta t, t) = \exp\left(-i \frac{\Delta t}{2} H(t + \Delta t)\right) \exp\left(-i \frac{\Delta t}{2} H(t)\right) \quad (2.22)$$

The approximated enforced time-reversal symmetry (AETRS)²⁷ is modification of ETRS. AETRS in this thesis performs a second-order polynomial extrapolation of $H(t + \Delta t)$.

2.5 Time-dependent density functional tight binding

The optical properties of a material can also be calculated through Linear Response TD-DFTB (LR-TDDFTB). LR-TDDFTB is a DFTB analog of the linear response TDDFT. The excitation energy is calculated through the Casida equation^{28,29}

$$\begin{bmatrix} A & B \\ B^* & A^* \end{bmatrix} \begin{bmatrix} X \\ Y \end{bmatrix} = \omega \begin{bmatrix} 1 & 0 \\ 0 & -1 \end{bmatrix} \begin{bmatrix} X \\ Y \end{bmatrix} \quad (2.23)$$

LR-TDDFTB is derived from the LR-TDDFT formalism with a pure functional without Hartree Fock exchange, which means $c_{HF} = 0$ in equation (2.18). In the SCC-DFTB, the coupling matrix has been parameterized in advance.^{30,31} Using Hubbard parameters of neutral atoms, the coupling matrix can be extracted from SCC-DFTB.^{30,32} Therefore, the LR-TDDFTB can apply to systems where ground state SCC-TDDFTB parameters are available.

For the quantum dynamics calculations, the real-time, time-dependent DFTB (RT-TDDFTB) approach is utilized to propagate the one electron density matrix in the presence of external time-varying electric fields to obtain the time-dependent electronic excitation transfer (EET) response of the system.^{33–35} The Hamiltonian in the dynamics process can be written as,

$$\hat{H}(t) = \hat{H}^0 - E_0(t) \cdot \hat{\mu}(t) \quad (2.24)$$

where $E_0(t)$ is the applied electric field and $\hat{\mu}(t)$ is the dipole moment operator. As we are directly propagating the quantum system in the time domain, we can choose $E_0(t)$ to have any time-dependent form. For example, if $E_0(t)$ is a Dirac delta function, this corresponds to an optical absorption spectrum in the frequency domain (obtained after a Fourier transform of the time-evolving dipole moment). However, if we choose $E_0(t)$ to take the form of a sinusoidal perturbation, it represents a continuous interaction of the system with monochromatic light in the time domain. Both of these different choices give different but complementary viewpoints of quantum dynamics. Upon application of either of these time-dependent fields, the density matrix, $\hat{\rho}$, will evolve according to the Liouville–von Neumann equation of motion which, in the nonorthogonal-DFTB basis, is given by

$$\frac{\partial \hat{\rho}}{\partial t} = \frac{1}{i\hbar} \left(S^{-1} \cdot \hat{H}[\hat{\rho}] \cdot \hat{\rho} - \hat{\rho} \cdot \hat{H}[\hat{\rho}] \cdot S^{-1} \right) \quad (2.25)$$

where \hat{H} is the Hamiltonian matrix (which implicitly depends on the density matrix), S^{-1} is the inverse of the overlap matrix, and \hbar is Planck's constant divided by 2π . When the applied incident fields are smaller than the internal fields within the matter, the system is found to be in the linear response regime. Under these conditions, the time evolution of the dipole moment operator can be expressed as the convolution between the applied electric field perturbation and the response function of the system

$$\langle \hat{\mu}(t) \rangle = \int_0^\infty \alpha(t - \tau) E(\tau) d\tau \quad (2.26)$$

where $E(\tau)$ is the electric field used to induce a perturbation in the system Hamiltonian, and $\alpha(t - \tau)$ is the polarizability tensor. Upon application of the convolution theorem, it can be expressed in the frequency (ω) domain as $\langle \hat{\mu}(t) \rangle = \alpha(\omega) E(\omega)$. The imaginary part of the average polarizability, $\bar{\alpha}$, is an experimentally measurable quantity related to the photo absorption cross section by the expression $\sigma(\omega) = 4\pi\omega/c \cdot \text{Im}(\bar{\alpha})$, where c is the speed of light, and $\text{Im}(\bar{\alpha})$ is the imaginary part of the average polarizability.

2.6 Transient absorption spectroscopy simulation

Transient absorption spectroscopy is a powerful tool for studying the electronic properties of short-lived excited states.³⁶ In the transient absorption as shown in Figure 2.1, when $T < 0$, the peak in the absorption spectrum describes the ground state to a certain excited state transition, which is similar to static state absorption and is a reference in the transient absorption spectrum. At $T = 0$, the pump pulse reaches the sample and makes certain excitation happens. In this case,

the pump is exciting the population from ground state G to excited state A. At $T > 0$, the probe pulse reaches the sample. The transition from ground state G to excited state A is smaller compared to the reference because the pump depleted the population in ground state, which is known as ground state bleach (GSB). A new peak corresponding to the transition between excited state A and excited state B can be detected, which is not observable in ground state absorption. The observation of the excited state A to excited state B transition is called excited state absorption (ESA) because of the population build up in excited state A by the pump pulse.

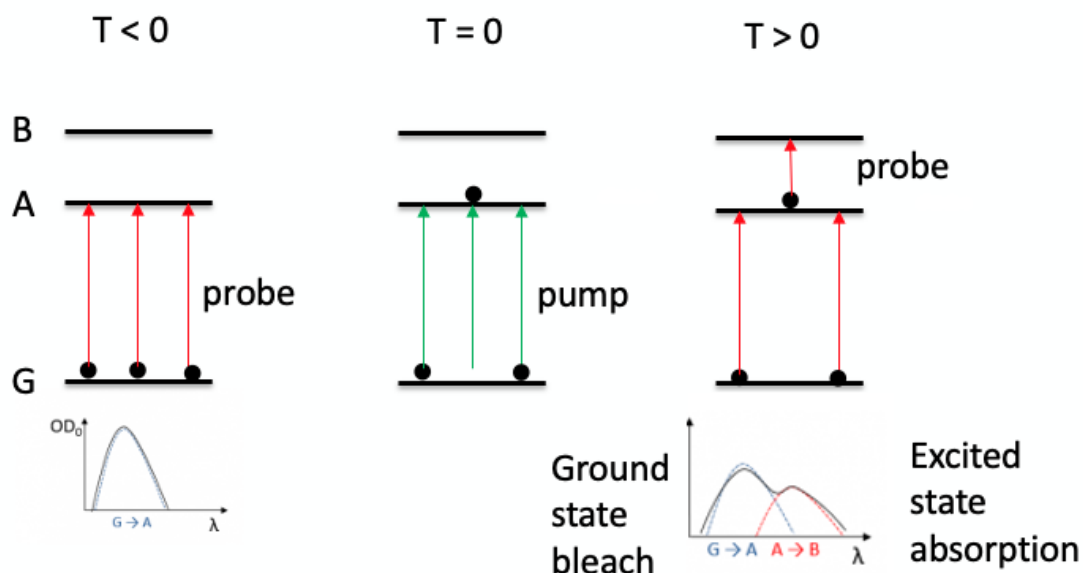


Figure 2.1 Electronic transition of a transient absorption experiment

In the transient absorption simulation as shown in Figure 2.2, the pump is a Gaussian envelope with energy tuned to excite certain transitions. After a time delay, the probe pulse reaches the sample. In all projects in this thesis, the probe is a delta kick, which can theoretically make all the dipole allowed excitations happens. After the probe, the electron dipole fluctuation of 10 fs propagation is collected. At every time delay, one set of dipole fluctuation is collected to do the

Fast Fourier Transform (FFT). By subtracting the reference absorption spectrum, the change of the absorption spectrum at different time delays can be obtained.³⁷

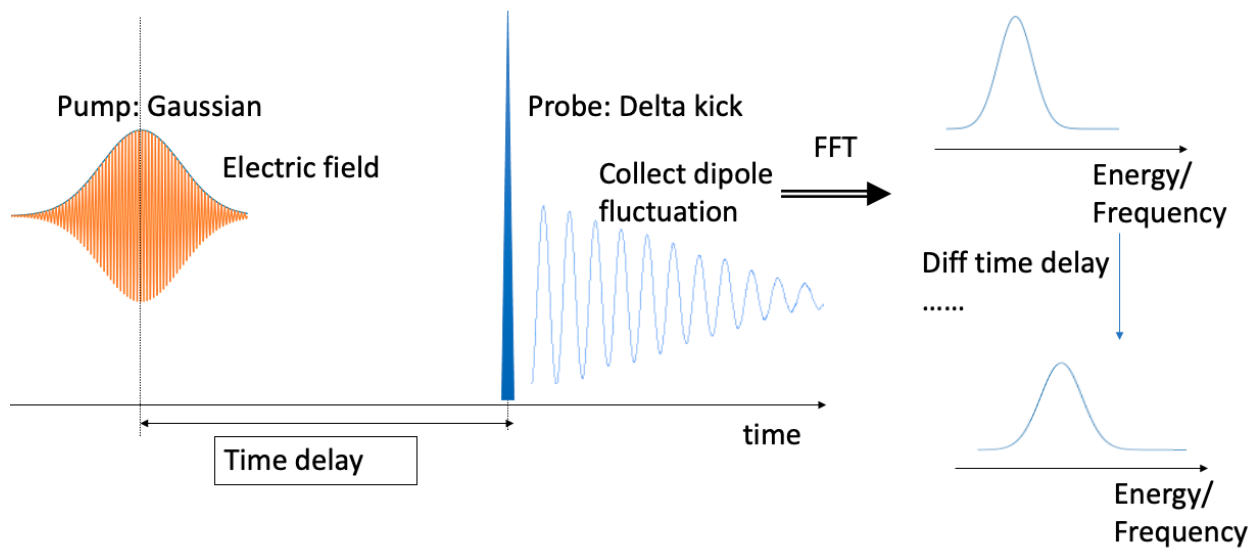


Figure 2.2 Simulation process of a transient absorption experiment

2.7 References

- (1) Levine, I. N. *Quantum Chemistry*, Seventh edition.; Pearson: Boston, 2014.
- (2) Jensen, F. *Introduction to Computational Chemistry*, Third edition.; John Wiley & Sons: Chichester, UK ; Hoboken, NJ, 2017.
- (3) Cramer, C. J. *Essentials of Computational Chemistry: Theories and Models*, 2nd ed.; Wiley: Chichester, West Sussex, England ; Hoboken, NJ, 2004.
- (4) Griffiths, D. J. *Introduction to Quantum Mechanics*, 2nd ed.; Pearson Prentice Hall: Upper Saddle River, NJ, 2005.
- (5) Born–Oppenheimer Approximation. *Wikipedia*; 2022.
- (6) Slater, J. C. Atomic Shielding Constants. *Phys. Rev.* **1930**, *36* (1), 57–64. <https://doi.org/10.1103/PhysRev.36.57>.
- (7) Electronic Wave Functions - I. A General Method of Calculation for the Stationary States of Any Molecular System. *Proc. R. Soc. Lond. A* **1950**, *200* (1063), 542–554. <https://doi.org/10.1098/rspa.1950.0036>.
- (8) Kato, T. On the Eigenfunctions of Many-Particle Systems in Quantum Mechanics. *Comm. Pure Appl. Math.* **1957**, *10* (2), 151–177. <https://doi.org/10.1002/cpa.3160100201>.
- (9) te Velde, G.; Bickelhaupt, F. M.; Baerends, E. J.; Fonseca Guerra, C.; van Gisbergen, S. J. A.; Snijders, J. G.; Ziegler, T. Chemistry with ADF. *J. Comput. Chem.* **2001**, *22* (9), 931–967. <https://doi.org/10.1002/jcc.1056>.
- (10) ADF, 2016.1 *SCM, Theoretical Chemistry*; 2016.
- (11) Becke, A. D. Basis-Set-Free Density-Functional Quantum Chemistry. *Int. J. Quantum Chem.* **2009**, *36* (S23), 599–609. <https://doi.org/10.1002/qua.560360862>.
- (12) Chelikowsky, J. R.; Troullier, N.; Saad, Y. Finite-Difference-Pseudopotential Method: Electronic Structure Calculations without a Basis. *Phys. Rev. Lett.* **1994**, *72* (8), 1240–1243. <https://doi.org/10.1103/PhysRevLett.72.1240>.
- (13) Hohenberg, P.; Kohn, W. Inhomogeneous Electron Gas. *Phys. Rev.* **1964**, *136* (3B), B864–B871. <https://doi.org/10.1103/PhysRev.136.B864>.
- (14) Kohn, W.; Sham, L. J. Self-Consistent Equations Including Exchange and Correlation Effects. *Phys. Rev.* **1965**, *140* (4A), A1133–A1138. <https://doi.org/10.1103/PhysRev.140.A1133>.
- (15) Parr, R. G.; Yang, W. *Density-Functional Theory of Atoms and Molecules*, 1. iss. as ... paperback.; International series of monographs on chemistry; Oxford Univ. Press [u.a.]: New York, NY, 1994.
- (16) Perdew, J. P.; Chevary, J. A.; Vosko, S. H.; Jackson, K. A.; Pederson, M. R.; Singh, D. J.; Fiolhais, C. Atoms, Molecules, Solids, and Surfaces: Applications of the Generalized Gradient Approximation for Exchange and Correlation. *Phys. Rev. B* **1992**, *46* (11), 6671–6687. <https://doi.org/10.1103/PhysRevB.46.6671>.
- (17) Becke, A. D. Density-Functional Exchange-Energy Approximation with Correct Asymptotic Behavior. *Phys. Rev. A* **1988**, *38* (6), 3098–3100. <https://doi.org/10.1103/PhysRevA.38.3098>.
- (18) Langreth, D. C.; Mehl, M. J. Beyond the Local-Density Approximation in Calculations of Ground-State Electronic Properties. *Phys. Rev. B* **1983**, *28* (4), 1809–1834. <https://doi.org/10.1103/PhysRevB.28.1809>.
- (19) Perdew, J. P.; Burke, K.; Ernzerhof, M. Generalized Gradient Approximation Made Simple. *Phys. Rev. Lett.* **1996**, *77*, 3865.

- (20) Yang, Y.; Yu, H.; York, D.; Cui, Q.; Elstner, M. Extension of the Self-Consistent-Charge Density-Functional Tight-Binding Method: Third-Order Expansion of the Density Functional Theory Total Energy and Introduction of a Modified Effective Coulomb Interaction. *J. Phys. Chem. A* **2007**, *111* (42), 10861–10873. <https://doi.org/10.1021/jp074167r>.
- (21) Porezag, D.; Frauenheim, T.; Kohler, T.; Seifert, G.; Kaschner, R. Construction of Tight-Binding-Like Potentials on the Basis of Density-Functional Theory – Application to Carbon. *Phys. Rev. B* **1995**, *51*, 12947.
- (22) Runge, E.; Gross, E. K. U. Density-Functional Theory for Time-Dependent Systems. *Phys. Rev. Lett.* **1984**, *52* (12), 997–1000. <https://doi.org/10.1103/PhysRevLett.52.997>.
- (23) Ullrich, C. A. *Time-Dependent Density-Functional Theory: Concepts and Applications*; Oxford University Press, 2011. <https://doi.org/10.1093/acprof:oso/9780199563029.001.0001>.
- (24) Casida, M. E. Time-Dependent Density Functional Response Theory for Molecules. In *Recent Advances in Computational Chemistry*; WORLD SCIENTIFIC, 1995; Vol. 1, pp 155–192. https://doi.org/10.1142/9789812830586_0005.
- (25) Yabana, K.; Bertsch, G. F. Time-Dependent Local-Density Approximation in Real Time. *Phys. Rev. B* **1996**, *54* (7), 4484–4487. <https://doi.org/10.1103/PhysRevB.54.4484>.
- (26) Yabana, K.; Bertsch, G. F. *Phys. Rev. A* **1999**, *60*, 3809.
- (27) Castro, A.; Marques, M. A. L.; Rubio, A. Propagators for the Time-Dependent Kohn–Sham Equations. *The Journal of Chemical Physics* **2004**, *121* (8), 3425–3433. <https://doi.org/10.1063/1.1774980>.
- (28) Rüger, R.; van Lenthe, E.; Lu, Y.; Frenzel, J.; Heine, T.; Visscher, L. Efficient Calculation of Electronic Absorption Spectra by Means of Intensity-Selected Time-Dependent Density Functional Tight Binding. *J. Chem. Theory Comput.* **2015**, *11* (1), 157–167. <https://doi.org/10.1021/ct500838h>.
- (29) Rüger, R.; van Lenthe, E.; Lu, Y.; Frenzel, J.; Heine, T.; Visscher, L. Correction to Efficient Calculation of Electronic Absorption Spectra by Means of Intensity-Selected Time-Dependent Density Functional Tight Binding. *J. Chem. Theory Comput.* **2017**, *13* (7), 3424–3425. <https://doi.org/10.1021/acs.jctc.7b00564>.
- (30) Niehaus, T. A.; Suhai, S.; Sala, F. D.; Lugli, P.; Elstner, M.; Seifert, G.; Frauenheim, T. Tight-Binding Approach to Time-Dependent Density-Functional Response Theory. *Phys. Rev. B* **2001**, *63*, 085108.
- (31) Frauenheim, T.; Seifert, G.; Elstner, M.; Niehaus, T.; Kohler, C.; Amkreutz, M.; Sternberg, M.; Hajnal, Z.; Di Carlo, A.; Suhai, S. Atomistic Simulations of Complex Materials: Ground-State and Excited-State Properties. *J. Phys.: Condens. Matter* **2002**, *14*, 3015.
- (32) Elstner, M.; Porezag, D.; Jungnickel, G.; Elsner, J.; Haugk, M.; Frauenheim, T.; Suhai, S.; Seifert, G. Self-Consistent-Charge Density-Functional Tight-Binding Method for Simulations of Complex Materials Properties. *Phys. Rev. B* **1998**, *58*, 7260.
- (33) Oviedo, M. B.; Wong, B. M. Real-Time Quantum Dynamics Reveals Complex, Many-Body Interactions in Solvated Nanodroplets. *J. Chem. Theory Comput.* **2016**, *12* (4), 1862–1871. <https://doi.org/10.1021/acs.jctc.5b01019>.
- (34) Ilawe, N. V.; Oviedo, M. B.; Wong, B. M. Correction to Real-Time Quantum Dynamics of Long-Range Electronic Excitation Transfer in Plasmonic Nanoantennas. *J. Chem. Theory Comput.* **2017**, *13* (12), 6433–6433. <https://doi.org/10.1021/acs.jctc.7b01150>.

- (35) Belén Oviedo, M.; Sánchez, C. G. *Full Quantum Dynamics of the Electronic Coupling between Photosynthetic Pigments*; 2015.
<https://ui.adsabs.harvard.edu/abs/2015arXiv150200491B> (accessed 2022-11-30).
- (36) *Pump Probe / What is Transient Absorption? / Edinburgh Instruments*.
<https://www.edinst.com/us/blog/what-is-transient-absorption-spectroscopy/> (accessed 2022-11-30).
- (37) Krumland, J.; Valencia, A. M.; Pittalis, S.; Rozzi, C. A.; Cocchi, C. Understanding Real-Time Time-Dependent Density-Functional Theory Simulations of Ultrafast Laser-Induced Dynamics in Organic Molecules. *J. Chem. Phys.* **2020**, *153* (5), 054106.
<https://doi.org/10.1063/5.0008194>.
- (38) Zhu, M.; Aikens, C. M.; Hollander, F. J.; Schatz, G. C.; Jin, R. Correlating the Crystal Structure of A Thiol-Protected Au₂₅ Cluster and Optical Properties. *J. Am. Chem. Soc.* **2008**, *130* (18), 5883–5885. <https://doi.org/10.1021/ja801173r>.
- (39) Lopez-Acevedo, O.; Tsunoyama, H.; Tsukuda, T.; Häkkinen, H.; Aikens, C. M. Chirality and Electronic Structure of the Thiolate-Protected Au₃₈ Nanocluster. *J. Am. Chem. Soc.* **2010**, *132* (23), 8210–8218. <https://doi.org/10.1021/ja102934q>.

Chapter 3 - TD-DFTB Study of Optical Properties of Silver

Nanoparticle Homodimers and Heterodimers

Reproduced with permission from:

Z. Liu, F. Alkan, and C. M. Aikens, J. Chem. Phys. 153(14), 144711 (2020).

3.1 Abstract

The absorption spectra for face-centered cubic nanoparticle dimers at various interparticle distances are investigated using time-dependent density functional tight binding (TD-DFTB). Both homodimers and heterodimers are investigated in this work. By studying nanoparticles at various interparticle distances and analyzing their vertical excitations, we found that as the interparticle distance decreases, a red shift arises from contributions of the transition dipole moment that are aligned along the z-axis with nondegenerate features; blue shifts occur for peaks that originate from transition dipole moment components in the x and y directions with double degeneracy. When the nanoparticles are similar in size, the features in the absorption spectra become more sensitive to the interparticle distances. The best-fit curves from vertical excitation energy in the form of AR^{-b} for $\Delta E_{\text{redshift}}/\Delta E_{\text{blueshift}}$ vs. R are determined. In this way, we determined the trends for absorption peak shifts and how these depend on interparticle distance and found the agreement of this trend with distance dependence of plasmon coupling.

3.2 Introduction

Nanoparticles such as gold and silver have many applications in chemistry, physics, and biology due to their optical properties and their high physical and chemical stability.¹⁻⁴ Localized surface plasmon resonances (LSPRs)⁵⁻¹⁰ are unique optical characteristics of nanoparticles. The LSPR originates from the collective oscillation of conduction electrons upon excitation with an external electric field. Due to plasmonic coupling, the optical properties of nanoparticles are highly affected by their neighboring particles.¹¹⁻¹⁶

A nanoparticle dimer is the simplest model to study nanoparticle interactions. Dimers can provide a system for the systematic study of nanoparticle plasmonic interactions and can pave the way for further understanding of hybridized plasmons^{11,17,18} in more complex systems. When the surface plasmons are excited, a large electromagnetic field enhancement can occur in a nanoparticle junction. Studying nanoparticles not only provides physical insights about nanoparticle interaction, but also provides more understanding regarding the resulting electromagnetic field enhancements.¹⁶

Many previous theoretical studies have employed density functional theory (DFT) and time-dependent density functional theory (TD-DFT)^{15,19-28} for describing quantum mechanical effects on the optical properties of large systems.²⁹⁻³¹ Density functional tight binding (DFTB)^{32,33} and its time-dependent formalism (TD-DFTB)^{34,35} are great potential candidates to improve the computational efficiency of these methods with a small decrease in accuracy. Sanchez and co-workers have used TD-DFTB to investigate the relaxation dynamics of LSPRs in nanoclusters.³⁶⁻³⁸ Wong and co-workers used real-time TD-DFTB to study the electron dynamics of a plasmonic antenna and showed the capabilities of TD-DFTB for the calculation of plasmonicity.³⁹⁻⁴¹ In 2018, Alkan et al. used the TD-DFTB formalism to study the optical properties and electronic structures

of silver nanorods and nanorod dimers.¹³ Their results shows a good agreement between TD-DFTB and TD-DFT in that the spectral shapes, energies, and intensity trends from the TD-DFT calculations can be reproduced by TD-DFTB.

Due to the high computational efficiency of DFTB and TD-DFTB, these methods can be used on large systems. Moreover, because DFTB and TD-DFTB allow for explicit treatment of electronic structure, they can more accurately predict absorption spectra compared to classical methods in the cases where quantum mechanical effects become important. Quantum mechanical methods are required to treat effects such as electron tunneling and charge transfer plasmons that are especially evident when the interparticle distance between nanoparticles becomes small. In this study, we employ the TD-DFTB method to examine how the optical properties of homodimers and heterodimers are tuned as the interparticle distance changes. The questions that we are going to study is related to the polarization of the transition dipole moment. As the distance of the silver nanoparticle dimer decreases, we find that the excitation energy will blue shift when it comes from a dipole transition perpendicular to the dimer interaction axis (i.e. polarized in the x and y directions) and shows up with a doubly degenerate feature. Furthermore, the excitation energy will red shift when it comes from a dipole transition polarized along the dimer interaction axis (z direction) and shows up with no degeneracy. Our study can answer three important questions regarding dimer nanoparticle systems:

- (1) Why do new peaks show up upon decreasing the interparticle distance?
- (2) When the distance between the nanoparticles in the dimer decreases, why does the highest peak blue shift for some systems and red shift for other systems?
- (3) When the distance decreases for one dimer system, why does the highest peak blue shift for some distance range, but red shift for another range?

3.3 Computational Details

All density functional tight binding (DFTB) calculations of face-centered cubic (FCC) silver nanoparticles are performed using the Amsterdam Density Functional (ADF) 2016 program.^{33–35} Time-dependent density functional tight binding (TD-DFTB)^{43–47} calculations are performed using the self-consistent-charge (SCC) formalism and the Hyb-0-2 parameter set.^{48,49} The SCC convergence threshold is defined by maximum change between two succeeding SCC cycles. In the calculation, we set the charge convergence tolerance to 1×10^{-9} . The linear-response TD-DFTB method allows for each excited state to be represented with multiple determinants, each of which represents a single orbital-to-orbital transition. Prior to the linear response TD-DFTB calculation, the single orbital transitions with an oscillator strength smaller than 1×10^{-4} are removed, and the rest are coupled into the excited state. The smoothed absorption spectra are convoluted with Gaussian broadening with a full width at half-maximum (FWHM) of 0.05 eV.

The geometries of the monomers are created by a FCC coordinate generator using a lattice spacing of 4.0853 Å (from bulk silver) and choosing desired silver FCC spherical radius cutoffs of 4 Å, 7 Å, 8 Å and 8.5 Å. The FCC silver nanoparticles Ag₁₄, Ag₉₂, Ag₁₁₆ and Ag₁₆₄ are generated; their coordinates are provided in the Supporting Information in Appendix A. We construct the dimer structures by using different combinations of monomers at various interparticle distances (6 Å, 7 Å, 8 Å, 9 Å, 10 Å, 12 Å, 15 Å, 17 Å, 20 Å, 25 Å, 30 Å, 40 Å and 50 Å). The distances are measured by considering the distances between the two closest atoms from different nanoparticles in the dimer structure along the z-axis. No geometrical optimizations are performed for these structures.

Four homodimer systems are studied in this work (Figure 3.1): Ag₁₄ dimer, Ag₉₂ dimer, Ag₁₁₆ dimer and Ag₁₆₄ dimer. Six heterodimer systems are also examined (Figure 3.2): Ag₁₄ and Ag₉₂, Ag₁₄ and Ag₁₁₆, Ag₁₄ and Ag₁₆₄, Ag₉₂ and Ag₁₁₆, Ag₉₂ and Ag₁₆₄, and Ag₁₁₆ and Ag₁₆₄.

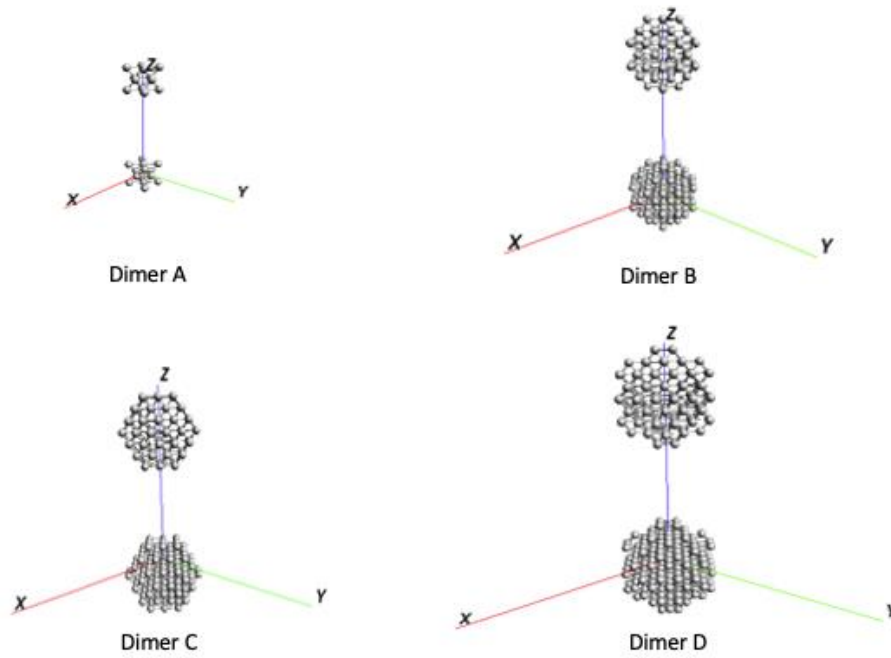


Figure 3.1 Structures for FCC homodimer nanoparticles.

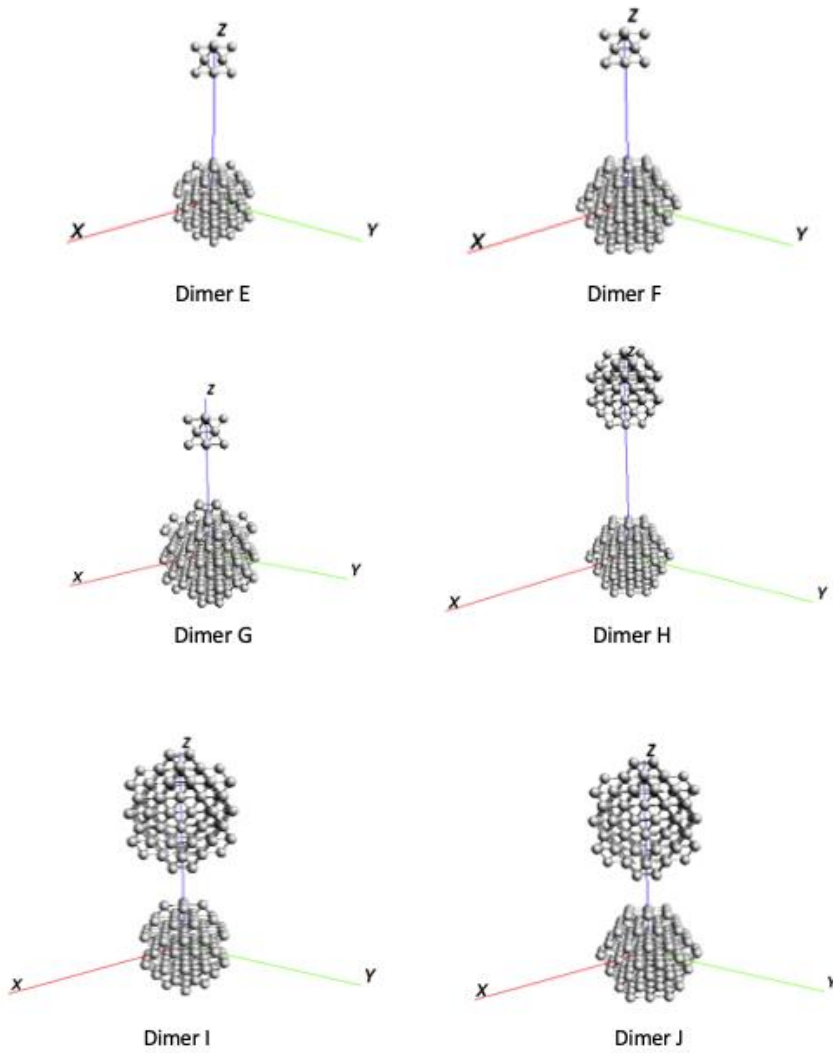


Figure 3.2 Structures for FCC heterodimer nanoparticles.

The interaction between the excited states of two nanoparticles are sometimes treated as a weak perturbation to the Hamiltonian and expressed as a dipole-dipole interaction.^{18,50} Then, both $\Delta E_{\text{redshift}}$ and $\Delta E_{\text{blueshift}}$ would be proportional to $|\mu|^2 R^{-3}$, where μ is the dipole moment of the excited state for the monomer and R is the distance between two dipoles. The best-fit curves in the form of AR^{-b} for $\Delta E_{\text{redshift}}/\Delta E_{\text{blueshift}}$ vs. R are determined. In the equation, R is the distance between the two monomer nanoparticles and A and b are the parameters to be optimized. $\Delta E_{\text{redshift}}/\Delta E_{\text{blueshift}}$ is

the energy difference between the energy of the absorption peak at a given value of R and the energy of absorption at a long distance (50 Å). For optimized A and b , the $\Delta E_{\text{redshift}}$ and $\Delta E_{\text{blueshift}}$ from the best fit curve agree with the $\Delta E_{\text{redshift}}$ and $\Delta E_{\text{blueshift}}$ from the TD-DFTB calculation.

In this paper, we present two approaches to analyze the absorption spectra of nanoparticle dimers. In the first approach, we study the highest peak and the overall profile of the absorption spectra and compare with experimental results. The next approach is to analyze individual vertical excitation energies, which are also called “stick spectra”. Spectral broadening is included in the first approach by convolving the stick spectra with a Gaussian line shape of a given width. The stick spectra are the source of the simulated absorption spectra. The highest peak in the overall absorption spectrum may be formed from a single excited state with a very high intensity. However, it may also be caused by several close excited states. Thus, it is helpful to employ both approaches when analyzing absorption spectra.

Using the vertical excitation energy information, we can determine the transitions that are responsible for the highest intensity peak and why the highest peak will blue shift at one distance range and red shift over another range. By using the vertical excitation energies, we can analyze a specific excited state, which is critical for studying the absorption peak shifts in nanoparticle dimers. In this paper, we use vertical excited state information to analyze several high intensity peaks. In the vertical excitation energy analysis, we found that the exponential function can be fitted to the energies, whereas it is not feasible to do this for the broadened spectra.

3.4 Result and Discussion

3.4.1 Absorption spectra of monomers of FCC-structured silver nanoparticles

Absorption spectra for monomer nanoparticles with different sizes are shown in Figure 3.3. For Ag₁₄, the strongest peak is located at 3.22 eV (Figure 3.3a). For Ag₉₂, two strong peaks at 2.87 eV and 2.99 eV are observed (Figure 3.3b). Numerous low-intensity peaks are also present in this system. Above 3.5 eV, the absorption spectra profile is governed by the high density of states. For Ag₁₁₆, the highest peak is at 2.87 eV (Figure 3.3c). Similar to Ag₉₂, the absorption profile above 3.2 eV is determined by the density of states. For Ag₁₆₄, the absorption spectra profile is determined both by distinct peaks at 2.89 eV and 2.96 eV and the high density of states (Figure 3.3d). The solid-state features (i.e. that the absorption profile is governed by a high density of states instead of a strong electronic state) become clearer for Ag₁₆₄.

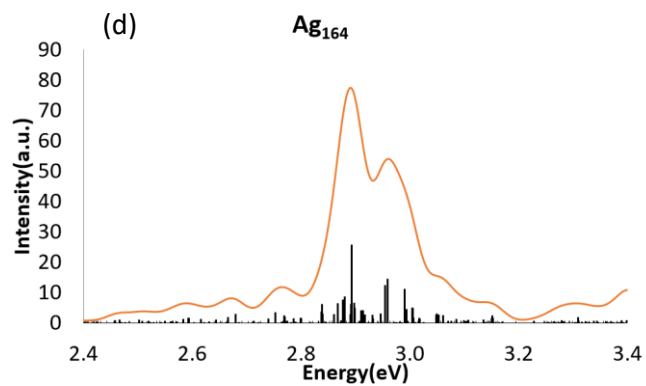
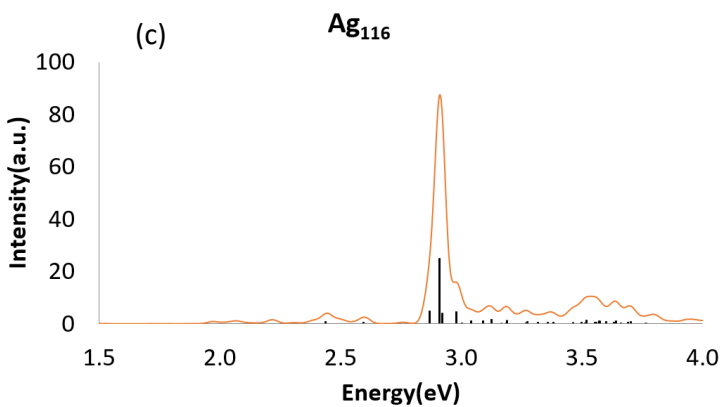
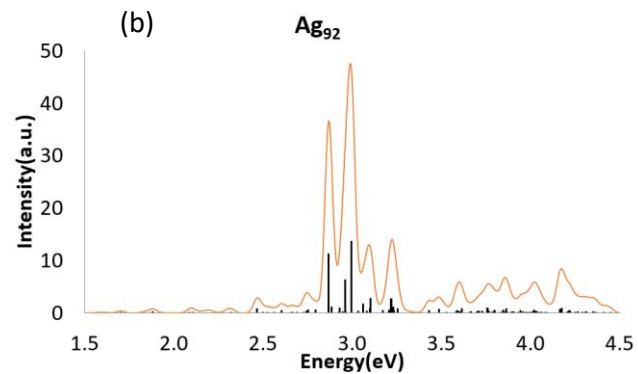
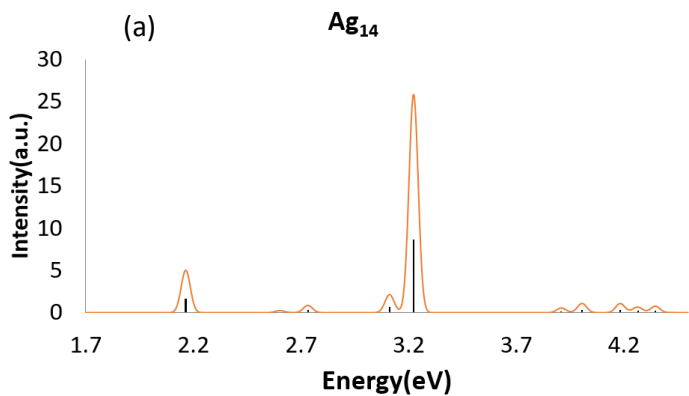
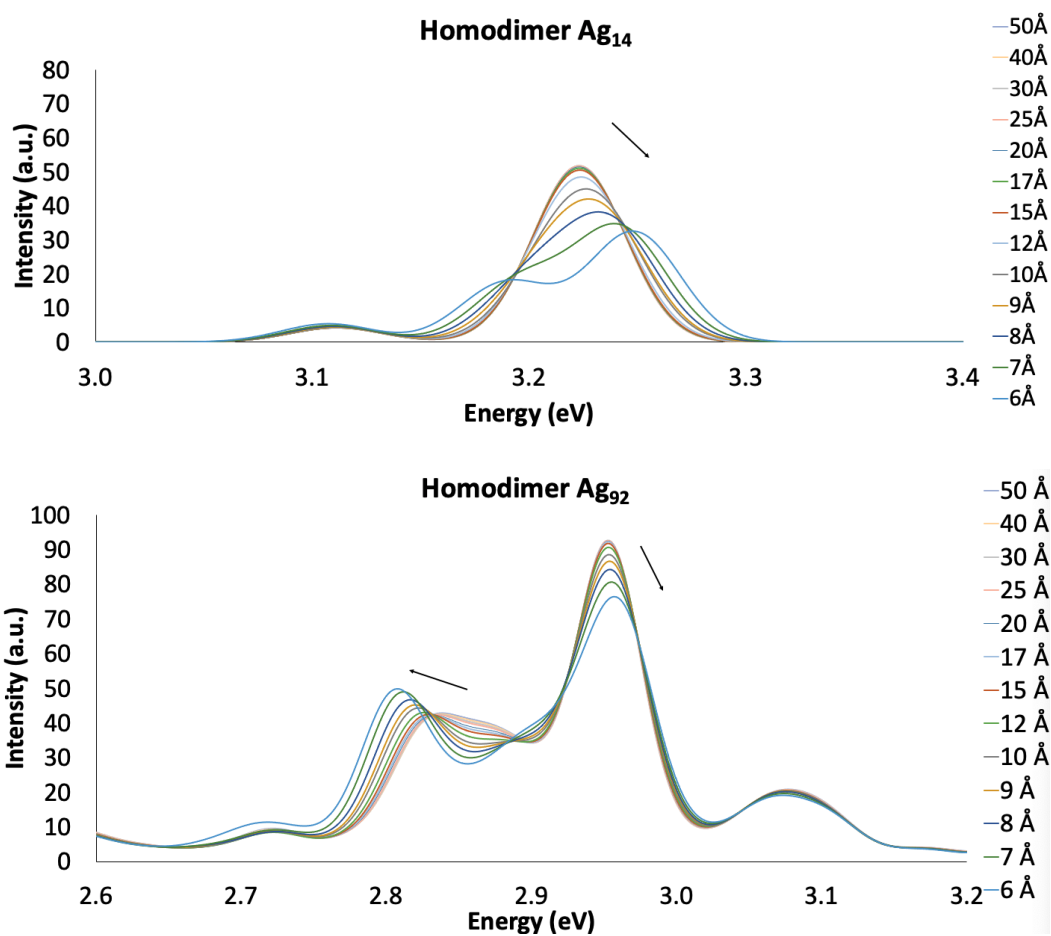


Figure 3.3 Calculated absorption spectra for FCC silver nanoparticle monomers. (a) Ag_{14} , (b) Ag_{92} , (c) Ag_{116} , (d) Ag_{164} .

3.4.2 Absorption spectra of silver nanoparticle homodimers

In this section, we investigate the absorption spectra of homodimers of FCC silver nanoparticles (Ag_{14} , Ag_{92} , Ag_{116} , Ag_{164}) at different interparticle distances (6 Å, 7 Å, 8 Å, 9 Å, 10 Å, 12 Å, 15 Å, 17 Å, 20 Å, 25 Å, 30 Å, 40 Å, 50 Å) (Figure 3.4).



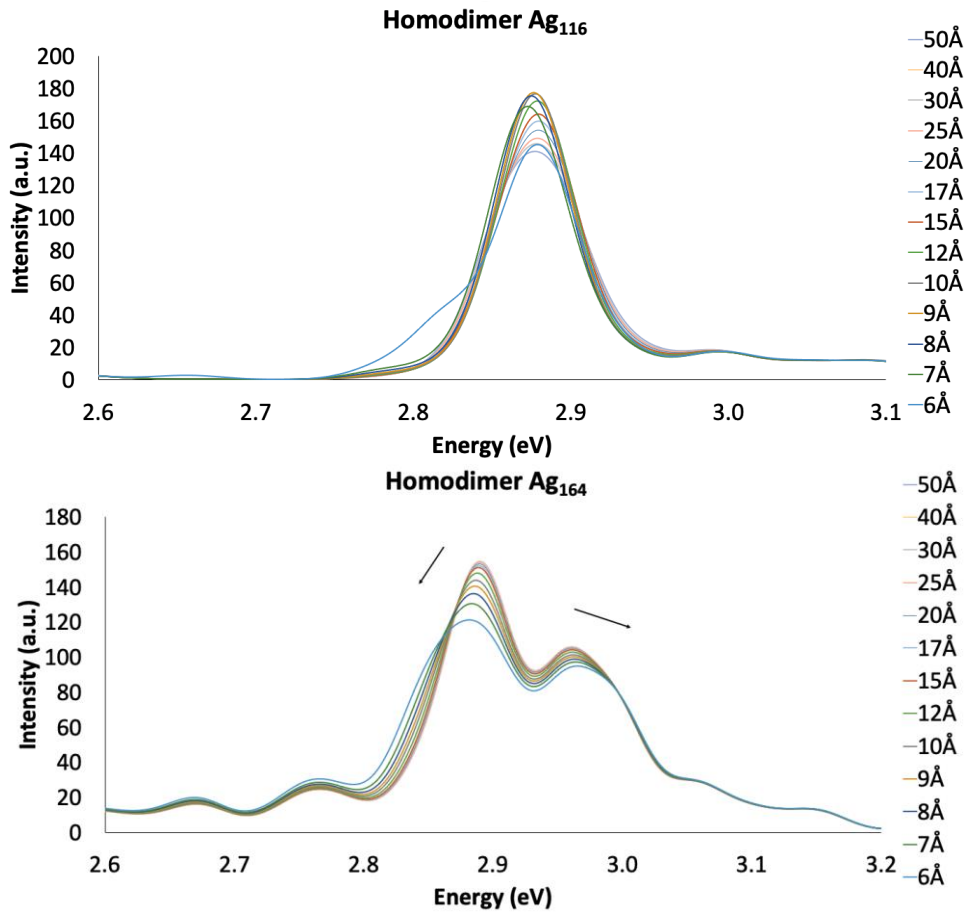


Figure 3.4 Calculated absorption spectra for FCC silver nanoparticle dimers. (a) Ag₁₄, (b) Ag₉₂, (c) Ag₁₁₆, (d) Ag₁₆₄.

For the Ag₁₄ dimer (Figure 3.4a) at an interparticle separation of 50 Å, we found the highest intensity peak at 3.22 eV, which is the same excitation energy as the Ag₁₄ monomer. However, the intensity is twice that of the Ag₁₄ monomer due to the doubling of the number of electrons in the system. As the interparticle distance decreases from 50 Å to 15 Å, the energies of the highest peaks remain at 3.22 eV. However, from 15 Å to 6 Å, the intensity decreases and the highest peak energy blue shifts from 3.22 eV to 3.24 eV. In addition, a new peak appears at 3.18 eV when the interparticle distance decreases to 6 Å.

For Ag₉₂ (Figure 3.4b), similar characteristics to the Ag₁₄ dimer are found. At large interparticle distance (i.e. from 50 Å to 15 Å), the highest intensity peaks all occur at 2.99 eV, similar to the monomer nanoparticle. For this dimer system, the highest peak (at 2.99 eV) blue shifts as the interparticle distance decreases from 15 Å to 6 Å. The second highest peak red shifts from 2.82 eV to 2.81 eV.

For Ag₁₁₆ (Figure 3.4c) at large interparticle distances, the absorption peaks occur at 2.87 eV, which is the same as the absorption peak of monomer. From 50 Å to 12 Å, the highest absorption peak blue shifts from 2.87 eV to 2.89 eV. From 12 Å to 6 Å, the peak red shifts from 2.89 eV to 2.87 eV. To understand these shifts, it is not sufficient just to analyze the highest peak from the absorption spectrum because the highest peak blue shifts at longer range and red shift at shorter range. However, these shifts can be explained by analyzing the origin of each excitation, via the study of the specific excited states that comprise each strong peak.

For Ag₁₆₄ (Figure 3.4d), we found that the highest peak red shifts and the second highest peak blue shifts as the distance decreases, which is exactly opposite to the trends for Ag₉₂.

With the discussion above, three specific questions arise: (1) Why does a new peak show up at short distance for the Ag₁₄ dimer, or why does the peak split? (2) Why for the Ag₁₁₆ dimer,

does the highest absorption peak blue shift at longer range and red shift at shorter range? (3) Why does the Ag₁₆₄ dimer display opposite trends compared to Ag₉₂ with decreasing interparticle distance? All of these questions can be answered by studying the vertical excited states, which correspond to the transitions between different electronic states.

The Ag₁₁₆ dimer is analyzed by studying the excited states that comprise its absorption spectra. In Figures 3.5-3.8, the best-fit curve is expressed in the more general form of AR^{-b} , for the calculated $\Delta E_{\text{redshift}}$ and $\Delta E_{\text{blueshift}}$ at the TD-DFTB level of theory for this system. A similar detailed study of the vertical excitations of Ag₁₄, Ag₉₂ and Ag₁₆₄ homodimers can be found in the Supporting Information (Figures S3.2-S3.8) in Appendix A. The best-fit curve for vertical excitation energies do not follow an AR^{-3} relationship, which is expected because the dipole-dipole interaction does not hold at short distance, due in part to the interaction and mixing of higher multipolar oscillations of nanoparticle dimers.^{51,52} The b value observed in our work is less than 2, which was the value observed in the “plasmon ruler” work of Jain and El-Sayed.^{53,54}

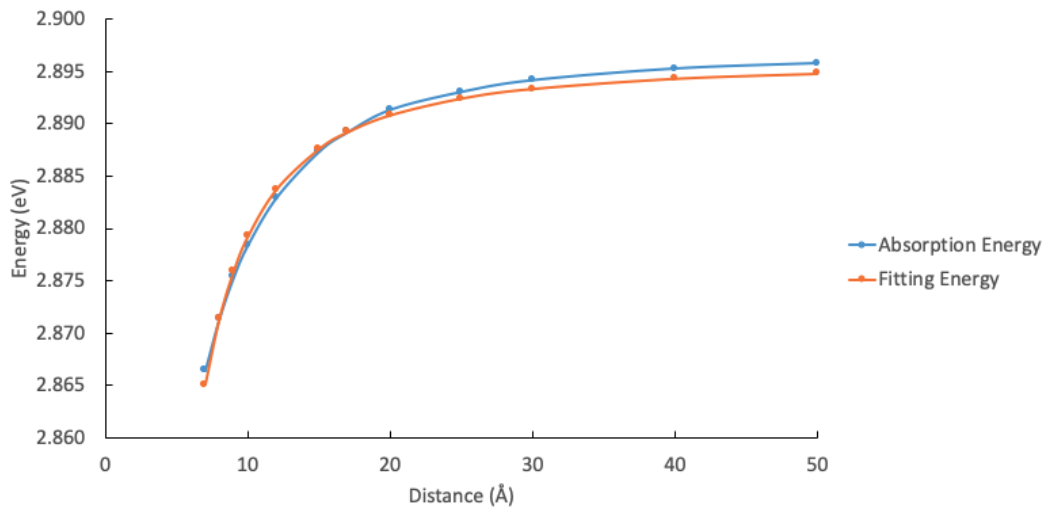


Figure 3.5 Distance dependence of the absorption energy from the highest intensity excitation of the Ag_{116} dimer and the predicted distance dependence of this absorption energy in the form of $E=AR^{-b}$, where the best-fit curve corresponds to $A=-0.8968$, $b=1.7331$.

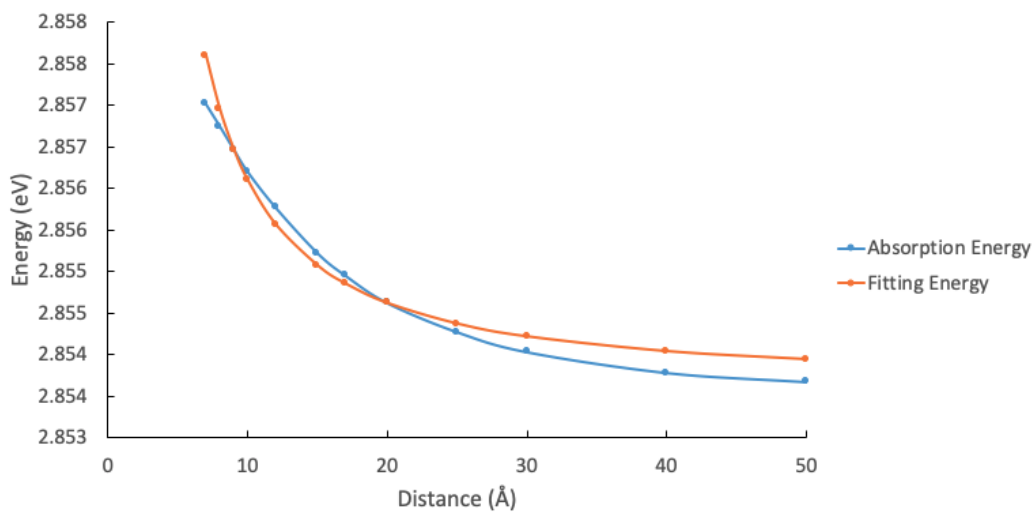


Figure 3.6 Distance dependence of the absorption energy from the second highest intensity excitation of the Ag_{116} dimer and the predicted distance dependence of this absorption energy in the form of $E = AR^{-b}$, with $A=0.0545$, $b=1.3521$.

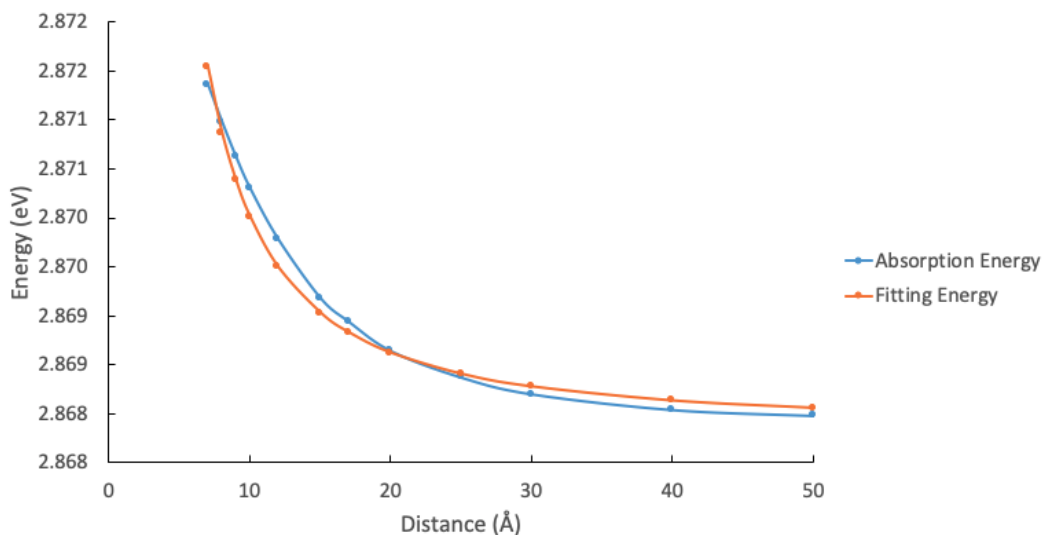


Figure 3.7 Distance dependence of the absorption energy from the third highest intensity excitation of the Ag_{116} dimer and the predicted distance dependence of this absorption energy in the form of $E = AR^{-b}$, with $A=0.0696$, $b=1.5119$.

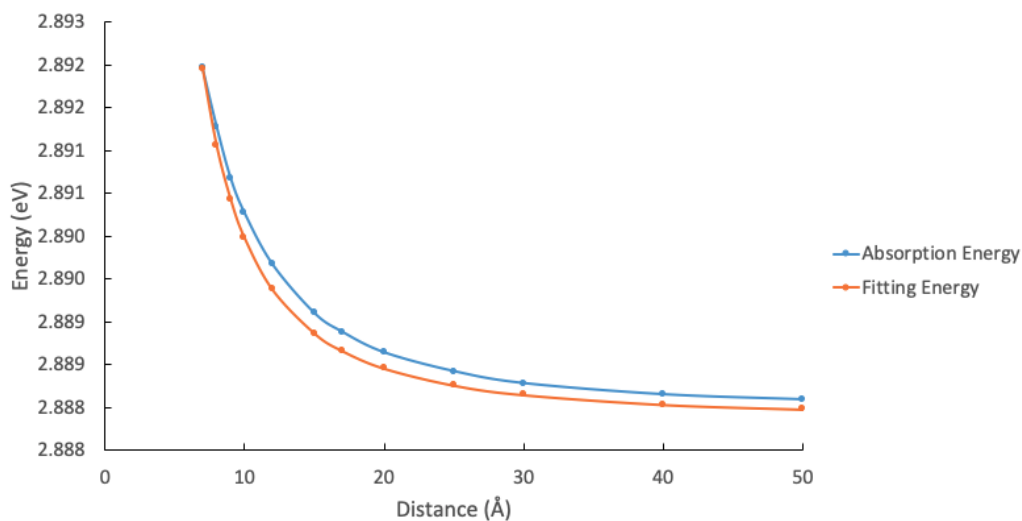


Figure 3.8 Distance dependence of absorption energy from the fourth highest energy excitation of the Ag_{116} dimer and the predicted distance dependence of this absorption energy in the form of $E = AR^{-b}$, with $A=0.1500$, $b=1.8516$.

For the Ag_{116} dimer, the vertical excitation energies are shown in Figures 3.5-3.8 with detailed data in Tables S3.1-S3.4. As shown in Figure 3.5 and Table A.1, as the distance decreases from 50 Å to 6 Å, the highest intensity peak red shifts from 2.90 eV to 2.87 eV. The overall trend

of the shifts agrees with distance dependence function AR^{-b} that would be expected from a classical dipole-dipole interaction. Figure 3.6 and Table A.2 show the distance-dependent shift in the second highest intensity peak of the Ag_{116} dimer, which is doubly degenerate (arising from x and y polarized excitations). The trend of the second highest peak agrees with a distance dependence function AR^{-b} ; however, it has positive sign of A which is the opposite compared to the highest intensity peak, which means that the peak blue shifts as the distance decreases. Figure 3.7 and Table A.1 show a similar trend to the second highest peak with a doubly degenerate state that also fits the distance dependence function; similarly, the peak blue shifts as the interparticle distance decreases. As shown in Figure 3.8 and Table A.4, the fourth highest intensity peak, which is also doubly degenerate, shares similar trends as the second and third highest intensity states.

By analyzing the direction of the transition dipole moment, we found that the highest peak arises from a transition dipole moment in the z direction in agreement with the nondegenerate feature we found in the excitation energy. In contrast, the second, third and fourth highest peaks come from transition dipole moments in the x and y directions, which agree with the doubly degenerate features in the excitation energy.

For the three other homodimer systems, the relation between absorption peak shifting and the direction of the transition dipole moment involved is the same as described for Ag_{116} (Figures S3.2-S3.23). All transition dipole moments in the z direction are nondegenerate; for these states, as the distance between nanoparticles decrease, the absorption energy red shifts. Double degeneracies are observed for all transition dipole moments in the x and y directions; with decreasing interparticle distance, the absorption energies for these features blue shift.

All of the vertical excitation energies polarized along the z-axis decrease in energy as the distance decreases (corresponding to a negative A value) and all of the vertical excitation energies

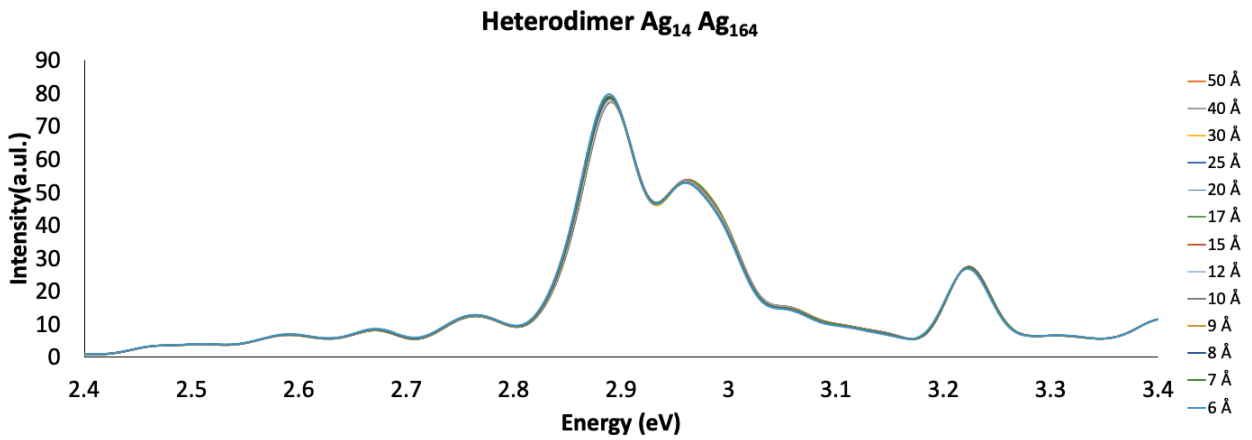
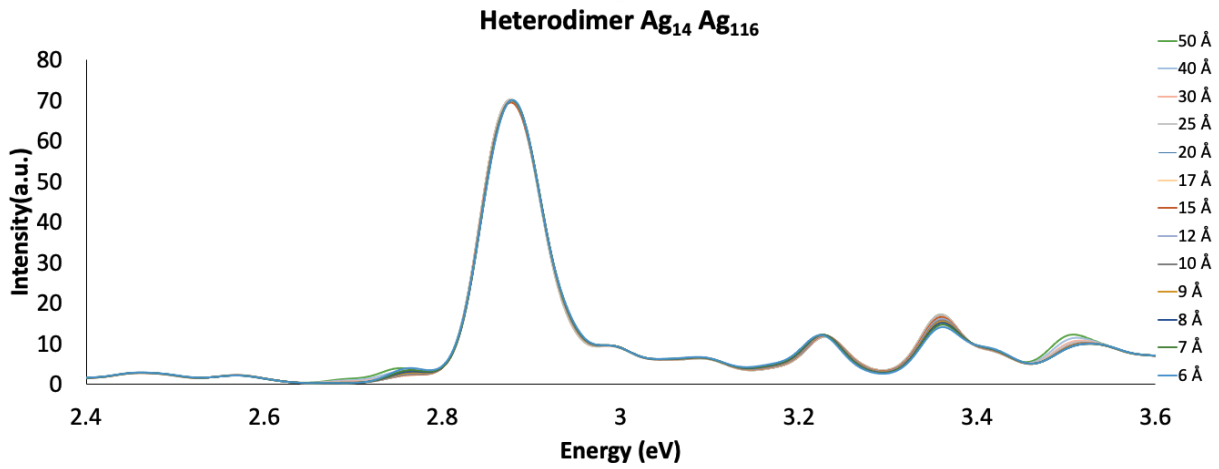
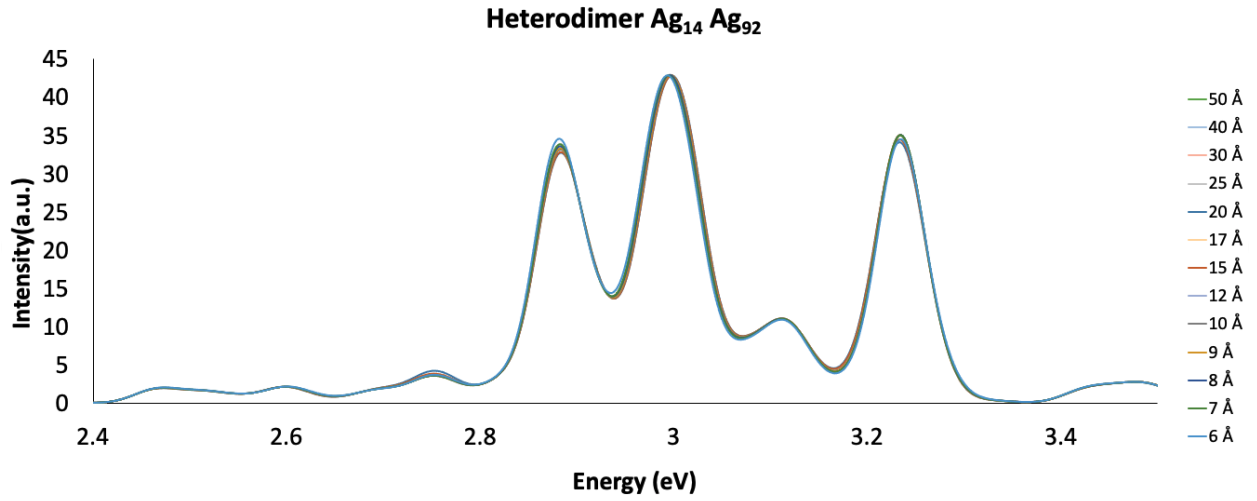
polarized in the x-y plane increase as the interparticle distance decreases (with a positive A value). When the highest peak is dominated by dipole-dipole interaction polarized along the z-axis, the highest peak in the absorption spectra red shifts as the nanoparticles in the dimer become closer. However, when the highest peak is dominated by dipole-dipole interaction that are polarized in the x-y plane, the highest peak in the absorption spectra blue shifts as the interparticle distance decreases.

When an overall peak in an absorption spectrum has significant contributions from vertical excited states with different polarization, the highest peak can blue shift over a certain range and red shift at another range. As an example, in the Ag_{116} homodimer, the highest peak blue shifts when the nanoparticle distance decreases from 50 Å to 20 Å, and red shifts from 15 Å to 6 Å (Figure 3.4c). Moreover, by comparing the intensities of the vertical excitations, we found that the highest intensity excitation at 50 Å arises from a z-polarized excitation with an intensity of 57.55, the second highest intensity feature is doubly degenerate and polarized in the x-y plane with an intensity of 26.39. The peak near 2.89 eV in the broadened absorption spectra of Figure 3.4c arises primarily from a combination of the states presented in Figures 3.5-3.8, which means that as the interparticle distance decreases from 50 Å to 6 Å, one vertical excitation red shifts (Figure 3.5) while three vertical excitations blue shift. All of these individual shifts combined yields the overall absorption peak shift for Ag_{116} . In the case of Ag_{116} , the total intensity of contributions polarized in the x-y plane combined is close to that polarized along the z-axis. The reason why it is difficult to see a consistent trend for highest energy peak is because the individual vertical excitation energies are very close in energy. This provides an answer for the second question regarding why Ag_{116} experiences a blue shift at intermediate distances and a red shift at the shortest interparticle distance.

Using data from vertical excitation energies of Ag_{14} , we found the highest energy peak red shift. And the energies with double degenerate blue shift. The new peak shows up at short distance is corresponding to the energy that red shifts, explaining the reason why the new peaks show up upon decreasing the interparticle distance. As interparticle distance decrease, the highest absorption peak of Ag_{14} is blue shift, due to the profile is dominated by vertical excitation from z direction and vertical excitation from x and y direction is relative difficult to recognized. In short interparticle distance, the vertical excitation in x and direction shift to lower energy and become recognizable from the overall profile. The opposite trend for Ag_{164} compared to Ag_{92} arises because the highest peak for Ag_{164} is dominated by the dipole-dipole interaction in the z-axis and the highest peak for Ag_{92} is dominated by the dipole-dipole interaction polarized in the x-y plane. For Ag_{92} , the dipole-dipole interaction in the x-y plane increase as the interparticle distance decrease, which shows a blue shift trend in absorption profile. On the contrary, for Ag_{164} , the dipole-dipole interaction in z-axis decrease as the interparticle distance decrease, which shows a red shift trend in the absorption profile. The peak shifting is related to direction of polarized dipole-dipole interaction. In the case of Ag_{116} , the contributions polarized in the x-y plane combined is close to that polarized along the z-axis so that it shows as blue shift in certain distance range and red shift in another distance range in the absorption profile.

3.4.3 Absorption spectra of heterodimer FCC structure silver nanoparticles

Similar to the homodimer at large interparticle distance, the intensity of the absorption spectra of heterodimer is essentially the sum of the intensities of the two constituent monomer nanoparticles, because of the lack of interaction at large interparticle distance. The absorption spectra for heterodimer nanoparticles comprised of different monomer combinations (Ag_{14} , Ag_{92} , Ag_{116} , Ag_{164}) at different distances are shown in Figure 3.9. For Ag_{14} interacting with Ag_{92} , and Ag_{116} interacting with Ag_{164} , only minor peak shifting in the absorption profile is observed (Figure 3.9a-c), which we attribute to the relatively small size of Ag_{14} compared to the other three nanoparticles. Due to the comparable size and similar absorption energies of Ag_{92} , Ag_{116} and Ag_{164} , the peak shift and the intensity change at different interparticle distances (Figure 3.9d-3.9f) is more obvious compared to heterodimer systems involving Ag_{14} . For Ag_{92} interacting with Ag_{116} and Ag_{164} , the absorption peak shifts are relatively large compared to the case when Ag_{14} interacts with Ag_{116} and Ag_{164} . Only a very small shift in the absorption peak occurs when Ag_{92} interacts with Ag_{14} at different distances (Figure 3.9a). In contrast, the peak shift is much larger when Ag_{92} interacts with Ag_{116} (Figure 3.9d) at different interparticle distances. We conclude that size is one of the key features for understanding nanoparticle heterodimer optical properties. When monomers are similar in size, the distance-dependent sensitivity of various features in the overall profile of the absorption spectra also increases; for example, peak shifting is found to be greater when two monomers are similar in size. In systems where the two sizes of nanoparticles are relatively distinct, the distance dependent shifts observed in the absorption spectra are relatively weak. Considering the difference excitation energy of Ag_{14} and the other nanoparticles, excitation energy is another potential key factor that affects peak shifting in the absorption spectra.



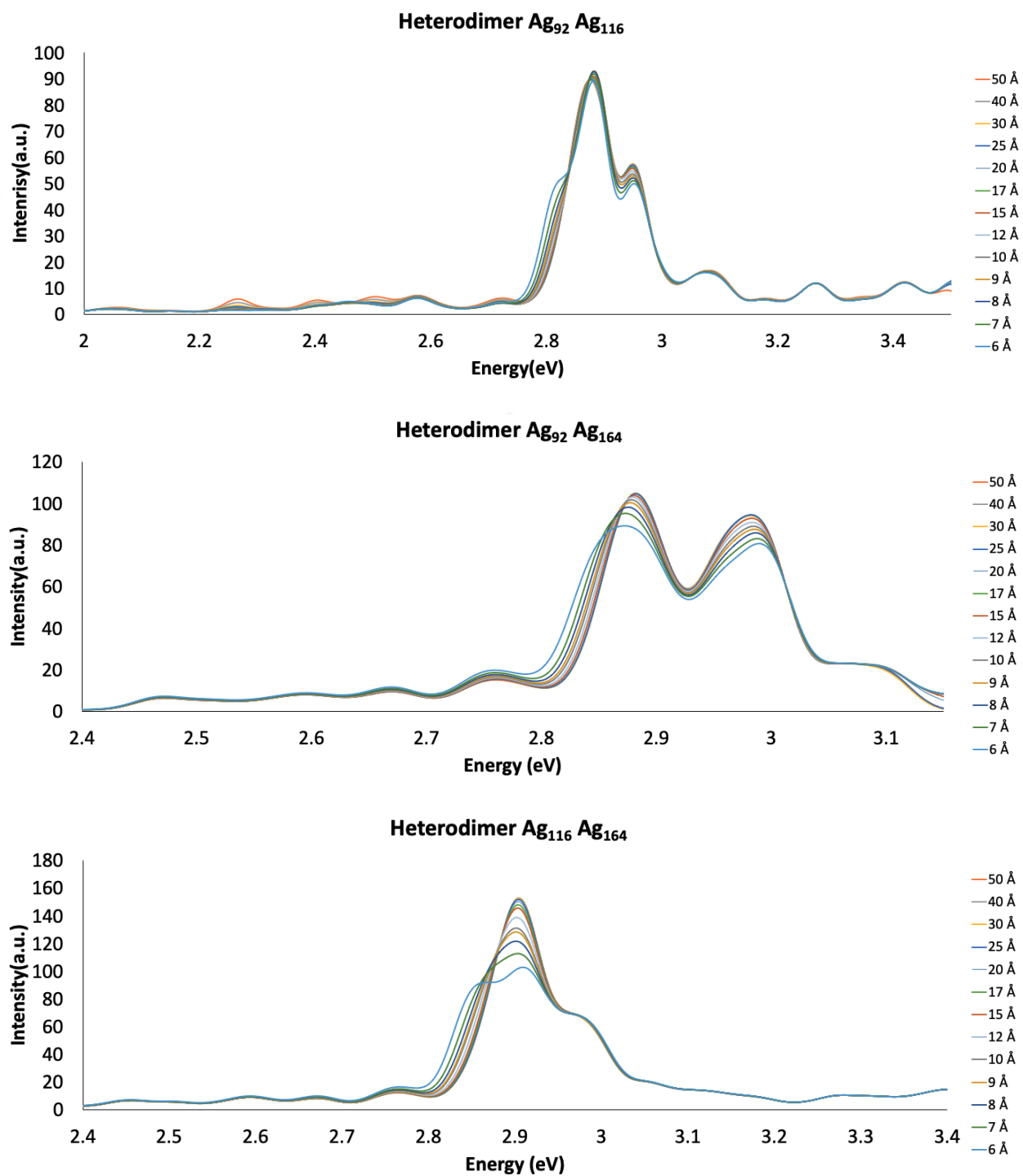


Figure 3.9 Calculated absorption spectra for FCC silver nanoparticle heterodimers. (a) Ag₁₄ and Ag₉₂, (b) Ag₁₄ and Ag₁₁₆, (c) Ag₁₄ and Ag₁₆₄, (d) Ag₉₂ and Ag₁₁₆, (e) Ag₉₂ and Ag₁₆₄, (f) Ag₁₁₆ and Ag₁₆₄.

For a heterodimer composed of Ag₁₁₆ and Ag₁₆₄, only one absorption peak is observed at large interparticle distance. When the distance between monomers decreases, the highest peak red shifts and then blue shifts. From Figures S3.20 – S3.22, we can find the highest peak from absorption profile come from different polarization in similar energy ranges (2.89 eV, 2.91 eV and 2.85 eV). As distance between nanoparticles get closer, the red shift trend competes with the trend of the blue shift. Thus, at large interparticle distances, the dipole-dipole interaction in the z direction is dominant, which appears as the red shift of the highest peak. At shorter distances, the trend is dominated by the dipole-dipole interaction between excitations polarized in the x-y plane; the two different interactions lead to peaks that begin to separate from each other. Starting from interparticle distances of 8 Å and shorter, during the red shifting process the second highest peak becomes distinct from the peak with the highest oscillator strength.

By analyzing the vertical excitation energies, we found that the origin of the absorption at large interparticle distances arises from a combination of the interaction of dipole moments polarized in the z direction and polarized in the x-y plane. As the distance decreases, the interaction of the dipole moment in the z direction is smaller and the interaction of the dipole moment polarized in the x-y plane increases, which corresponds to the red shifts and blue shifts of the peak.

3.5 Conclusion

In conclusion, we have investigated the optical properties of monomers and dimers of face centered cubic (FCC) Ag nanoparticles. By theoretically studying the absorption spectra, we can find the origin of the red shifts and blue shifts of absorption peaks. Due to the three-dimensional complexity of isotropic nanoparticles compared to one-dimensional nanowires and nanorods, the transition dipole moments that arise in the FCC dimer system are more complex.

For homodimer nanoparticles with two strong peaks (e.g. homodimer Ag₉₂ and homodimer Ag₁₆₄), one blue shift is observed with the distance decrease from 50 Å to 6 Å, while the other peak red shifts as the dimer get closer. For homodimer nanoparticles with one peak (e.g. homodimer Ag₁₄), the highest peak blue shifts as the distance decreases because the dipole-dipole interaction is polarized in the x-y plane. For Ag₁₁₆, the dipole-dipole interaction from both z direction and x-y plane are similar in energy so that the highest peak blue shifts 50 Å to 20 Å and the highest peak red shifts from 15 Å to 7 Å. As the interparticle distance decreases, the red shift of the highest peak comes from contributions to the transition dipole moment with components along the z-axis. In contrast, the peak blue shift as interparticle distance decreases mostly comes from the contributions of the transition dipole moment in the x and y directions and shows up with a doubly degenerate feature.

This provides a physically intuitive analysis for understanding why the highest peak blue shifts and red shifts at certain distance ranges. The calculated transition energy between different states from DFT methods can be reasonably well fit by a function of the form of AR^{-b} by the classical dipole-dipole interaction analysis.

We also found the size dependence of absorption spectra for heterodimer systems and analyzed them quantitatively. When the difference in the size of the two nanoparticles is large, the

spectra are only weakly sensitive to the interparticle distance. However, when the size of two nanoparticles in a heterodimer system is similar, the distance-dependent features become more sensitive.

In conclusion, TD-DFTB is an efficient method to study large plasmonic systems that contain quantum mechanical characteristics. By studying the vertical excitation energies, we can discover more profound physical meaning than by comparing broadened absorption spectra.

3.6 Acknowledgement

This material is based on work supported by the Air Force Office of Scientific Research under Grant FA9550-15-0114. The computing for this project was performed on the Beocat Research Cluster at Kansas State University, which is funded in part by NSF Grants CHE-1726332, CNS-1006860, EPS-1006860, and EPS-0919443.

3.7 References

- (1) Huang, X.; El-Sayed, I. H.; Qian, W.; El-Sayed, M. A. Cancer Cell Imaging and Photothermal Therapy in the Near-Infrared Region by Using Gold Nanorods. *J. Am. Chem. Soc.* 2006, 128 (6), 2115–2120. <https://doi.org/10.1021/ja057254a>.
- (2) Cognet, L.; Tardin, C.; Boyer, D.; Choquet, D.; Tamarat, P.; Lounis, B. Single Metallic Nanoparticle Imaging for Protein Detection in Cells. *Proc. Natl. Acad. Sci.* 2003, 100 (20), 11350–11355. <https://doi.org/10.1073/pnas.1534635100>.
- (3) Skirtach, A. G.; Dejugnat, C.; Braun, D.; Susha, A. S.; Rogach, A. L.; Parak, W. J.; Möhwald, H.; Sukhorukov, G. B. The Role of Metal Nanoparticles in Remote Release of Encapsulated Materials. *Nano Lett.* 2005, 5 (7), 1371–1377. <https://doi.org/10.1021/nl050693n>.
- (4) Nie, S. Probing Single Molecules and Single Nanoparticles by Surface-Enhanced Raman Scattering. *Science* 1997, 275 (5303), 1102–1106. <https://doi.org/10.1126/science.275.5303.1102>.
- (5) Yu; Chang, S.-S.; Lee, C.-L.; Wang, C. R. C. Gold Nanorods: Electrochemical Synthesis and Optical Properties. *J. Phys. Chem. B* 1997, 101 (34), 6661–6664. <https://doi.org/10.1021/jp971656q>.
- (6) Link, S.; El-Sayed, M. A. Spectral Properties and Relaxation Dynamics of Surface Plasmon Electronic Oscillations in Gold and Silver Nanodots and Nanorods. *J. Phys. Chem. B* 1999, 103 (40), 8410–8426. <https://doi.org/10.1021/jp9917648>.
- (7) Burda, C.; Chen, X.; Narayanan, R.; El-Sayed, M. A. Chemistry and Properties of Nanocrystals of Different Shapes. *Chem. Rev.* 2005, 105 (4), 1025–1102. <https://doi.org/10.1021/cr030063a>.
- (8) Eustis, S.; El-Sayed, M. A. Why Gold Nanoparticles Are More Precious than Pretty Gold: Noble Metal Surface Plasmon Resonance and Its Enhancement of the Radiative and Nonradiative Properties of Nanocrystals of Different Shapes. *Chem Soc Rev* 2006, 35 (3), 209–217. <https://doi.org/10.1039/B514191E>.
- (9) Link, S.; Mohamed, M. B.; El-Sayed, M. A. Simulation of the Optical Absorption Spectra of Gold Nanorods as a Function of Their Aspect Ratio and the Effect of the Medium Dielectric Constant. *J. Phys. Chem. B* 1999, 103 (16), 3073–3077. <https://doi.org/10.1021/jp990183f>.

- (10) Guidez, E. B.; Aikens, C. M. Quantum Mechanical Origin of the Plasmon: From Molecular Systems to Nanoparticles. *Nanoscale* 2014, 6 (20), 11512–11527. <https://doi.org/10.1039/C4NR02225D>.
- (11) Nordlander, P.; Oubre, C.; Prodan, E.; Li, K.; Stockman, M. I. Plasmon Hybridization in Nanoparticle Dimers. *Nano Lett* 2004, 4, 899.
- (12) Aćimović, S. S.; Kreuzer, M. P.; González, M. U.; Quidant, R. Plasmon Near-Field Coupling in Metal Dimers as a Step toward Single-Molecule Sensing. *ACS Nano* 2009, 3, 1231.
- (13) Alkan, F.; Aikens, C. M. TD-DFT and TD-DFTB Investigation of the Optical Properties and Electronic Structure of Silver Nanorods and Nanorod Dimers. *J. Phys. Chem. C* 2018, 122 (41), 23639–23650. <https://doi.org/10.1021/acs.jpcc.8b05196>.
- (14) Alkan, F.; Aikens, C. M. Understanding Plasmon Coupling in Nanoparticle Dimers Using Molecular Orbitals and Configuration Interaction. *Phys. Chem. Chem. Phys.* 2019, 21 (41), 23065–23075. <https://doi.org/10.1039/C9CP03890F>.
- (15) Bae, G. T.; Aikens, C. M. TDDFT and CIS Studies of Optical Properties of Dimers of Silver Tetrahedra. *J Phys Chem A* 2012, 116, 8260.
- (16) Marinica, D. C.; Kazansky, A. K.; Nordlander, P.; Aizpurua, J.; Borisov, A. G. Quantum Plasmonics: Nonlinear Effects in the Field Enhancement of a Plasmonic Nanoparticle Dimer. *Nano Lett* 2012, 12, 1333.
- (17) Prodan, E.; Radloff, C.; Halas, N. J.; Nordlander, P. A Hybridization Model for the Plasmon Response of Complex Nanostructures. *Science* 2003, 302, 419.
- (18) Willingham, B.; Brandl, D. W.; Nordlander, P. Plasmon Hybridization in Nanorod Dimers. *Appl Phys B* 2008, 93, 209.
- (19) Aikens, C. M.; Li, S. Z.; Schatz, G. C. From Discrete Electronic States to Plasmons: TDDFT Optical Absorption Properties of Ag_n (n = 10, 20, 35, 56, 84, 120) Tetrahedral Clusters. *J Phys Chem C* 2008, 112, 11272.
- (20) Johnson, H. E.; Aikens, C. A. Electronic Structure and TDDFT Optical Absorption Spectra of Silver Nanorods. *J Phys Chem A* 2009, 113, 4445.
- (21) Guidez, E. B.; Aikens, C. M. Diameter Dependence of the Excitation Spectra of Silver and Gold Nanorods. *J Phys Chem C* 2013, 117, 12325.

- (22) Stener, M.; Nardelli, A.; De Francesco, R.; Fronzoni, G. Optical Excitations of Gold Nanoparticles: A Quantum Chemical Scalar Relativistic Time Dependent Density Functional Study. *J Phys Chem C* 2007, 111, 11862.
- (23) Durante, N.; Fortunelli, A.; Broyer, M.; Stener, M. Optical Properties of Au Nanoclusters from TD-DFT Calculations. *J Phys Chem C* 2011, 115, 6277.
- (24) Barcaro, G.; Sementa, L.; Fortunelli, A.; Stener, M. Optical Properties of Silver Nanoshells from Time-Dependent Density Functional Theory Calculations. *J Phys Chem C* 2014, 118, 12450.
- (25) Weissker, H. C.; Mottet, C. Optical Properties of Pure and Core-Shell Noble-Metal Nanoclusters from TDDFT: The Influence of the Atomic Structure. *Phys Rev B* 2011, 84, 165443.
- (26) López-Lozano, X.; Barron, H.; Mottet, C.; Weissker, H.-C. Aspect-Ratio- and Size-Dependent Emergence of the Surface-Plasmon Resonance in Gold Nanorods – an Ab Initio TDDFT Study. *Phys Chem Chem Phys* 2014, 16, 1820.
- (27) Liao, M. S.; Bonifassi, P.; Leszczynski, J.; Ray, P. C.; Huang, M. J.; Watts, J. D. Structure, Bonding, and Linear Optical Properties of a Series of Silver and Gold Nanorod Clusters: DFT/TDDFT Studies. *J Phys Chem A* 2010, 114, 12701.
- (28) Iida, K.; Noda, M.; Ishimura, K.; Nobusada, K. First-Principles Computational Visualization of Localized Surface Plasmon Resonance in Gold Nanoclusters. *J Phys Chem A* 2014, 118, 11317.
- (29) Asadi-Aghbolaghi, N.; Rüger, R.; Jamshidi, Z.; Visscher, L. TD-DFT+TB: An Efficient and Fast Approach for Quantum Plasmonic Excitations. *J. Phys. Chem. C* 2020, 124 (14), 7946–7955. <https://doi.org/10.1021/acs.jpcc.0c00979>.
- (30) D'Agostino, S.; Rinaldi, R.; Cuniberti, G.; Della Sala, F. Density Functional Tight Binding for Quantum Plasmonics. *J. Phys. Chem. C* 2018, 122 (34), 19756–19766. <https://doi.org/10.1021/acs.jpcc.8b05278>.
- (31) Douglas-Gallardo, O. A.; Berdakin, M.; Frauenheim, T.; Sánchez, C. G. Plasmon-Induced Hot-Carrier Generation Differences in Gold and Silver Nanoclusters. *Nanoscale* 2019, 11 (17), 8604–8615. <https://doi.org/10.1039/C9NR01352K>.

- (32) Porezag, D.; Frauenheim, T.; Kohler, T.; Seifert, G.; Kaschner, R. Construction of Tight-Binding-Like Potentials on the Basis of Density-Functional Theory – Application to Carbon. *Phys Rev B* 1995, 51, 12947.
- (33) Seifert, G.; Porezag, D.; Frauenheim, T. Calculations of Molecules, Clusters, and Solids with a Simplified LCAO-DFT-LDA Scheme. *Int J Quantum Chem* 1996, 58, 185.
- (34) Niehaus, T. A.; Suhai, S.; Sala, F. D.; Lugli, P.; Elstner, M.; Seifert, G.; Frauenheim, T. Tight-Binding Approach to Time-Dependent Density-Functional Response Theory. *Phys Rev B* 2001, 63, 085108.
- (35) Frauenheim, T.; Seifert, G.; Elstner, M.; Niehaus, T.; Kohler, C.; Amkreutz, M.; Sternberg, M.; Hajnal, Z.; Di Carlo, A.; Suhai, S. Atomistic Simulations of Complex Materials: Ground-State and Excited-State Properties. *J Phys Condens Matter* 2002, 14, 3015.
- (36) Douglas-Gallardo, O. A.; Berdakin, M.; Sanchez, C. G. Atomistic Insights into Chemical Interface Damping of Surface Plasmon Excitations in Silver Nanoclusters. *J Phys Chem C* 2016, 120, 24389.
- (37) Bonafé, F. P.; Aradi, B.; Guan, M. X.; Douglas-Gallardo, O. A.; Lian, C.; Meng, S.; Frauenheim, T.; Sánchez, C. G. Plasmon-Driven Sub-Picosecond Breathing of Metal Nanoparticles. *Nanoscale* 2017, 9, 12391.
- (38) Douglas-Gallardo, O. A.; Soldano, G. J.; Mariscal, M. M.; Sanchez, C. G. Effects of Oxidation on the Plasmonic Properties of Aluminum Nanoclusters. *Nanoscale* 2017, 9, 17471.
- (39) Ilawe, N. V.; Oviedo, M. B.; Wong, B. M. Real-Time Quantum Dynamics of Long-Range Electronic Excitation Transfer in Plasmonic Nanoantennas. *J Chem Theory Comput* 2017, 13, 3442.
- (40) Ilawe, N. V.; Oviedo, M. B.; Wong, B. M. Effect of Quantum Tunneling on the Efficiency of Excitation Energy Transfer in Plasmonic Nanoparticle Chain Waveguides. *J. Mater. Chem. C* 2018, 6 (22), 5857–5864. <https://doi.org/10.1039/C8TC01466C>.
- (41) Oviedo, M. B.; Wong, B. M. Real-Time Quantum Dynamics Reveals Complex, Many-Body Interactions in Solvated Nanodroplets. *J. Chem. Theory Comput.* 2016, 12 (4), 1862–1871. <https://doi.org/10.1021/acs.jctc.5b01019>.
- (42) te Velde, G.; Bickelhaupt, F. M.; Baerends, E. J.; Fonseca Guerra, C.; van Gisbergen, S. J. A.; Snijders, J. G.; Ziegler, T. Chemistry with ADF. *J. Comput. Chem.* 2001, 22 (9), 931–967. <https://doi.org/10.1002/jcc.1056>.

- (43) Van Gisbergen, S. J. A.; Snijders, J. G.; Baerends, E. J. Implementation of Time-Dependent Density Functional Response Equations. *Comput. Phys. Commun.* 1999, 118 (2), 119–138. [https://doi.org/10.1016/S0010-4655\(99\)00187-3](https://doi.org/10.1016/S0010-4655(99)00187-3).
- (44) Rürger, R.; Van Lenthe, E.; Lu, Y.; Frenzel, J.; Heine, T.; Visscher, L. Efficient Calculation of Electronic Absorption Spectra by Means of Intensity-Selected Time-Dependent Density Functional Tight Binding. *J. Chem. Theory Comput.* 2015, 11 (1), 157–167. <https://doi.org/10.1021/ct500838h>.
- (45) Ru, R.; Lenthe, E. Van; Lu, Y.; Frenzel, J.; Heine, T.; Visscher, L. Correction: Efficient Calculation of Electronic Absorption Spectra by Means of Intensity-Selected Time-Dependent Density Functional Tight Binding (*Journal of Chemical Theory and Computation* (2015) 11:1 (157-167) DOI: 10.1021/Ct500838h). *J. Chem. Theory Comput.* 2017, 13 (7), 3424–3425. <https://doi.org/10.1021/acs.jctc.7b00564>.
- (46) Elstner, M.; Porezag, D.; Jungnickel, G.; Elsner, J.; Haugk, M.; Frauenheim, Th.; Suhai, S.; Seifert, G. Self-Consistent-Charge Density-Functional Tight-Binding Method for Simulations of Complex Materials Properties. *Phys. Rev. B* 1998, 58 (11), 7260–7268. <https://doi.org/10.1103/PhysRevB.58.7260>.
- (47) Elstner, M.; Frauenheim, T.; Kaxiras, E.; Seifert, G.; Suhai, S. A Self-Consistent Charge Density-Functional Based Tight-Binding Scheme for Large Biomolecules. *Phys. Status Solidi B Basic Res.* 2000, 217 (1), 357–376. [https://doi.org/10.1002/\(SICI\)1521-3951\(200001\)217:1<357::AID-PSSB357>3.0.CO;2-J](https://doi.org/10.1002/(SICI)1521-3951(200001)217:1<357::AID-PSSB357>3.0.CO;2-J).
- (48) Rürger, R.; van Lenthe, E.; Lu, Y.; Frenzel, J.; Heine, T.; Visscher, L.; Szűcs, B.; Hajnal, Z.; Frauenheim, Th.; González, C.; Ortega, J.; Pérez, R.; Flores, F.; Rürger, R.; van Lenthe, E.; Lu, Y.; Frenzel, J.; Heine, T.; Visscher, L. Chalcogen Passivation of GaAs(1 0 0) Surfaces: Theoretical Study. In *Applied Surface Science*; North-Holland, 2003; Vol. 212–213, pp 861–865. [https://doi.org/10.1016/S0169-4332\(03\)00016-3](https://doi.org/10.1016/S0169-4332(03)00016-3).
- (49) Szűcs, B.; Hajnal, Z.; Scholz, R.; Sanna, S.; Frauenheim, T. Theoretical Study of the Adsorption of a PTCDA Monolayer on S-Passivated GaAs(1 0 0). *Appl. Surf. Sci.* 2004, 234 (1–4), 173–177. <https://doi.org/10.1016/J.APSUSC.2004.05.181>.
- (50) Jain, P. K.; El-Sayed, M. A. Plasmonic Coupling in Noble Metal Nanostructures. *Chem Phys Lett* 2010, 487, 153.

- (51) Ekardt, W. Collective Multipole Excitations in Small Metal Particles: Critical Angular Momentum Lex for the Existence of Collective Surface Modes. *Phys Rev B* 1985, 32, 1961.
- (52) Khlebtsov, B. N.; Khlebtsov, N. G. Multipole Plasmons in Metal Nanorods: Scaling Properties and Dependence on Particle Size, Shape, Orientation, and Dielectric Environment. *J Phys Chem C* 2007, 111, 11516.
- (53) Jain, P. K.; Eustis, S.; El-Sayed, M. A. Plasmon Coupling in Nanorod Assemblies: Optical Absorption, Discrete Dipole Approximation Simulation, and Exciton-Coupling Model. *J Phys Chem B* 2006, 110, 18243.
- (54) Jain, P. K.; Huang, W.; El-Sayed, M. A. On the Universal Scaling Behavior of the Distance Decay of Plasmon Coupling in Metal Nanoparticle Pairs: A Plasmon Ruler Equation. *Nano Lett* 2007, 7, 2080.

Chapter 4 - Plasmon induced excitation energy transfer in silver nanoparticle dimers: A real-time TDDFTB investigation

Reproduced with permission from:

Zhen Liu, M. Belén Oviedo, Bryan M. Wong, and Christine M. Aikens, *J. Chem. Phys.* 156, 154705 (2022)

4.1 Abstract

Using real-time quantum dynamics calculations, we perform theoretical investigations of light-induced interactions and electronic excitation transfer in a silver nanoparticle dimer. Real-time time-dependent density functional tight-binding (RT-TDDFTB) calculations provide details of the quantum dynamical processes at an electronic/atomistic level with attosecond resolution. The computational efficiency of RT-TDDFTB allows us to examine electronic dynamics up to picosecond time scales. With time scales varying over six orders of magnitude, we provide insight into interactions between the nanoparticle and laser and between nanoparticles. Our results show that the coupling between nanoparticle monomers is dependent on the separation distance between the nanoparticles in the dimer. As the interparticle distance is varied, the dipole-dipole interactions and electronic excitation transfer mechanisms are markedly different. At large distances (from 50 to 20 Å), the energy transfer from NP1 to NP2 becomes more efficient as the interparticle distance decreases. The total dipole moment of the Ag₁₄ nanoparticle dimer increases linearly at an interparticle distance of 2 nm and reaches its maximum after 1.2 ps. The electronic excitation transfer is also the most efficient at 2 nm. At short distances, back-transfer effects reduce the ability of the dimer and NP1 to accept energy from the incident electric field. We attribute the distance-

dependent features of the nanoparticle dimer to the beating between the laser acting on NP1 and the back transfer from NP2 to NP1.

4.2 Introduction

The interaction between noble-metal nanoparticles and light have many applications in chemistry, physics, and biology. Due to their high physical and chemical stability,¹⁻⁴ noble-metal nanoparticles present a unique opportunity for exploring different properties and applications with tremendous tunability. One of the unique properties of these systems is the appearance of localized surface plasmon resonances (LSPRs).⁵⁻¹⁰ LSPRs originate from the collective oscillation of free electrons of metal nanoparticles when excited by an external field. LSPRs enable high electric field intensities due to the plasmon resonance, high sensitivity to the environment, and strong interparticle coupling. In addition to the tunability of individual nanoparticles, the existence of neighboring particles can also modulate the optical properties of nanoparticle systems.¹¹⁻¹⁶

The simplest model to study plasmonic coupling is the nanoparticle dimer. A systematic study of nanoparticle dimers not only provides more insight about nanoparticle interactions but also paves the way for further study of hybridized plasmons in more complex systems.^{11,17,18} Beside hybridized plasmons, a large electromagnetic field enhancement can occur in a nanoparticle junction when the surface plasmon is excited. Studying nanoparticle dimers not only provides physical insights about nanoparticle interactions but also provides a deeper understanding of electromagnetic field enhancements.¹⁶ The coherent nature of the LSPR results in large dipole moments, and electronic excitation transfer (EET) mechanisms can transfer energy to neighboring nanoparticles via electrostatic coupling. In previous experiments, Maier and co-workers observed EET from a localized source to a localized detector in a plasmon waveguide.¹⁹ Yun et al. have

used a noble nanocluster as an acceptor and reported EET with more than double the traditional Förster range.²⁰ The long-ranged nature of plasmonic interactions in EET has been analyzed by quantum dynamics calculations by Ilawe et al.²¹ Investigations of electronic excitation transfer mechanisms in nanoparticles at a quantum dynamical level of detail can provide insights for future applications in directing and controlling excitation energy in even more complex systems.^{21–23}

Several previous theoretical studies have utilized density functional theory (DFT) and time-dependent density functional theory (TDDFT)^{15,24–33} for describing quantum mechanical effects on optical properties.^{34–36} Density functional tight-binding (DFTB)^{37,38} and its real-time formalism (RT-TDDFTB)²¹ are more computationally efficient for exploring large systems and longer time scales. Within the RT-TDDFTB formalism, the one-electron density matrix is propagated in the presence of an external electric field. The simulated optical absorption spectrum can be obtained by a Fourier transform of the time-evolving dipole moment into the frequency (energy) domain. Sanchez and co-workers have used RT-TDDFTB to investigate the relaxation dynamics of LSPRs in nanoclusters.^{39–41} Wong and co-workers used RT-TDDFTB to study the electron dynamics of a plasmonic antenna for understanding plasmonic effects.^{21–23} In addition to RT-TDDFTB, the linear response (LR) formalism of DFTB has also been used to calculate optical absorption spectra. In 2018, Alkan et al. used the LR-TDDFTB formalism to study the optical properties and electronic structures of silver nanorods and nanorod dimers.¹³ Their results showed good agreement in the spectral shapes, energies, and intensity trends between the LR-TDDFT and LR-TDDFTB calculations. Liu et al. observed different absorption peak shifts in different sizes of homodimers and heterodimers, which are related to the direction of the transition dipole moment.⁴²

Due to the high computational efficiency of DFTB and RT-TDDFTB, these methods can be used on simulations of large systems and long time scales. Moreover, because DFTB and RT-

TDDFTB allow for the explicit treatment of electronic structure in the presence of external fields, they can more accurately predict electron dynamics effects compared to classical methods, particularly in cases where quantum mechanical effects become important. Quantum mechanical methods are required to treat effects such as electron tunneling and charge transfer plasmons that emerge when the interparticle distance between nanoparticles becomes small. In this study, we employ RT-TDDFTB on a nanoparticle dimer system to examine each individual nanoparticle in the presence of an external electric field and understand the resulting dynamics as the distance between the nanoparticles is varied.

4.3 Computational Methods

The DFTB+ code⁴³ was used to calculate the ground-state Hamiltonian, overlap matrix elements, and the initial single-electron density matrix within the self-consistent density functional tight-binding (SCC-DFTB) formalism. SQUIRRELS (Streamlined QUantum Interface for Researching Real-Time ELectronic Systems),²¹ a real-time implementation of DFTB, is used to probe the nonequilibrium electron dynamics. This methodology has also been used by other authors to compute the photoinjection dynamics in dye-sensitized TiO₂ solar cells,^{44–46} excitation energy transfer in photosynthetic molecules,^{47,48} in noncovalently bonded molecular aggregates,⁴⁹ many-body interactions in solvated nanodroplets,²³ and excitation energy transfer dynamics in plasmonic arrays.^{21,22,36,50,51} Also, recently the implementation can be found in the DFTB+ code.⁵² 250,000 electron dynamics steps were taken with a time step of 0.2 a.u. (4.8 attoseconds). Because of the computational efficiency of RT-TDDFTB, our simulations can be carried out to picoseconds with an attosecond time step, which spans over six orders of magnitude of time. We used a continuous wave field, which mimics a laser field polarized in the z direction, with an electric field

strength of 0.0001 V/Angstrom. In our simulations, only the first Ag₁₄ nanoparticle was excited with a laser, which was tuned to the highest excitation peak of the monomer (3.22 eV). The induced dipole moment in the second Ag₁₄ nanoparticle was due to stimulation from the first Ag₁₄ nanoparticle.

For the quantum dynamics calculations, RT-TDDFTB propagates the one electron density matrix in the presence of an external time-varying electric field. The time-dependent Hamiltonian is given by:

$$H(t) = H^0 - E_0(t) \cdot \mu(t) \quad (1)$$

In equation (1), \hat{H}^0 is the reference Hamiltonian, $E_0(t)$ is the applied electric field, and $\hat{\mu}(t)$ is the dipole moment operator. Because the quantum system propagates in the time domain, $E_0(t)$ can be chosen to take any time-dependent form. To simulate an optical absorption spectrum, $E_0(t)$ can be chosen as a Dirac delta function and the absorption spectrum in the frequency domain can be obtained by a Fourier transform of the time-evolving dipole moment. To simulate the system interacting with monochromatic light, $E_0(t)$ can take the form of a sinusoidal perturbation. Different choices of the applied electric field give different but complementary viewpoints of quantum dynamics. According to the Liouville–von Neumann equation, upon interaction with time-dependent fields, the DFTB density matrix $\hat{\rho}$ will evolve as:²¹

$$\frac{\partial \rho}{\partial t} = \frac{1}{i\hbar} (S^{-1} \cdot H[\rho] \cdot \rho - \rho \cdot H[\rho] \cdot S^{-1}) \quad (2)$$

where \hat{H} is the Hamiltonian matrix (which implicitly depends on the density matrix).²¹ The hybrid set of Slater-Koster parameters^{53,54} for the silver atoms was used.

Two identical Ag_{14} were placed with different edge-to-edge interparticle distance (8, 9, 10, 12, 15, 20, 25, 30, 40, and 50 Å) as shown in Figure 4.1. These values correspond to the distances between the two closest atoms from different nanoparticles in the dimer structure along the z -axis. Only the first nanoparticle (donor) was excited with a laser (sinusoidal electric field perturbation) with its frequency equal to the monomer plasmonic energy (3.22 eV) and polarized along the intermolecular axis. Strong dipole moments are induced in the second nanoparticle (acceptor). The incident field is small enough (0.0001 V/Å) so that the system remains in the linear response regime. Based on previous work, we found an absorption peak of 3.2228 eV for the Ag_{14} monomer from LR-TDDFTB calculations,⁴² which is resonant with a laser frequency of 3.22 eV used in our current work.

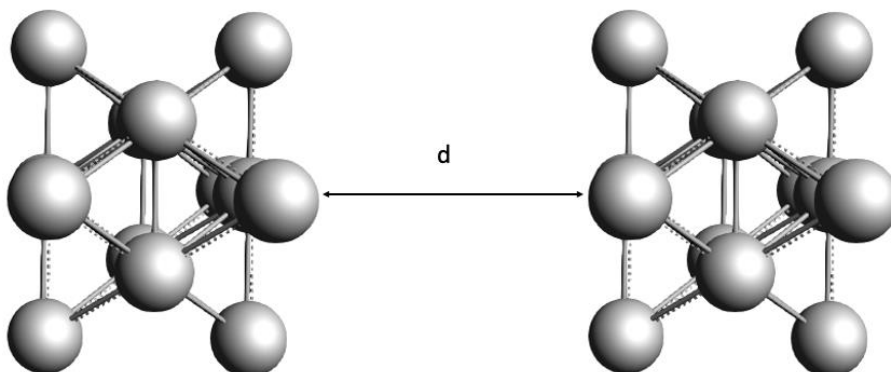


Figure 4.1 Interparticle distances between two identical Ag_{14} clusters.

4.4 Results and Discussion

4.4.1 Short-time dynamics

In our RT-TDDFTB study, initial excitation of NP1 in the z-direction leads to an increasing z-component of the dipole moment for NP1 followed by an induced dipole moment for NP2. The dipole moment components in the x and y direction are zero due to symmetry. In the short-time dynamics, the peak of the NP2 dipole moment occurs approximately when the NP1 dipole is zero, as shown in Figure 4.2. A previously formulated analytical model based on a two-level system (TLS)⁵⁵ is also used to analyze the nanoparticle dimer. Because the size of the Ag₁₄ nanoparticles (face-to-face distance of 4 Å) is smaller than the interparticle distance (from 8 Å to 50 Å), we use a dipole approximation, which approximates the coupling between the nanoparticles as a point dipole interacting with another point dipole. In the analytical TLS, the dipole moment in NP2 is induced by the direct excitation of NP1. Based on linear response theory⁵⁶ and an analytical TLS, the dipole moment in NP1 can be expressed as:

$$\mu_1(t) \approx \frac{E_0}{\hbar} |\mu_1|^2 t \cdot \cos(\omega_{ex} t) \hat{r} \quad (3)$$

where E_0 is the applied electric field, μ_1 is the transition dipole moment of NP1, $\omega_{ex} = \Delta E_{ex}/\hbar$ is the excitation energy, and \hat{r} is the direction of the transition dipole moment.

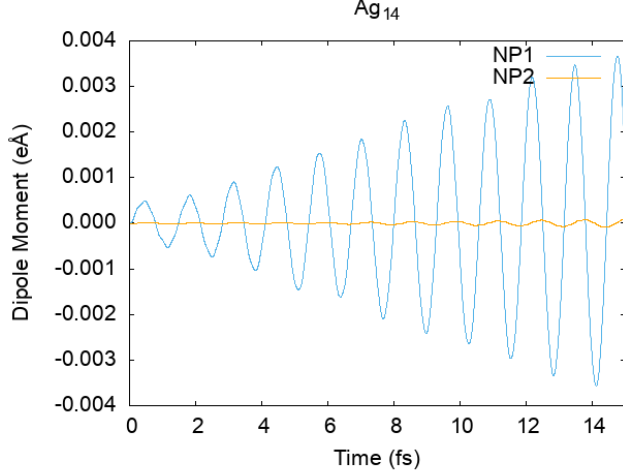


Figure 4.2 Short-time electron dynamics in our RT-TDDFTB simulation with an interparticle distance of 25 Å. The dipole moment of NP1 fluctuates under the external field, and the induced dipole moment of NP2 arises from the excitation of NP1.

Because both nanoparticles are identical, the transition dipole moment is the same. The induced dipole moment of NP2 in the homodimer system can be expressed as:

$$\mu_2(t) \approx -\frac{E_0}{4\pi\epsilon_0\hbar^2d^3}|\mu_1|^4t^2\sin(\omega_{\text{ex}}t)\hat{r} \quad (4)$$

where ϵ_0 is the vacuum permittivity and d is the distance between the nanoparticles.

4.4.2 Long-time dynamics

From the TLS model, the peak of the dipole moment in NP1 increases linearly, because of continuous laser field, while the peak of the dipole moment in NP2 increases quadratically as a function of time. These trends agree with short-time dynamics models. However, for longer times, we observe that the dipole moments of NP1 and NP2 deviate from this expectation. These deviations from the analytical model indicates the complexity of long-time electron dynamics in nanoparticles. To understand these effects, we now analyze each individual nanoparticle system with different interparticle distances.

The computational efficiency of RT-TDDFTB allows us to simulate electronic dynamics up to picosecond time scales. The simulation for the nanoparticle dimer with a 50 Å separation is shown in Figure 4.3. Because the main interaction is dipolar, the peak of the dipole moment of NP1 increases linearly until 400 fs (Figure 4.3(b)), and the dipole moment of NP2 increases quadratically (Figure 4.3(c)), which agrees with the analytical TLS model for short-time dynamics. For the first 700 fs, the dipole moment of the overall nanoparticle dimer mostly comes from NP1. Around 700 fs, the total dipole moment reaches its maximum, at which point NP2 contributes one-seventh of the dipole moment. After 700 fs, the contribution from NP1 decreases, while the contribution from NP2 still increases, although at a slower rate than before. The explanation to this phenomenon is given by the fact that the system cannot absorb more energy so that it starts to transfer to the field, because of the coupling between them. It also shows the advantage of the real-time simulation which, in the long time dynamics, even in LR regime, we can still observe the non-linear effect.

As the interparticle distance of the dimer decreases to 40 Å (Figure 4.4), the overall profile of the dipole moment fluctuation is similar to the simulations with a 50 Å separation. However, the dipole moment intensity in NP2 is larger than that at the 50 Å separation, which indicates that EET from NP1 to NP2 becomes more efficient at 40 Å than at 50 Å. The total dipole moment reaches its maximum at 800 fs. Approximately one-third of its contribution comes from NP2, which is larger than its contribution for an interparticle distance of 50 Å. The linear increase in the dipole moment for NP1 deviates after 300 fs.

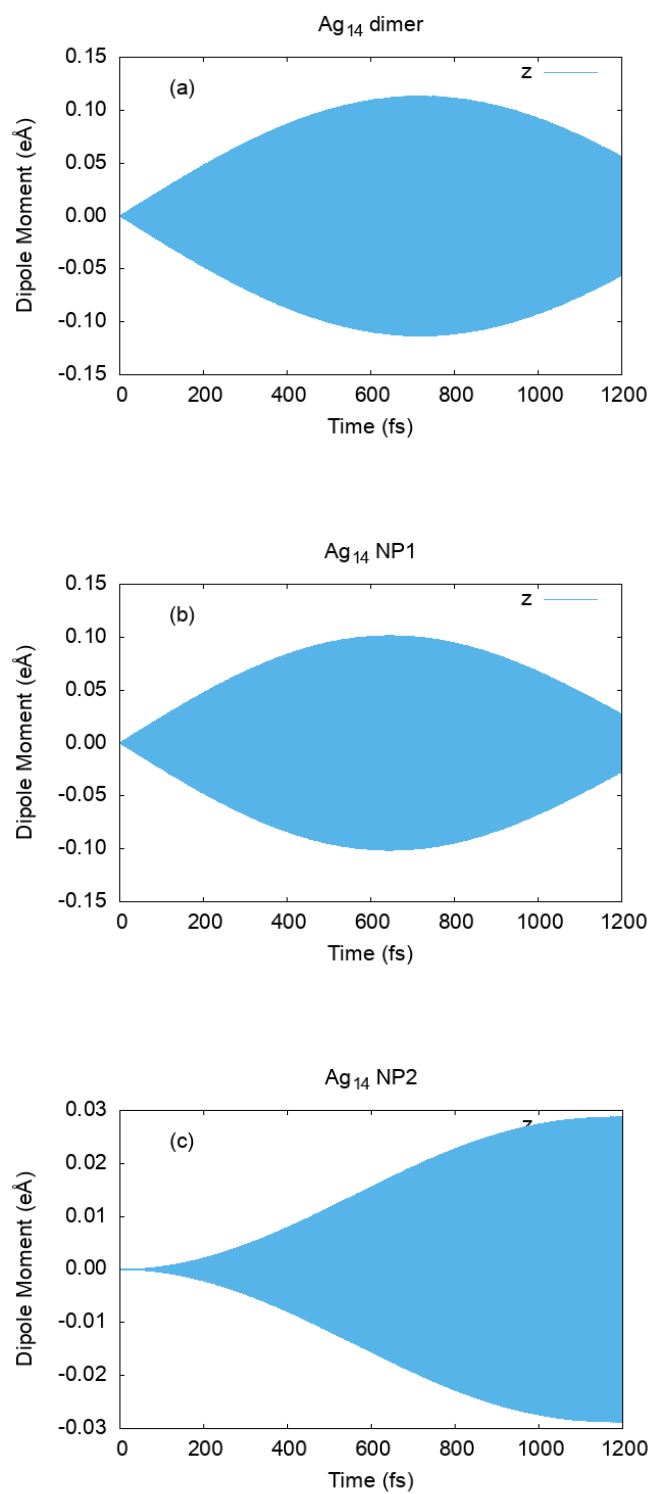


Figure 4.3 (a) Total dipole moment, (b) dipole moment of NP1, and (c) induced dipole moment of NP2 for a nanoparticle dimer with a 50 Å interparticle separation.

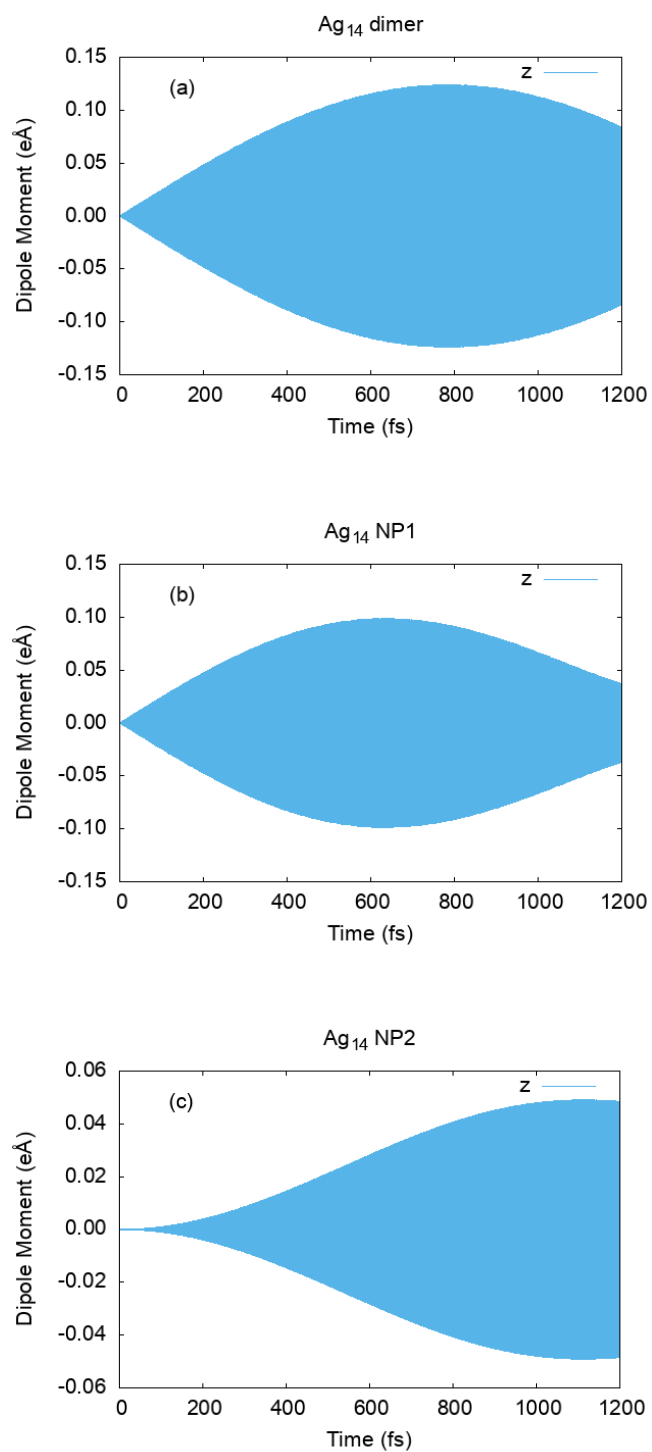


Figure 4.4 (a) Total dipole moment, (b) dipole moment of NP1, and (c) induced dipole moment of NP2 for a nanoparticle dimer with a 40 Å interparticle separation.

For the nanoparticle with an interparticle separation of 30 Å, the linear increase in the dipole moment for NP1 deviates after 200 fs. Around 1000 fs, the total dipole moment reaches its maximum. At a 30 Å separation, NP1 and NP2 have a nearly equal contribution to the total dipole moment after 600 fs. Comparing Figure 4.5(c) with Figure 4.3(c) and Figure 4.4(c), the induced dipole moment in NP2 for an interparticle distance of 30 Å is larger than the induced dipole moments for 50 and 40 Å. As shown in Figure 4.3(c), the induced dipole moment is around one-seventh of the total dipole moment in the dimer as shown in Figure 4.3(a). From Figure 4.4(c) and Figure 4.4(a), the contribution from NP2 is around one-third of the total. However, at a 30 Å separation, NP1 and NP2 have a similar contribution. An interesting phenomenon observed here is the plasmon excitation of NP1. The plateau observed comes from the electronic system reaching a quasi-stationary state after 400 fs of constant illumination due to the finite lifetime of the plasmonic excitation. This means basically that the whole electronic structure on the surface is being excited from the electric field and the NP2 since the second NP can generate an electric field that induces an excitation to the NP1. The EET to NP2 is more efficient at 30 Å than it is for 50 and 40 Å separations. At a smaller separation of 25 Å, the total dipole moment for the dimer (Figure 4.6(a)) is larger than the total dipole moment at longer distances of 50, 40, and 30 Å (Figures 4.3(a), 4.4(a), and 4.5(a), respectively), which indicates that energy transfer from the electric field to the dimer system is more efficient at an interparticle distance of 25 Å than at longer distances. In the range of interparticle separations from 25-50 Å, closer nanoparticles lead to more efficient EET.

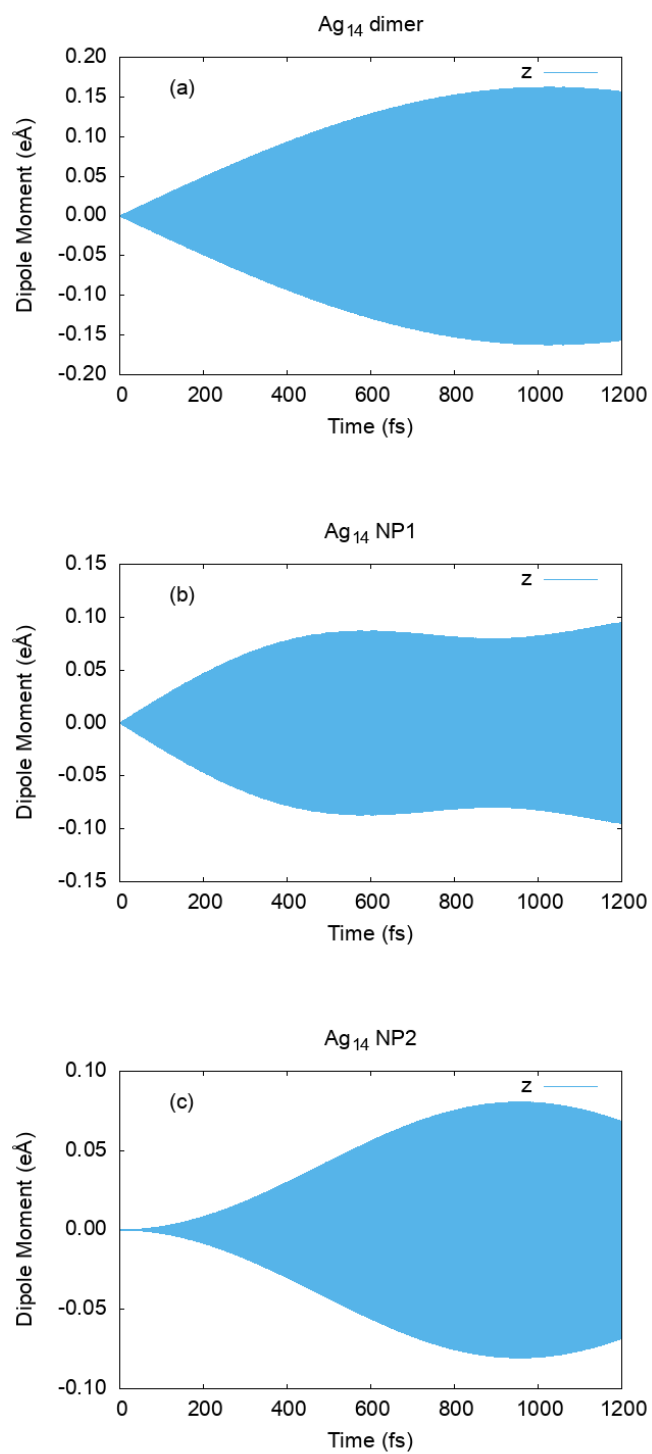


Figure 4.5 (a) Total dipole moment, (b) dipole moment of NP1, and (c) induced dipole moment of NP2 for a nanoparticle dimer with a 30 Å interparticle separation.

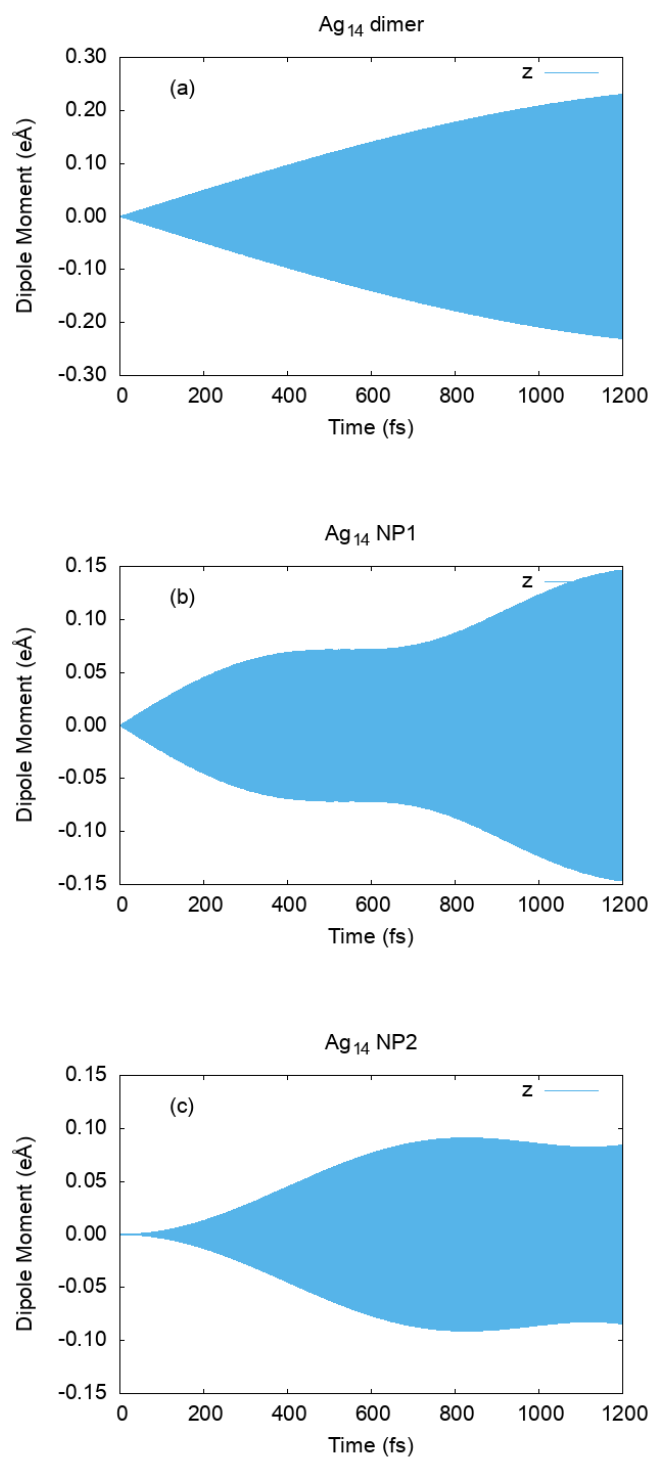


Figure 4.6 (a) Total dipole moment, (b) dipole moment of NP1, and (c) induced dipole moment of NP2 for a nanoparticle dimer with a 25 Å interparticle separation.

At a 20 Å interparticle distance, “wiggles” in the NP1 and NP2 dipole moments can be observed (Figure 4.7). However, the offset in phase between the two nanoparticles results in a linear increase in the total dipole moment. The linear behavior is also the result from electric field generated from NP2 to NP1 and current induction since the only route for electron transport is the coupling between the NP1 and NP2. The dipole moment intensities for NP1 and NP2 are similar. Because the total dipole moment for the dimer is the largest out of all the different interparticle distances examined in this project, this dimer system is the most efficient at harvesting energy from the electric field compared to longer distances such as 50 Å, 40 Å, 30 Å, 25 Å and shorter distances, such as 15 Å and below, which we discuss below.

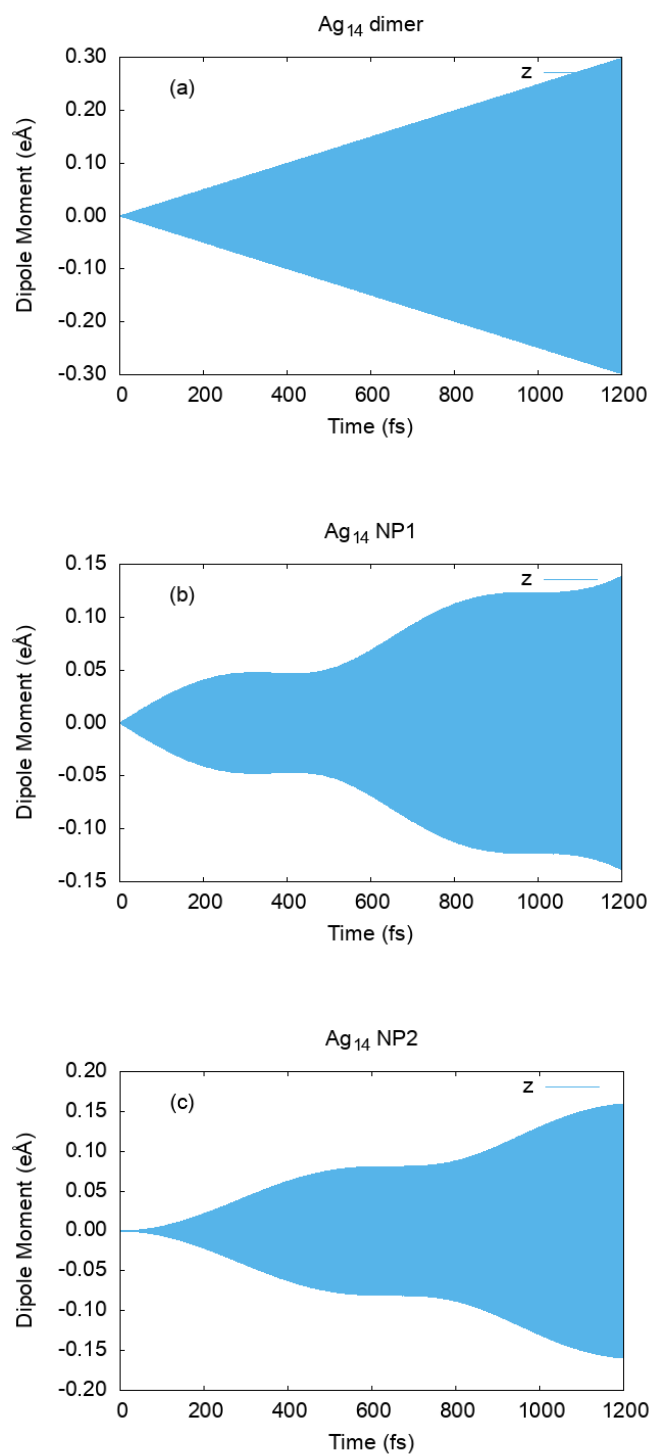


Figure 4.7 (a) Total dipole moment, (b) dipole moment of NP1, and (c) induced dipole moment of NP2 for a nanoparticle dimer with a 20 Å interparticle separation.

At a 15 Å separation distance, the total dipole moment is similar to that of 50 Å (Figure 4.8(a)); however, its origin is different. At a 50 Å interparticle distance, EET transfer is inefficient. The total dipole moment is mostly determined by the dipole moment of NP1. However, at a 15 Å interparticle distance, it is apparent that both NP1 and NP2 contribute substantially to the total dipole moment (Figures 4.8(b) and 4.8(c)). Examining the dipole moment profiles of NP1 and NP2 after 300 fs, the fluctuation in the magnitude of the dipole moment is out of phase for the two nanoparticles: as the dipole moment in NP2 increases, the dipole moment in NP1 decreases, and vice versa. The maximum of the total dipole moment occurs after 700 fs. The dipole moment intensities of both NP1 and NP2 show a decreasing trend after 700 fs. For NP1, the induced dipole moment from the electric field is less at larger interparticle distance, which indicates that back transfer^{21,55} from NP2 to NP1 occurs and has a negative affect for NP1 harvesting energy from the electric field. From Equation (3) and Equation (4), the sinusoidal electric field will induce a dipole fluctuation with a $\cos(\omega_{\text{ext}}t)$ component. The $\cos(\omega_{\text{ext}}t)$ fluctuation of NP1 will induced a dipole fluctuation in NP2 with a component of $\sin(\omega_{\text{ext}}t)$. However, from back transfer from NP2 to NP1, we can expect a $\cos(\omega_{\text{ext}}t)$ component with the opposite sign.

The back-transfer component is proportional to d^{-6} . At short distances, the dipole moment fluctuates dramatically with minor changes in the interparticle distance. The t^3 factor indicates that the back transfer can also have a greater impact for longer time dynamics. Although this analytical model is limited, it succinctly explains the underlying physics in the RT-TDDFTB simulations.

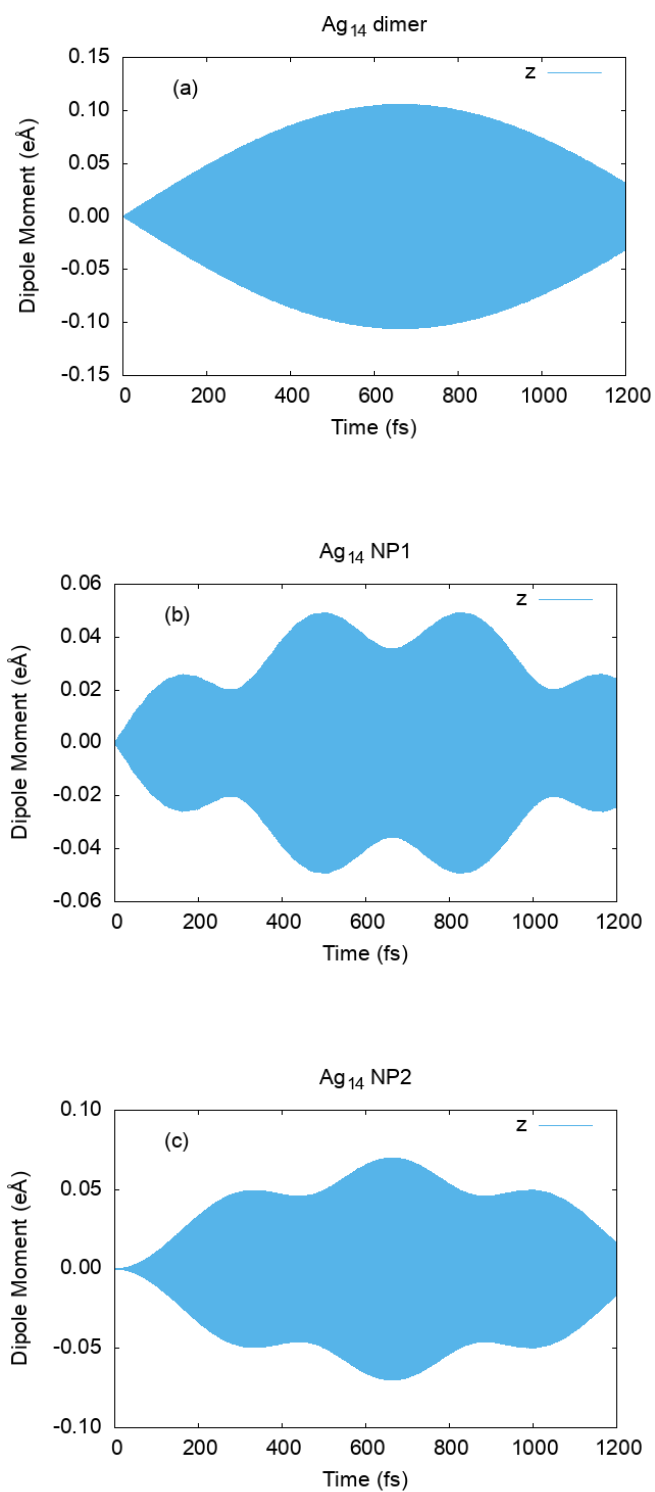


Figure 4.8 (a) Total dipole moment, (b) dipole moment of NP1, and (c) induced dipole moment of NP2 for a nanoparticle dimer with a 15 Å interparticle separation.

For a slightly smaller interparticle distance of 12 Å, one full cycle of the dipole moment fluctuation occurs near 600 fs (Figure 4.9). The total dipole moment and dipole moment of NP1 approaches zero, which indicates the back transfer from NP2 to NP1 is shielding NP1 from the electric field. However, the back transfer occurs earlier. From 0 to 100 fs, NP1 gains energy from the electric field and NP2 accepts energy from NP1. From 100 to 200 fs, the excitation energy transfer from NP1 to NP2 is larger than the energy transfer from the electric field to NP1, which leads to a decrease in the dipole moment from 100 to 200 fs for NP1 as shown in Figure 4.9(b). The back transfer reduces the ability of the dimer and NP1 to accept energy from the electric field. The maximum dipole moment intensity of the dimer is about half compared to its maximum intensity for the 15 Å separation, indicating the ability to harvest energy from the electric field has decreased. The dipole moment intensity of each individual nanoparticle is also halved compared to the respective energy for the 15 Å dimer.

From 10 to 8 Å (Figures 4.10-4.12), the overall dipole moment intensity of the dimer keeps decreasing as the interparticle distance in the dimer decreases. Within this distance range, the ability to harvest energy from the electric field also decreases. At short distances, the dipole moment of NP1 is smaller than NP2 due to back transfer from NP2 to NP1, reducing the energy absorption from the electric field. The oscillations and beating between back transfer and the laser acting on NP1 are even more pronounced as the interparticle distance decreases below 10 Å.

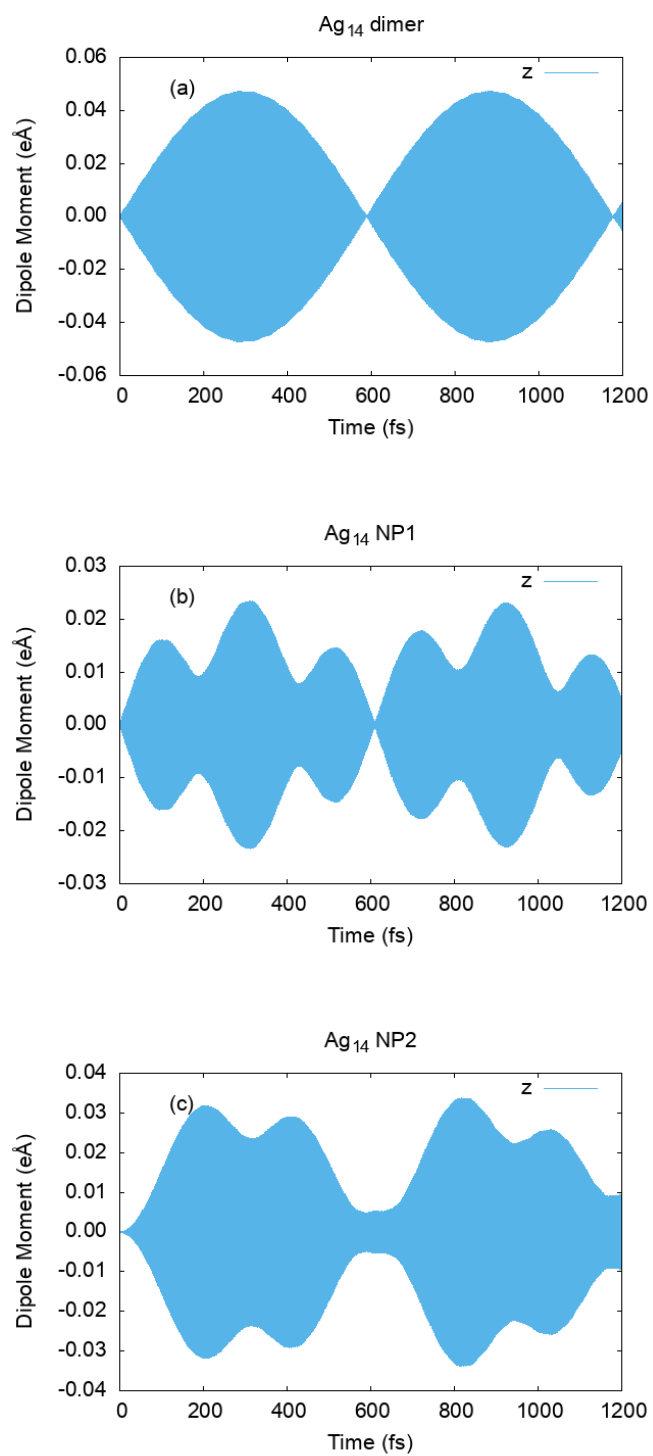


Figure 4.9 (a) Total dipole moment, (b) dipole moment of NP1, and (c) induced dipole moment of NP2 for a nanoparticle dimer with a 12 \AA interparticle separation.

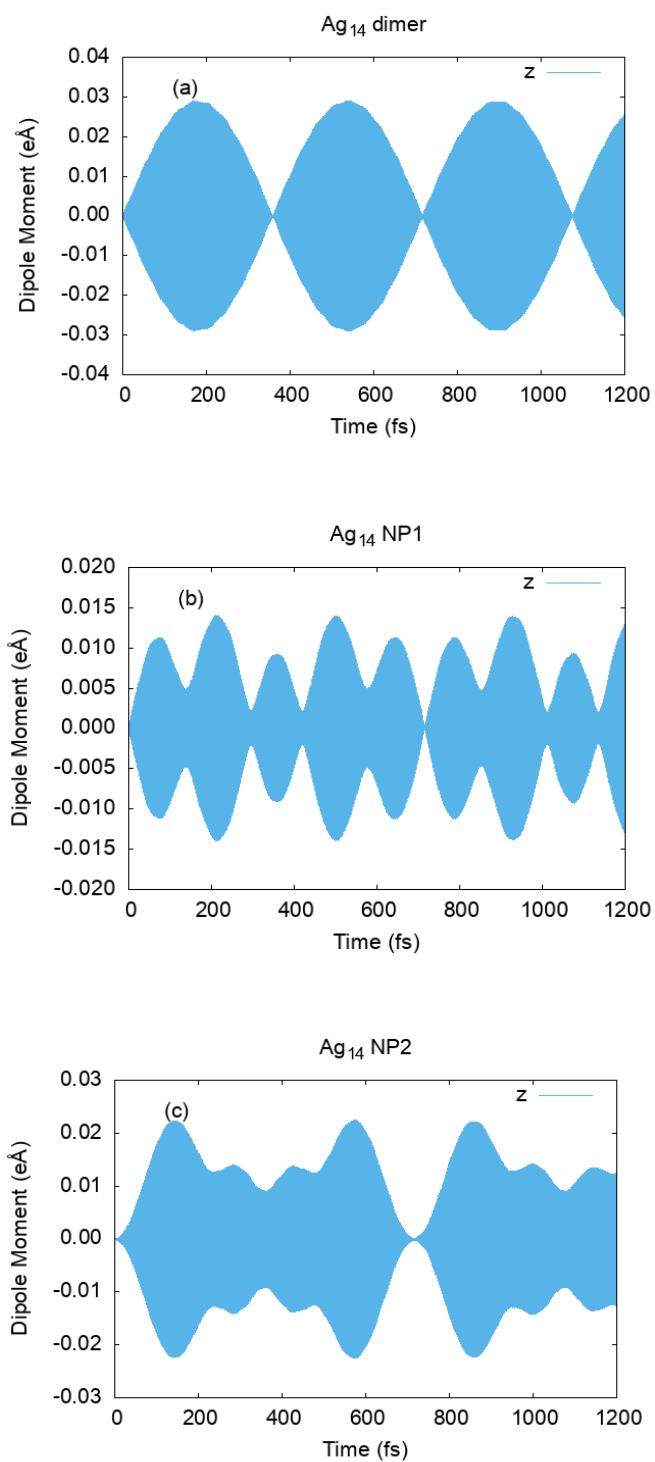


Figure 4.10 (a) Total dipole moment, (b) dipole moment of NP1, and (c) induced dipole moment of NP2 for a nanoparticle dimer with a 10 Å interparticle separation.

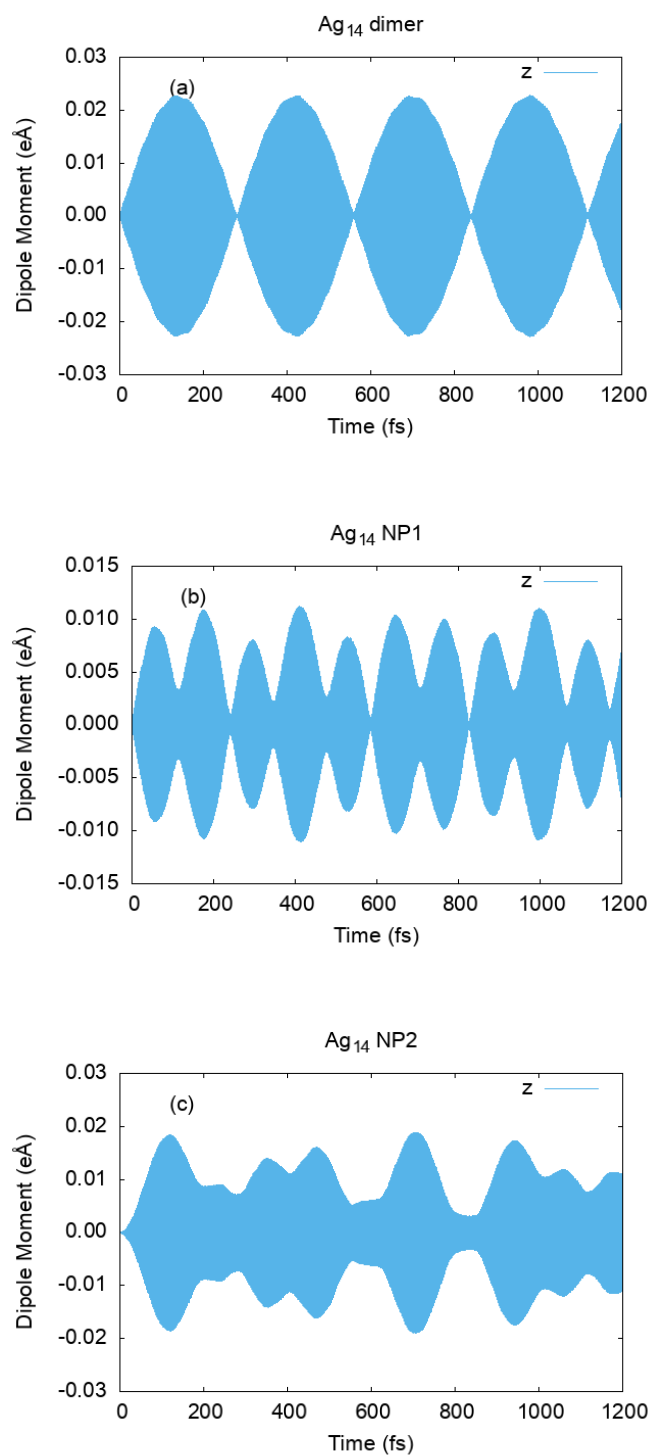


Figure 4.11 (a) Total dipole moment, (b) dipole moment of NP1, and (c) induced dipole moment of NP2 for a nanoparticle dimer with a 9 \AA interparticle separation.

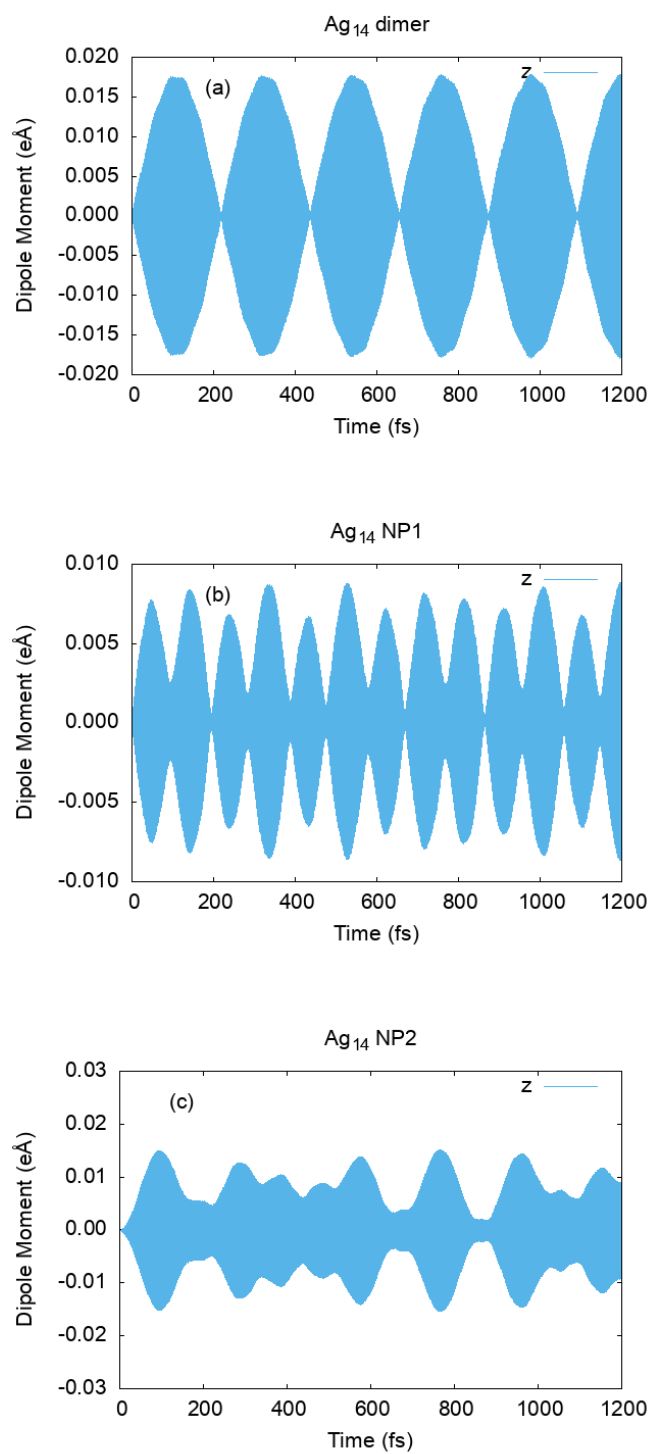


Figure 4.12 (a) Total dipole moment, (b) dipole moment of NP1, and (c) induced dipole moment of NP2 for a nanoparticle dimer with an 8 Å interparticle separation.

Based on these observations, we find that the dipole moment of the overall system has a sinusoidal envelope as a function of time, and the period of the overall oscillation envelope varies with interparticle distance. An exception occurs at 20 Å, which appears to exhibit a linear behavior for the total dipole moment. Based on the magnitude of the induced dipole moment for NP2, more energy can be transferred from NP1 to NP2 as the interparticle distance decreases towards 20 Å; in contrast, for distances below 20 Å, less energy transfers to NP2 since the induced dipole moment is smaller for distances smaller than 20 Å.

At 15 Å and below, numerous oscillations can be found in the individual dipole moments of NP1 and NP2. We observe that the period of oscillation arises due to “beating” between the back transfer from NP2 to NP1 and the laser energy acting on NP1. When the difference is small, the beating period is longer. For the 20 Å interparticle distance, the difference is approximately zero; as a result, the period of beating is approximately infinite, which can be seen as a linear increase in the total dipole moment.

4.5 Conclusions

In summary, using RT-TDDFTB, we simulated interactions of the Ag₁₄ nanoparticle dimer with an incident sinusoidal electric field and examined the interaction between the individual nanoparticles and trends in the electronic excitation transfer with different distances. Due to the computational efficiency of RT-TDDFTB, we are able to simulate electronic dynamics at the picosecond time scale. Because of the real-time simulation formalism, the non-linear effect can be observed in the long time dynamics, even in LR regime. By analyzing the dipole moments of the dimer, as well as NP1 and NP2 individually, we found that all dipole moments exhibit a unique dependence on the interparticle distance. At long interparticle distances, EET from NP1 to NP2 is not efficient. As this distance decreases, the dipole moment in NP2 changes significantly. The

dipole moment of a dimer with a large interparticle distance arises mainly from NP1. At a 20 Å interparticle distance, the dipole moment of the dimer increases linearly due to the offset in phase between NP1 and NP2. The efficiency of the Ag₁₄ dimer for gaining energy from the incident electric field is optimal at this distance. For shorter interparticle distances, back transfer can be observed, which has a strong dependence on distance and time. The back transfer from the RT-TDDFTB simulations shows a reduction in the ability of the dimer and NP1 to accept energy from the incident electric field when the interparticle distance is small. The dipole moment fluctuations in the Ag₁₄ nanoparticle dimer (and both monomers) are affected by the laser acting on NP1, the energy transfer from NP1 to NP2, and the back transfer from NP2 to NP1. Our analyses and results provide additional mechanistic insight for controlling energy transfer effects by modulating interparticle distances and propagation times in these plasmonic systems.

4.6 Acknowledgement

RT-TDDFTB analyses by B.M.W. were supported by the U.S. Department of Energy, Office of Science, Basic Energy Sciences, TCMP Program, under Award No. DE-SC0022209. We thank Dr. Fahri Alkan for helpful discussions.

4.7 Reference

- (1) Huang, X.; El-Sayed, I. H.; Qian, W.; El-Sayed, M. A. Cancer Cell Imaging and Photothermal Therapy in the Near-Infrared Region by Using Gold Nanorods. *J. Am. Chem. Soc.* **2006**, *128* (6), 2115–2120. <https://doi.org/10.1021/ja057254a>.
- (2) Cognet, L.; Tardin, C.; Boyer, D.; Choquet, D.; Tamarat, P.; Lounis, B. Single Metallic Nanoparticle Imaging for Protein Detection in Cells. *Proceedings of the National Academy of Sciences* **2003**, *100* (20), 11350–11355. <https://doi.org/10.1073/pnas.1534635100>.
- (3) Skirtach, A. G.; Dejugnat, C.; Braun, D.; Susha, A. S.; Rogach, A. L.; Parak, W. J.; Möhwald, H.; Sukhorukov, G. B. The Role of Metal Nanoparticles in Remote Release of Encapsulated Materials. *Nano Lett.* **2005**, *5* (7), 1371–1377. <https://doi.org/10.1021/nl050693n>.
- (4) Nie, S. Probing Single Molecules and Single Nanoparticles by Surface-Enhanced Raman Scattering. *Science* **1997**, *275* (5303), 1102–1106. <https://doi.org/10.1126/science.275.5303.1102>.
- (5) Yu; Chang, S.-S.; Lee, C.-L.; Wang, C. R. C. Gold Nanorods: Electrochemical Synthesis and Optical Properties. *J. Phys. Chem. B* **1997**, *101* (34), 6661–6664. <https://doi.org/10.1021/jp971656q>.
- (6) Link, S.; El-Sayed, M. A. Spectral Properties and Relaxation Dynamics of Surface Plasmon Electronic Oscillations in Gold and Silver Nanodots and Nanorods. *J. Phys. Chem. B* **1999**, *103* (40), 8410–8426. <https://doi.org/10.1021/jp9917648>.
- (7) Burda, C.; Chen, X.; Narayanan, R.; El-Sayed, M. A. Chemistry and Properties of Nanocrystals of Different Shapes. *Chem. Rev.* **2005**, *105* (4), 1025–1102. <https://doi.org/10.1021/cr030063a>.
- (8) Eustis, S.; El-Sayed, M. A. Why Gold Nanoparticles Are More Precious than Pretty Gold: Noble Metal Surface Plasmon Resonance and Its Enhancement of the Radiative and Nonradiative Properties of Nanocrystals of Different Shapes. *Chem. Soc. Rev.* **2006**, *35* (3), 209–217. <https://doi.org/10.1039/B514191E>.
- (9) Link, S.; Mohamed, M. B.; El-Sayed, M. A. Simulation of the Optical Absorption Spectra of Gold Nanorods as a Function of Their Aspect Ratio and the Effect of the Medium

- Dielectric Constant. *J. Phys. Chem. B* **1999**, *103* (16), 3073–3077.
<https://doi.org/10.1021/jp990183f>.
- (10) Guidez, E. B.; Aikens, C. M. Quantum Mechanical Origin of the Plasmon: From Molecular Systems to Nanoparticles. *Nanoscale* **2014**, *6* (20), 11512–11527.
<https://doi.org/10.1039/C4NR02225D>.
- (11) Nordlander, P.; Oubre, C.; Prodan, E.; Li, K.; Stockman, M. I. Plasmon Hybridization in Nanoparticle Dimers. *Nano Lett.* **2004**, *4*, 899.
- (12) Aćimović, S. S.; Kreuzer, M. P.; González, M. U.; Quidant, R. Plasmon Near-Field Coupling in Metal Dimers as a Step toward Single-Molecule Sensing. *ACS Nano* **2009**, *3*, 1231.
- (13) Alkan, F.; Aikens, C. M. TD-DFT and TD-DFTB Investigation of the Optical Properties and Electronic Structure of Silver Nanorods and Nanorod Dimers. *J. Phys. Chem. C* **2018**, *122* (41), 23639–23650. <https://doi.org/10.1021/acs.jpcc.8b05196>.
- (14) Alkan, F.; Aikens, C. M. Understanding Plasmon Coupling in Nanoparticle Dimers Using Molecular Orbitals and Configuration Interaction. *Phys. Chem. Chem. Phys.* **2019**, *21* (41), 23065–23075. <https://doi.org/10.1039/C9CP03890F>.
- (15) Bae, G. T.; Aikens, C. M. TDDFT and CIS Studies of Optical Properties of Dimers of Silver Tetrahedra. *J. Phys. Chem. A* **2012**, *116*, 8260.
- (16) Marinica, D. C.; Kazansky, A. K.; Nordlander, P.; Aizpurua, J.; Borisov, A. G. Quantum Plasmonics: Nonlinear Effects in the Field Enhancement of a Plasmonic Nanoparticle Dimer. *Nano Lett.* **2012**, *12*, 1333.
- (17) Prodan, E.; Radloff, C.; Halas, N. J.; Nordlander, P. A Hybridization Model for the Plasmon Response of Complex Nanostructures. *Science* **2003**, *302*, 419.
- (18) Willingham, B.; Brandl, D. W.; Nordlander, P. Plasmon Hybridization in Nanorod Dimers. *Appl. Phys. B* **2008**, *93*, 209.
- (19) Maier, S. A.; Kik, P. G.; Atwater, H. A.; Meltzer, S.; Harel, E.; Koel, B. E.; Requicha, A. A. G. Local Detection of Electromagnetic Energy Transport below the Diffraction Limit in Metal Nanoparticle Plasmon Waveguides. *Nature Mater* **2003**, *2* (4), 229–232.
<https://doi.org/10.1038/nmat852>.
- (20) Yun, C. S.; Javier, A.; Jennings, T.; Fisher, M.; Hira, S.; Peterson, S.; Hopkins, B.; Reich, N. O.; Strouse, G. F. Nanometal Surface Energy Transfer in Optical Rulers, Breaking the

- FRET Barrier. *J. Am. Chem. Soc.* **2005**, *127* (9), 3115–3119.
<https://doi.org/10.1021/ja043940i>.
- (21) Ilawe, N. V.; Oviedo, M. B.; Wong, B. M. Real-Time Quantum Dynamics of Long-Range Electronic Excitation Transfer in Plasmonic Nanoantennas. *J. Chem. Theory Comput.* **2017**, *13*, 3442.
- (22) Ilawe, N. V.; Oviedo, M. B.; Wong, B. M. Effect of Quantum Tunneling on the Efficiency of Excitation Energy Transfer in Plasmonic Nanoparticle Chain Waveguides. *J. Mater. Chem. C* **2018**, *6* (22), 5857–5864. <https://doi.org/10.1039/C8TC01466C>.
- (23) Oviedo, M. B.; Wong, B. M. Real-Time Quantum Dynamics Reveals Complex, Many-Body Interactions in Solvated Nanodroplets. *J. Chem. Theory Comput.* **2016**, *12* (4), 1862–1871. <https://doi.org/10.1021/acs.jctc.5b01019>.
- (24) Aikens, C. M.; Li, S. Z.; Schatz, G. C. From Discrete Electronic States to Plasmons: TDDFT Optical Absorption Properties of Ag_n (n = 10, 20, 35, 56, 84, 120) Tetrahedral Clusters. *J. Phys. Chem. C* **2008**, *112*, 11272.
- (25) Johnson, H. E.; Aikens, C. A. Electronic Structure and TDDFT Optical Absorption Spectra of Silver Nanorods. *J. Phys. Chem. A* **2009**, *113*, 4445.
- (26) Guidez, E. B.; Aikens, C. M. Diameter Dependence of the Excitation Spectra of Silver and Gold Nanorods. *J. Phys. Chem. C* **2013**, *117*, 12325.
- (27) Stener, M.; Nardelli, A.; De Francesco, R.; Fronzoni, G. Optical Excitations of Gold Nanoparticles: A Quantum Chemical Scalar Relativistic Time Dependent Density Functional Study. *J. Phys. Chem. C* **2007**, *111*, 11862.
- (28) Durante, N.; Fortunelli, A.; Broyer, M.; Stener, M. Optical Properties of Au Nanoclusters from TD-DFT Calculations. *J. Phys. Chem. C* **2011**, *115*, 6277.
- (29) Barcaro, G.; Sernenta, L.; Fortunelli, A.; Stener, M. Optical Properties of Silver Nanoshells from Time-Dependent Density Functional Theory Calculations. *J. Phys. Chem. C* **2014**, *118*, 12450.
- (30) Weissker, H. C.; Mottet, C. Optical Properties of Pure and Core-Shell Noble-Metal Nanoclusters from TDDFT: The Influence of the Atomic Structure. *Phys. Rev. B* **2011**, *84*, 165443.

- (31) López-Lozano, X.; Barron, H.; Mottet, C.; Weissker, H.-C. Aspect-Ratio- and Size-Dependent Emergence of the Surface-Plasmon Resonance in Gold Nanorods – an Ab Initio TDDFT Study. *Phys. Chem. Chem. Phys.* **2014**, *16*, 1820.
- (32) Liao, M. S.; Bonifassi, P.; Leszczynski, J.; Ray, P. C.; Huang, M. J.; Watts, J. D. Structure, Bonding, and Linear Optical Properties of a Series of Silver and Gold Nanorod Clusters: DFT/TDDFT Studies. *J. Phys. Chem. A* **2010**, *114*, 12701.
- (33) Iida, K.; Noda, M.; Ishimura, K.; Nobusada, K. First-Principles Computational Visualization of Localized Surface Plasmon Resonance in Gold Nanoclusters. *J. Phys. Chem. A* **2014**, *118*, 11317.
- (34) Asadi-Aghbolaghi, N.; Rüger, R.; Jamshidi, Z.; Visscher, L. TD-DFT+TB: An Efficient and Fast Approach for Quantum Plasmonic Excitations. *J. Phys. Chem. C* **2020**, *124* (14), 7946–7955. <https://doi.org/10.1021/acs.jpcc.0c00979>.
- (35) D’Agostino, S.; Rinaldi, R.; Cuniberti, G.; Della Sala, F. Density Functional Tight Binding for Quantum Plasmonics. *J. Phys. Chem. C* **2018**, *122* (34), 19756–19766. <https://doi.org/10.1021/acs.jpcc.8b05278>.
- (36) Douglas-Gallardo, O. A.; Berdakin, M.; Frauenheim, T.; Sánchez, C. G. Plasmon-Induced Hot-Carrier Generation Differences in Gold and Silver Nanoclusters. *Nanoscale* **2019**, *11* (17), 8604–8615. <https://doi.org/10.1039/C9NR01352K>.
- (37) Porezag, D.; Frauenheim, T.; Kohler, T.; Seifert, G.; Kaschner, R. Construction of Tight-Binding-Like Potentials on the Basis of Density-Functional Theory – Application to Carbon. *Phys. Rev. B* **1995**, *51*, 12947.
- (38) Seifert, G.; Porezag, D.; Frauenheim, T. Calculations of Molecules, Clusters, and Solids with a Simplified LCAO-DFT-LDA Scheme. *Int. J. Quantum Chem.* **1996**, *58*, 185.
- (39) Douglas-Gallardo, O. A.; Berdakin, M.; Sanchez, C. G. Atomistic Insights into Chemical Interface Damping of Surface Plasmon Excitations in Silver Nanoclusters. *J. Phys. Chem. C* **2016**, *120*, 24389.
- (40) Bonafé, F. P.; Aradi, B.; Guan, M. X.; Douglas-Gallardo, O. A.; Lian, C.; Meng, S.; Frauenheim, T.; Sánchez, C. G. Plasmon-Driven Sub-Picosecond Breathing of Metal Nanoparticles. *Nanoscale* **2017**, *9*, 12391.

- (41) Douglas-Gallardo, O. A.; Soldano, G. J.; Mariscal, M. M.; Sanchez, C. G. Effects of Oxidation on the Plasmonic Properties of Aluminum Nanoclusters. *Nanoscale* **2017**, *9*, 17471.
- (42) Liu, Z.; Alkan, F.; Aikens, C. M. TD-DFTB Study of Optical Properties of Silver Nanoparticle Homodimers and Heterodimers. *J. Chem. Phys.* **2020**, *153* (14), 144711. <https://doi.org/10.1063/5.0025672>.
- (43) Aradi, B.; Hourahine, B.; Frauenheim, Th. DFTB+, a Sparse Matrix-Based Implementation of the DFTB Method. *J. Phys. Chem. A* **2007**, *111* (26), 5678–5684. <https://doi.org/10.1021/jp070186p>.
- (44) Negre, C. F. A.; Fuertes, V. C.; Oviedo, M. B.; Oliva, F. Y.; Sánchez, C. G. Quantum Dynamics of Light-Induced Charge Injection in a Model Dye–Nanoparticle Complex. *J. Phys. Chem. C* **2012**, *116* (28), 14748–14753. <https://doi.org/10.1021/jp210248k>.
- (45) Oviedo, M. B.; Zarate, X.; Negre, C. F. A.; Schott, E.; Arratia-Pérez, R.; Sánchez, C. G. Quantum Dynamical Simulations as a Tool for Predicting Photoinjection Mechanisms in Dye-Sensitized TiO₂ Solar Cells. *J. Phys. Chem. Lett.* **2012**, *3* (18), 2548–2555. <https://doi.org/10.1021/jz300880d>.
- (46) Negre, C. F. A.; Young, K. J.; Oviedo, Ma. B.; Allen, L. J.; Sánchez, C. G.; Jarzemska, K. N.; Benedict, J. B.; Crabtree, R. H.; Coppens, P.; Brudvig, G. W.; Batista, V. S. Photoelectrochemical Hole Injection Revealed in Polyoxotitanate Nanocrystals Functionalized with Organic Adsorbates. *J. Am. Chem. Soc.* **2014**, *136* (46), 16420–16429. <https://doi.org/10.1021/ja509270f>.
- (47) Oviedo, M. B.; Negre, C. F. A.; Sánchez, C. G. Dynamical Simulation of the Optical Response of Photosynthetic Pigments. *Phys. Chem. Chem. Phys.* **2010**, *12* (25), 6706. <https://doi.org/10.1039/b926051j>.
- (48) Oviedo, M. B.; Sánchez, C. G. Transition Dipole Moments of the Q_y Band in Photosynthetic Pigments. *J. Phys. Chem. A* **2011**, *115* (44), 12280–12285. <https://doi.org/10.1021/jp203826q>.
- (49) Medrano, C. R.; Oviedo, M. B.; Sánchez, C. G. Photoinduced Charge-Transfer Dynamics Simulations in Noncovalently Bonded Molecular Aggregates. *Phys. Chem. Chem. Phys.* **2016**, *18* (22), 14840–14849. <https://doi.org/10.1039/C6CP00231E>.

- (50) Ilawe, N. V.; Oviedo, M. B.; Wong, B. M. Correction to Real-Time Quantum Dynamics of Long-Range Electronic Excitation Transfer in Plasmonic Nanoantennas. *J. Chem. Theory Comput.* **2017**, *13* (12), 6433–6433. <https://doi.org/10.1021/acs.jctc.7b01150>.
- (51) Berdakin, M.; Douglas-Gallardo, O. A.; Sánchez, C. G. Interplay between Intra- and Interband Transitions Associated with the Plasmon-Induced Hot Carrier Generation Process in Silver and Gold Nanoclusters. *J. Phys. Chem. C* **2020**, *124* (2), 1631–1639. <https://doi.org/10.1021/acs.jpcc.9b10871>.
- (52) Hourahine, B.; Aradi, B.; Blum, V.; Bonafé, F.; Buccheri, A.; Camacho, C.; Cevallos, C.; Deshayé, M. Y.; Dumitrică, T.; Dominguez, A.; Ehlert, S.; Elstner, M.; van der Heide, T.; Hermann, J.; Irle, S.; Kranz, J. J.; Köhler, C.; Kowalczyk, T.; Kubař, T.; Lee, I. S.; Lutsker, V.; Maurer, R. J.; Min, S. K.; Mitchell, I.; Negre, C.; Niehaus, T. A.; Niklasson, A. M. N.; Page, A. J.; Pecchia, A.; Penazzi, G.; Persson, M. P.; Řezáč, J.; Sánchez, C. G.; Sternberg, M.; Stöhr, M.; Stuckenberg, F.; Tkatchenko, A.; Yu, V. W. -z.; Frauenheim, T. DFTB+, a Software Package for Efficient Approximate Density Functional Theory Based Atomistic Simulations. *J. Chem. Phys.* **2020**, *152* (12), 124101. <https://doi.org/10.1063/1.5143190>.
- (53) Szűcs, B.; Hajnal, Z.; Frauenheim, T.; Gonzalez, C.; Ortega, J.; Perez, R.; Flores, F. Chalcogen Passivation of GaAs(100) Surfaces: Theoretical Study. *Appl. Surf. Sci.* **2003**, *212–213*, 861.
- (54) Szűcs, B.; Hajnal, Z.; Scholz, R.; Sanna, S.; Frauenheim, T. Theoretical Study of the Adsorption of a PTCDA Monolayer on S-Passivated GaAs(100). *Appl. Surf. Sci.* **2004**, *234*, 173.
- (55) Oviedo, M. B.; Sánchez, C. G. Full Quantum Dynamics of the Electronic Coupling between Photosynthetic Pigments. *arXiv:1502.00491 [cond-mat, physics:physics]* **2015**.
- (56) Mukamel, S. Principles of Nonlinear Optical Spectroscopy; 1995.

Chapter 5 - Electronic Excited State Dynamics of Naphthalene

Studied by Simulated Transient Absorption Spectroscopy

Zhen Liu, Jannis Krumland, Caterina Cocchi, Christine M. Aikens

5.1 Abstract

Naphthalene, a polycyclic aromatic hydrocarbon and the smallest oligoacene, exhibits collective electronic effects. In this work, we simulate the first principles transient absorption spectra of naphthalene in order to investigate how collectivity affects its electronic excited state dynamics. In this study, the steady state absorption spectrum of naphthalene is calculated both by real-time time-dependent density functional theory and by linear-response time-dependent density functional theory (LR-TDDFT). The LR-TDDFT data is used to resolve the specific transitions in the dynamics process. In the transient absorption simulation, a Gaussian pump is used to excite the plasmonic β peak. An instantaneous, broadband probe pulse is applied to monitor the electronic dynamics. A beating pattern in the excited state absorption after excitation of the plasmonic β peak is found on the sub 100 fs time scale. On the contrary, excited state absorption after an excitation dominated by a single particle transition exhibits constant intensity.

5.2 Introduction

Due to its strong light confinement and tunability, graphene is regarded as an ideal platform for optoelectronics research.^{1,2} Graphene³ has been the first and the most studied two-dimensional material for fundamental photonics research, and it is of interest in a variety of applications including photodetectors,⁴ optical modulators⁵ and photovoltaic devices.¹ Understanding its

interaction with light is vital for further exploring these applications. The plasmon resonance therein arises from a collective electron oscillation after interaction with light with a specific frequency.^{6–8} The strong plasmon confinement is an important feature of graphene beside the high electron mobility and high mechanical strengths.^{5,9,10} Previous research demonstrated that graphene has two orders magnitude higher of light confinement than traditional plasmonic metals.¹¹ The strong light confinement makes graphene a great material for a high-sensitivity plasmonic biosensor.¹¹

Polycyclic aromatic hydrocarbons (PAHs) made of fused benzene rings are regarded as a building block of graphene.¹² Because of the constructive interaction between two or more single particle transitions in acenes and other PAHs,^{13,14} these carbon-based systems possess strong excitations known as molecular plasmons.^{15–18} Naphthalene, the simplest molecule with plasmon-like character, is an ideal structure for understanding the origin of plasmon resonances. The strong β peak in the absorption spectrum of naphthalene has been revealed to arise from constructive interaction of two single particle transitions.¹⁵ To better understand its plasmonic dynamics on the sub 100 fs time scale, ab-initio transient absorption spectroscopy (TAS) simulations are performed in this work. By utilizing the advantages of state-specific results from linear-response time-dependent density functional theory (LR-TDDFT) and the electronic dynamics from real-time time-dependent density functional theory (RT-TDDFT), the excited state absorption in naphthalene is analyzed in the energy and time domains. Beating on the sub 100 fs time scale is discovered in the excited absorption signal from the plasmonic peak. The beating observed in naphthalene may pave the way for understanding similar beating in other systems that experience more complex collective electronic effects. We observe that the beating shows some functional dependent features, which demands more accurate methods of calculation.

5.3 Result and Discussion

The ground state absorption spectra of naphthalene calculated by LR-TDDFT and by RT-TDDFT with a δ -kick excitation (see Computational Methods below) are shown in Figure 5.1. The main spectral features of naphthalene can be observed. The most obvious plasmonic β peak located at 5.74 eV and polarized in the x direction is due to the constructive interaction of two molecular orbital transitions (also called single particle transitions), HOMO-1 to LUMO and HOMO to LUMO+1. Three p band peaks polarized in the y direction can be found at 4.10 eV (arising primarily from the HOMO to LUMO transition), 5.94 eV (from HOMO-1 to LUMO+1) and 7.45 eV (from HOMO-2 to LUMO+2). Other excited states calculated by LR-TDDFT are shown in Table B.1.

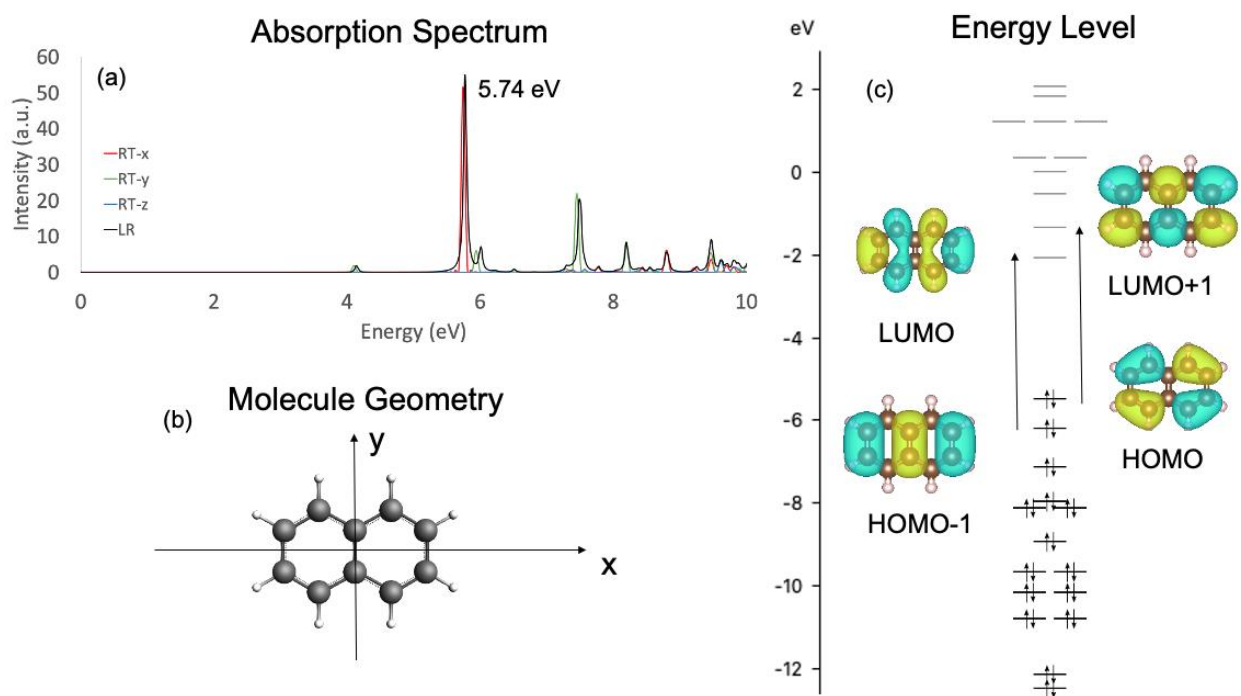


Figure 5.1 (a) Ground state absorption spectrum of naphthalene calculated from LR-TDDFT and RT-TDDFT showing the plasmonic β peak at 5.74 eV with polarization in the x direction. (b) Orientation of naphthalene. (c) Electronic energy levels and the primary orbital transitions involved in the plasmonic β peak, as determined by LR-TDDFT. Note that all apparent degeneracies are accidental degeneracies; naphthalene belongs to the D_{2h} point group which has irreducible representations with dimension 1.

Next, transient absorption simulations are performed using RT-TDDFT. The initial pump pulse chosen is a Gaussian envelope with a frequency centered at 5.74 eV and polarized in the x direction to excite the plasmon peak. The probe is a delta kick, which can theoretically make all possible absorptions happen. For the transient absorption simulations, the $t = 0$ fs spectrum is used as a reference, which is the ground state absorption spectrum. After a given time delay, the probe pulse produces a different spectrum. The differential absorption spectrum is obtained by subtracting the reference absorption spectrum. The calculation is repeated multiple times, cycling the phase of the pump pulse in steps of $\pi/2$, and finally averaging them.¹⁹ The energy transfer from the electric field to the system is shown as Figure B5.1.

From analysis of the LR-TDDFT ground state absorption spectrum, we know that the first excitation peak is located at 4.10 eV, which corresponds to the HOMO to LUMO transition. Any signal in the transient absorption spectrum below 4.10 eV must arise from excited state absorption and can be easily distinguished from other peaks arising from differences in ground state population (such as the ground state bleach).

After the excitation of the plasmon peak (excited state S₅, see Table B.1), electronic population is initially present in this state, which can be expressed approximately by a sum of two dominant singly excited determinants as^{15,20}

$$S \approx \frac{1}{\sqrt{2}} |\dots \Phi_{H-1}^2 \Phi_H^1 \Phi_L^0 \Phi_{L+1}^1 \dots \rangle + \frac{1}{\sqrt{2}} |\dots \Phi_{H-1}^1 \Phi_H^2 \Phi_L^1 \Phi_{L+1}^0 \dots \rangle$$

This state has B_{3u} symmetry and arises primarily from the HOMO (a_u) \rightarrow LUMO+1 (b_{3g}) and HOMO-1 (b_{1u}) \rightarrow LUMO (b_{2g}) transitions. Then, excited state absorption signals in the transient absorption spectrum can arise when electronic population in the LUMO and LUMO+1 orbitals are excited to higher energy orbitals. (We find that an orbital picture is sufficient to

obtain insights into the transient absorption process, although the full multideterminantal state could also be considered. Note: The term LUMO will continue to be used throughout this text to refer to the orbitals that were initially unoccupied in the ground state, although they gain some population during the excitation process.) We initially consider states that can be accessed by an x-polarized probe. In order to detect an allowed transition in the x direction by the probe, the direct product between the initially excited orbital and the orbital accessed after the probe should be B_{3u} . From the D_{2h} point group representation, $b_{2g} \times b_{1u} = B_{3u}$ and $b_{3g} \times a_u = B_{3u}$. (Note: We use the standard notation in which orbital symmetries are represented by lowercase letters and states are represented by capital letters.) Because the pump created the S_5 excited state with occupation in the newly occupied LUMO with b_{2g} symmetry and in LUMO+1 with b_{3g} symmetry, the x-polarized probe will detect transitions into orbitals with b_{1u} and a_u symmetry. Thus, electronic population in the LUMO (b_{2g}) could be excited into orbitals with b_{1u} symmetry, which include LUMO+2 and LUMO+10 (Table B.2). Electronic population from the LUMO+1 (b_{3g}) could be excited into an orbital with a_u symmetry, i.e., LUMO+9.

As shown in Figure 5.2, the lowest excited state absorption in the TAS simulation is found at 1.50 eV, which we assign to the LUMO to LUMO+2 transition, which has a difference in orbital energy values ($\Delta\varepsilon$) of 1.53 eV (Table B.3). The difference in orbital energy values only provides an approximation because this approach does not account for orbital relaxation effects, excited determinant coupling, etc. in excited states, but the similarity of the values provides a reasonable check on the excited state absorption assignments. The second electronic excited state absorption located at 2.13 eV is assigned to the LUMO+1 to LUMO+9 transition ($\Delta\varepsilon = 2.55$ eV). The third electronic excited state can be found at 3.24 eV, which is assigned to the LUMO to LUMO+10 transition ($\Delta\varepsilon = 3.43$ eV). Since the hole is created in HOMO and HOMO-1, the

excited state hole transition from HOMO and HOMO-1 to other HOMOs can be detected by the probe pulse. As shown in Figure 5.2, the small bright signal indicated around 1.7 eV is assigned to the HOMO to HOMO-2 hole transition, which has a difference in orbital energy values of $\Delta\epsilon = 1.71$ eV (Table B.4). Another bright state hole transition arises from HOMO-1 to HOMO-5, which has $\Delta\epsilon = 1.99$ eV. Both excited state hole transitions are close to excited state electron transitions in energy and may mix with them.

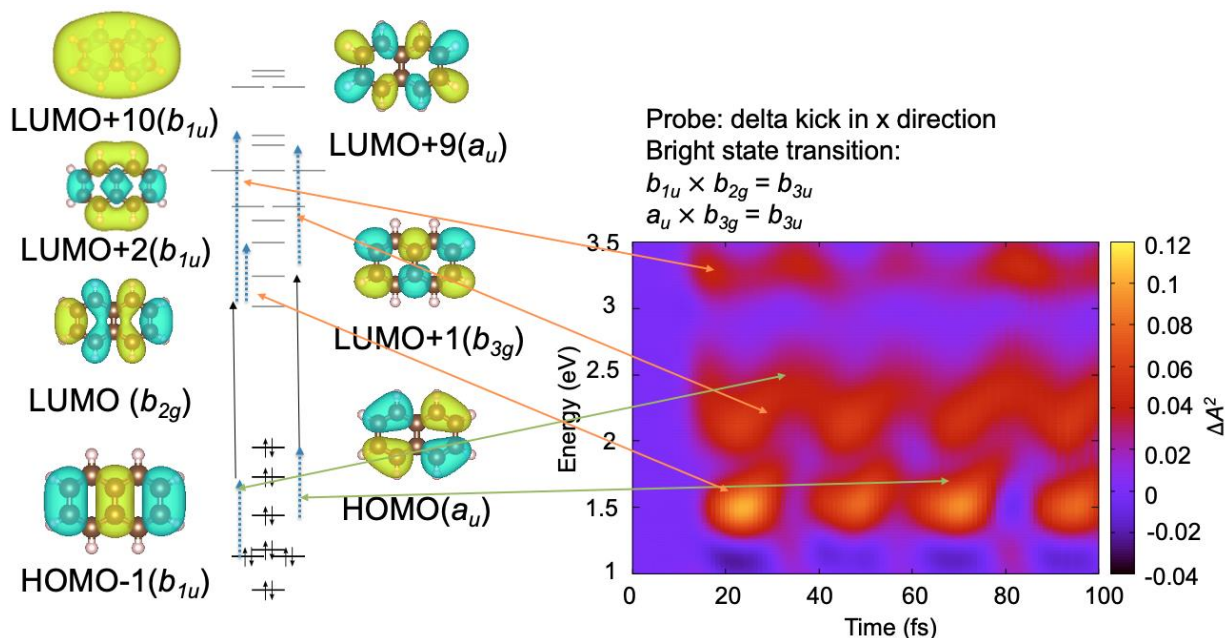


Figure 5.2 Transient absorption spectrum of naphthalene with x-polarized probe after excitation of the plasmonic β peak. Orbital transitions excited with the 5.74 eV pump are shown in black; the orbital transitions determined to be responsible for the indicated excited state absorptions are shown with blue dotted arrows. A transient absorption spectrum covering the range of 0 to 5 eV is shown in Figure B5.2.

Next, we consider states that can be accessed by a y-polarized probe. After the excitation of the plasmonic β peak, the delta kick probe in the y direction can cause all of the transitions from LUMO and LUMO+1 into higher energy orbitals. An allowed transition in the y direction

should have a direct product of B_{2u} symmetry as shown in Figure 5.3. From the D_{2h} point group representations, $b_{2g} \times a_u = B_{2u}$ and $b_{3g} \times b_{1u} = B_{2u}$. Starting from the LUMO with b_{2g} symmetry, the allowed transition will be from the LUMO to LUMO+9 with a_u symmetry, which has a difference in orbital energy values of $\Delta\varepsilon = 3.33$ eV. Starting from LUMO+1 with b_{3g} symmetry, the allowed transitions will be LUMO+1 to LUMO+2 and LUMO+10 with b_{1u} symmetry, which have $\Delta\varepsilon$ values of 0.75 eV and 2.66 eV, respectively (Table B.3). The probe can also detect excited state hole transitions with B_{2u} symmetry from HOMO and HOMO-1 to other HOMOs. The allowed transitions (Table B.4) are HOMO to HOMO-5 with $\Delta\varepsilon = 2.75$ eV and HOMO-1 to HOMO-2 with $\Delta\varepsilon = 0.94$ eV. In both transient absorption simulations discussed so far, a beating pattern in the excited state absorption signals can be observed (Figures 5.2 and 5.3). However, minor fluctuations are observed with other functionals instead of a clear beating feature, which will be examined more in the future.

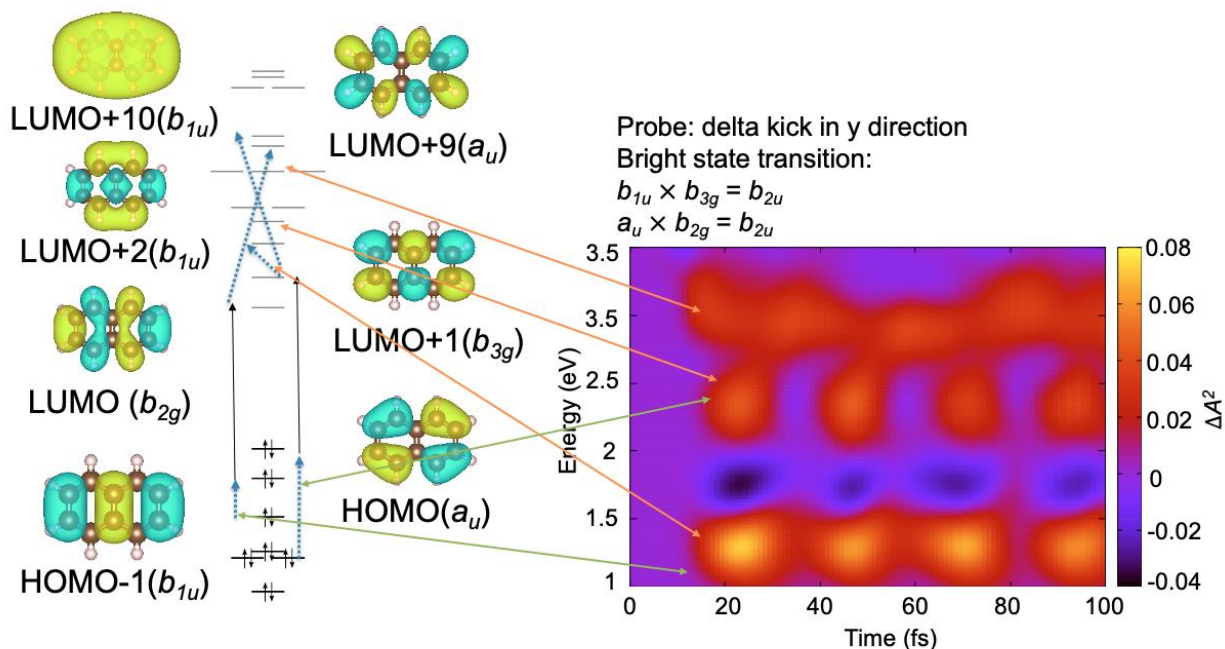


Figure 5.3 Transient absorption spectrum of naphthalene with y-polarized probe after excitation of the plasmonic β peak. Orbital transitions excited with the 5.74 eV pump are shown in black; the orbital transitions determined to be responsible for the indicated excited state absorptions are shown with blue dotted arrows.

Overall, different features of plasmonic transitions and states dominated by a single particle transition can be revealed by the presence or absence of beating in the excited state absorption signal. As discussed above, the beating found in excited state absorption involved in plasmonic β peak; however, pumping a single particle transition such as the HOMO to LUMO transition leads to a constant intensity in the excited state absorption as shown in Figure 5.4.

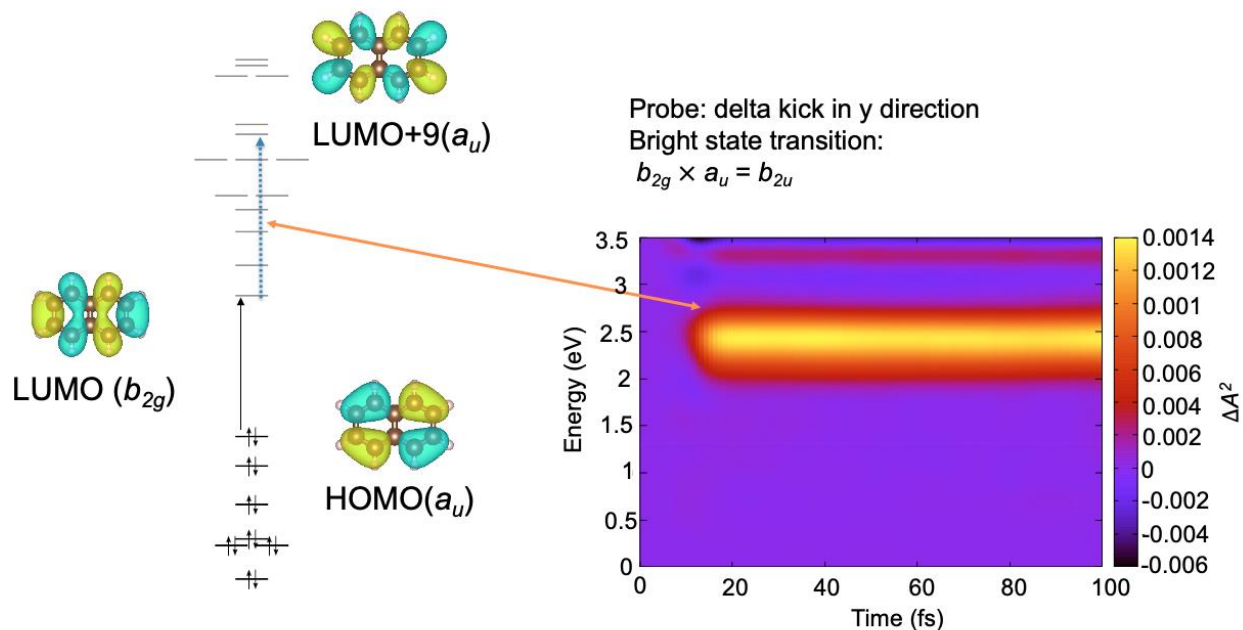


Figure 5.4 Transient absorption spectrum of naphthalene with y-polarized probe after excitation of y-polarized pump at 4.1 eV. The orbitals shown are involved in the excited state absorption polarized in the y direction. Orbital transitions excited with the pump are shown in black; the orbital transitions determined to be responsible for the indicated excited state absorptions are shown with blue dotted arrows.

In a p band excitation using a pump polarized in the y direction with an energy of 4.10 eV, no beating exists (Figure 5.4). This pump excites the HOMO to LUMO transition, which is a single particle transition. The excited state absorption signal at 2.44 eV can be detected by the probe, which is attributed to the mixture of hole transition from HOMO to HOMO-5 ($\Delta\varepsilon = 2.75$ eV, Table B.4) and electron transition from LUMO to LUMO+9 ($\Delta\varepsilon = 3.33$ eV, Table B.3).

To further examine the beating observed in Figures 5.2 and 5.3, we also performed Ehrenfest dynamics on naphthalene and observed similar beating features for both the fixed nuclear coordinate and Ehrenfest dynamics simulations. The fact that the beating is observed in the fixed nuclear simulations indicates that the beating arises because of electronic effects and not because of vibrational effects.

Because the plasmon peak arises from the constructive interference of the different excitations, we expect that this type of beating pattern can be seen in other molecules and nanoparticles with plasmonic character. Because the energy difference responsible for the beating is close to the energy of a phonon mode, it is possible that this will affect electron-phonon coupling in plasmonic systems.

Overall, the transient absorption simulations in this work show that naphthalene exhibits interesting collective effects in its excited state absorption spectra. In particular, beating is observed may be a characteristic of these collective electronic effects, which may have important implications for the plasmonics field. Although transient absorption using these high energy pump pulses may be experimentally challenging, this work suggests that similar beating may be observed with lower energy pumps in other systems that experience related collective electronic effects, such as silver nanowires.

5.4 Computational Methods

All of the calculations were performed using the real-space Octopus code.²¹ The LDA (local-density approximation)^{22,23} with the Perdew-Zunger parameterization and norm-conserving Troullier-Martins pseudopotentials²⁴ were employed. The spacing in the real-space grid was set to 0.2 Å. The radius of the sphere centered on each atom was set to 5 Å. All of the calculations were performed on the optimized geometry of naphthalene. The FIRE algorithm²⁵ was used in the geometry optimization to minimize the force lower than 0.05 eV/Å.

A ground state calculation was performed to obtain ground state orbitals. The LR-TDDFT optical spectra was calculated with the Casida formulation²⁶ with 200 extra states. The orbitals involved in single-particle transitions were visualized by VESTA.²⁷ The well-resolved

transitions in the LR-TDDFT optical spectrum can be used to choose peaks of interest for electronic dynamics simulation by RT-TDDFT.

In the real-time simulation of the absorption spectrum, the approximate enforced time-reversal symmetry²⁸ was used in propagation with a time step of 2 as. After the kick in x, y and z direction, the total propagation time was set to 10 fs in order to fully resolve the absorption peak in the ground state absorption.

In the transient absorption spectroscopy (TAS) simulation,²⁹ the pump pulse has a Gaussian envelope function with a standard deviation of 3 fs. The pump is either polarized in the x direction with a frequency of 5.74 eV, which is the plasmon-like peak for naphthalene, or polarized in the y direction with a frequency of 4.10 eV, corresponding to a p band peak of naphthalene. In the simulation, the time delays went from 0-100 fs with a spacing of 1 fs. After a given time delay, a delta kick probe is used to excite all absorptions. To consider the interference effect between two field, the phase-cycling was adopted by performing the two simulations with a phase difference of $\pi/2$.¹⁹ The transient absorption spectra can then be obtained after Fourier Transform of the dipole fluctuations that arise after each delta kick, after subtracting the spectrum at 0 fs.

5.5 Acknowledgement

This material is based on work supported by the Department of Energy under grant DE-SC0012273. The computing for this project was performed on the Beocat Research Cluster at Kansas State University, which is funded in part by NSF grants CHE-1726332, CNS-1006860, EPS-1006860, and EPS-0919443.

5.6 Reference

- (1) Bonaccorso, F.; Sun, Z.; Hasan, T.; Ferrari, A. C. Graphene Photonics and Optoelectronics. *Nature Photon* 2010, 4 (9), 611–622. <https://doi.org/10.1038/nphoton.2010.186>.
- (2) Grigorenko, A. N.; Polini, M.; Novoselov, K. S. Graphene Plasmonics. *Nature Photon* 2012, 6 (11), 749–758. <https://doi.org/10.1038/nphoton.2012.262>.
- (3) Castro Neto, A. H.; Guinea, F.; Peres, N. M. R.; Novoselov, K. S.; Geim, A. K. The Electronic Properties of Graphene. *Rev. Mod. Phys.* 2009, 81 (1), 109–162. <https://doi.org/10.1103/RevModPhys.81.109>.
- (4) Xia, F.; Mueller, T.; Lin, Y.; Valdes-Garcia, A.; Avouris, P. Ultrafast Graphene Photodetector. *Nature Nanotech* 2009, 4 (12), 839–843. <https://doi.org/10.1038/nnano.2009.292>.
- (5) Liu, M.; Yin, X.; Ulin-Avila, E.; Geng, B.; Zentgraf, T.; Ju, L.; Wang, F.; Zhang, X. A Graphene-Based Broadband Optical Modulator. *Nature* 2011, 474 (7349), 64–67. <https://doi.org/10.1038/nature10067>.
- (6) Schuller, J. A.; Barnard, E. S.; Cai, W.; Jun, Y. C.; White, J. S.; Brongersma, M. L. Plasmonics for Extreme Light Concentration and Manipulation. *Nature Mater* 2010, 9 (3), 193–204. <https://doi.org/10.1038/nmat2630>.
- (7) Ozbay, E. Plasmonics: Merging Photonics and Electronics at Nanoscale Dimensions. *Science* 2006, 311, 189.
- (8) Rivera, N.; Kaminer, I.; Zhen, B.; Joannopoulos, J. D.; Soljačić, M. Shrinking Light to Allow Forbidden Transitions on the Atomic Scale. *Science* 2016, 353 (6296), 263–269. <https://doi.org/10.1126/science.aaf6308>.
- (9) Ju, L.; Geng, B.; Horng, J.; Girit, C.; Martin, M.; Hao, Z.; Bechtel, H. A.; Liang, X.; Zettl, A.; Shen, Y. R.; Wang, F. Graphene Plasmonics for Tunable Terahertz Metamaterials. *Nature Nanotech* 2011, 6 (10), 630–634. <https://doi.org/10.1038/nnano.2011.146>.
- (10) Low, T.; Avouris, P. Graphene Plasmonics for Terahertz to Mid-Infrared Applications. *ACS Nano* 2014, 8 (2), 1086–1101. <https://doi.org/10.1021/nn406627u>.
- (11) Rodrigo, D.; Limaj, O.; Janner, D.; Etezadi, D.; García de Abajo, F. J.; Pruneri, V.; Altug, H. Mid-Infrared Plasmonic Biosensing with Graphene. *Science* 2015, 349 (6244), 165–168. <https://doi.org/10.1126/science.aab2051>.

- (12) Chen, L.; Hernandez, Y.; Feng, X.; Müllen, K. From Nanographene and Graphene Nanoribbons to Graphene Sheets: Chemical Synthesis. *Angew. Chem. Int. Ed.* 2012, 51 (31), 7640–7654. <https://doi.org/10.1002/anie.201201084>.
- (13) Cocchi, C.; Prezzi, D.; Ruini, A.; Benassi, E.; Caldas, M. J.; Corni, S.; Molinari, E. Optical Excitations and Field Enhancement in Short Graphene Nanoribbons. *J. Phys. Chem. Lett.* 2012, 3 (7), 924–929. <https://doi.org/10.1021/jz300164p>.
- (14) Cocchi, C.; Prezzi, D.; Ruini, A.; Caldas, M. J.; Molinari, E. Anisotropy and Size Effects on the Optical Spectra of Polycyclic Aromatic Hydrocarbons. *J. Phys. Chem. A* 2014, 118 (33), 6507–6513. <https://doi.org/10.1021/jp503054j>.
- (15) Guidez, E. B.; Aikens, C. M. Origin and TDDFT Benchmarking of the Plasmon Resonance in Acenes. *J. Phys. Chem. C* 2013, 117 (41), 21466–21475. <https://doi.org/10.1021/jp4059033>.
- (16) Guidez, E. B.; Aikens, C. M. Plasmon Resonance Analysis with Configuration Interaction. *Phys. Chem. Chem. Phys.* 2014, 16 (29), 15501. <https://doi.org/10.1039/c4cp01365d>.
- (17) Guidez, E. B.; Aikens, C. M. Quantum Mechanical Origin of the Plasmon: From Molecular Systems to Nanoparticles. *Nanoscale* 2014, 6 (20), 11512–11527. <https://doi.org/10.1039/C4NR02225D>.
- (18) Chapkin, K. D.; Bursi, L.; Stec, G. J.; Lauchner, A.; Hogan, N. J.; Cui, Y.; Nordlander, P.; Halas, N. J. Lifetime Dynamics of Plasmons in the Few-Atom Limit. *Proc. Natl. Acad. Sci. U.S.A.* 2018, 115 (37), 9134–9139. <https://doi.org/10.1073/pnas.1805357115>.
- (19) Seidner, L.; Stock, G.; Domcke, W. Nonperturbative Approach to Femtosecond Spectroscopy: General Theory and Application to Multidimensional Nonadiabatic Photoisomerization Processes. *The Journal of Chemical Physics* 1995, 103 (10), 3998–4011. <https://doi.org/10.1063/1.469586>.
- (20) Clar, E. *Polycyclic Hydrocarbons*; Springer Berlin Heidelberg: Berlin, Heidelberg, 1964. <https://doi.org/10.1007/978-3-662-01668-8>.
- (21) Tancogne-Dejean, N.; Oliveira, M. J. T.; Andrade, X.; Appel, H.; Borca, C. H.; Le Breton, G.; Buchholz, F.; Castro, A.; Corni, S.; Correa, A. A.; De Giovannini, U.; Delgado, A.; Eich, F. G.; Flick, J.; Gil, G.; Gomez, A.; Helbig, N.; Hübener, H.; Jestädt, R.; Jorner-Somoza, J.; Larsen, A. H.; Lebedeva, I. V.; Lüders, M.; Marques, M. A. L.; Ohlmann, S. T.; Pipolo, S.; Rampp, M.; Rozzi, C. A.; Strubbe, D. A.; Sato, S. A.; Schäfer, C.; Theophilou, I.;

Welden, A.; Rubio, A. Octopus, a Computational Framework for Exploring Light-Driven Phenomena and Quantum Dynamics in Extended and Finite Systems. *J. Chem. Phys.* 2020, 152 (12), 124119. <https://doi.org/10.1063/1.5142502>.

(22) Quantised Singularities in the Electromagnetic Field,. *Proc. R. Soc. Lond. A* 1931, 133 (821), 60–72. <https://doi.org/10.1098/rspa.1931.0130>.

(23) Perdew, J. P.; Zunger, A. Self-Interaction Correction to Density-Functional Approximations for Many-Electron Systems. *Phys. Rev. B* 1981, 23 (10), 5048–5079. <https://doi.org/10.1103/PhysRevB.23.5048>.

(24) Troullier, N.; Martins, J. L. Efficient Pseudopotentials for Plane-Wave Calculations. *Phys. Rev. B* 1991, 43 (3), 1993–2006. <https://doi.org/10.1103/PhysRevB.43.1993>.

(25) Bitzek, E.; Koskinen, P.; Gähler, F.; Moseler, M.; Gumbusch, P. Structural Relaxation Made Simple. *Phys. Rev. Lett.* 2006, 97 (17), 170201. <https://doi.org/10.1103/PhysRevLett.97.170201>.

(26) Casida, M. E. Time-Dependent Density Functional Response Theory for Molecules. In *Recent Advances in Computational Chemistry*; WORLD SCIENTIFIC, 1995; Vol. 1, pp 155–192. https://doi.org/10.1142/9789812830586_0005.

(27) Momma, K.; Izumi, F. VESTA : A Three-Dimensional Visualization System for Electronic and Structural Analysis. *J Appl Crystallogr* 2008, 41 (3), 653–658. <https://doi.org/10.1107/S0021889808012016>.

(28) Castro, A.; Marques, M. A. L.; Rubio, A. Propagators for the Time-Dependent Kohn–Sham Equations. *The Journal of Chemical Physics* 2004, 121 (8), 3425–3433. <https://doi.org/10.1063/1.1774980>.

(29) Krumland, J.; Valencia, A. M.; Pittalis, S.; Rozzi, C. A.; Cocchi, C. Understanding Real-Time Time-Dependent Density-Functional Theory Simulations of Ultrafast Laser-Induced Dynamics in Organic Molecules. *J. Chem. Phys.* 2020, 153 (5), 054106. <https://doi.org/10.1063/5.0008194>.

Chapter 6 - Electronic Excited State Dynamics of Au₂₅ and Au₃₈

Studied by Simulated Transient Absorption Spectroscopy

Zhen Liu, Jannis Krumland, Caterina Cocchi, Christine M. Aikens

6.1 Abstract

For many years, transient absorption experiments have been carried out to study the excited state dynamics of atomically precise gold nanoparticles such as Au₂₅ and Au₃₈. Different mechanisms have been proposed to explain the excited state dynamics on various timescales, ranging from the femtosecond to nanosecond time scale. Using simulated transient absorption spectroscopy (TAS), we perform the ab initio calculations to investigate excited state dynamics of Au₂₅ and Au₃₈. This is the first time that atomically precise nanoparticles have been studied by ab initio transient absorption spectroscopy calculations, which enables state-specific resolution. In this study, the static absorption spectra of Au₂₅ and Au₃₈ are calculated both by real-time time-dependent density functional theory (RT-TDDFT) and linear-response time-dependent density functional theory (LR-TDDFT). The consistency of spectra from RT-TDDFT and LR-TDDFT is used to elucidate the specific transitions involved in the dynamics process. In the transient absorption simulation, a pump pulse with a Gaussian envelope was applied with a carrier frequency chosen to selectively excite certain transitions. The probe used is an instantaneous broadband electric field, which is represented by a delta function. The transient absorption spectrum was simulated by repeating the procedure with different time delays. For Au₂₅, the electron and hole excitations in the simulated pump-probe experiment can be distinguished with the information from electronic structure calculations such as orbital energies and symmetries. For Au₃₈, different energies and directions of the pump laser are applied to Au₃₈ to induce absorptions polarized in different directions. Benefitting from electronic structure calculations, the time-resolved information in the sub-100 fs regime can be explored for gold nanoclusters.

6.2 Introduction

The successful determination of atomically precise thiolate-protected gold nanoclusters plays an important role in the correlation of nanocluster structure with properties, such as quantized optical absorption spectra, fluorescence, and catalysis.¹⁻¹² The crystallographic determination of Au₁₀₂ in 2007,¹³ represented the first time that a fully determined metal nanocluster structure had been achieved. In 2008, the crystal structure of another nanocluster, Au₂₅,¹⁴⁻¹⁶ was determined. Using time-dependent density functional theory calculations,¹⁴ the electronic structure and optical absorption spectrum was fully resolved, which marked the first time that the correlation of the exact cluster structure and unique optical properties had been achieved. Thus, the Au₂₅ nanocluster has now been fully resolved in its spatial coordinates as well as in the energy regime, in order to decipher the information in the optical absorption spectroscopy. Later, in 2010, the structure, electronic, and optical properties of Au₃₈ were explored by density functional theory and X-ray diffraction.¹⁷ The chirality and the role of ligand in the thiolate-protected gold nanocluster were studied. The total structure determination of Au₃₈ was done independently by Jin's group.¹⁸

In this work, we move beyond exploration in the spatial and energy regimes to examine nanoclusters in the time regime by simulating transient absorption spectroscopy. Transient absorption spectroscopy is a powerful tool for characterizing and probing the excited state dynamics.¹⁹⁻²¹ It can provide both physical insights into phenomena occurring during the dynamics process as well as advance the applications of nanoclusters in energy harvesting. Ultrafast excited state dynamics of nanoparticles had been studied using excitation with femtosecond laser pulses even before the geometries of these nanoparticles had been fully determined.²² Now, with the help of simulated transient absorption spectroscopy, Au₂₅ and Au₃₈ are being resolved in the time regime through ab initio calculations.

The first transient absorption spectroscopy experiment on $\text{Au}_{25}(\text{SG})_{18}^-$ showed a biexponential decay with a fast sub picosecond and a much slower nanosecond decay.²² Later, Moran and coworkers performed a pump-probe experiment that excited the Au_{13} core in Au_{25} and monitored the relaxation of cluster. They found a sub 200 fs internal conversion process between the multilevel electronic structure and a 1.2 ps relaxation that they proposed was due to core to semiring relaxation.²³ Knappenberger and coworkers performed the first femtosecond two-dimensional spectroscopy experiments that distinguished the 200 ± 15 fs timescale of hot electron relaxation within the manifold of superatom D states from the 290 ± 200 fs hot hole relaxation within the superatom P states.²⁴

Zhou and coworkers observed two-state relaxations in two different Au_{38} isomers despite significant differences in their geometrical structure.²⁵ Knappenberger and coworkers performed both femtosecond transient absorption and two-dimensional electronic spectroscopy to study the electronic charge carrier relaxation dynamics of $\text{Au}_{38}(\text{SC}_6\text{H}_{13})_{24}$. They found a rapid 120 ± 20 fs and a slower 905 ± 115 fs decay, and the off-diagonal cross peaks indicated sub 100 fs state-to-state dynamics.²⁶

In this work, simulated transient absorption spectroscopy is used to study the excited state dynamics of Au_{25} and Au_{38} . The structure of Au_{25} consists of a nearly icosahedral Au_{13} core protected by six -S-Au-S-Au-S- dimeric semiring motifs. This nanocluster is essentially isotropic. The core of Au_{38} has a D_3 -symmetric cylinder-like shape, and exhibits characteristics of a longitudinal axis and degenerate transverse axes. The structure of Au_{38} consists of a Au_{23} bi-icosahedral core surrounded by three short -S-Au-S- monomeric semirings and six long -S-Au-S-Au-S- dimeric semirings. Because of the elongated nanorod-shaped gold core structure of Au_{38} , the orbitals around HOMO and LUMO can be expressed with Σ , Π , and Δ symmetries similar to

the orbitals of silver nanorods.²⁷ The orbitals are labeled with uppercase Greek letters Σ , Π , and Δ to represent the azimuthal quantum number. The orbitals with nodal planes perpendicular to the long axis are assigned as Σ orbitals. The Π orbitals have one nodal plane containing the long axis and other nodal planes perpendicular to the long axis. The Δ orbitals have two nodal planes containing the long axis and other nodal planes perpendicular to the long axis.

After ground state excitation, the details of absorption can be analyzed. The transient absorption simulation excites a specific absorption peak and then probes the electronic dynamics of the system. The energy transfer in the atomically precise isotropic Au₂₅ nanocluster and the anisotropic nanorod-like Au₃₈ system can then be observed through sub-hundred femtosecond dynamics.

6.3 Computational Methods

All real-time time dependent density functional theory (RT-TDDFT) calculations were performed using the real-space Octopus code.²⁸ We employed the PBE exchange-correlation functional²⁹ and norm-conserving Troullier-Martins pseudopotentials.³⁰ The pseudopotentials included a relativistic correction in the radial part. The spacing in the real-space grid was set to 0.18 Å. The radius of the sphere centered on each atom was set to 6 Å. Previous calculations from Weerawardene³¹ showed that the spacing of 0.18 Å and radius parameter of 6 Å were able to obtain the spectra converged to results with a large Slater-type all-electron quadruple- ζ polarized (QZ4P) basis set.

At the beginning, Kohn-Sham orbitals were obtained by a ground state calculation. Then, the system was excited by a delta kick pulse, and time-dependent Kohn-Sham equations were

propagated for 60 fs to obtain a good resolution of the absorption spectrum. The approximate enforced time-reversal symmetry (AETRS)³² was used in propagation with a time step of 2 as. The absorption spectrum was obtained through the default “oct-propagation_spectrum” utility by Fourier transformation of the time-dependent dipole moment.

In order to obtain detailed electronic structure information, linear response TDDFT (LR-TDDFT) calculations were performed using the Amsterdam Modeling Suite (AMS) 2021.102 software.³³ We employed the PBE functional²⁹ and a triple-zeta basis set with polarization functions.³⁴ Scalar relativistic effects were incorporated using zeroth-order regular approximation (ZORA).^{35,36} In the linear response calculations,³⁷ 1000 excited states are included. The absorption spectra plotted with intensity (in arbitrary units) versus energy were fit with a Lorentzian with a full width at half-maximum (FWHM) of 0.05 eV. The orbitals involved in single-particle transitions were visualized by VESTA.³⁸

For the transient absorption spectroscopy (TAS) simulation,³⁹ well-resolved transitions in the LR-TDDFT optical spectrum were used to choose peaks of interest to pump in an electronic dynamics simulation performed using RT-TDDFT. For Au₂₅, the pump was tuned to have energies of 1.40 eV, 1.92 eV, 2.06 eV, and 2.40 eV. For Au₃₈, different polarization directions of the pump need to be considered because of its rod-like shape. To excite states in the longitudinal direction of Au₃₈, the pump was polarized in the z direction, with an energy of 1.04 eV, 1.62 eV, and 1.93 eV. Fewer strong transverse peaks were noted in the LR-TDDFT optical spectrum. Due to the similarity of the x and y direction, only one pump energy of 1.37 eV polarized in the x direction was considered. All pump pulses have a Gaussian envelope function with a standard deviation of 3 fs. The peak amplitude of pump and probe are 3.51×10^{10} W/cm². To obtain more

transient absorption information and save computing resource, the pump center was moved 5 fs, which did not affect the physical phenomena.

In the simulation, the probe time delays range from 0-100 fs with a spacing of 1 fs. For every time delay, a delta kick probe was used to excite all absorptions using the data obtained from the pulse calculations. The transient absorption spectra can then be obtained via Fourier transformation of the dipole fluctuations that arise after each delta kick after subtracting the spectrum at 0 fs.

6.4 Results and Discussion

6.4.1 Au₂₅

In the electronic structure calculation of Au₂₅, we observe that the superatom P shell “HOMO” consists of three nearly degenerate orbitals, which are HOMO 150 a_u , HOMO-1 149 a_u and HOMO-2 148 a_u (Figure 6.1). The HOMO-3 and HOMO-4 (151 a_g , 150 a_g) arise from mixed contributions of sulfur p orbitals and gold d orbitals. The HOMO-5 to HOMO-10 (147 a_u , 146 a_u , 145 a_u , 149 a_g , 148 a_g , 147 a_g) and HOMO-13, HOMO-14 (143 a_u , 142 a_u) are mainly composed of sulfur p orbitals in the staple and of 5d atomic orbitals of gold in the staple. The HOMO-11, HOMO-12 and HOMO-15 through HOMO-21 are not orbitals of interest in the current study. The HOMO-22 and HOMO-23 (141 a_g and 140 a_g) are made of d band orbitals of gold from both staple and core atoms.

The superatom D shell consists of the orbitals LUMO to LUMO+4 (152 a_g , 153 a_g , 154 a_g , 155 a_g and 156 a_g), which have their main contribution from 6sp orbitals of gold. The higher

energy LUMO+5, LUMO+6 and LUMO+7 ($151a_u$, $152a_u$ and $153a_u$) are also composed of gold 6sp orbitals.

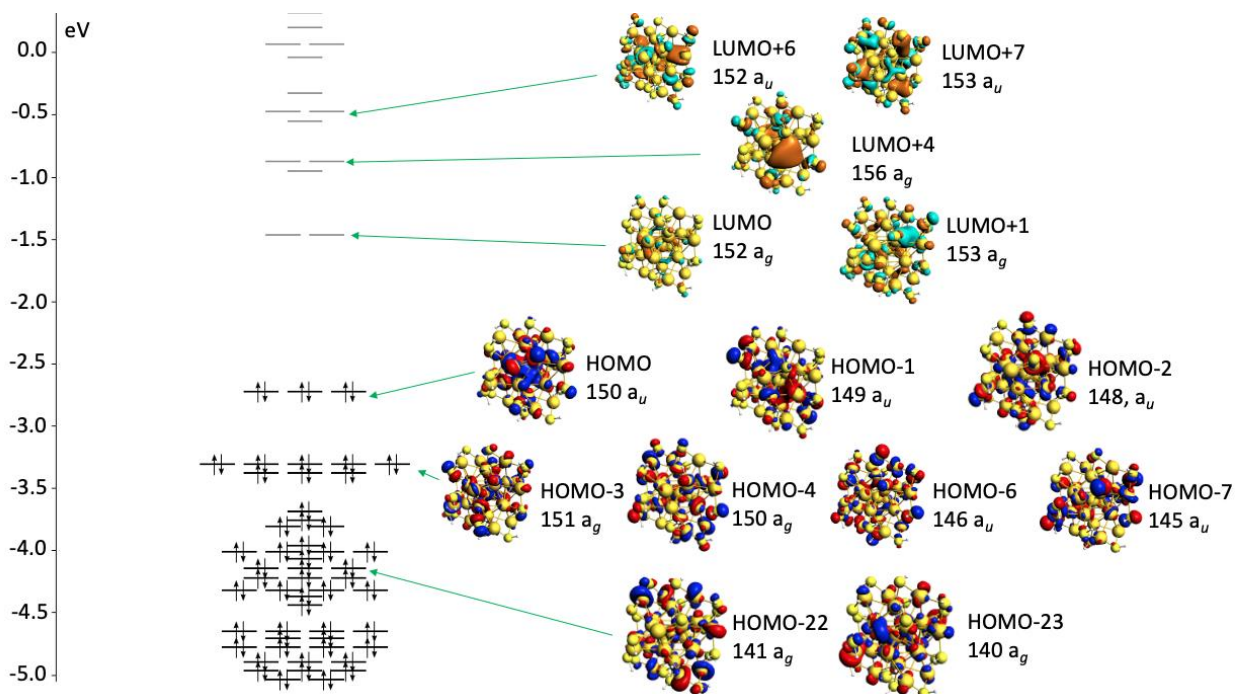


Figure 6.1 Kohn–Sham energy level and orbital diagram for Au_{25}

The ground state absorption spectra of Au_{25} calculated by LR-TDDFT and RT-TDDFT are shown in Figure 6.2. The first excitation peak at 1.40 eV arises from a transition from HOMO, HOMO-1 and HOMO-2 to LUMO and LUMO+1. The next excitation located at 1.92 eV is from HOMO-6 and HOMO-7 to LUMO and LUMO+1. The absorption peak at 2.06 eV arises from HOMO and HOMO-1 to LUMO+4. The peak at 2.40 eV comes from HOMO-13 and HOMO-14 to LUMO and LUMO+1. These most notable absorption peaks are used as pump energies in the transient absorption spectroscopy calculations.

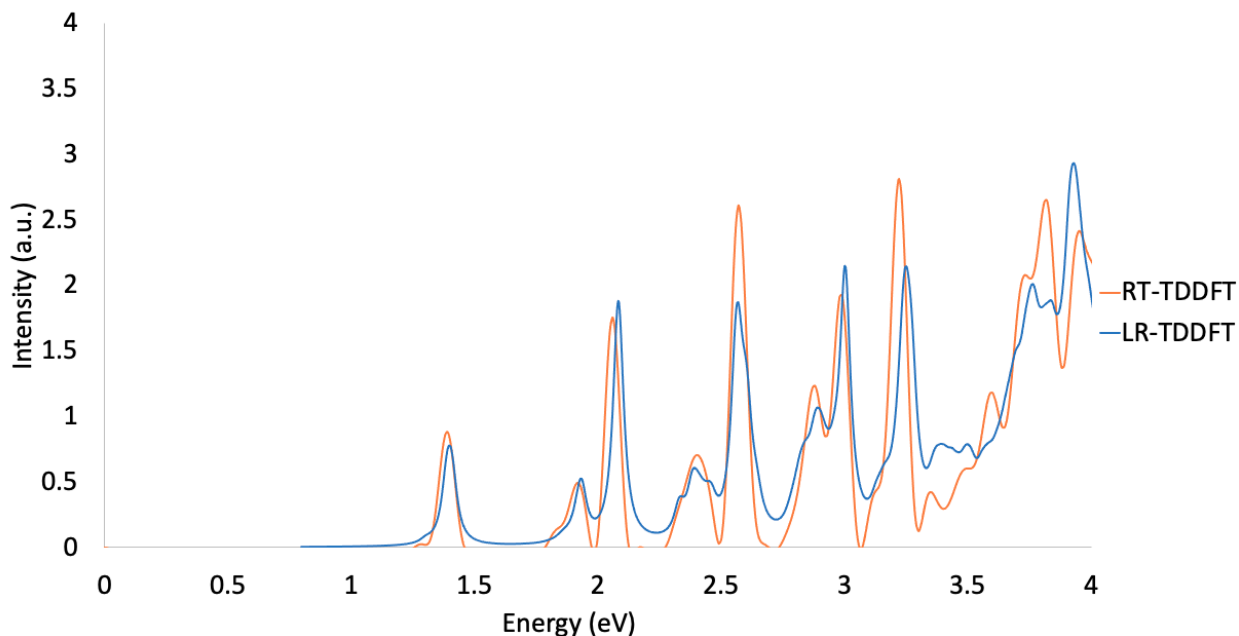


Figure 6.2 Ground state absorption of Au₂₅ from LR-TDDFT and RT-TDDFT

6.4.1.1 Pump energy of 1.40 eV

For all transient absorption simulations of Au₂₅, the only variable is the pump energy so that the different excited state dynamics can be analyzed in detail. The first simulation is performed with a pump energy of 1.40 eV, which induced the HOMO, HOMO-1, and HOMO-2 to LUMO and LUMO+1 transition. Because no signal was found from 0 to 1 eV in the ground state absorption, the bright state transition between 0.6-1.0 eV in Figure 6.3 is the first transient absorption signal arising from excitations of the electronic population in LUMO and LUMO+1 to higher energy level(s) and hole population in HOMO, HOMO-1 and HOMO-2 to lower energy level(s).

Considering the a_u symmetry of HOMO and HOMO-1 with nearly degenerate energies of -2.73 eV and -2.75 eV, the first allowed excited state hole transition will occur into orbitals with a_g symmetry, which are HOMO-3 and HOMO-4 with nearly degenerate energies of -3.31 eV and

-3.32 eV. The difference in orbital energy values ($\Delta\varepsilon$) will be around 0.58 eV. Considering the a_g symmetry of LUMO and LUMO+1 with nearly degenerate energies of -1.47 eV and -1.48 eV, the first allowed excited state electronic transition will excite into orbitals of a_u symmetry, which are LUMO+5, LUMO+6 and LUMO+7 with energies of -0.55, -0.52 eV and -0.47 eV. The difference in orbital energy values ($\Delta\varepsilon$) will be around 0.96 eV. Thus, the first positive signals found in the excited state absorption between 0.6-1.0 eV can be attributed to the excited state hole excitation (HOMO and HOMO-1 to HOMO-3 and HOMO-4) and electron excitation (LUMO and LUMO+1 to LUMO+5, LUMO+6 and LUMO+7).

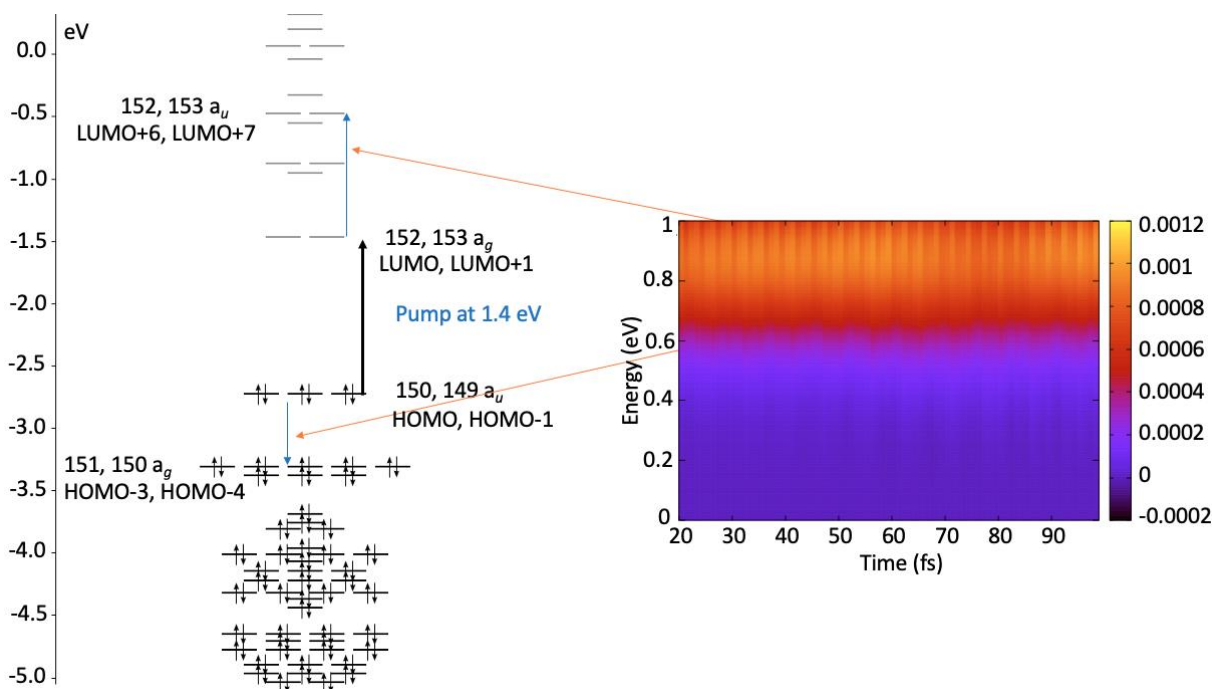


Figure 6.3 Transient absorption spectrum of Au_{25} with pump energy of 1.40 eV

6.4.1.2 Pump energy of 1.92 eV and 2.06 eV

The second and third transient absorption simulations are performed with pump energies of 1.92 eV and 2.06 eV as shown in Figure 6.4. Because of the similarity of pump energy (within 0.14 eV) and use of Gaussian envelope pump with a standard deviation of 3 fs, the two pump

pulses are exciting both peaks at the same time, which results in the similarity of the first observed excited state absorption in Figure 6.4 (a) and Figure 6.4 (b).

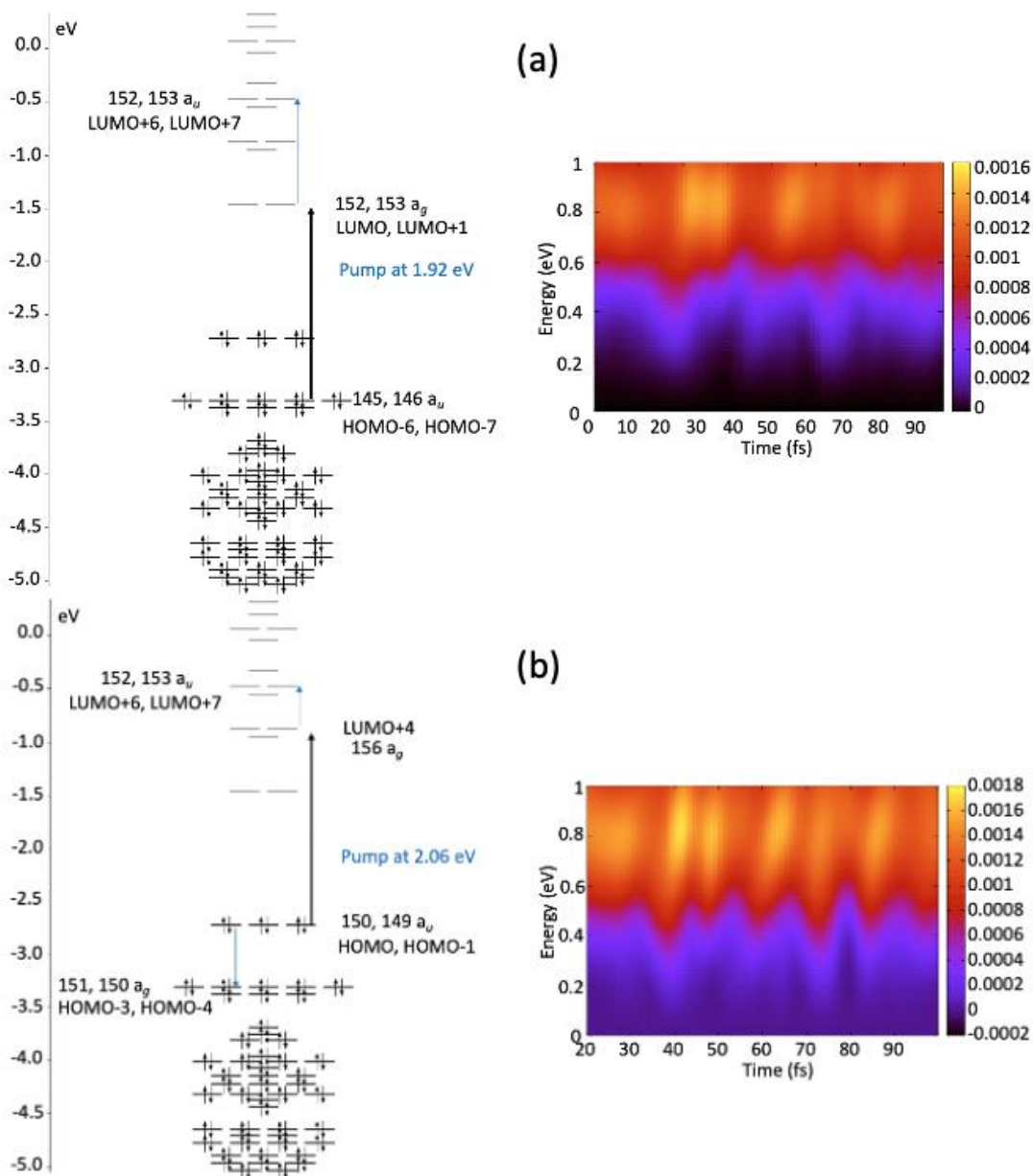


Figure 6.4 (a) Transient absorption spectrum of Au_{25} with pump energy of 1.92 eV and (b) Transient absorption spectrum of Au_{25} with pump energy of 2.06 eV

From analysis of ground state excitations using LR-TDDFT, we found that the peak at 1.92 eV corresponds to transitions from HOMO-6 and HOMO-7 to LUMO and LUMO+1. The peak at 2.06 eV originates from HOMO, HOMO-1, and HOMO-2 to LUMO+4. Comparing to the first excited state absorption signal in the transient absorption spectrum with pump energy of 1.40 eV (Figure 6.3), the first excited state absorption signal in both Figure 6.4 (a) and Figure 6.4 (b) are shifted to lower energy. Similarly, the lowest energy excited state absorption can arise from excited state hole transition, such as HOMO and HOMO-1 to HOMO-3 and HOMO-4 with $\Delta\varepsilon \sim 0.58$ eV. Due to the similarity of pump energy and complexity of transitions involved in these two transient absorption spectra, the specific transitions cannot be fully assigned.

6.4.1.3 Pump energy of 2.40 eV

The fourth transient absorption simulation is performed with a pump energy of 2.40 eV (Figure 6.5). Compared to other pump energy simulations in this work, very obvious sub-hundred femtosecond dynamics can be observed in the transient absorption spectra. Since the pump excited the electron into LUMO and LUMO+1, the electron excited state transition should be similar to the pump energy of 1.40 eV and 1.92 eV. Because of the a_g symmetry of LUMO and LUMO+1, the excited electronic population must then be excited into orbitals of a_u symmetry, the first of which are LUMO+5, LUMO+6 and LUMO+7 as discussed in the analysis of the transient absorption with a pump energy of 1.40 eV. The positive signal around 0.96 eV is attributed to the electronic transition from LUMO and LUMO+1 into LUMO+6 and LUMO+7. Because the pump energy of 2.40 eV involves excitation into the same unoccupied orbitals as the 1.40 and 1.92 eV pumps, but from different occupied orbitals, the sub-hundred femtosecond

dynamics around 0.4 eV observed in Figure 6.5 is attributed to the hole dynamics in Au_{25} created by the 2.40 eV pump.

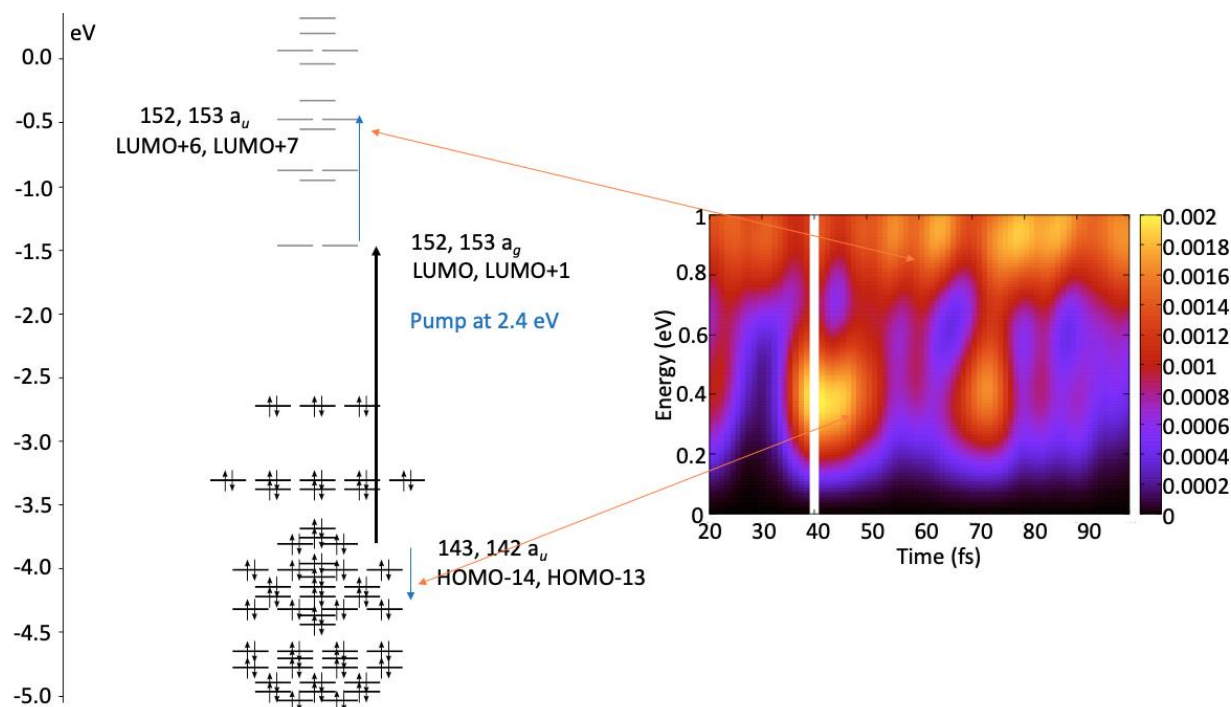


Figure 6.5 Transient absorption spectrum of Au_{25} with pump energy of 2.40 eV

From ground state absorption calculated by LR-TDDFT, we found that the peak at 2.40 eV arises from excitations out of HOMO-13 and HOMO-14 ($142a_u$ and $143a_u$), composed of atomic sulfur p orbitals and gold 5d orbitals, to LUMO and LUMO+1 ($152a_g$, $153a_g$). The gold 5d orbital contributions in HOMO-13 and HOMO-14 come both from core and staple atoms. Because of the a_u symmetry of HOMO-13 and HOMO-14 ($142a_u$ and $143a_u$), with energies of -3.81 eV and -3.82 eV, the allowed excited state hole transition will occur into orbitals with a_g symmetry. The possible orbitals involved are HOMO-15 to HOMO-17 with energies ranging from -3.96 eV to -4.04 eV and HOMO-21 to HOMO-23 with energies ranging from -4.15 eV to -4.18 eV. Therefore, the difference in orbital energy values ($\Delta\varepsilon$) will range from 0.15 eV to 0.22

eV and 0.34 eV to 0.36 eV, and thus are likely responsible for the positive feature around 0.2-0.5 eV shown in Figure 6.5. Since the orbitals involved are mainly arising from d electrons in gold, the sub-hundred femtosecond hole dynamics observed in Figure 6.5 can be attributed to the d electron from gold.

6.4.2 Au₃₈

We now examine the ground and excited state absorption of the Au₃₈ nanocluster. The ground state absorption spectra of Au₃₈ calculated by LR-TDDFT and RT-TDDFT is shown in Figure 6.6 (a). Because of the cylinder-like shape of Au₃₈, the absorption peaks have different polarizations; RT-TDDFT spectra with different polarization directions are shown in Figure 6.6 (b). The longitudinal z direction has the most contribution to the profile of the absorption spectrum. The strongest low-energy peaks in the absorption spectrum are absorption peaks at 1.04 eV, 1.62 eV and 1.93 eV. All three peaks are polarized in the z direction (longitudinal). The transverse x and y polarization directions lead to spectra with identical shapes due to symmetry, with the highest contribution to the peak at 1.37 eV and the shoulder peaks at 1.70 eV and 1.86 eV.

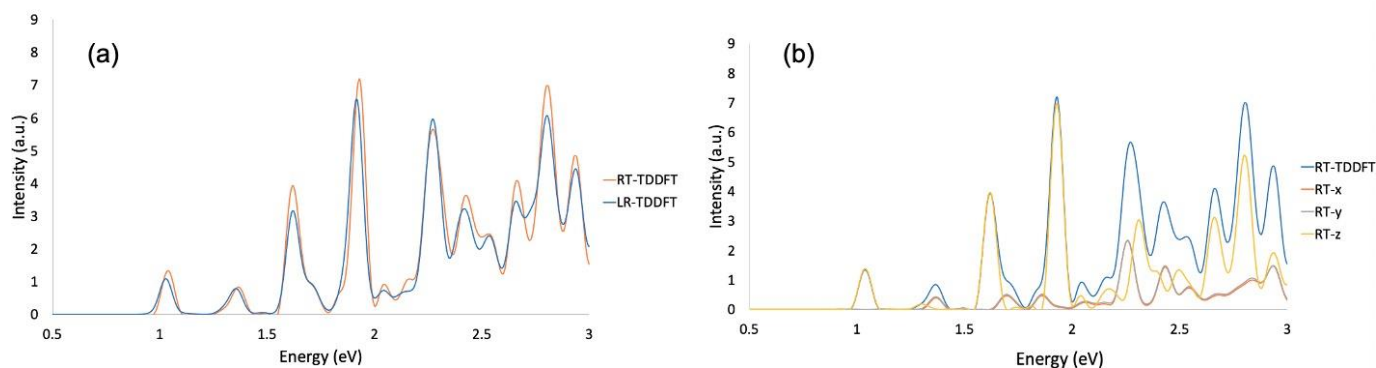


Figure 6.6 (a) Ground state absorption of Au₃₈ from LR-TDDFT and RT-TDDFT, (b) Calculated RT-TDDFT absorption spectrum of Au₃₈ with contributions from x, y, and z polarization directions

The first absorption peak at 1.04 eV is from the HOMO to LUMO+1 and HOMO-1 to LUMO transition (Π_2 to Π_3). According to the character table for the D_3 point group, $E \times E = A_1 + A_2 + E$, so this transition accounts for the first four excited states. In this excitation, the strongest one, S_4 , has A_2 symmetry, which is polarized in the longitudinal z direction and is responsible for the peak observed at 1.04 eV. The second and third excited states, S_2 and S_3 , arise from a degenerate excitation with E symmetry, which is two orders smaller in oscillator strength. The first excitation, S_1 , is a dark state with A_1 symmetry, with oscillator strength that is six orders of magnitude smaller than S_4 . (Note: Because the symmetry of the cluster varies slightly from perfect D_3 , the oscillator strength is not calculated to be exactly zero, although it is close.)

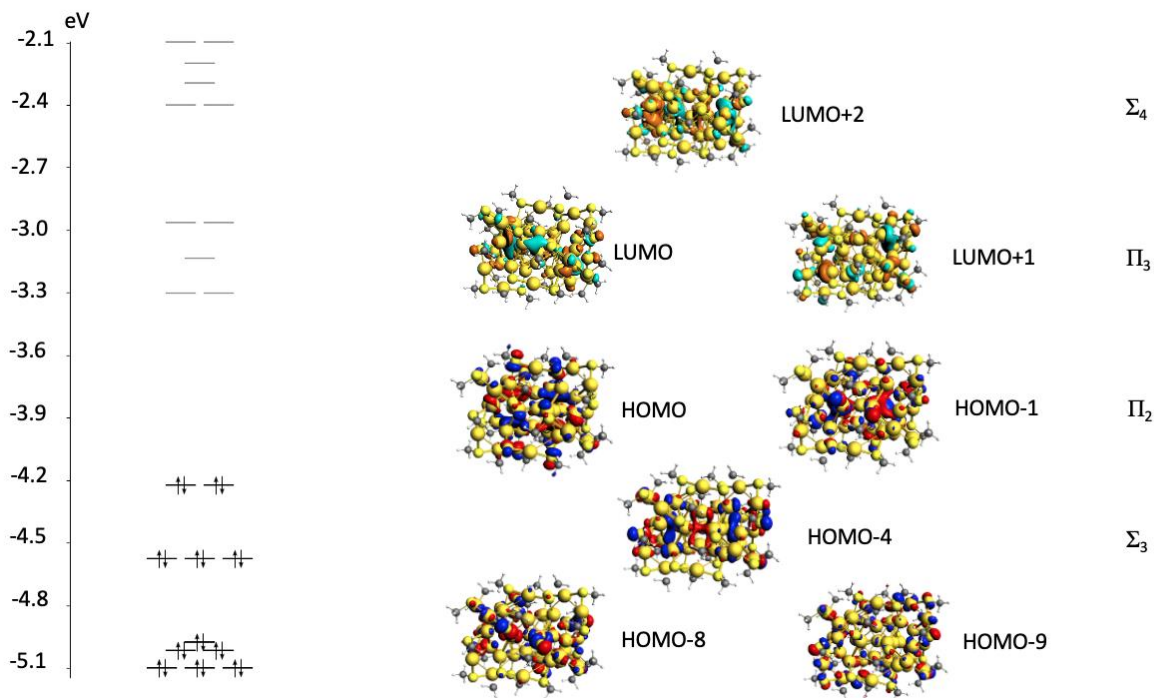


Figure 6.7 Kohn–Sham energy levels and orbital diagram for Au₃₈

The second absorption peak at 1.37 eV polarized in the x and y directions arises from HOMO-4 to LUMO and LUMO+1 transition (Σ_3 to Π_3). According to the character table for the point group D_3 , $A_1 \times E = E$, where HOMO-4 is A_1 and nearly degenerate LUMO and LUMO+1 are E . The cross-product E represents the degeneracy of the x-polarized and y-polarized excitations for the 1.37 eV absorption peak as shown in Figure 6.6 (b). The third peak at 1.62 eV arises from the HOMO-4 to LUMO+2 transition (Σ_3 to Σ_4). According to the character table for the point group D_3 , $A_1 \times A_2 = A_2$, where HOMO-4 is A_1 and LUMO+2 is A_2 . The nondegenerate bright transition A_2 polarized in the longitudinal z direction is the absorption peak at 1.62 eV. The first three absorption peaks (Π to Π , Σ to Π , and Σ to Σ) are features of molecules and materials with cylindrical shapes. The fourth peak at 1.93 eV comes from HOMO-8 and HOMO-9 to LUMO and LUMO+1, which represents a ligand to core excitation.

6.4.2.1 Pump energy of 1.04 eV

Because the first absorption peak in the ground state absorption spectra of Au₃₈ is located at 1.04 eV, the signals below 1.04 eV in the transient absorption spectra must be excited state absorption signals. The first transient absorption spectrum simulation in this work uses a pump polarized in the z direction with an energy of 1.04 eV (Figure 6.8). The HOMO/HOMO-1 to LUMO/LUMO+1 transition (Π_2 to Π_3) happens after the pump. A hole is created in the degenerate HOMO and HOMO-1 orbitals and the electron is created in degenerate LUMO and LUMO+1 orbitals, so that new signals show up in the transient absorption spectrum because of the newly created electron and hole. The very weak excited state absorption around 0.3 eV is attributed to the hole excited state excitation from the degenerate HOMO and HOMO-1 to the degenerate HOMO-2 and HOMO-3, which has $\Delta\varepsilon \sim 0.25$ eV (Table C6.1). The HOMO-4 is not involved in this transition because of the difference of the Π symmetry of HOMO-2 and HOMO-3 and the Σ symmetry of HOMO-4, even though their energies are close (and artifactually appear degenerate in the figure).

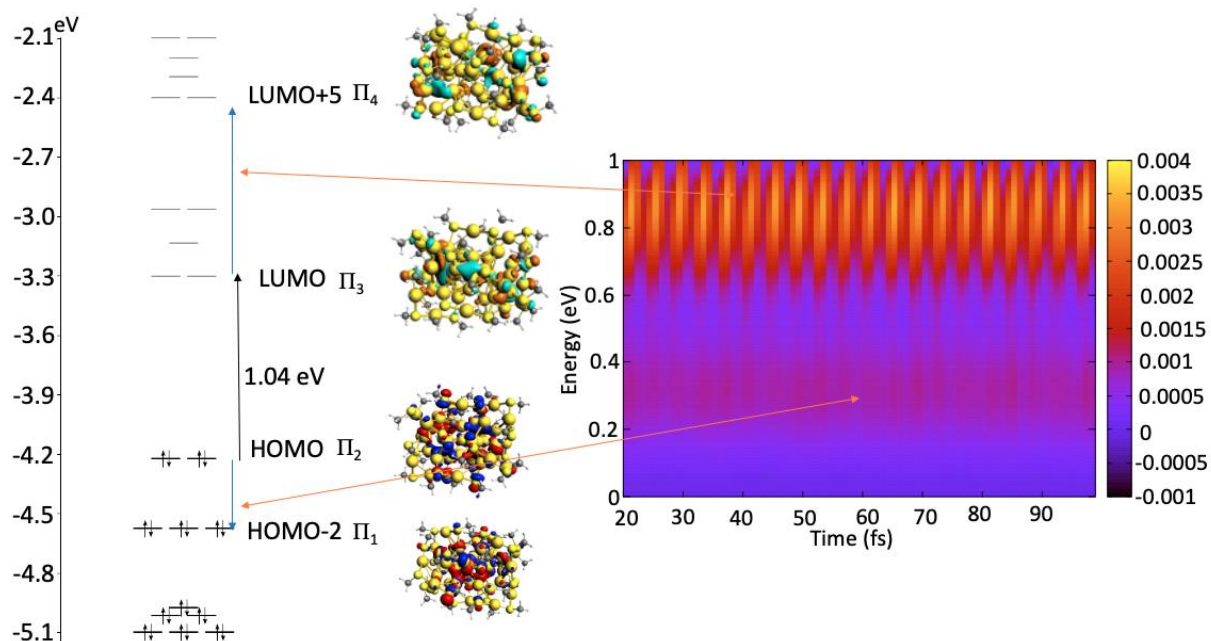


Figure 6.8 Transient absorption spectrum of Au_{38} with pump energy of 1.04 eV polarized in the z direction

An important feature in Figure 6.8 (that also shows up after other pulses, as described later) arises from excitation involving the newly created electronic population in LUMO/LUMO+1. The excited state absorption around 0.8 eV should originate from the LUMO and LUMO+1 to LUMO+5 and LUMO+6, which is a Π_3 to Π_4 transition. As shown in table C6.1, the energy difference between LUMO and LUMO+5 is 0.90 eV, which is close to the excited state absorption signal observed between 0.7-1.0 eV.

6.4.2.2 Pump energy of 1.37 eV

For the transient absorption spectrum with a pump polarized in the x direction with an energy of 1.37 eV, the HOMO-4 to LUMO transition initially occurs (Σ_3 to Π_3). Even though the

excitation direction and energy are different, both the pump with energy of 1.04 eV polarized in the z direction and the pump with energy of 1.37 eV polarized in the x direction create excited state electron population in LUMO and LUMO+1. A similar electron excited state absorption around 0.85 eV can be observed in Figure 6.8 and Figure 6.9. The differences in Figure 6.8 and Figure 6.9 can be attributed to the hole excited state absorption; as discussed above, the hole excited state absorption around 0.25 eV in Figure 6.8 is due to the degenerate HOMO and HOMO-1 to degenerate HOMO-2 and HOMO-3 (Π_2 to Π_1) transition. According to symmetry of the orbitals, the hole created at HOMO-4 (Σ_3) created by pump energy of 1.37 eV polarized in the x direction could excite to a lower occupied orbital with Σ_2 symmetry. However, the lower occupied Σ_2 orbital was not found due to mixing with ligand contributions. In Figure 6.9, the most obvious signal around 0.8 eV is attributed to the excited state electronic transition from the LUMO and LUMO+1 to LUMO+5 and LUMO+6, which is a Π_3 to Π_4 transition.

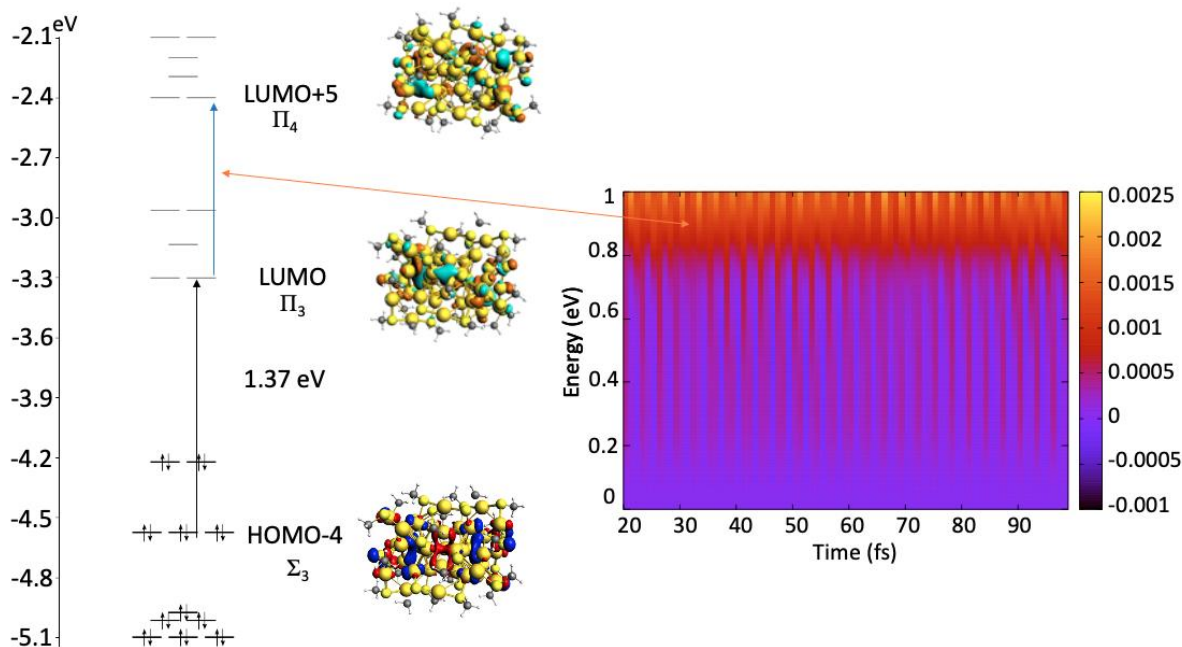


Figure 6.9 Transient absorption spectrum of Au_{38} with pump energy of 1.37 eV polarized in the x direction

6.4.2.3 Pump energy of 1.62 eV

For the transient absorption spectrum with the pump polarized in the z direction with an energy of 1.62 eV, the pump excites the HOMO-4 to LUMO+2 transition (Σ_3 to Σ_4) (Figure 6.10). Compared to Figure 6.8, with the 1.04 eV pulse polarized in the z direction, the main differences are the pump energy and the orbitals involved in the transitions. The pump energy of 1.62 eV polarized in the z direction is the only transition that induces a Σ to Σ transition. The newly created electron in LUMO+2 and hole in HOMO-4 will generate the signals in transient absorption spectroscopy. The LUMO+2 with symmetry of Σ_4 will be excited to degenerate LUMO+5 and LUMO+6 with symmetry of Π_4 . Under the D_3 symmetry expression, the Σ_4 is A_1 and nearly degenerate LUMO+5 and LUMO+6 are E . According to $A_1 \times E = E$, the cross-product E represents a bright state transition in x and y direction, which can be observed with a probe that is polarized in the x direction (Figure 6.10). The bright signal around 0.8 eV is

assigned to the LUMO+2 to degenerate LUMO+5 and LUMO+6 transition (Σ_4 to Π_4) with energy difference $\Delta\varepsilon = 0.75$ eV.

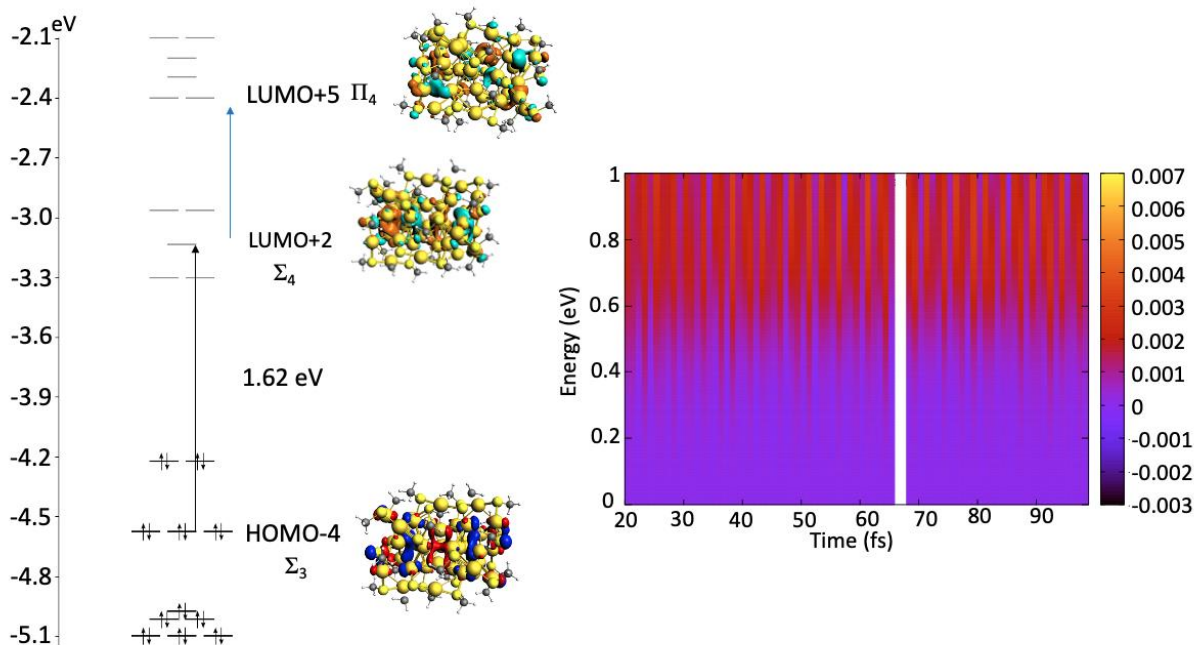


Figure 6.10 Transient absorption spectrum of Au₃₈ with pump energy of 1.62 eV polarized in the z direction and probe in x direction

6.4.2.4 Pump energy of 1.93 eV

As shown in Figure 6.11, the pump polarized in the z direction with an energy of 1.93 eV excites the HOMO-8 and HOMO-9 to LUMO and LUMO+1 transition, which mostly arises from a ligand orbital to core transition. The newly created electronic population in LUMO and LUMO+1 can again be excited into LUMO+5 and LUMO+6, and thus the electron excited state absorption between 0.7-1.0 eV is attributed to this excited state absorption (Figure 6.11), which is similar to results with the pump polarized in the z direction with an energy of 1.04 eV (Figure 6.8) and the pump polarized in the x direction with an energy of 1.37 eV (Figure 6.9). The signal

around 0.3 eV is attributed to the hole excitation from HOMO-8 and HOMO-9 to deeper occupied orbitals.

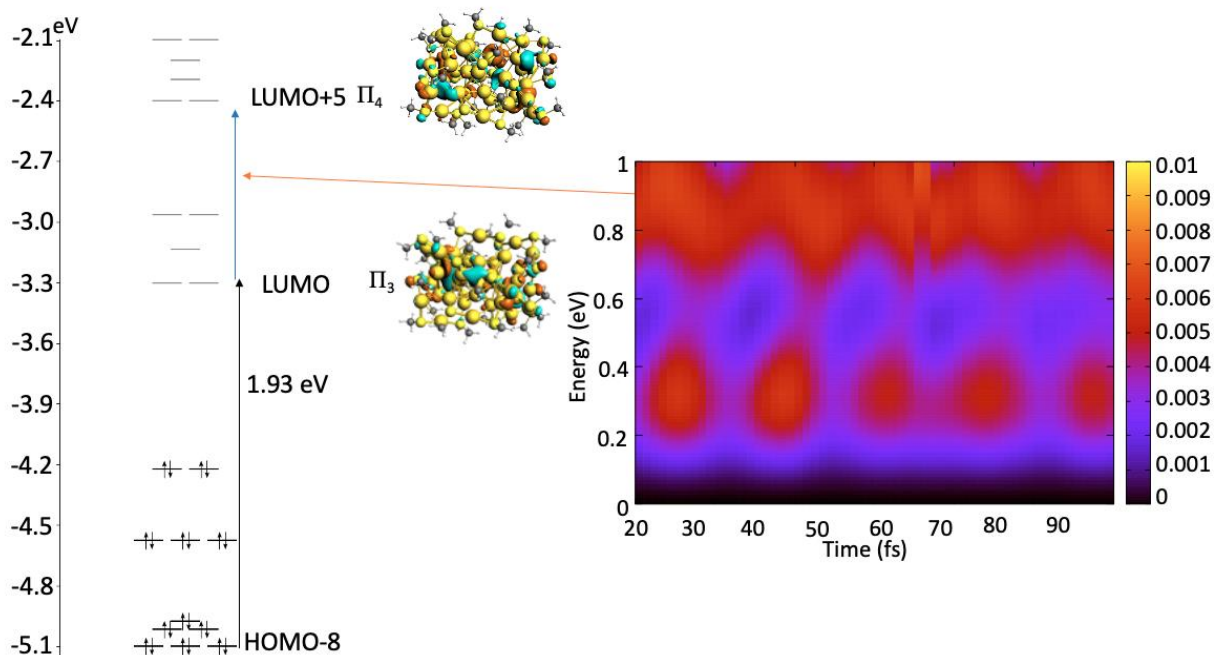


Figure 6.11 Transient absorption spectrum of Au₃₈ with pump energy of 1.93 eV polarized in the z direction

6.4.3 Comparison of Au₂₅ and Au₃₈

For Au₂₅ and Au₃₈, one important difference between the nanoclusters is the core shape, with an icosahedral Au₁₃ core in Au₂₅ and a bi-icosahedral Au₂₅ core in Au₃₈. As shown in Figure 6.12, the dipole fluctuation is mostly in polarization direction of pump, which is x direction in our calculation. Around 30 fs, the dipole fluctuation in y and z directions can be observed. Around 90 fs, dipole fluctuation in x, y, and z directions are reaching the similar scale. The similar transfer

pattern can be found in Figure C6.1-C6.3. On the other hand, the dipole fluctuation for Au₃₈ is coming from the z direction, which is the polarization direction of pump. In sub-hundred femtosecond time scale, only dipole fluctuation in z direction can be observed. For pump energy of 1.37 eV and polarized in x direction, as shown in Figure C6.5, only dipole fluctuation in x direction can be observed. By comparing the dipole fluctuations in both nanoparticles, the spherical Au₂₅ can more easily transfer energy from the pump direction to the other two directions (Figure 6.12 and Figure C6.1-C6.3), while excitation in the nanorod Au₃₈ confines the dipole in the pump direction (Figure 6.13 and Figure C6.4-C6.6). By performing transient absorption with different pump energies and pump polarization directions, this work shows that energy transfers among different dipole moment directions are more dependent on the structure of the nanoparticle rather than the pump energy.

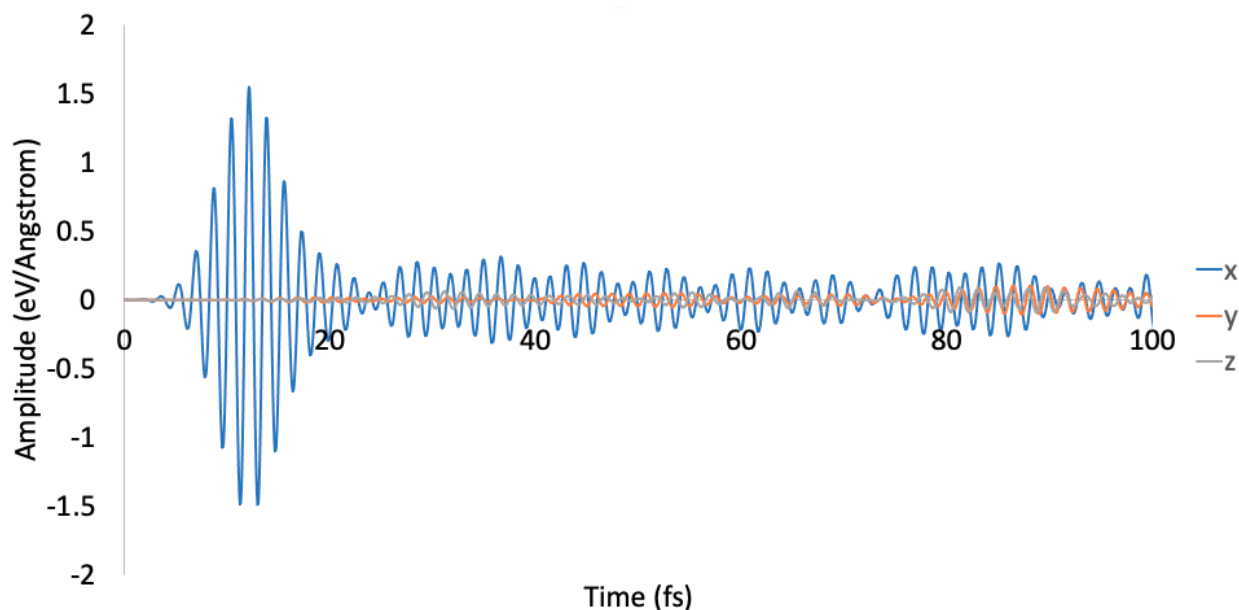


Figure 6.12 Dipole fluctuation of Au₂₅ with pump energy of 2.40 eV

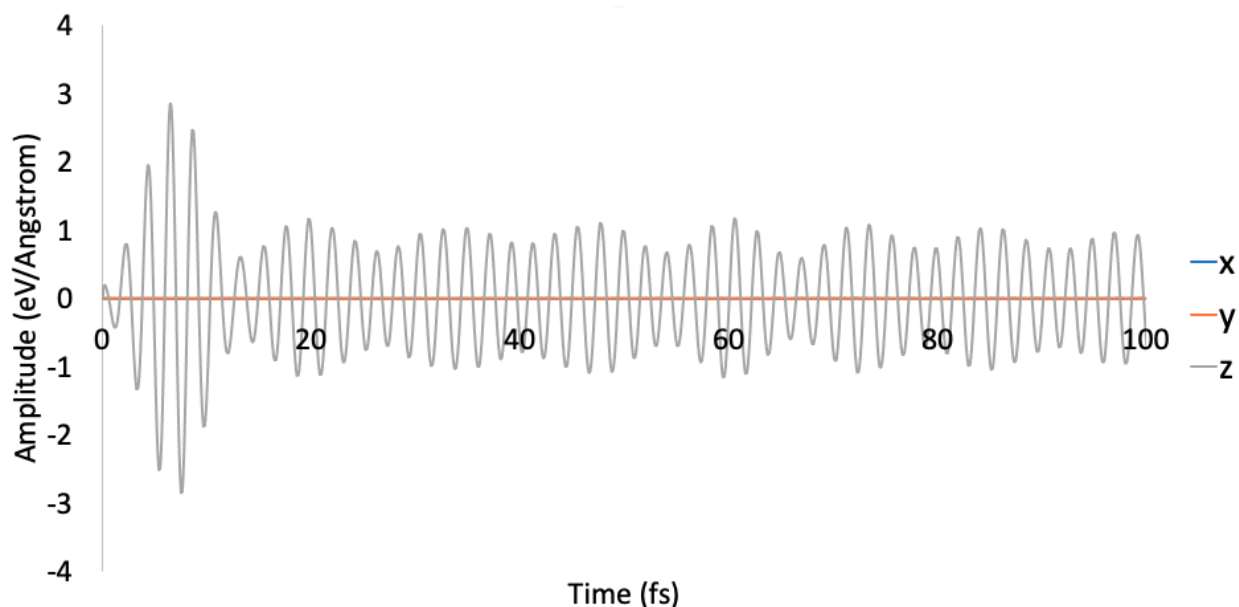


Figure 6.13 Dipole fluctuation of Au₃₈ with pump energy of 1.93 eV polarized in z direction

6.5 Conclusions

In conclusion, we have presented the first simulated transient absorption spectroscopy study of atomically precise nanoparticles. For Au₂₅, pump energies of 1.40 eV, 1.92 eV, 2.06 eV, and 2.40 eV are applied to excite the nanocluster. By analyzing the orbitals involved in the simulated transient absorption spectroscopy, we found different kinds of signal for Au₂₅. With a pump energy of 1.40 eV, the newly created electron can be found in the LUMO and LUMO+1 and the newly created hole in the HOMO, HOMO-1, and HOMO-2, which then generate the signals in the transient absorption spectra due to excitations into higher energy LUMO+6 and LUMO+7 and lower energy HOMO-3 and HOMO-4. The pump energies of 1.92 eV and 2.06 eV create similar transient absorption signals due to the similarity of pump energy and the complexity of transitions involved. The pump energy of 2.40 eV witnesses the most obvious dynamics process in the sub-hundred femtosecond regime. By detailed analysis of the orbitals involved, we separated

the contribution of electron excited state absorption and hole excited state absorption and attributed the sub-hundred femtosecond dynamics to the transitions between d electron in gold.

For Au₃₈, different excitation pump energies and pump polarization directions are used to excite different transitions. A common feature in excited state absorptions can be found with a newly created electron in LUMO and LUMO+1 transitioning to LUMO+5 and LUMO+6 using pump energies of 1.04 eV, 1.37 eV and 1.93 eV. By comparing the three transient absorption spectra, the differences that appear originate from the holes created by each pump. Due to the high tunability of simulated lasers, different kinds of transition can be studied in the same nanoparticle, including Π_2 to Π_3 from the 1.04 eV pump polarized in the z direction, Σ_3 to Π_3 from the 1.37 eV pump polarized in the x direction, Σ_3 to Σ_4 from the 1.62 eV pump polarized in the z direction, and ligand to core excitation from the 1.93 eV pump polarized in the z direction. Even though the excitation direction and energy are different, both the pump energy of 1.04 eV polarized in the z direction and the pump energy of 1.37 eV polarized in the x direction create an excited state electron in LUMO and LUMO+1. Then, a similar electron excited state absorption around 0.85 eV can be observed.

In this study, the energy transfer within Au₂₅ and Au₃₈ is analyzed through the fluctuation of dipole moment in different direction. For Au₂₅, the dipole fluctuation induced from pump in x direction can be transferred to y and z directions due to the spherical structure of Au₂₅. For Au₃₈, when pump polarized in z direction (longitudinal) excites the nanocluster, the dipole fluctuation of Au₃₈ is confined in z direction (longitudinal). When the pump polarized in x direction (transverse) excites the nanocluster, the dipole fluctuation will be confined in x direction (transverse). In the sub-hundred femtosecond dynamics, the energy transfer among different are dependent on the structure of nanocluster rather than the pump energy. Nanorod Au₃₈ confines the

induced dipole moment in the pump direction, whereas the more isotropic Au₂₅ is more easily able to transfer the energy from the pump direction to the other two directions.

6.6 Acknowledgement

Z.L. and C.M.A were supported by the National Science Foundation (CHE-1905048) of the United States. The computing for this work was performed on the Beocat Research Cluster at Kansas State University, which is funded in part by NSF grants CHE-1726332, CNS-1006860, EPS-1006860, and EPS-0919443.

6.6 Reference

- (1) Whetten, R. L.; Khoury, J. T.; Alvarez, M. M.; Murthy, S.; Vezmar, I.; Wang, Z. L.; Stephens, P. W.; Cleveland, C. L.; Luedtke, W. D.; Landman, U. Nanocrystal Gold Molecules. *Adv. Mater.* **1996**, *8* (5), 428–433. <https://doi.org/10.1002/adma.19960080513>.
- (2) Templeton, A. C.; Wuelfing, W. P.; Murray, R. W. Monolayer-Protected Cluster Molecules. *Acc. Chem. Res.* **2000**, *33* (1), 27–36. <https://doi.org/10.1021/ar9602664>.
- (3) Daniel, M.-C.; Astruc, D. Gold Nanoparticles: Assembly, Supramolecular Chemistry, Quantum-Size-Related Properties, and Applications toward Biology, Catalysis, and Nanotechnology. *Chem. Rev.* **2004**, *104* (1), 293–346. <https://doi.org/10.1021/cr030698+>.
- (4) Sardar, R.; Funston, A. M.; Mulvaney, P.; Murray, R. W. Gold Nanoparticles: Past, Present, and Future. *Langmuir* **2009**, *25* (24), 13840–13851. <https://doi.org/10.1021/la9019475>.
- (5) Elghanian, R.; Storhoff, J. J.; Mucic, R. C.; Letsinger, R. L.; Mirkin, C. A. Selective Colorimetric Detection of Polynucleotides Based on the Distance-Dependent Optical Properties of Gold Nanoparticles. *Science* **1997**, *277* (5329), 1078–1081. <https://doi.org/10.1126/science.277.5329.1078>.
- (6) Chen, S.; Ingram, R. S.; Hostetler, M. J.; Pietron, J. J.; Murray, R. W.; Schaaff, T. G.; Khoury, J. T.; Alvarez, M. M.; Whetten, R. L. Gold Nanoelectrodes of Varied Size: Transition to Molecule-Like Charging. *Science* **1998**, *280* (5372), 2098–2101. <https://doi.org/10.1126/science.280.5372.2098>.
- (7) El-Sayed, I. H.; Huang, X. H.; El-Sayed, M. A. Surface Plasmon Resonance Scattering and Absorption of Anti-EGFR Antibody Conjugated Gold Nanoparticles in Cancer Diagnostics: Applications in Oral Cancer. *Nano Lett.* **2005**, *5*, 829.
- (8) Huang, X.; El-Sayed, I. H.; Qian, W.; El-Sayed, M. A. Cancer Cell Imaging and Photothermal Therapy in the Near-Infrared Region by Using Gold Nanorods. *J. Am. Chem. Soc.* **2006**, *128* (6), 2115–2120. <https://doi.org/10.1021/ja057254a>.
- (9) Bowman, M.-C.; Ballard, T. E.; Ackerson, C. J.; Feldheim, D. L.; Margolis, D. M.; Melander, C. Inhibition of HIV Fusion with Multivalent Gold Nanoparticles. *J. Am. Chem. Soc.* **2008**, *130* (22), 6896–6897. <https://doi.org/10.1021/ja710321g>.
- (10) Tsunoyama, H.; Sakurai, H.; Negishi, Y.; Tsukuda, T. Size-Specific Catalytic Activity of Polymer-Stabilized Gold Nanoclusters for Aerobic Alcohol Oxidation in Water. *J. Am. Chem. Soc.* **2005**, *127* (26), 9374–9375. <https://doi.org/10.1021/ja052161e>.
- (11) Han, J.; Liu, Y.; Guo, R. Facile Synthesis of Highly Stable Gold Nanoparticles and Their Unexpected Excellent Catalytic Activity for Suzuki–Miyaura Cross-Coupling Reaction in Water. *J. Am. Chem. Soc.* **2009**, *131* (6), 2060–2061. <https://doi.org/10.1021/ja808935n>.
- (12) Zhu, Y.; Qian, H.; Drake, B. A.; Jin, R. Atomically Precise Au₂₅(SR)₁₈ Nanoparticles as Catalysts for the Selective Hydrogenation of α,β -Unsaturated Ketones and Aldehydes. *Angewandte Chemie International Edition* **2010**, *49* (7), 1295–1298. <https://doi.org/10.1002/anie.200906249>.
- (13) Jadzinsky, P. D.; Calero, G.; Ackerson, C. J.; Bushnell, D. A.; Kornberg, R. D. Structure of a Thiol Monolayer-Protected Gold Nanoparticle at 1.1 Å Resolution. *Science* **2007**, *318* (5849), 430–433. <https://doi.org/10.1126/science.1148624>.
- (14) Zhu, M.; Aikens, C. M.; Hollander, F. J.; Schatz, G. C.; Jin, R. Correlating the Crystal Structure of A Thiol-Protected Au₂₅ Cluster and Optical Properties. *J. Am. Chem. Soc.* **2008**, *130* (18), 5883–5885. <https://doi.org/10.1021/ja801173r>.

- (15) Heaven, M. W.; Dass, A.; White, P. S.; Holt, K. M.; Murray, R. W. Crystal Structure of the Gold Nanoparticle $[\text{N}(\text{C}_8\text{H}_{17})_4][\text{Au}_{25}(\text{SCH}_2\text{CH}_2\text{Ph})_{18}]$. *J. Am. Chem. Soc.* **2008**, *130* (12), 3754–3755. <https://doi.org/10.1021/ja800561b>.
- (16) Akola, J.; Walter, M.; Whetten, R. L.; Häkkinen, H.; Grönbeck, H. On the Structure of Thiolate-Protected Au_{25} . *J. Am. Chem. Soc.* **2008**, *130* (12), 3756–3757. <https://doi.org/10.1021/ja800594p>.
- (17) Lopez-Acevedo, O.; Tsunoyama, H.; Tsukuda, T.; Häkkinen, H.; Aikens, C. M. Chirality and Electronic Structure of the Thiolate-Protected Au_{38} Nanocluster. *J. Am. Chem. Soc.* **2010**, *132* (23), 8210–8218. <https://doi.org/10.1021/ja102934q>.
- (18) Qian, H.; Eckenhoff, W. T.; Zhu, Y.; Pintauer, T.; Jin, R. Total Structure Determination of Thiolate-Protected Au_{38} Nanoparticles. *J. Am. Chem. Soc.* **2010**, *132* (24), 8280–8281. <https://doi.org/10.1021/ja103592z>.
- (19) Maiuri, M.; Garavelli, M.; Cerullo, G. Ultrafast Spectroscopy: State of the Art and Open Challenges. *J. Am. Chem. Soc.* **2020**, *142* (1), 3–15. <https://doi.org/10.1021/jacs.9b10533>.
- (20) Norrish, R. G. W.; Porter, G. Chemical Reactions Produced by Very High Light Intensities. *Nature* **1949**, *164* (4172), 658–658. <https://doi.org/10.1038/164658a0>.
- (21) Zewail, A. H. Femtochemistry: Atomic-Scale Dynamics of the Chemical Bond. *J. Phys. Chem. A* **2000**, *104* (24), 5660–5694. <https://doi.org/10.1021/jp001460h>.
- (22) Link, S.; El-Sayed, M. A.; Gregory Schaaff, T.; Whetten, R. L. Transition from Nanoparticle to Molecular Behavior: A Femtosecond Transient Absorption Study of a Size-Selected 28 Atom Gold Cluster. *Chemical Physics Letters* **2002**, *356* (3), 240–246. [https://doi.org/10.1016/S0009-2614\(02\)00306-8](https://doi.org/10.1016/S0009-2614(02)00306-8).
- (23) Miller, S. A.; Womick, J. M.; Parker, J. F.; Murray, R. W.; Moran, A. M. Femtosecond Relaxation Dynamics of $\text{Au}_{25}\text{L}_{18}^-$ Monolayer-Protected Clusters. *J. Phys. Chem. C* **2009**, *113* (22), 9440–9444. <https://doi.org/10.1021/jp9025046>.
- (24) Stoll, T.; Sgrò, E.; Jarrett, J. W.; Réhault, J.; Oriana, A.; Sala, L.; Branchi, F.; Cerullo, G.; Knappenberger, K. L. Superatom State-Resolved Dynamics of the $\text{Au}_{25}(\text{SC}_8\text{H}_9)_{18}^-$ Cluster from Two-Dimensional Electronic Spectroscopy. *J. Am. Chem. Soc.* **2016**, *138* (6), 1788–1791. <https://doi.org/10.1021/jacs.5b12621>.
- (25) Zhou, M.; Tian, S.; Zeng, C.; Sfeir, M. Y.; Wu, Z.; Jin, R. Ultrafast Relaxation Dynamics of $\text{Au}_{38}(\text{SC}_2\text{H}_4\text{Ph})_{24}$ Nanoclusters and Effects of Structural Isomerism. *J. Phys. Chem. C* **2017**, *121* (20), 10686–10693. <https://doi.org/10.1021/acs.jpcc.6b10360>.
- (26) Jeffries, W. R.; Wallace, J. L.; Knappenberger, K. L. Ultrafast Relaxation Dynamics of $\text{Au}_{38}(\text{SC}_6\text{H}_{13})_{24}$ Monolayer-Protected Clusters Resolved by Two-Dimensional Electronic Spectroscopy. *J. Chem. Phys.* **2021**, *155* (12), 124303. <https://doi.org/10.1063/5.0056832>.
- (27) Johnson, H. E.; Aikens, C. A. Electronic Structure and TDDFT Optical Absorption Spectra of Silver Nanorods. *J. Phys. Chem. A* **2009**, *113*, 4445.
- (28) Tancogne-Dejean, N.; Oliveira, M. J. T.; Andrade, X.; Appel, H.; Borca, C. H.; Le Breton, G.; Buchholz, F.; Castro, A.; Corni, S.; Correa, A. A.; De Giovannini, U.; Delgado, A.; Eich, F. G.; Flick, J.; Gil, G.; Gomez, A.; Helbig, N.; Hübener, H.; Jestädt, R.; Jorner-Somoza, J.; Larsen, A. H.; Lebedeva, I. V.; Lüders, M.; Marques, M. A. L.; Ohlmann, S. T.; Pipolo, S.; Rampp, M.; Rozzi, C. A.; Strubbe, D. A.; Sato, S. A.; Schäfer, C.; Theophilou, I.; Welden, A.; Rubio, A. Octopus, a Computational Framework for Exploring Light-Driven Phenomena and Quantum Dynamics in Extended and Finite Systems. *J. Chem. Phys.* **2020**, *152* (12), 124119. <https://doi.org/10.1063/1.5142502>.

- (29) Perdew, J. P.; Burke, K.; Ernzerhof, M. Generalized Gradient Approximation Made Simple. *Phys. Rev. Lett.* **1996**, *77*, 3865.
- (30) Troullier, N.; Martins, J. L. Efficient Pseudopotentials for Plane-Wave Calculations. *Phys. Rev. B* **1991**, *43* (3), 1993–2006. <https://doi.org/10.1103/PhysRevB.43.1993>.
- (31) Weerawardene, K. L. D. M.; Aikens, C. M. Comparison and Convergence of Optical Absorption Spectra of Noble Metal Nanoparticles Computed Using Linear-Response and Real-Time Time-Dependent Density Functional Theories. *Computational and Theoretical Chemistry* **2018**, *1146*, 27–36. <https://doi.org/10.1016/j.comptc.2018.11.005>.
- (32) Castro, A.; Marques, M. A. L.; Rubio, A. Propagators for the Time-Dependent Kohn–Sham Equations. *The Journal of Chemical Physics* **2004**, *121* (8), 3425–3433. <https://doi.org/10.1063/1.1774980>.
- (33) te Velde, G.; Bickelhaupt, F. M.; Baerends, E. J.; Fonseca Guerra, C.; van Gisbergen, S. J. A.; Snijders, J. G.; Ziegler, T. Chemistry with ADF. *J. Comput. Chem.* **2001**, *22* (9), 931–967. <https://doi.org/10.1002/jcc.1056>.
- (34) Van Lenthe, E.; Baerends, E. J. Optimized Slater-Type Basis Sets for the Elements 1-118. *J. Comput. Chem.* **2003**, *24* (9), 1142–1156. <https://doi.org/10.1002/jcc.10255>.
- (35) Lenthe, E. van; Baerends, E. J.; Snijders, J. G. Relativistic Regular Two-component Hamiltonians. *The Journal of Chemical Physics* **1993**, *99* (6), 4597–4610. <https://doi.org/10.1063/1.466059>.
- (36) van Lenthe, E.; Baerends, E. J.; Snijders, J. G. Relativistic Total Energy Using Regular Approximations. *The Journal of Chemical Physics* **1994**, *101* (11), 9783–9792. <https://doi.org/10.1063/1.467943>.
- (37) van Gisbergen, S. J. A.; Snijders, J. G.; Baerends, E. J. Implementation of Time-Dependent Density Functional Response Equations. *Computer Physics Communications* **1999**, *118* (2–3), 119–138. [https://doi.org/10.1016/S0010-4655\(99\)00187-3](https://doi.org/10.1016/S0010-4655(99)00187-3).
- (38) Momma, K.; Izumi, F. VESTA : A Three-Dimensional Visualization System for Electronic and Structural Analysis. *J Appl Crystallogr* **2008**, *41* (3), 653–658. <https://doi.org/10.1107/S0021889808012016>.
- (39) Krumland, J.; Valencia, A. M.; Pittalis, S.; Rozzi, C. A.; Cocchi, C. Understanding Real-Time Time-Dependent Density-Functional Theory Simulations of Ultrafast Laser-Induced Dynamics in Organic Molecules. *J. Chem. Phys.* **2020**, *153* (5), 054106. <https://doi.org/10.1063/5.0008194>.

Chapter 7 - Conclusion

The major findings from this work are pioneering in several areas of research. First of all, we find the origins of the red shifts and blue shifts of absorption peaks of silver homodimers and heterodimers. We found that the peak shifting is highly related to the direction of transition dipole moment. As the interparticle distance decreases, the red shift of the highest peak comes from contributions to the transition dipole moment with components along the interaction axis. In contrast, the blue shift of the peak as interparticle distance decreases mostly comes from the contributions of the transition dipole moment in the directions perpendicular to the interaction axis and shows up with a doubly degenerate feature. In another project, we found different electronic excitation transfer patterns for silver dimers at different interparticle distance. At long interparticle distance (from 50 to 20 Å), electronic excitation transfer from one nanoparticle to another nanoparticle will become more efficient as interparticle distance decreases. The electronic excitation transfer is the most efficient at 20 Å. At short distances, back-transfer was observed, which reduced the ability of the dimer and the first nanoparticle to accept energy from the incident electric field.

The transient absorption simulations of naphthalene exhibit collective effects in its excited state absorption spectra. Beating is observed may be a characteristic of these collective electronic effects, which may have important implications for the plasmonics field.

Ab initio transient absorption spectroscopy studies of atomically precise nanoclusters Au₂₅ and Au₃₈ open the door for exploring the time resolution of nanoclusters, which adds to previous knowledge about their space resolution and energy resolution. With the help of electronic structure and group theory, the transient absorption signals have been analyzed. The most obvious sub-hundred femtosecond dynamics was observed in the transient absorption spectrum with a 2.40 eV

pump energy for Au₂₅. The sub-hundred femtosecond dynamics is attributed to the transitions between d electron in gold. By comparing the spherical Au₂₅ and nanorod Au₃₈, different kinds of energy transfer were observed. In the sub-hundred femtosecond dynamics, the energy transfer among different dipole moments in the nanoclusters depends on the structure of nanocluster rather than the pump energy. Nanorod Au₃₈ confines the induced dipole moment in the pump direction, whereas the more isotropic Au₂₅ is more easily able to transfer the energy from the pump direction to the other two directions.

**Appendix A - Supporting Information for “TD-DFTB Study of
Optical Properties of Silver Nanoparticle Homodimers and
Heterodimers”**

Table A.1 Calculated absorption spectra for FCC silver nanoparticle dimers at 50 Å.

Distance (Å)	Energy (eV)	Fitting Energy (eV)
50	2.89582	2.89480
40	2.89530	2.89432
30	2.89419	2.89335
25	2.89307	2.89243
20	2.89136	2.89083
17	2.88921	2.88921
15	2.88736	2.88761
12	2.88295	2.88373
10	2.87843	2.87924
9	2.87536	2.87592
8	2.87141	2.87141
7	2.86643	2.86505

Table A.2 Comparison of Energy of Second Highest Peak (Peak 2) for Ag₁₁₆, A = 0.0545, b = 1.3521

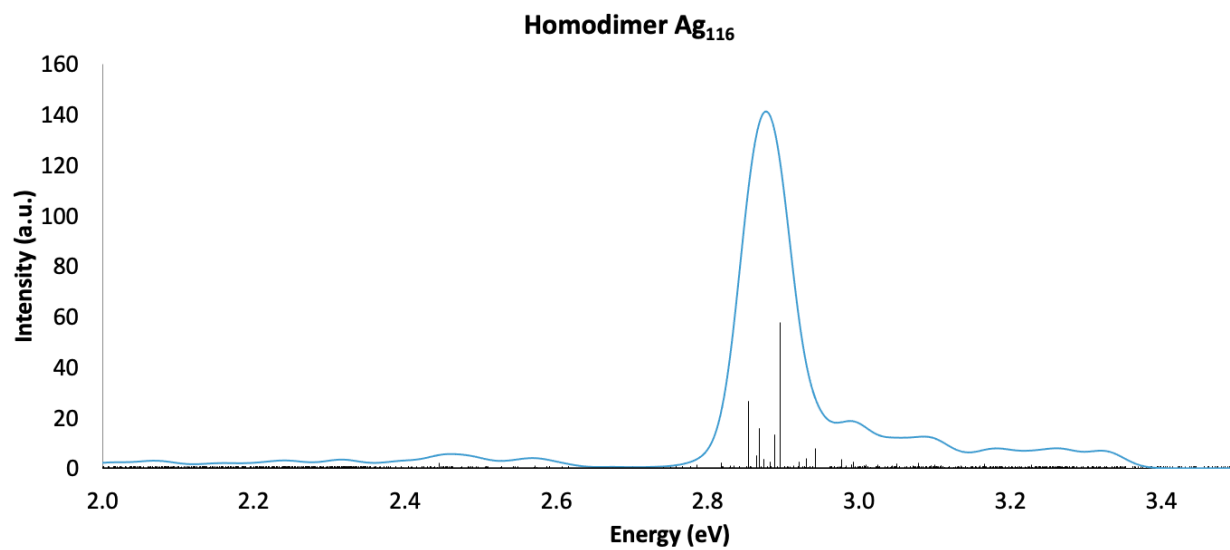
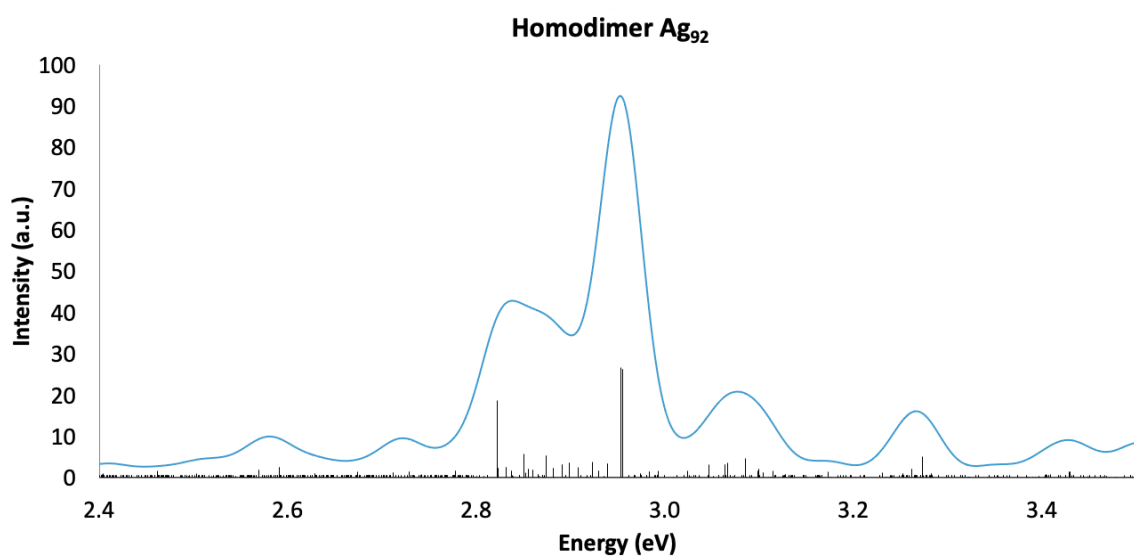
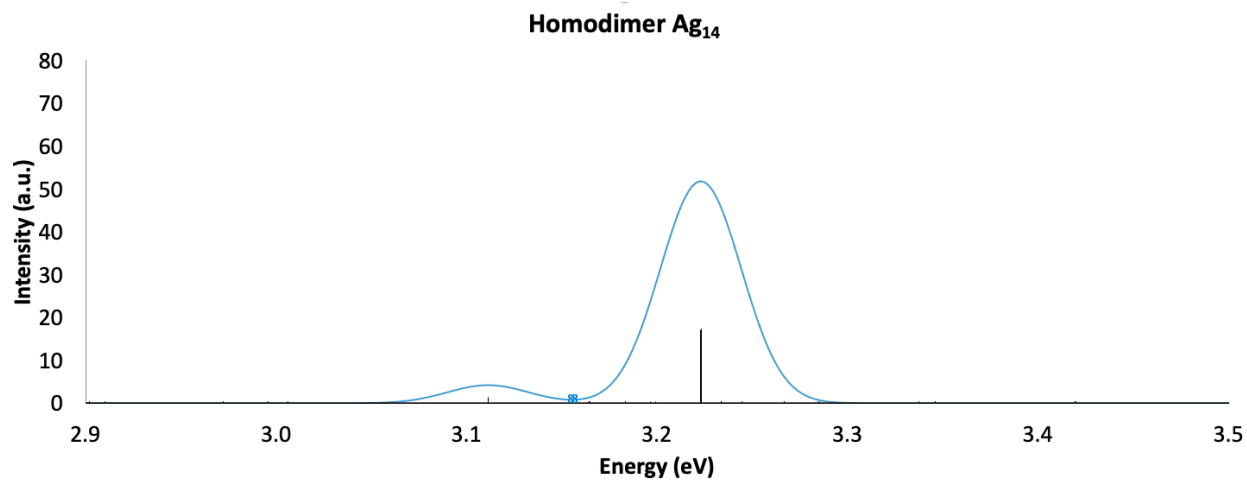
Distance (Å)	Energy (eV)	Fitting Energy (eV)
50	2.85367	2.85395
40	2.85378	2.85404
30	2.85403	2.85422
25	2.85427	2.85437
20	2.85462	2.85462
17	2.85495	2.85485
15	2.85522	2.85507
12	2.85577	2.85557
10	2.85620	2.85610
9	2.85647	2.85647
8	2.85675	2.85695
7	2.85702	2.85760

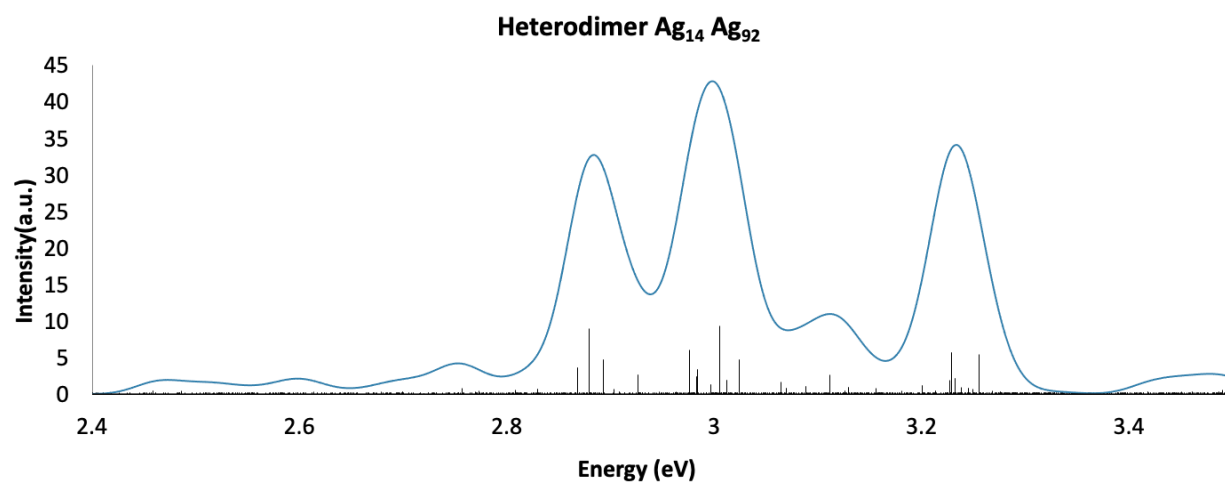
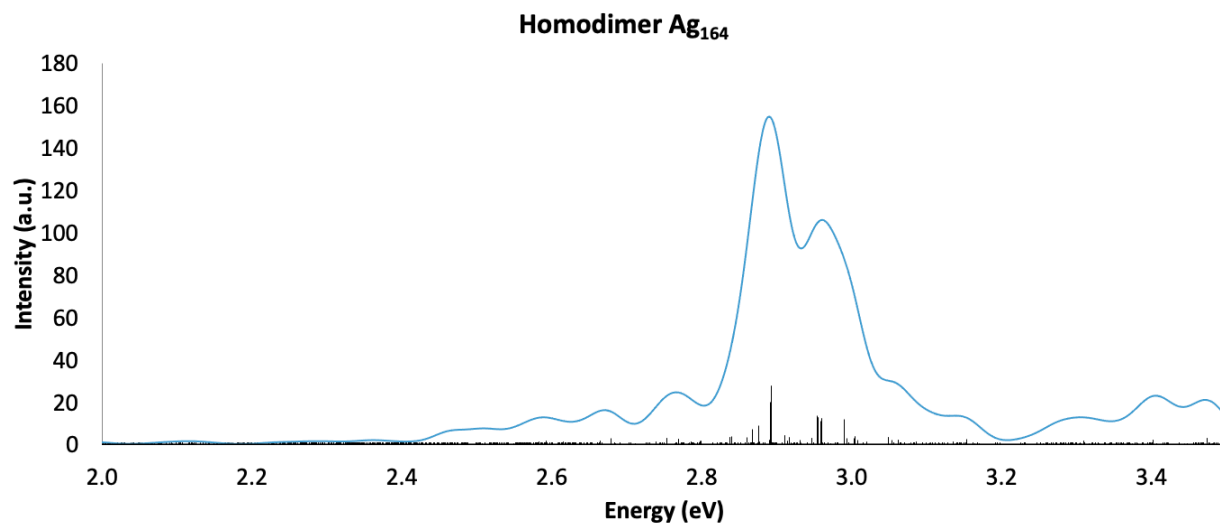
Table A.3 Comparison of Energy of Third Highest Peak (Peak 3) for Ag₁₁₆, A = 0.0696, b = 1.5119

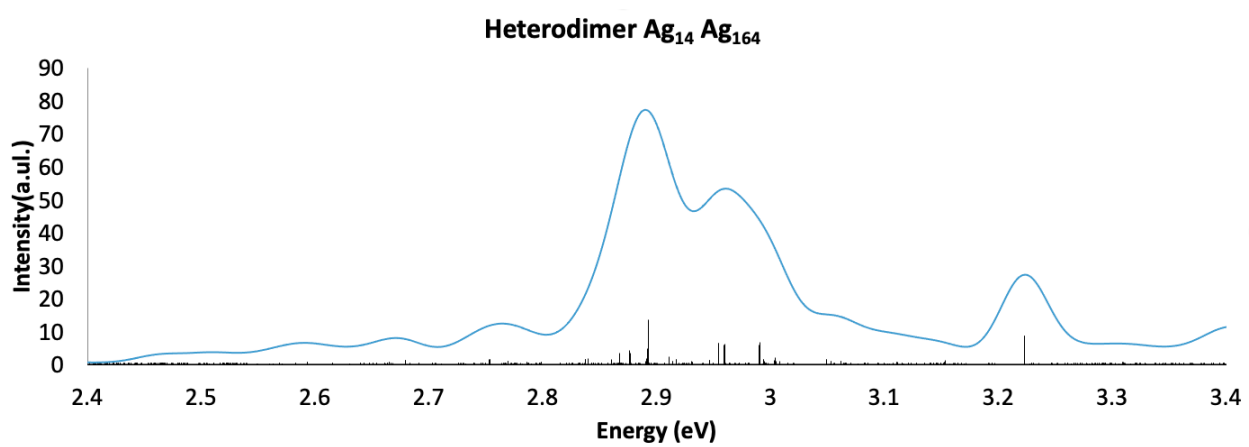
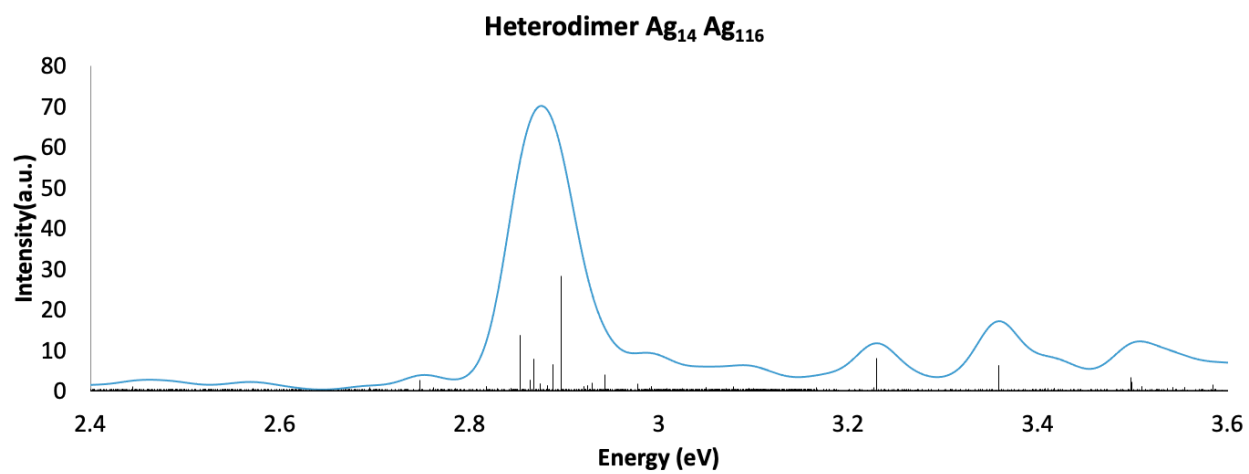
Distance (Å)	Energy (eV)	Fitting Energy (eV)
50	2.86798	2.86806
40	2.86804	2.86813
30	2.86820	2.86828
25	2.86837	2.86841
20	2.86864	2.86862
17	2.86894	2.86883
15	2.86918	2.86903
12	2.86978	2.86950
10	2.87030	2.87001
9	2.87062	2.87038
8	2.87098	2.87087
7	2.87136	2.87154

Table A.4 Comparison of Energy of Fourth Highest Peak (Peak 4) for Ag₁₁₆, A = 0.1500, b = 1.8516

Distance (Å)	Energy (eV)	Fitting Energy (eV)
50	2.88809	2.88798
40	2.88815	2.88803
30	2.88828	2.88815
25	2.88842	2.88826
20	2.88864	2.88845
17	2.88888	2.88866
15	2.88910	2.88887
12	2.88967	2.88938
10	2.89027	2.88998
9	2.89068	2.89043
8	2.89128	2.89106
7	2.89196	2.89195







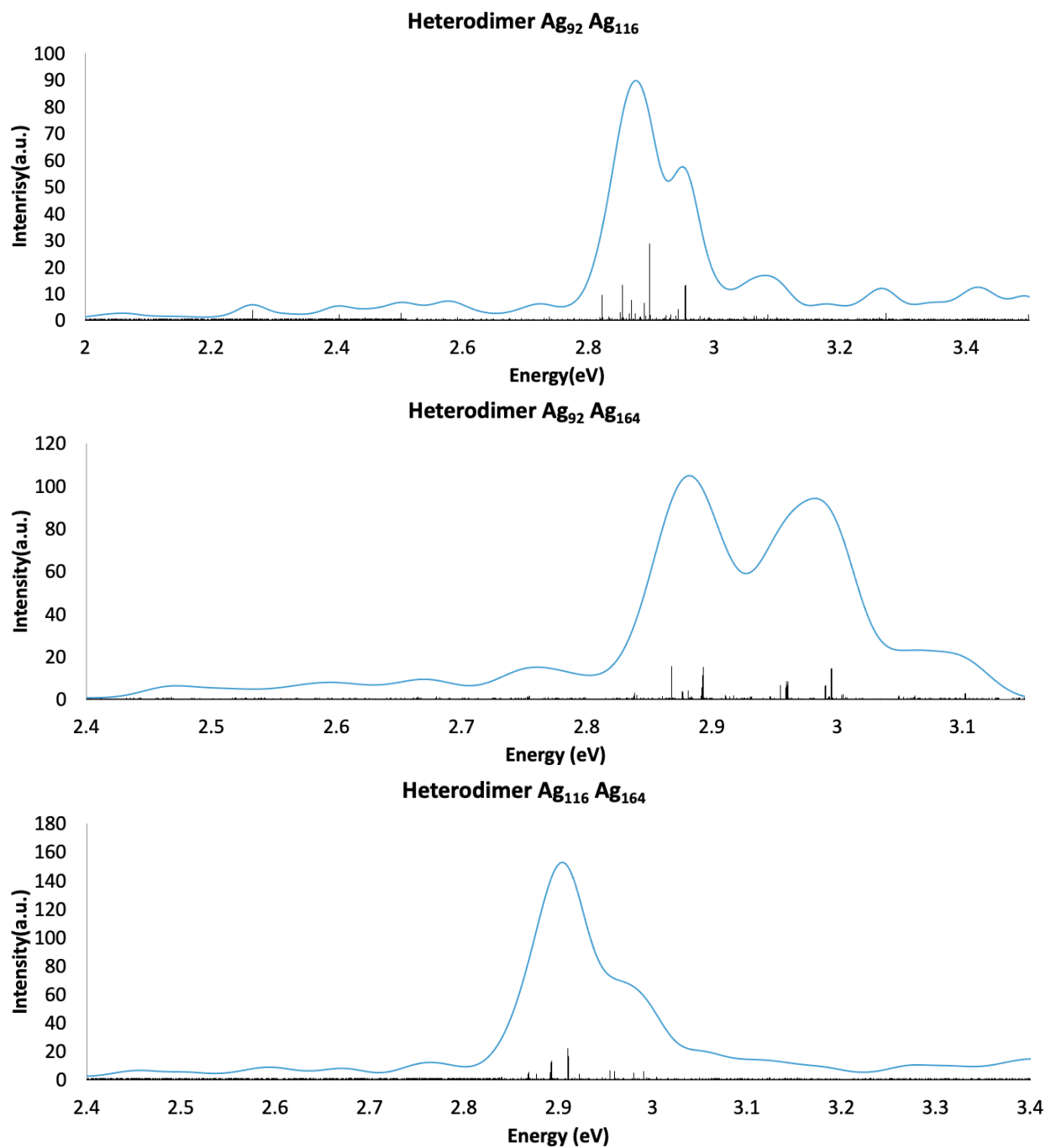


Figure A.1 Calculated absorption spectra for FCC silver nanoparticle dimers at 50 Å.

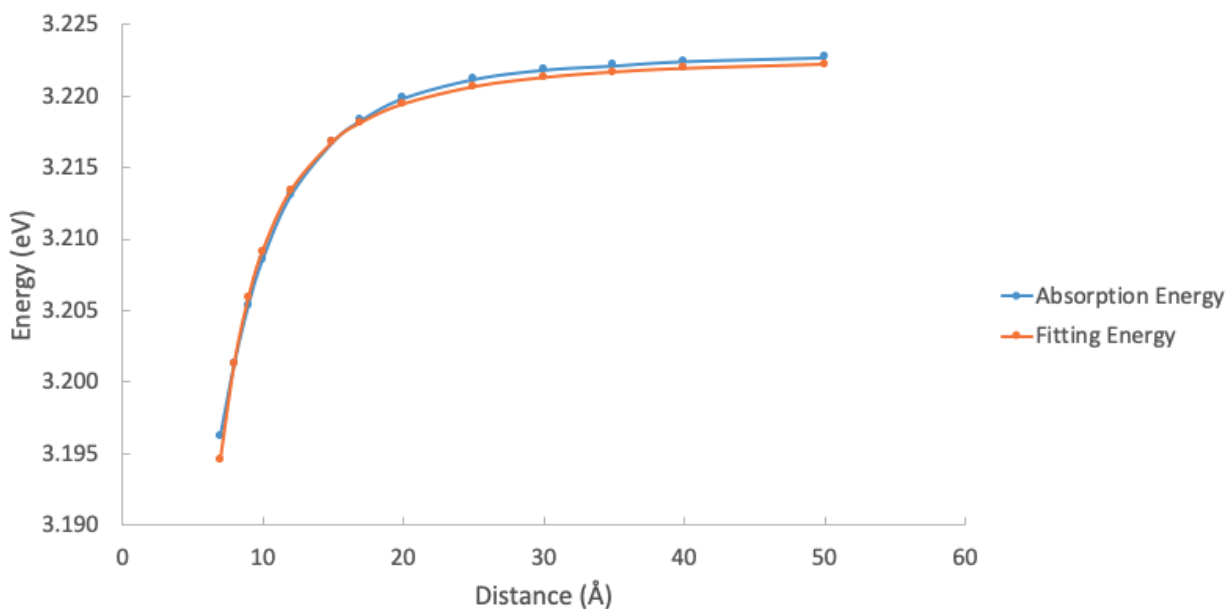


Figure A.2 Energy of highest peak (Peak 1) for different interparticle distance of dimer Ag_{14} , $A = -1.5030$, $b = 2.0440$

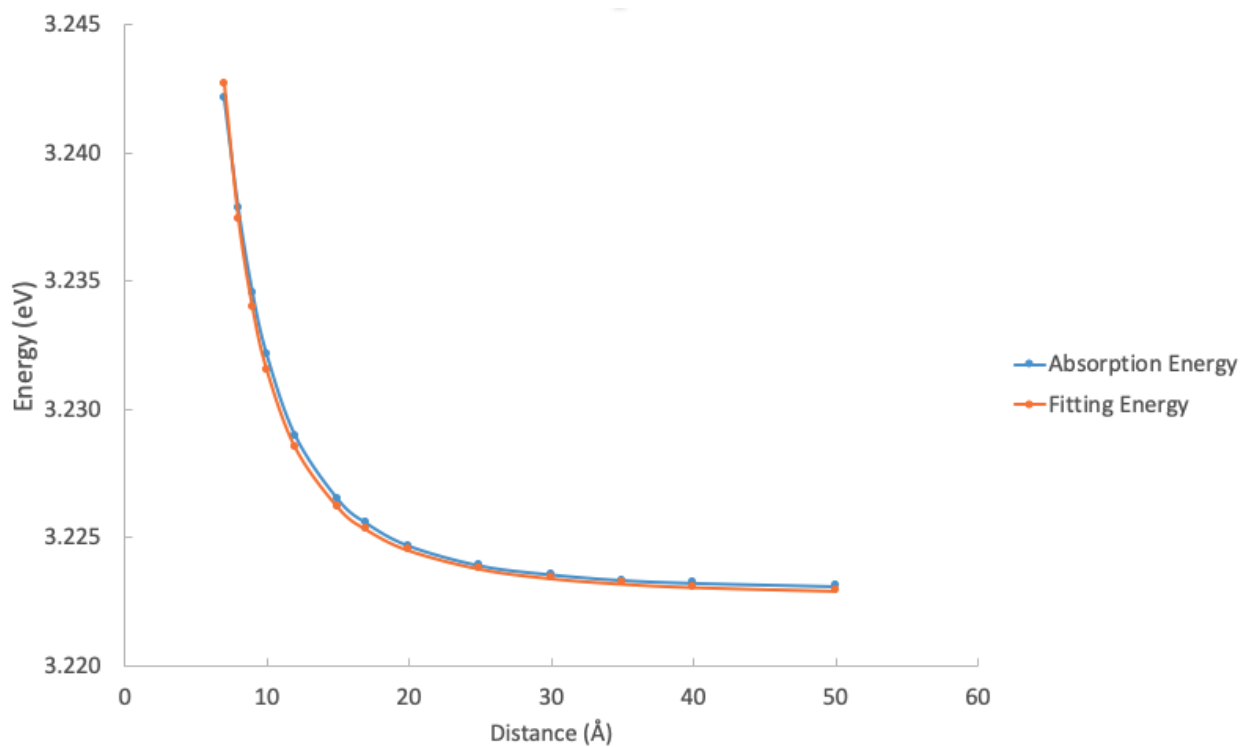


Figure A.3 Energy of second highest peak (Peak 2) for different interparticle distance of dimer Ag_{14} , $A = 1.7394$, $b = 2.2949$

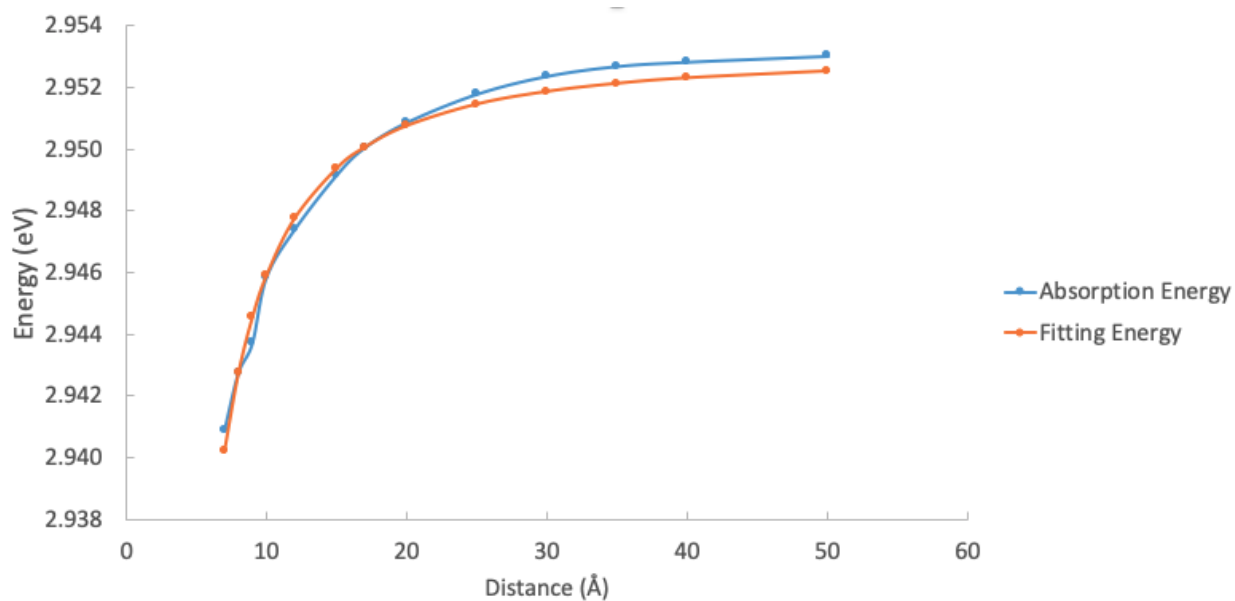


Figure A.4 Energy of highest peak (Peak 1) for different interparticle distance of dimer Ag_{92} , $A = -0.3172$, $b = 1.6486$

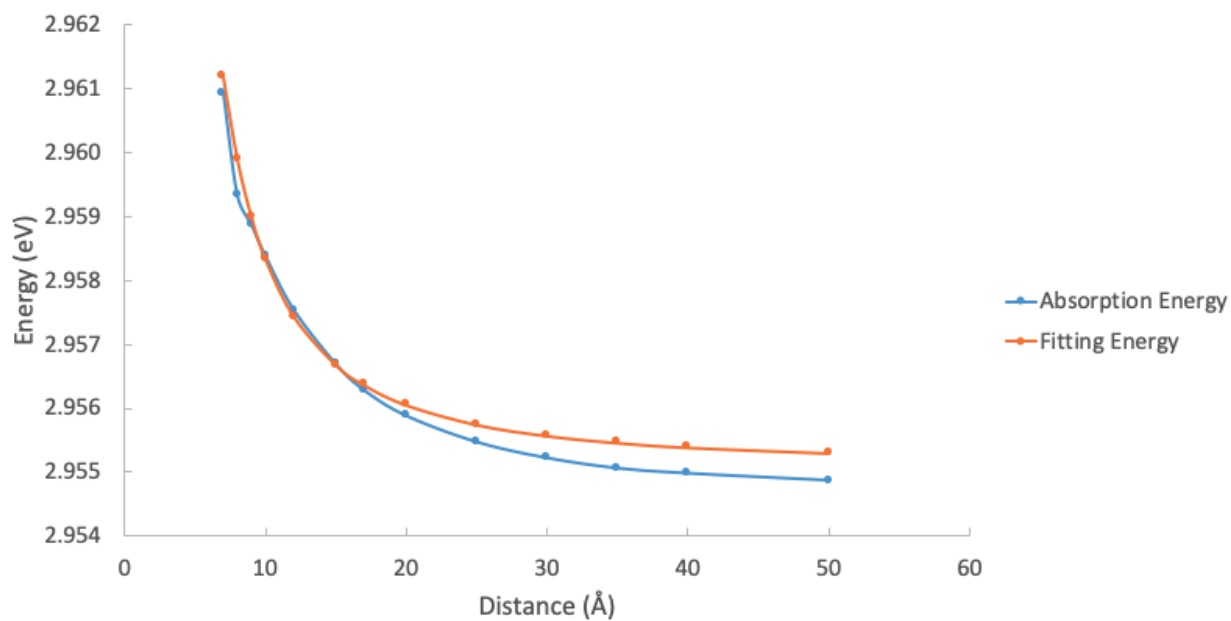


Figure A.5 Energy of second highest peak (Peak 2) for different interparticle distance of dimer Ag_{92} , $A = 0.1942$, $b = 1.7809$

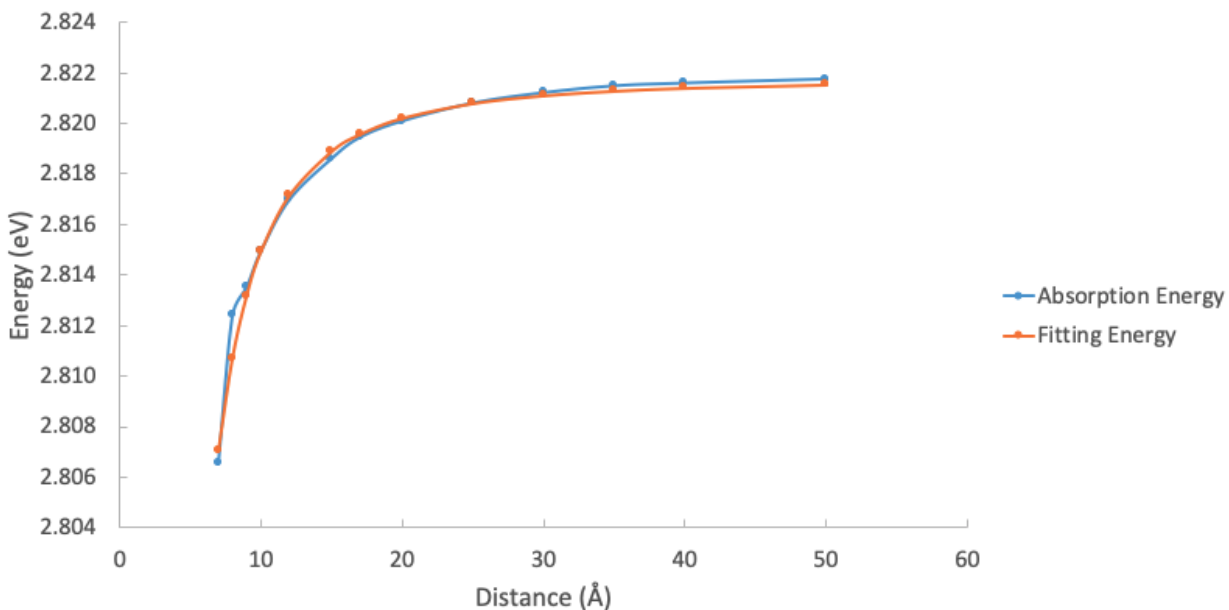


Figure A.6 Energy of third highest peak (Peak 3) for different interparticle distance of dimer Ag_{92} , $A = -0.9710$, $b = 2.1528$

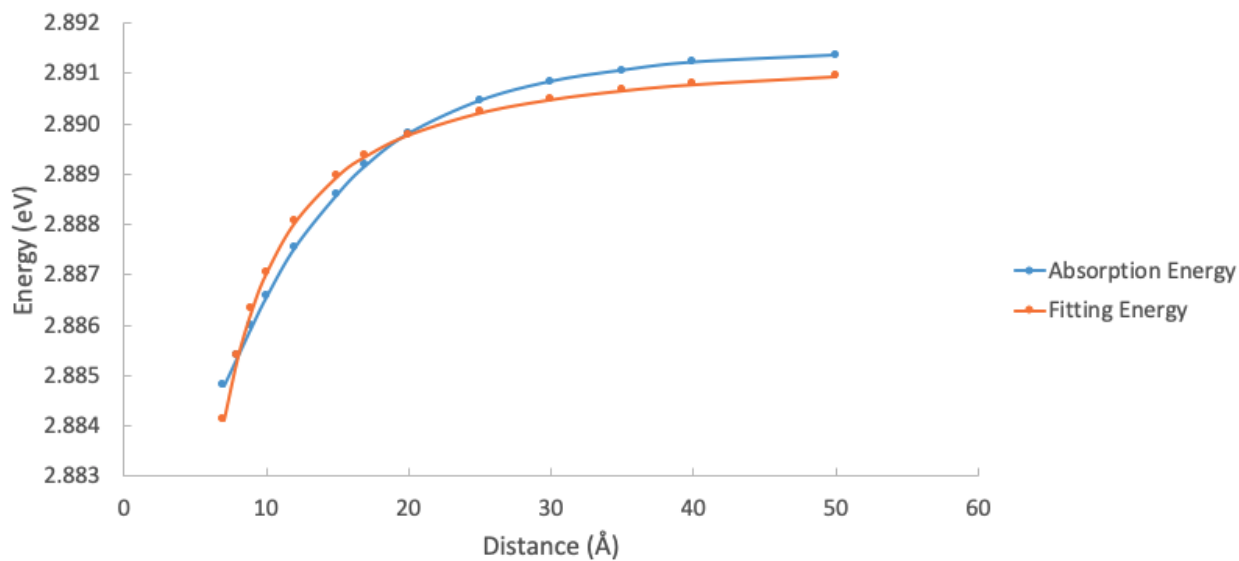


Figure A.7 Energy of highest peak (Peak 1) for different interparticle distance of dimer Ag_{164} , $A = -0.1228$, $b = 1.4550$

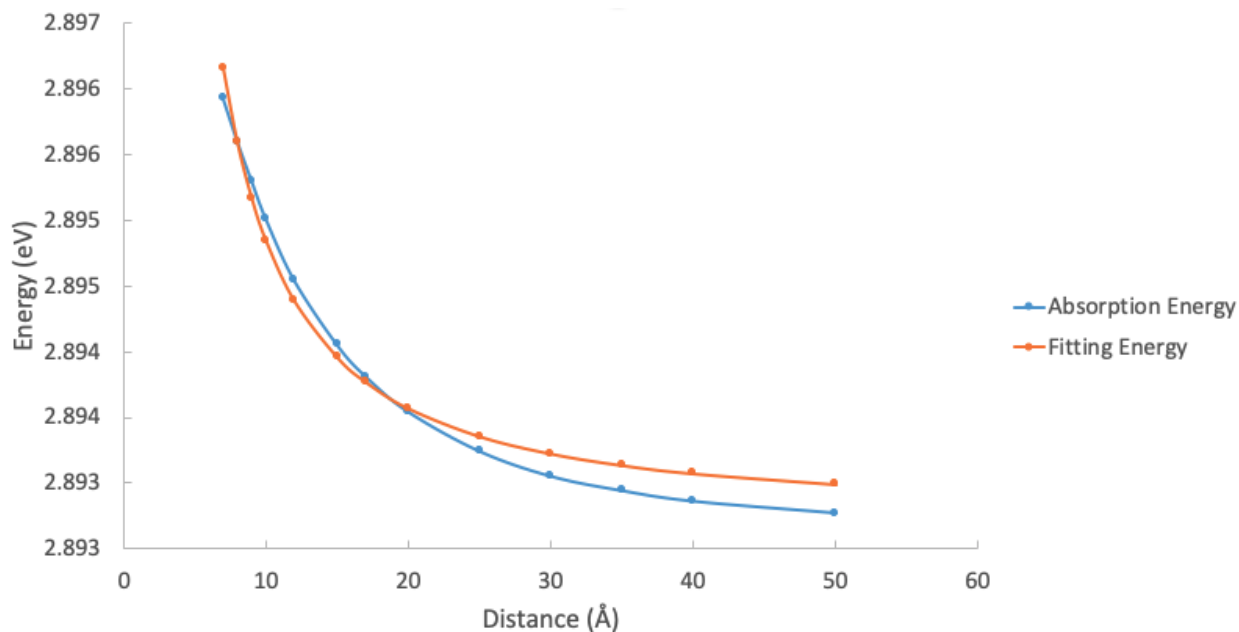


Figure A.8 Energy of second highest peak (Peak 2) for different interparticle distance of dimer Ag_{164} , $A = 0.0487$, $b = 1.3679$

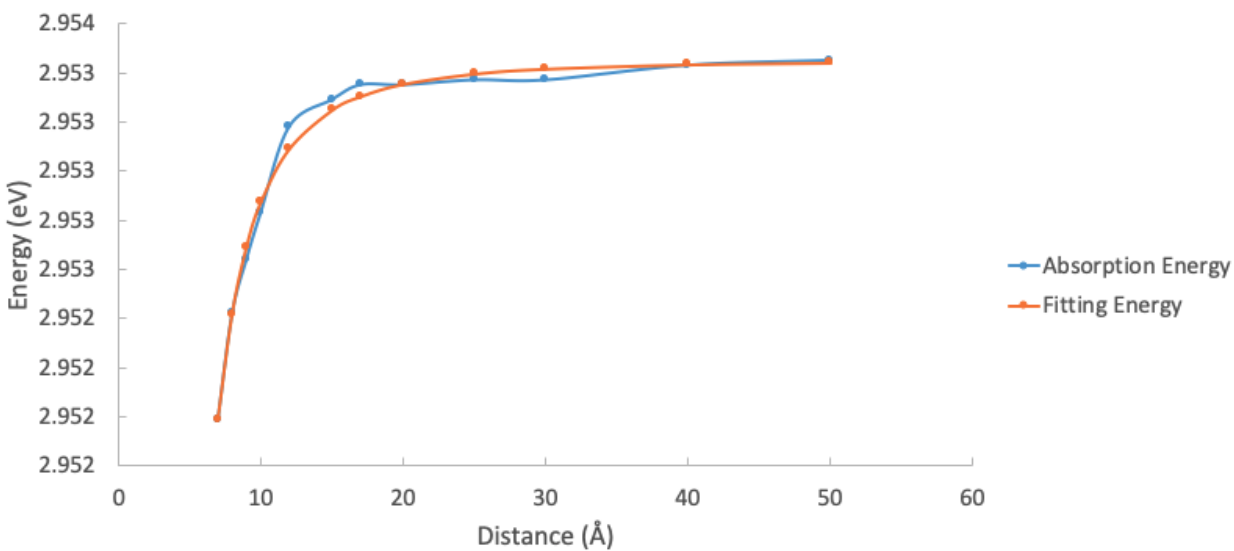


Figure A.9 Energy of highest peak (Peak 1) for different interparticle distance of heterodimer Ag_{14} , $A = -0.2276$, $b = 2.5947$

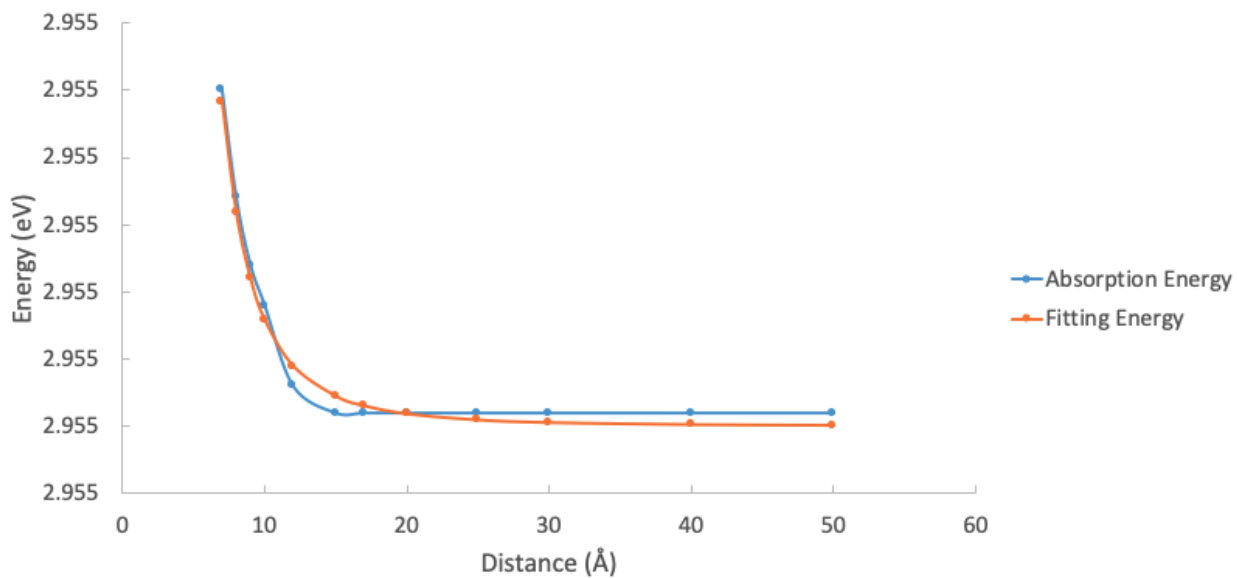


Figure A.10 Energy of second highest peak (Peak 2) for different interparticle distance of heterodimer $\text{Ag}_{14} \text{Ag}_{92}$, $A = 0.1069$, $b = 3.1307$

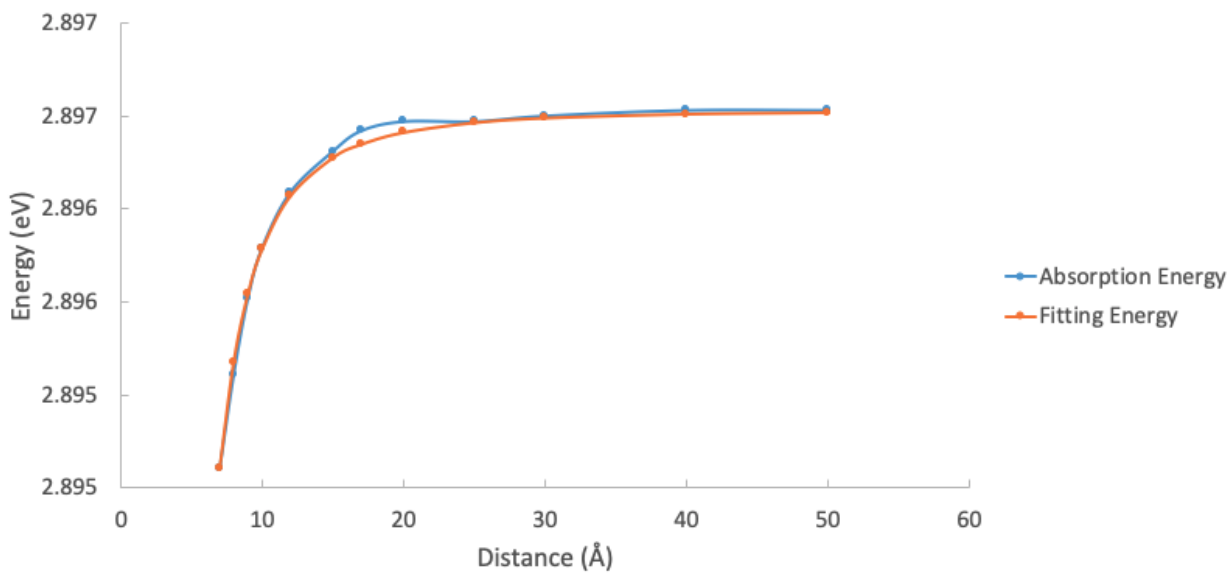


Figure A.11 Energy of highest peak (Peak 1) for different interparticle distance of heterodimer $\text{Ag}_{14} \text{Ag}_{116}$, $A = -0.3429$, $b = 2.6619$

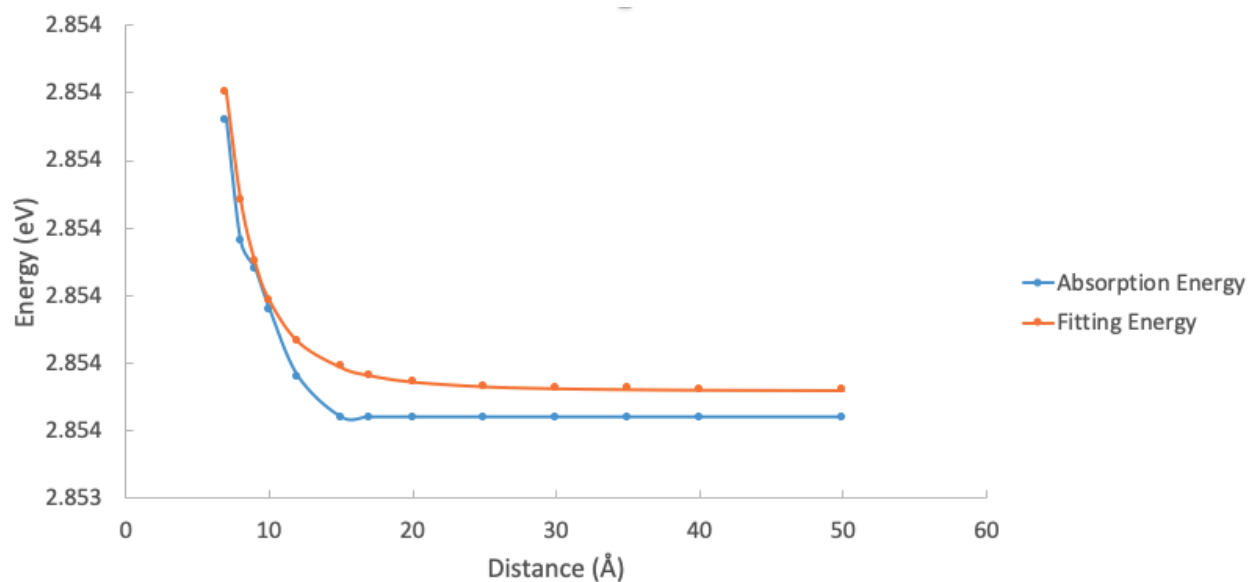


Figure A.12 Energy of second highest peak (Peak 2) for different interparticle distance of heterodimer $\text{Ag}_{14} \text{Ag}_{116}$, $A = 0.1467$, $b = 3.3415$

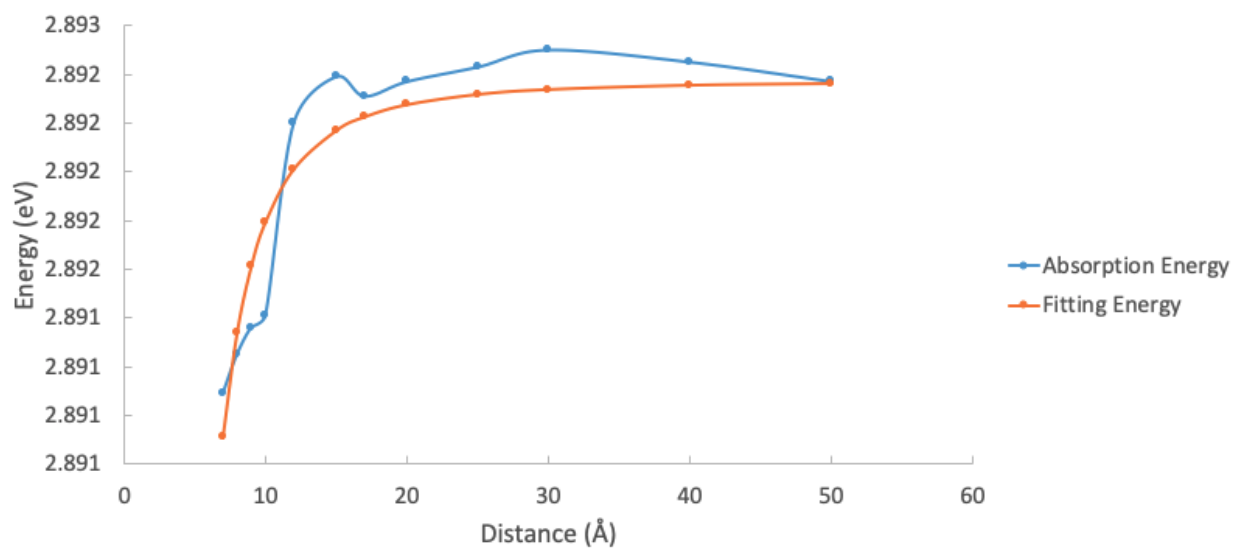


Figure A.13 Energy of highest peak (Peak 1) for different interparticle distance of heterodimer $\text{Ag}_{14} \text{Ag}_{164}$, $A = -0.2276$, $b = 2.5947$

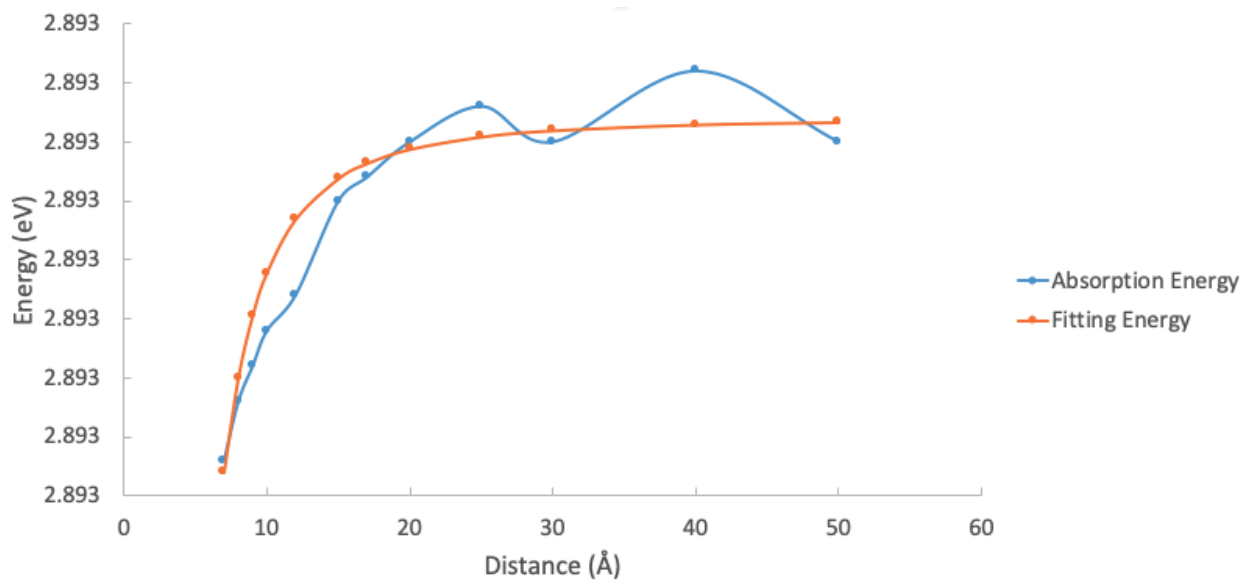


Figure A.14 Energy of second highest peak (Peak 2) for different interparticle distance of heterodimer $\text{Ag}_{14} \text{Ag}_{164}$, $A = -0.0278$, $b = 2.3269$

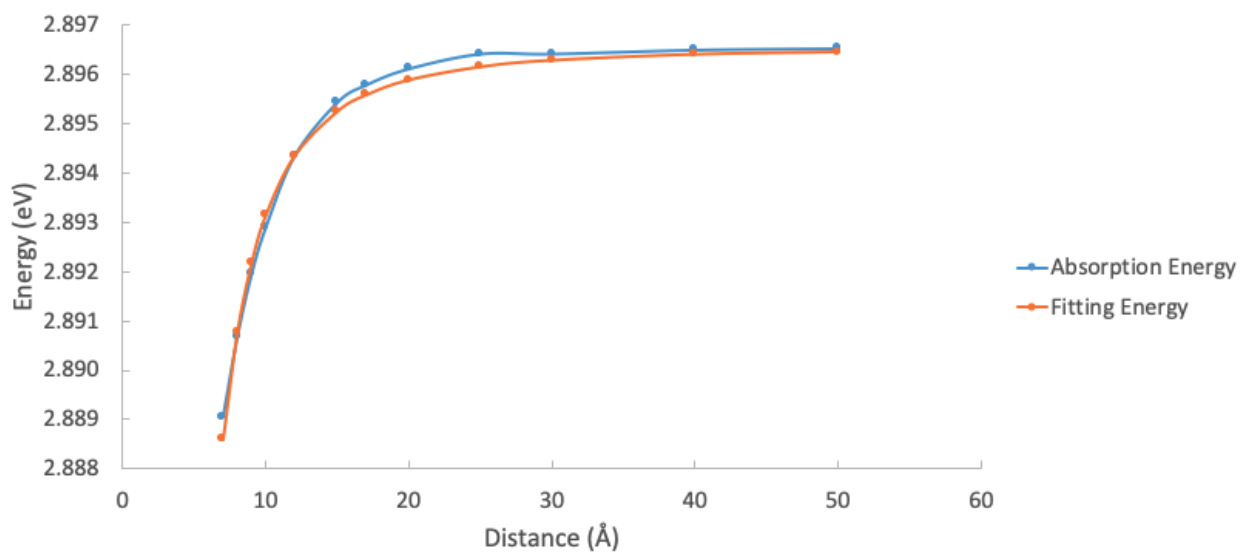


Figure A.15 Energy of highest peak (Peak 1) for different interparticle distance of heterodimer $\text{Ag}_{92} \text{Ag}_{116}$, $A = -0.8416$, $b = 2.3968$

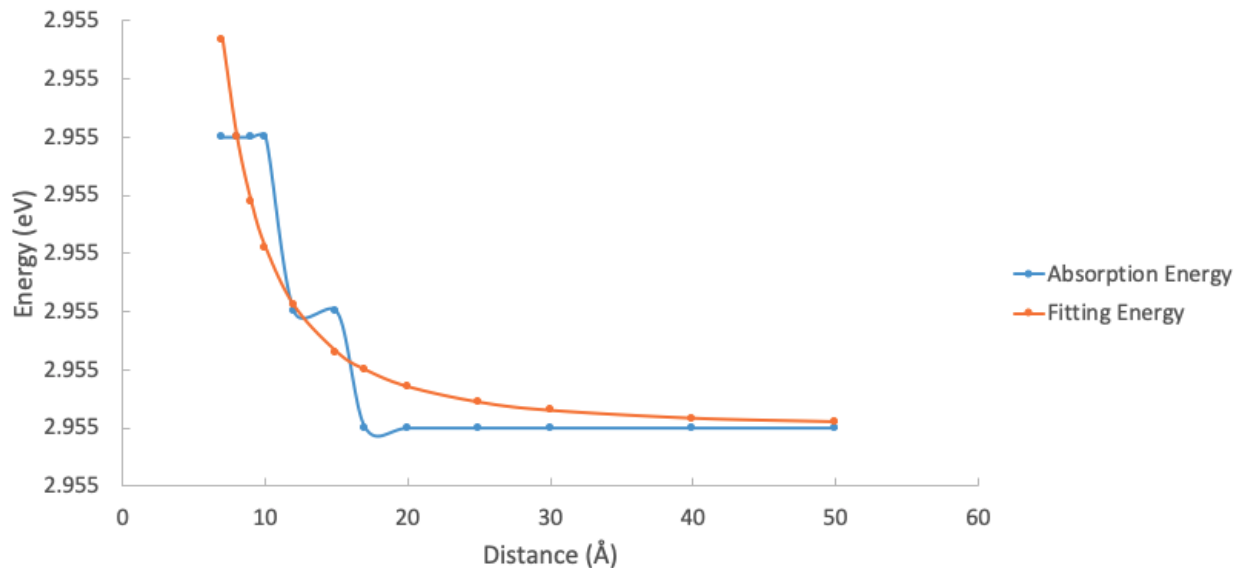


Figure A.16 Energy of second highest peak (Peak 2) for different interparticle distance of heterodimer $\text{Ag}_{92}\text{Ag}_{116}$, $A = 0.0043$, $b = 2.1439$

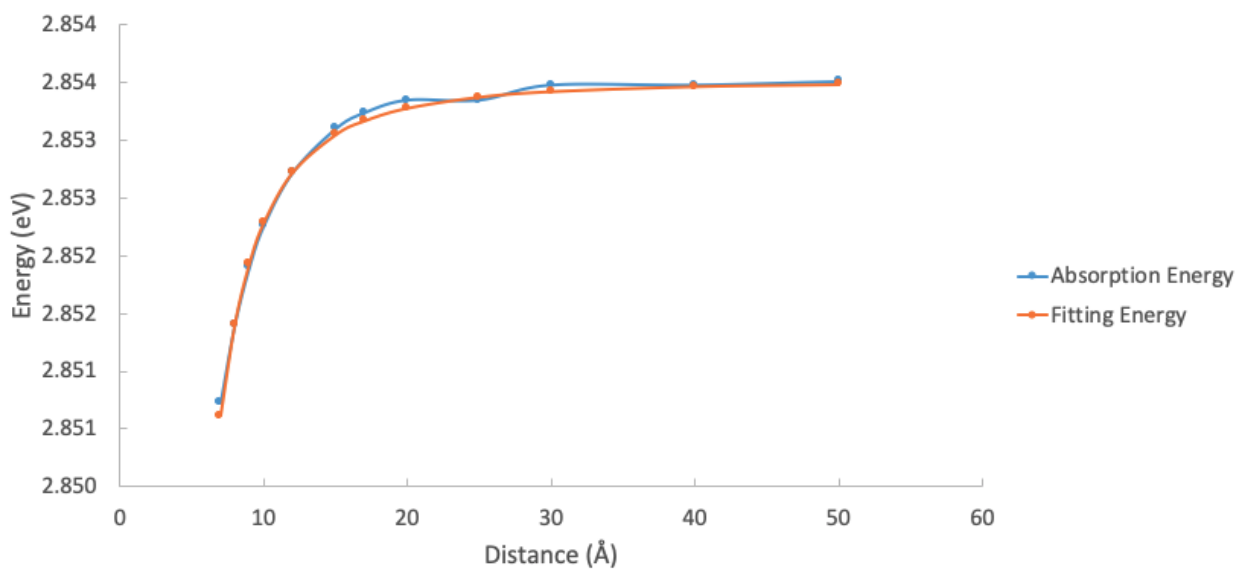


Figure A.17 Energy of third highest peak (Peak 3) for different interparticle distance of heterodimer $\text{Ag}_{92}\text{Ag}_{116}$, $A = -0.3142$, $b = 2.4084$

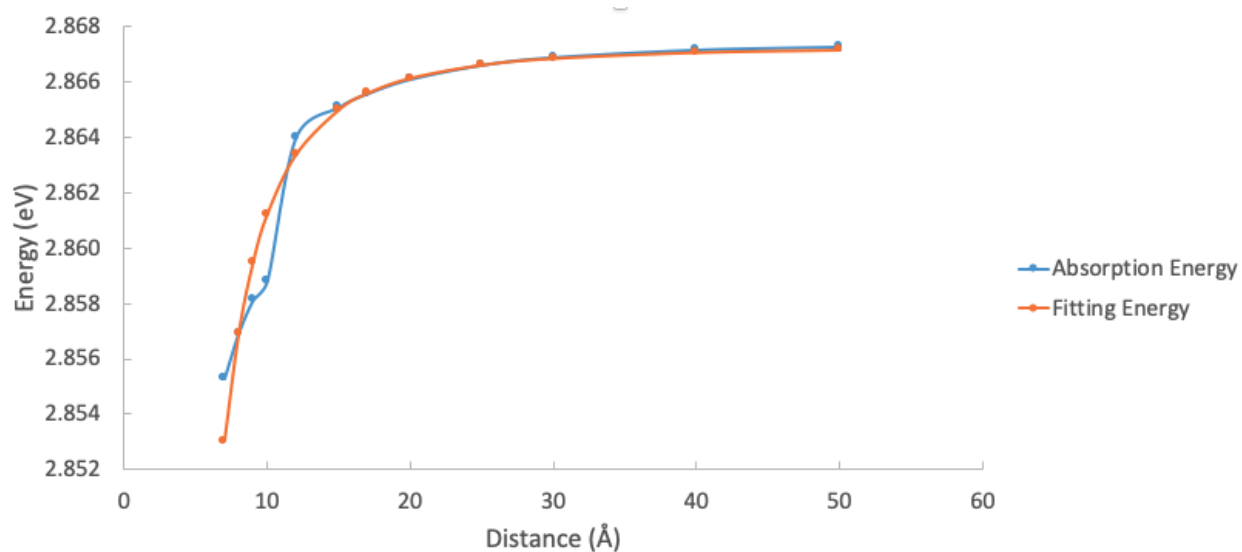


Figure A.18 Energy of highest peak (Peak 1) for different interparticle distance of heterodimer $\text{Ag}_{92} \text{Ag}_{164}$, $A = -1.5342$, $b = 2.4044$

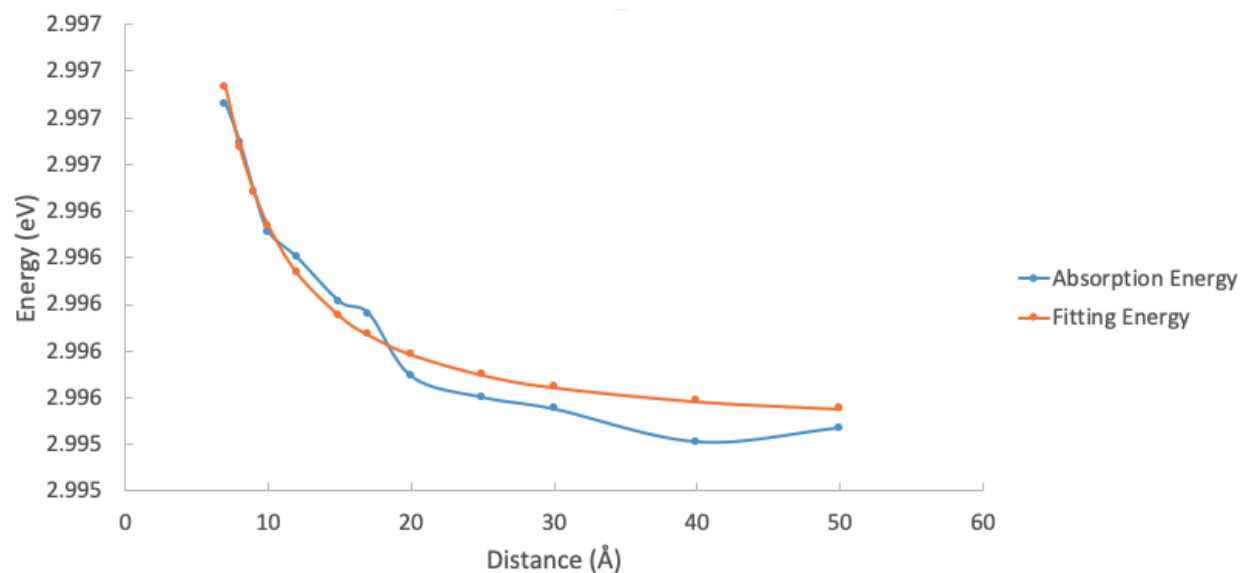


Figure A.19 Energy of second highest peak (Peak 2) for different interparticle distance of heterodimer $\text{Ag}_{92} \text{Ag}_{164}$, $A = 0.0249$, $b = 1.4583$

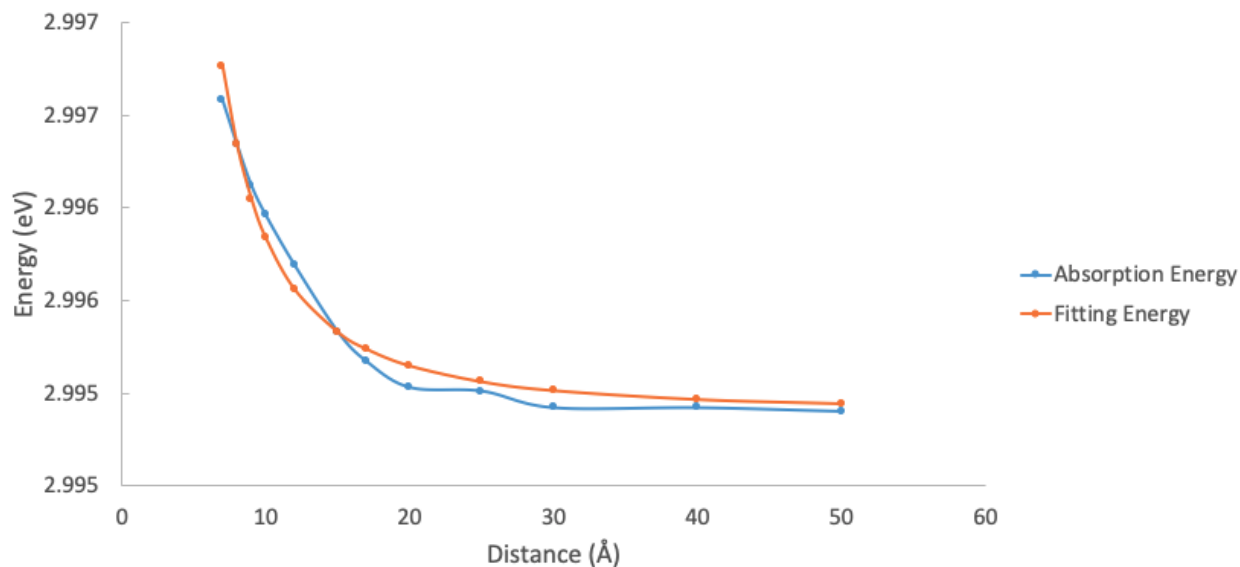


Figure A.20 Energy of third highest peak (Peak 3) for different interparticle distance of heterodimer $\text{Ag}_{92} \text{Ag}_{164}$, $A = 0.0789$, $b = 1.9251$

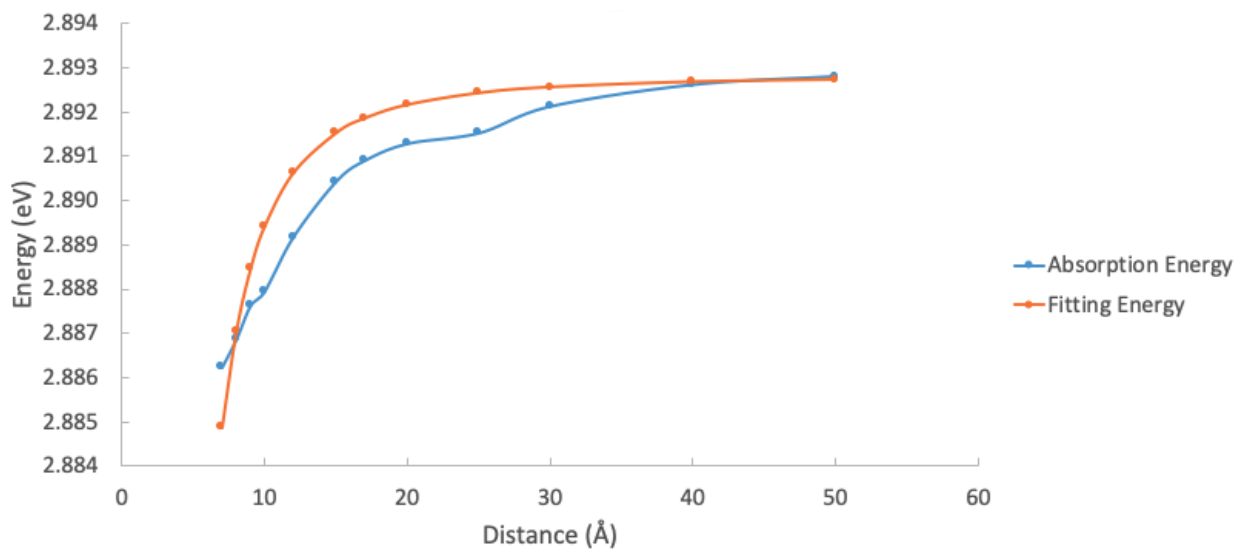


Figure A.21 Energy of highest peak (Peak 1) for different interparticle distance of heterodimer $\text{Ag}_{116} \text{Ag}_{164}$, $A = -0.8416$, $b = 2.3968$

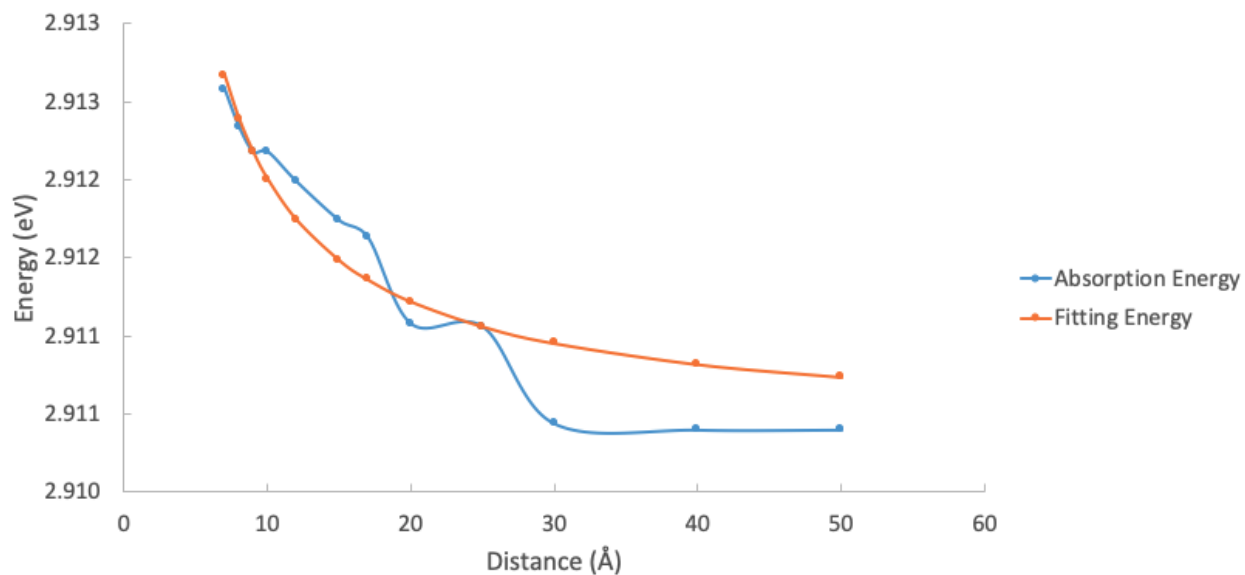


Figure A.22 Energy of second highest peak (Peak 2) for different interparticle distance of heterodimer $\text{Ag}_{116}\text{Ag}_{164}$, $A = 0.0149$, $b = 0.9688$

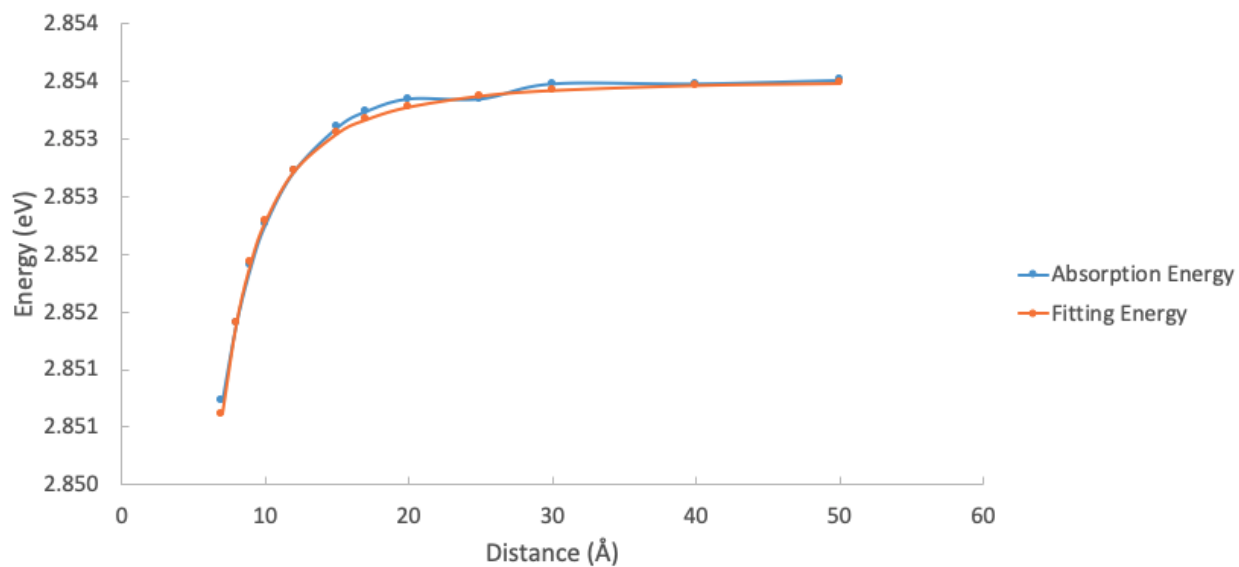


Figure A.23 Energy of third highest peak (Peak 3) for different interparticle distance of heterodimer $\text{Ag}_{116}\text{Ag}_{164}$, $A = -0.3142$, $b = 2.4084$

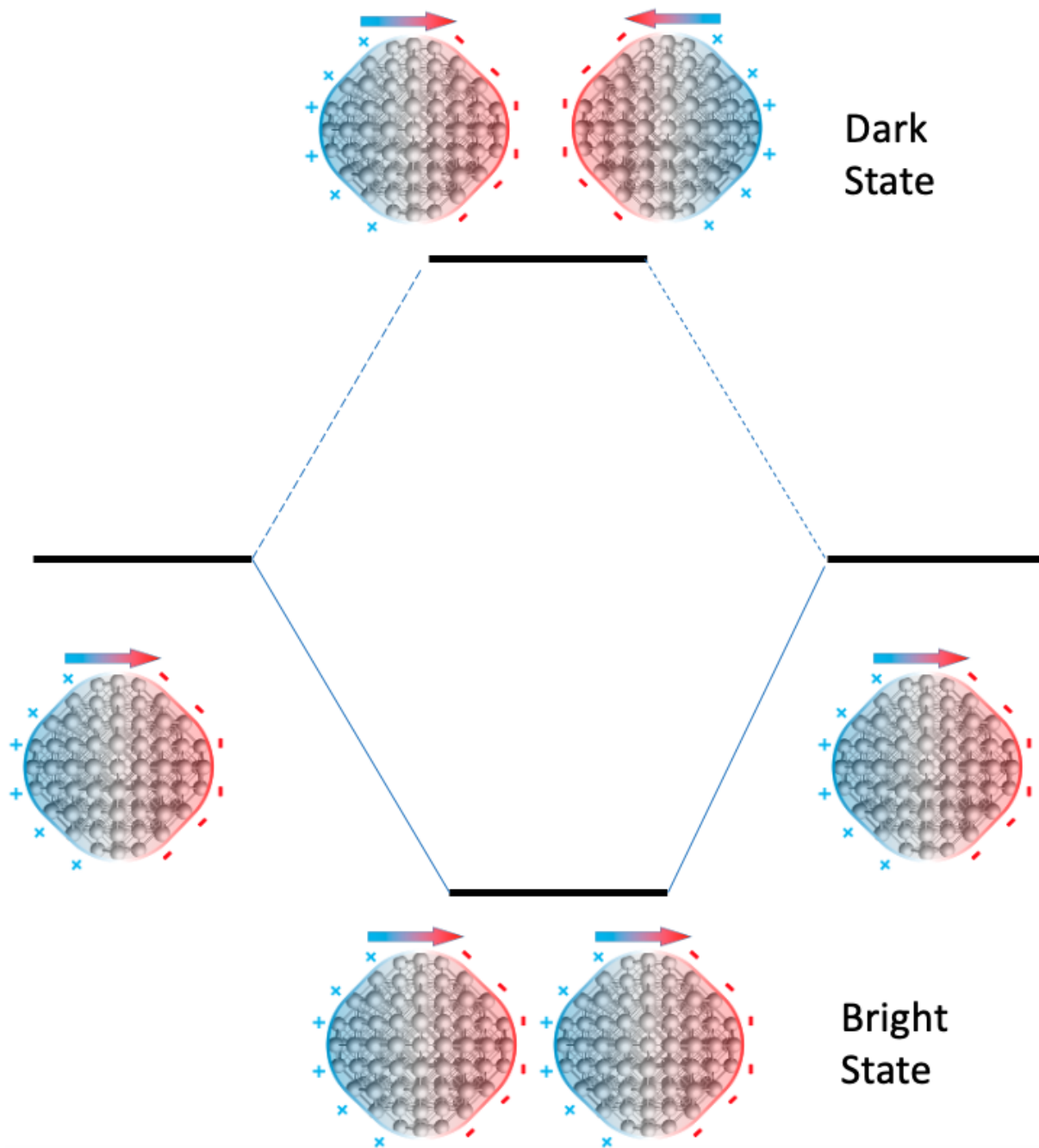


Figure A.24 Plasmon interaction diagram that causes a red-shift in the absorption peak upon decreasing the distance between monomers.

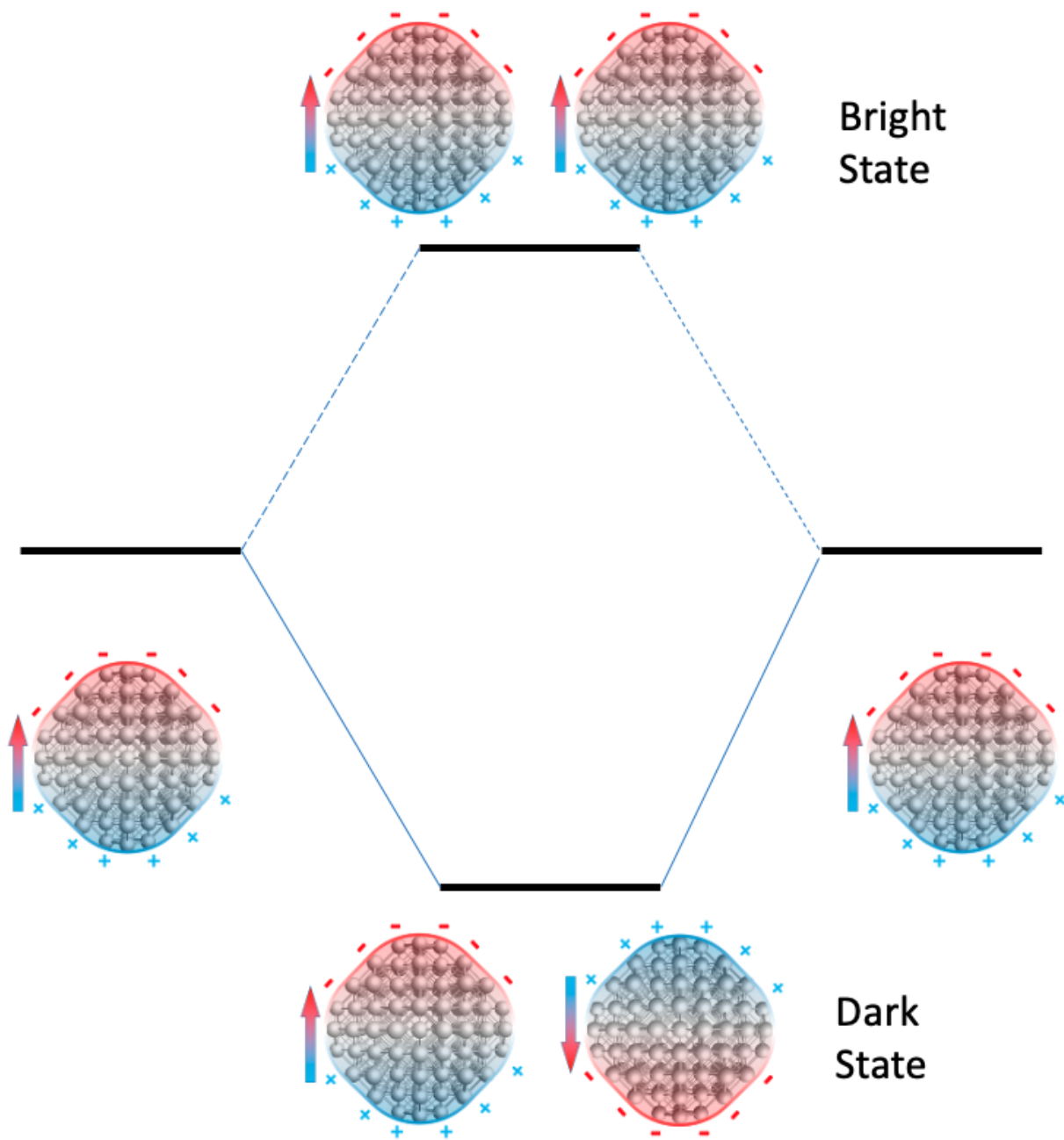


Figure A.25 Plasmon interaction diagram that causes a blue-shift in the absorption peak upon decreasing the distance between monomers.

Coordinate of Ag₁₄

Ag -2.04264998435974	-2.04264998435974	-2.04264998435974
Ag -2.04264998435974	-2.04264998435974	2.04264998435974
Ag -2.04264998435974	2.04264998435974	-2.04264998435974
Ag -2.04264998435974	2.04264998435974	2.04264998435974
Ag 2.04264998435974	-2.04264998435974	-2.04264998435974
Ag 2.04264998435974	-2.04264998435974	2.04264998435974
Ag 2.04264998435974	2.04264998435974	-2.04264998435974
Ag 2.04264998435974	2.04264998435974	2.04264998435974
Ag -2.04264998435974	0.00000000000000	0.00000000000000
Ag 2.04264998435974	0.00000000000000	0.00000000000000
Ag 0.00000000000000	-2.04264998435974	0.00000000000000
Ag 0.00000000000000	2.04264998435974	0.00000000000000
Ag 0.00000000000000	0.00000000000000	-2.04264998435974
Ag 0.00000000000000	0.00000000000000	2.04264998435974

Coordinate of Ag₉₂

Ag	-6.12794995307922	-2.04264998435974	-2.04264998435974
Ag	-6.12794995307922	-2.04264998435974	2.04264998435974
Ag	-6.12794995307922	2.04264998435974	-2.04264998435974
Ag	-6.12794995307922	2.04264998435974	2.04264998435974
Ag	-2.04264998435974	-6.12794995307922	-2.04264998435974
Ag	-2.04264998435974	-6.12794995307922	2.04264998435974
Ag	-2.04264998435974	-2.04264998435974	-6.12794995307922
Ag	-2.04264998435974	-2.04264998435974	-2.04264998435974
Ag	-2.04264998435974	-2.04264998435974	2.04264998435974
Ag	-2.04264998435974	-2.04264998435974	6.12794995307922
Ag	-2.04264998435974	2.04264998435974	-6.12794995307922
Ag	-2.04264998435974	2.04264998435974	-2.04264998435974
Ag	-2.04264998435974	2.04264998435974	2.04264998435974
Ag	-2.04264998435974	2.04264998435974	6.12794995307922
Ag	-2.04264998435974	6.12794995307922	-2.04264998435974
Ag	-2.04264998435974	6.12794995307922	2.04264998435974
Ag	2.04264998435974	-6.12794995307922	-2.04264998435974
Ag	2.04264998435974	-6.12794995307922	2.04264998435974
Ag	2.04264998435974	-2.04264998435974	-6.12794995307922
Ag	2.04264998435974	-2.04264998435974	-2.04264998435974
Ag	2.04264998435974	-2.04264998435974	2.04264998435974
Ag	2.04264998435974	-2.04264998435974	6.12794995307922
Ag	2.04264998435974	2.04264998435974	-6.12794995307922
Ag	2.04264998435974	2.04264998435974	-2.04264998435974
Ag	2.04264998435974	2.04264998435974	2.04264998435974
Ag	2.04264998435974	2.04264998435974	6.12794995307922
Ag	2.04264998435974	6.12794995307922	-2.04264998435974
Ag	2.04264998435974	6.12794995307922	2.04264998435974
Ag	6.12794995307922	-2.04264998435974	-2.04264998435974

Ag	6.12794995307922	-2.04264998435974	2.04264998435974
Ag	6.12794995307922	2.04264998435974	-2.04264998435974
Ag	6.12794995307922	2.04264998435974	2.04264998435974
Ag	-6.12794995307922	0.00000000000000	0.00000000000000
Ag	-2.04264998435974	-4.08529996871948	-4.08529996871948
Ag	-2.04264998435974	-4.08529996871948	0.00000000000000
Ag	-2.04264998435974	-4.08529996871948	4.08529996871948
Ag	-2.04264998435974	0.00000000000000	-4.08529996871948
Ag	-2.04264998435974	0.00000000000000	0.00000000000000
Ag	-2.04264998435974	0.00000000000000	4.08529996871948
Ag	-2.04264998435974	4.08529996871948	-4.08529996871948
Ag	-2.04264998435974	4.08529996871948	0.00000000000000
Ag	-2.04264998435974	4.08529996871948	4.08529996871948
Ag	2.04264998435974	-4.08529996871948	-4.08529996871948
Ag	2.04264998435974	-4.08529996871948	0.00000000000000
Ag	2.04264998435974	-4.08529996871948	4.08529996871948
Ag	2.04264998435974	0.00000000000000	-4.08529996871948
Ag	2.04264998435974	0.00000000000000	0.00000000000000
Ag	2.04264998435974	0.00000000000000	4.08529996871948
Ag	2.04264998435974	4.08529996871948	-4.08529996871948
Ag	2.04264998435974	4.08529996871948	0.00000000000000
Ag	2.04264998435974	4.08529996871948	4.08529996871948
Ag	6.12794995307922	0.00000000000000	0.00000000000000
Ag	0.00000000000000	-6.12794995307922	0.00000000000000
Ag	-4.08529996871948	-2.04264998435974	-4.08529996871948
Ag	0.00000000000000	-2.04264998435974	-4.08529996871948
Ag	4.08529996871948	-2.04264998435974	-4.08529996871948
Ag	-4.08529996871948	-2.04264998435974	0.00000000000000
Ag	0.00000000000000	-2.04264998435974	0.00000000000000
Ag	4.08529996871948	-2.04264998435974	0.00000000000000
Ag	-4.08529996871948	-2.04264998435974	4.08529996871948

Ag	0.000000000000000	-2.04264998435974	4.08529996871948
Ag	4.08529996871948	-2.04264998435974	4.08529996871948
Ag	-4.08529996871948	2.04264998435974	-4.08529996871948
Ag	0.000000000000000	2.04264998435974	-4.08529996871948
Ag	4.08529996871948	2.04264998435974	-4.08529996871948
Ag	-4.08529996871948	2.04264998435974	0.000000000000000
Ag	0.000000000000000	2.04264998435974	0.000000000000000
Ag	4.08529996871948	2.04264998435974	0.000000000000000
Ag	-4.08529996871948	2.04264998435974	4.08529996871948
Ag	0.000000000000000	2.04264998435974	4.08529996871948
Ag	4.08529996871948	2.04264998435974	4.08529996871948
Ag	0.000000000000000	6.12794995307922	0.000000000000000
Ag	0.000000000000000	0.000000000000000	-6.12794995307922
Ag	-4.08529996871948	-4.08529996871948	-2.04264998435974
Ag	-4.08529996871948	0.000000000000000	-2.04264998435974
Ag	-4.08529996871948	4.08529996871948	-2.04264998435974
Ag	0.000000000000000	-4.08529996871948	-2.04264998435974
Ag	0.000000000000000	0.000000000000000	-2.04264998435974
Ag	0.000000000000000	4.08529996871948	-2.04264998435974
Ag	4.08529996871948	-4.08529996871948	-2.04264998435974
Ag	4.08529996871948	0.000000000000000	-2.04264998435974
Ag	4.08529996871948	4.08529996871948	-2.04264998435974
Ag	-4.08529996871948	-4.08529996871948	2.04264998435974
Ag	-4.08529996871948	0.000000000000000	2.04264998435974
Ag	-4.08529996871948	4.08529996871948	2.04264998435974
Ag	0.000000000000000	-4.08529996871948	2.04264998435974
Ag	0.000000000000000	0.000000000000000	2.04264998435974
Ag	0.000000000000000	4.08529996871948	2.04264998435974
Ag	4.08529996871948	-4.08529996871948	2.04264998435974
Ag	4.08529996871948	0.000000000000000	2.04264998435974
Ag	4.08529996871948	4.08529996871948	2.04264998435974

Ag 0.0000000000000000 0.0000000000000000 6.12794995307922

Coordinate of Ag₁₁₆

Ag	-6.12794995307922	-2.04264998435974	-2.04264998435974
Ag	-6.12794995307922	-2.04264998435974	2.04264998435974
Ag	-6.12794995307922	2.04264998435974	-2.04264998435974
Ag	-6.12794995307922	2.04264998435974	2.04264998435974
Ag	-2.04264998435974	-6.12794995307922	-2.04264998435974
Ag	-2.04264998435974	-6.12794995307922	2.04264998435974
Ag	-2.04264998435974	-2.04264998435974	-6.12794995307922
Ag	-2.04264998435974	-2.04264998435974	-2.04264998435974
Ag	-2.04264998435974	-2.04264998435974	2.04264998435974
Ag	-2.04264998435974	-2.04264998435974	6.12794995307922
Ag	-2.04264998435974	2.04264998435974	-6.12794995307922
Ag	-2.04264998435974	2.04264998435974	-2.04264998435974
Ag	-2.04264998435974	2.04264998435974	2.04264998435974
Ag	-2.04264998435974	2.04264998435974	6.12794995307922
Ag	-2.04264998435974	6.12794995307922	-2.04264998435974
Ag	-2.04264998435974	6.12794995307922	2.04264998435974
Ag	2.04264998435974	-6.12794995307922	-2.04264998435974
Ag	2.04264998435974	-6.12794995307922	2.04264998435974
Ag	2.04264998435974	-2.04264998435974	-6.12794995307922
Ag	2.04264998435974	-2.04264998435974	-2.04264998435974
Ag	2.04264998435974	-2.04264998435974	2.04264998435974
Ag	2.04264998435974	-2.04264998435974	6.12794995307922
Ag	2.04264998435974	2.04264998435974	-6.12794995307922
Ag	2.04264998435974	2.04264998435974	-2.04264998435974
Ag	2.04264998435974	2.04264998435974	2.04264998435974
Ag	2.04264998435974	2.04264998435974	6.12794995307922
Ag	2.04264998435974	6.12794995307922	-2.04264998435974
Ag	2.04264998435974	6.12794995307922	2.04264998435974
Ag	6.12794995307922	-2.04264998435974	-2.04264998435974

Ag 6.12794995307922	-2.04264998435974	2.04264998435974
Ag 6.12794995307922	2.04264998435974	-2.04264998435974
Ag 6.12794995307922	2.04264998435974	2.04264998435974
Ag -6.12794995307922	-4.08529996871948	0.00000000000000
Ag -6.12794995307922	0.00000000000000	-4.08529996871948
Ag -6.12794995307922	0.00000000000000	0.00000000000000
Ag -6.12794995307922	0.00000000000000	4.08529996871948
Ag -6.12794995307922	4.08529996871948	0.00000000000000
Ag -2.04264998435974	-4.08529996871948	-4.08529996871948
Ag -2.04264998435974	-4.08529996871948	0.00000000000000
Ag -2.04264998435974	-4.08529996871948	4.08529996871948
Ag -2.04264998435974	0.00000000000000	-4.08529996871948
Ag -2.04264998435974	0.00000000000000	0.00000000000000
Ag -2.04264998435974	0.00000000000000	4.08529996871948
Ag -2.04264998435974	4.08529996871948	-4.08529996871948
Ag -2.04264998435974	4.08529996871948	0.00000000000000
Ag -2.04264998435974	4.08529996871948	4.08529996871948
Ag 2.04264998435974	-4.08529996871948	-4.08529996871948
Ag 2.04264998435974	-4.08529996871948	0.00000000000000
Ag 2.04264998435974	-4.08529996871948	4.08529996871948
Ag 2.04264998435974	0.00000000000000	-4.08529996871948
Ag 2.04264998435974	0.00000000000000	0.00000000000000
Ag 2.04264998435974	0.00000000000000	4.08529996871948
Ag 2.04264998435974	4.08529996871948	-4.08529996871948
Ag 2.04264998435974	4.08529996871948	0.00000000000000
Ag 2.04264998435974	4.08529996871948	4.08529996871948
Ag 6.12794995307922	-4.08529996871948	0.00000000000000
Ag 6.12794995307922	0.00000000000000	-4.08529996871948
Ag 6.12794995307922	0.00000000000000	0.00000000000000
Ag 6.12794995307922	0.00000000000000	4.08529996871948
Ag 6.12794995307922	4.08529996871948	0.00000000000000

Ag	0.000000000000000	-6.12794995307922	-4.08529996871948
Ag	-4.08529996871948	-6.12794995307922	0.000000000000000
Ag	0.000000000000000	-6.12794995307922	0.000000000000000
Ag	4.08529996871948	-6.12794995307922	0.000000000000000
Ag	0.000000000000000	-6.12794995307922	4.08529996871948
Ag	-4.08529996871948	-2.04264998435974	-4.08529996871948
Ag	0.000000000000000	-2.04264998435974	-4.08529996871948
Ag	4.08529996871948	-2.04264998435974	-4.08529996871948
Ag	-4.08529996871948	-2.04264998435974	0.000000000000000
Ag	0.000000000000000	-2.04264998435974	0.000000000000000
Ag	4.08529996871948	-2.04264998435974	0.000000000000000
Ag	-4.08529996871948	-2.04264998435974	4.08529996871948
Ag	0.000000000000000	-2.04264998435974	4.08529996871948
Ag	4.08529996871948	-2.04264998435974	4.08529996871948
Ag	-4.08529996871948	2.04264998435974	-4.08529996871948
Ag	0.000000000000000	2.04264998435974	-4.08529996871948
Ag	4.08529996871948	2.04264998435974	-4.08529996871948
Ag	-4.08529996871948	2.04264998435974	0.000000000000000
Ag	0.000000000000000	2.04264998435974	0.000000000000000
Ag	4.08529996871948	2.04264998435974	0.000000000000000
Ag	-4.08529996871948	2.04264998435974	4.08529996871948
Ag	0.000000000000000	2.04264998435974	4.08529996871948
Ag	4.08529996871948	2.04264998435974	4.08529996871948
Ag	0.000000000000000	6.12794995307922	-4.08529996871948
Ag	-4.08529996871948	6.12794995307922	0.000000000000000
Ag	0.000000000000000	6.12794995307922	0.000000000000000
Ag	4.08529996871948	6.12794995307922	0.000000000000000
Ag	0.000000000000000	6.12794995307922	4.08529996871948
Ag	-4.08529996871948	0.000000000000000	-6.12794995307922
Ag	0.000000000000000	-4.08529996871948	-6.12794995307922
Ag	0.000000000000000	0.000000000000000	-6.12794995307922

Ag	0.000000000000000	4.08529996871948	-6.12794995307922
Ag	4.08529996871948	0.000000000000000	-6.12794995307922
Ag	-4.08529996871948	-4.08529996871948	-2.04264998435974
Ag	-4.08529996871948	0.000000000000000	-2.04264998435974
Ag	-4.08529996871948	4.08529996871948	-2.04264998435974
Ag	0.000000000000000	-4.08529996871948	-2.04264998435974
Ag	0.000000000000000	0.000000000000000	-2.04264998435974
Ag	0.000000000000000	4.08529996871948	-2.04264998435974
Ag	4.08529996871948	-4.08529996871948	-2.04264998435974
Ag	4.08529996871948	0.000000000000000	-2.04264998435974
Ag	4.08529996871948	4.08529996871948	-2.04264998435974
Ag	-4.08529996871948	-4.08529996871948	2.04264998435974
Ag	-4.08529996871948	0.000000000000000	2.04264998435974
Ag	-4.08529996871948	4.08529996871948	2.04264998435974
Ag	0.000000000000000	-4.08529996871948	2.04264998435974
Ag	0.000000000000000	0.000000000000000	2.04264998435974
Ag	0.000000000000000	4.08529996871948	2.04264998435974
Ag	4.08529996871948	-4.08529996871948	2.04264998435974
Ag	4.08529996871948	0.000000000000000	2.04264998435974
Ag	4.08529996871948	4.08529996871948	2.04264998435974
Ag	-4.08529996871948	0.000000000000000	6.12794995307922
Ag	0.000000000000000	-4.08529996871948	6.12794995307922
Ag	0.000000000000000	0.000000000000000	6.12794995307922
Ag	0.000000000000000	4.08529996871948	6.12794995307922
Ag	4.08529996871948	0.000000000000000	6.12794995307922

Coordinate of Ag₁₆₄

Ag -6.1279499530792236	-2.0426499843597412	-2.0426499843597412
Ag -6.1279499530792236	-2.0426499843597412	2.0426499843597412
Ag -6.1279499530792236	2.0426499843597412	-2.0426499843597412
Ag -6.1279499530792236	2.0426499843597412	2.0426499843597412
Ag -2.0426499843597412	-6.1279499530792236	-2.0426499843597412
Ag -2.0426499843597412	-6.1279499530792236	2.0426499843597412
Ag -2.0426499843597412	-2.0426499843597412	-6.1279499530792236
Ag -2.0426499843597412	-2.0426499843597412	-2.0426499843597412
Ag -2.0426499843597412	-2.0426499843597412	2.0426499843597412
Ag -2.0426499843597412	-2.0426499843597412	6.1279499530792236
Ag -2.0426499843597412	2.0426499843597412	-6.1279499530792236
Ag -2.0426499843597412	2.0426499843597412	-2.0426499843597412
Ag -2.0426499843597412	2.0426499843597412	2.0426499843597412
Ag -2.0426499843597412	2.0426499843597412	6.1279499530792236
Ag -2.0426499843597412	6.1279499530792236	-2.0426499843597412
Ag -2.0426499843597412	6.1279499530792236	2.0426499843597412
Ag 2.0426499843597412	-6.1279499530792236	-2.0426499843597412
Ag 2.0426499843597412	-6.1279499530792236	2.0426499843597412
Ag 2.0426499843597412	-2.0426499843597412	-6.1279499530792236
Ag 2.0426499843597412	-2.0426499843597412	-2.0426499843597412
Ag 2.0426499843597412	-2.0426499843597412	2.0426499843597412
Ag 2.0426499843597412	-2.0426499843597412	6.1279499530792236
Ag 2.0426499843597412	2.0426499843597412	-6.1279499530792236
Ag 2.0426499843597412	2.0426499843597412	-2.0426499843597412
Ag 2.0426499843597412	2.0426499843597412	2.0426499843597412
Ag 2.0426499843597412	2.0426499843597412	6.1279499530792236
Ag 2.0426499843597412	6.1279499530792236	-2.0426499843597412
Ag 2.0426499843597412	6.1279499530792236	2.0426499843597412
Ag 6.1279499530792236	-2.0426499843597412	-2.0426499843597412

Ag 6.1279499530792236	-2.0426499843597412	2.0426499843597412
Ag 6.1279499530792236	2.0426499843597412	-2.0426499843597412
Ag 6.1279499530792236	2.0426499843597412	2.0426499843597412
Ag -6.1279499530792236	-4.0852999687194824	-4.0852999687194824
Ag -6.1279499530792236	-4.0852999687194824	0.0000000000000000
Ag -6.1279499530792236	-4.0852999687194824	4.0852999687194824
Ag -6.1279499530792236	0.0000000000000000	-4.0852999687194824
Ag -6.1279499530792236	0.0000000000000000	0.0000000000000000
Ag -6.1279499530792236	0.0000000000000000	4.0852999687194824
Ag -6.1279499530792236	4.0852999687194824	-4.0852999687194824
Ag -6.1279499530792236	4.0852999687194824	0.0000000000000000
Ag -6.1279499530792236	4.0852999687194824	4.0852999687194824
Ag -2.0426499843597412	-8.1705999374389648	0.0000000000000000
Ag -2.0426499843597412	-4.0852999687194824	-4.0852999687194824
Ag -2.0426499843597412	-4.0852999687194824	0.0000000000000000
Ag -2.0426499843597412	-4.0852999687194824	4.0852999687194824
Ag -2.0426499843597412	0.0000000000000000	-8.1705999374389648
Ag -2.0426499843597412	0.0000000000000000	-4.0852999687194824
Ag -2.0426499843597412	0.0000000000000000	0.0000000000000000
Ag -2.0426499843597412	0.0000000000000000	4.0852999687194824
Ag -2.0426499843597412	0.0000000000000000	8.1705999374389648
Ag -2.0426499843597412	4.0852999687194824	-4.0852999687194824
Ag -2.0426499843597412	4.0852999687194824	0.0000000000000000
Ag -2.0426499843597412	4.0852999687194824	4.0852999687194824
Ag -2.0426499843597412	8.1705999374389648	0.0000000000000000
Ag 2.0426499843597412	-8.1705999374389648	0.0000000000000000
Ag 2.0426499843597412	-4.0852999687194824	-4.0852999687194824
Ag 2.0426499843597412	-4.0852999687194824	0.0000000000000000
Ag 2.0426499843597412	-4.0852999687194824	4.0852999687194824
Ag 2.0426499843597412	0.0000000000000000	-8.1705999374389648
Ag 2.0426499843597412	0.0000000000000000	-4.0852999687194824

Ag	2.0426499843597412	0.0000000000000000	0.0000000000000000
Ag	2.0426499843597412	0.0000000000000000	4.0852999687194824
Ag	2.0426499843597412	0.0000000000000000	8.1705999374389648
Ag	2.0426499843597412	4.0852999687194824	-4.0852999687194824
Ag	2.0426499843597412	4.0852999687194824	0.0000000000000000
Ag	2.0426499843597412	4.0852999687194824	4.0852999687194824
Ag	2.0426499843597412	8.1705999374389648	0.0000000000000000
Ag	6.1279499530792236	-4.0852999687194824	-4.0852999687194824
Ag	6.1279499530792236	-4.0852999687194824	0.0000000000000000
Ag	6.1279499530792236	-4.0852999687194824	4.0852999687194824
Ag	6.1279499530792236	0.0000000000000000	-4.0852999687194824
Ag	6.1279499530792236	0.0000000000000000	0.0000000000000000
Ag	6.1279499530792236	0.0000000000000000	4.0852999687194824
Ag	6.1279499530792236	4.0852999687194824	-4.0852999687194824
Ag	6.1279499530792236	4.0852999687194824	0.0000000000000000
Ag	6.1279499530792236	4.0852999687194824	4.0852999687194824
Ag	-4.0852999687194824	-6.1279499530792236	-4.0852999687194824
Ag	0.0000000000000000	-6.1279499530792236	-4.0852999687194824
Ag	4.0852999687194824	-6.1279499530792236	-4.0852999687194824
Ag	-4.0852999687194824	-6.1279499530792236	0.0000000000000000
Ag	0.0000000000000000	-6.1279499530792236	0.0000000000000000
Ag	4.0852999687194824	-6.1279499530792236	0.0000000000000000
Ag	-4.0852999687194824	-6.1279499530792236	4.0852999687194824
Ag	0.0000000000000000	-6.1279499530792236	4.0852999687194824
Ag	4.0852999687194824	-6.1279499530792236	4.0852999687194824
Ag	0.0000000000000000	-2.0426499843597412	-8.1705999374389648
Ag	-4.0852999687194824	-2.0426499843597412	-4.0852999687194824
Ag	0.0000000000000000	-2.0426499843597412	-4.0852999687194824
Ag	4.0852999687194824	-2.0426499843597412	-4.0852999687194824
Ag	-8.1705999374389648	-2.0426499843597412	0.0000000000000000
Ag	-4.0852999687194824	-2.0426499843597412	0.0000000000000000

Ag	0.0000000000000000	-2.0426499843597412	0.0000000000000000
Ag	4.0852999687194824	-2.0426499843597412	0.0000000000000000
Ag	8.1705999374389648	-2.0426499843597412	0.0000000000000000
Ag	-4.0852999687194824	-2.0426499843597412	4.0852999687194824
Ag	0.0000000000000000	-2.0426499843597412	4.0852999687194824
Ag	4.0852999687194824	-2.0426499843597412	4.0852999687194824
Ag	0.0000000000000000	-2.0426499843597412	8.1705999374389648
Ag	0.0000000000000000	2.0426499843597412	-8.1705999374389648
Ag	-4.0852999687194824	2.0426499843597412	-4.0852999687194824
Ag	0.0000000000000000	2.0426499843597412	-4.0852999687194824
Ag	4.0852999687194824	2.0426499843597412	-4.0852999687194824
Ag	-8.1705999374389648	2.0426499843597412	0.0000000000000000
Ag	-4.0852999687194824	2.0426499843597412	0.0000000000000000
Ag	0.0000000000000000	2.0426499843597412	0.0000000000000000
Ag	4.0852999687194824	2.0426499843597412	0.0000000000000000
Ag	8.1705999374389648	2.0426499843597412	0.0000000000000000
Ag	-4.0852999687194824	2.0426499843597412	4.0852999687194824
Ag	0.0000000000000000	2.0426499843597412	4.0852999687194824
Ag	4.0852999687194824	2.0426499843597412	4.0852999687194824
Ag	0.0000000000000000	2.0426499843597412	8.1705999374389648
Ag	-4.0852999687194824	6.1279499530792236	-4.0852999687194824
Ag	0.0000000000000000	6.1279499530792236	-4.0852999687194824
Ag	4.0852999687194824	6.1279499530792236	-4.0852999687194824
Ag	-4.0852999687194824	6.1279499530792236	0.0000000000000000
Ag	0.0000000000000000	6.1279499530792236	0.0000000000000000
Ag	4.0852999687194824	6.1279499530792236	0.0000000000000000
Ag	-4.0852999687194824	6.1279499530792236	4.0852999687194824
Ag	0.0000000000000000	6.1279499530792236	4.0852999687194824
Ag	4.0852999687194824	6.1279499530792236	4.0852999687194824
Ag	-4.0852999687194824	-4.0852999687194824	-6.1279499530792236
Ag	-4.0852999687194824	0.0000000000000000	-6.1279499530792236

Ag	-4.0852999687194824	4.0852999687194824	-6.1279499530792236
Ag	0.0000000000000000	-4.0852999687194824	-6.1279499530792236
Ag	0.0000000000000000	0.0000000000000000	-6.1279499530792236
Ag	0.0000000000000000	4.0852999687194824	-6.1279499530792236
Ag	4.0852999687194824	-4.0852999687194824	-6.1279499530792236
Ag	4.0852999687194824	0.0000000000000000	-6.1279499530792236
Ag	4.0852999687194824	4.0852999687194824	-6.1279499530792236
Ag	-8.1705999374389648	0.0000000000000000	-2.0426499843597412
Ag	-4.0852999687194824	-4.0852999687194824	-2.0426499843597412
Ag	-4.0852999687194824	0.0000000000000000	-2.0426499843597412
Ag	-4.0852999687194824	4.0852999687194824	-2.0426499843597412
Ag	0.0000000000000000	-8.1705999374389648	-2.0426499843597412
Ag	0.0000000000000000	-4.0852999687194824	-2.0426499843597412
Ag	0.0000000000000000	0.0000000000000000	-2.0426499843597412
Ag	0.0000000000000000	4.0852999687194824	-2.0426499843597412
Ag	0.0000000000000000	8.1705999374389648	-2.0426499843597412
Ag	4.0852999687194824	-4.0852999687194824	-2.0426499843597412
Ag	4.0852999687194824	0.0000000000000000	-2.0426499843597412
Ag	4.0852999687194824	4.0852999687194824	-2.0426499843597412
Ag	8.1705999374389648	0.0000000000000000	-2.0426499843597412
Ag	-8.1705999374389648	0.0000000000000000	2.0426499843597412
Ag	-4.0852999687194824	-4.0852999687194824	2.0426499843597412
Ag	-4.0852999687194824	0.0000000000000000	2.0426499843597412
Ag	-4.0852999687194824	4.0852999687194824	2.0426499843597412
Ag	0.0000000000000000	-8.1705999374389648	2.0426499843597412
Ag	0.0000000000000000	-4.0852999687194824	2.0426499843597412
Ag	0.0000000000000000	0.0000000000000000	2.0426499843597412
Ag	0.0000000000000000	4.0852999687194824	2.0426499843597412
Ag	0.0000000000000000	8.1705999374389648	2.0426499843597412
Ag	4.0852999687194824	-4.0852999687194824	2.0426499843597412
Ag	4.0852999687194824	0.0000000000000000	2.0426499843597412

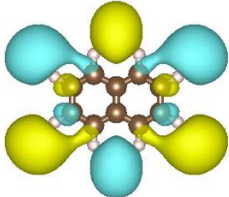
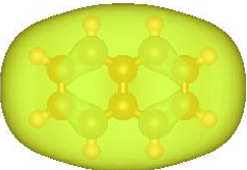
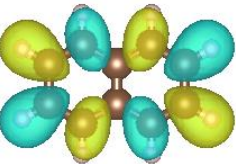
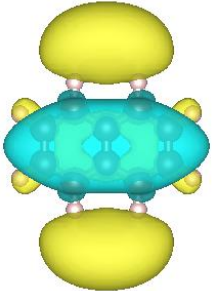
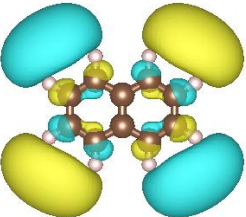
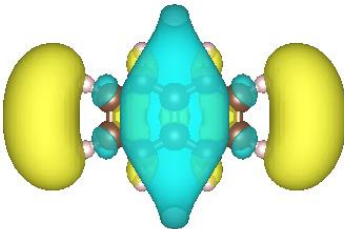
Ag	4.0852999687194824	4.0852999687194824	2.0426499843597412
Ag	8.1705999374389648	0.0000000000000000	2.0426499843597412
Ag	-4.0852999687194824	-4.0852999687194824	6.1279499530792236
Ag	-4.0852999687194824	0.0000000000000000	6.1279499530792236
Ag	-4.0852999687194824	4.0852999687194824	6.1279499530792236
Ag	0.0000000000000000	-4.0852999687194824	6.1279499530792236
Ag	0.0000000000000000	0.0000000000000000	6.1279499530792236
Ag	0.0000000000000000	4.0852999687194824	6.1279499530792236
Ag	4.0852999687194824	-4.0852999687194824	6.1279499530792236
Ag	4.0852999687194824	0.0000000000000000	6.1279499530792236
Ag	4.0852999687194824	4.0852999687194824	6.1279499530792236

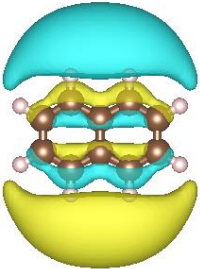
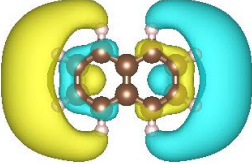
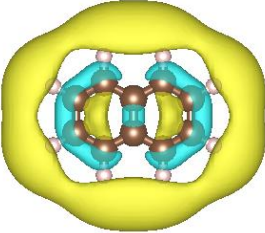
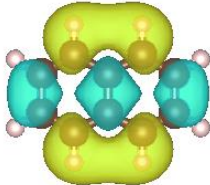
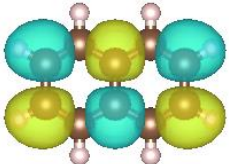
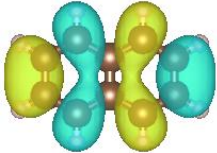
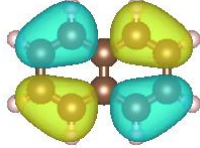
**Appendix B - Supporting Information for “Electronic Excited State
Dynamics of Naphthalene Studied by Simulated Transient
Absorption Spectroscopy”**

Table B.5 The first ten excited states calculated by LR-TDDFT

Excitation	Energy (eV)	Oscillator strength	Weight	Transitions
1	4.14	4.36×10^{-2}	0.9602	HOMO→LUMO
2	4.30	2.46×10^{-5}	0.7137 0.6998	HOMO→LUMO+1 HOMO-1→LUMO
3	5.05	3.59×10^{-13}	0.6043	HOMO-2→LUMO
4	5.45	1.09×10^{-16}	0.9998	HOMO→LUMO+3
5	5.77	1.21×10^0	0.6765 0.6882	HOMO→LUMO+1 HOMO-1→LUMO
6	5.79	9.33×10^{-15}	0.9998	HOMO→LUMO+4
7	5.80	1.01×10^{-13}	0.9741	HOMO-3→LUMO
8	5.86	1.92×10^{-15}	0.9746	HOMO→LUMO+5
9	5.90	6.10×10^{-11}	0.8215	HOMO-1→LUMO+2
10	6.01	1.46×10^{-1}	0.9445	HOMO-1→LUMO+1

Table B.6 Frontier orbitals with their orbital energy and symmetry representation

	Molecular Orbital	Energy (eV)	Symmetry Representation
LUMO+11		1.39	b_{2u}
LUMO+10		1.13	b_{1u}
LUMO+9		1.03	a_u
LUMO+8		0.90	a_g
LUMO+7		0.79	b_{1g}
LUMO+6		0.73	a_g

LUMO+5		0.13	b_{2u}
LUMO+4		0.06	b_{3u}
LUMO+3		-0.28	a_g
LUMO+2		-0.77	b_{1u}
LUMO+1		-1.53	b_{3g}
LUMO		-2.30	b_{2g}
HOMO		-5.73	a_u

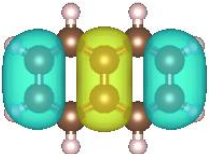
HOMO-1		-6.50	b_{1u}
--------	---	-------	----------

Table B.7 Possible excited state absorptions induced by the probe pulse due to electronic excitation out of the newly occupied LUMO with b_{2g} symmetry and LUMO+1 with b_{3g} symmetry. The states with B_{3u} symmetry (x-polarized) would be bright state transitions from LUMO and LUMO+1. The states with green font with B_{2u} symmetry (green font) are the y-polarized bright state transitions from LUMO and LUMO+1. The states with B_{1u} symmetry (blue font) are the bright state transitions from LUMO and LUMO+1 polarized in the z direction.

			LUMO		LUMO+1	
	Energy (eV)	symmetry	Energy (eV)	symmetry	Energy (eV)	symmetry
			-2.30	b_{2g}	-1.53	b_{3g}
LUMO+2	-0.77	b_{1u}	1.53	B_{3u}	0.75	B_{2u}
LUMO+3	-0.28	a_g	2.03	B_{2g}	1.25	B_{3g}
LUMO+4	0.06	b_{3u}	2.36	B_{1u}	1.59	A_u
LUMO+5	0.13	b_{2u}	2.43	A_u	1.65	B_{1u}
LUMO+6	0.73	a_g	3.03	B_{2g}	2.26	B_{3g}
LUMO+7	0.79	b_{1g}	3.09	B_{3g}	2.32	B_{2g}
LUMO+8	0.90	a_g	3.20	B_{2g}	2.43	B_{3g}
LUMO+9	1.03	a_u	3.33	B_{2u}	2.56	B_{3u}
LUMO+10	1.13	b_{1u}	3.44	B_{3u}	2.66	B_{2u}
LUMO+11	1.39	b_{2u}	3.70	A_u	2.92	B_{1u}

Table B.8 Possible hole excited state absorptions induced by the probe that involve the HOMO with a_u symmetry and HOMO-1 with b_{1u} symmetry. The B_{3u} states (red font) are the x-polarized bright state transitions from HOMO and HOMO-1. The green font with B_{2u} symmetry states (green font) are the y-polarized bright state transitions from HOMO and HOMO-1. The B_{1u} states (blue font) are the z-polarized bright state transitions from HOMO and HOMO-1.

	Energy (eV)	symmetry	HOMO Energy (eV) -5.73	symmetry a_u	HOMO-1 Energy (eV) -6.50	symmetry b_{1u}
HOMO-2	-7.44	b_{3g}	1.71	B_{3u}	0.94	B_{2u}
HOMO-3	-8.04	a_g	2.31	A_u	1.54	B_{1u}
HOMO-4	-8.29	b_{1g}	2.56	B_{1u}	1.79	A_u
HOMO-5	-8.48	b_{2g}	2.75	B_{2u}	1.98	B_{3u}
HOMO-6	-9.03	b_{3u}	3.30	B_{3g}	2.53	B_{2g}
HOMO-7	-9.71	b_{2u}	3.98	B_{2g}	3.21	B_{3g}
HOMO-8	-10.07	b_{1u}	4.34	B_{1g}	3.57	A_g
HOMO-9	-10.25	b_{1g}	4.52	B_{1u}	3.75	A_u
HOMO-10	-10.42	b_{3u}	4.69	B_{3g}	3.92	B_{2g}
HOMO-11	-10.88	b_{2u}	5.15	B_{2g}	4.38	B_{3g}

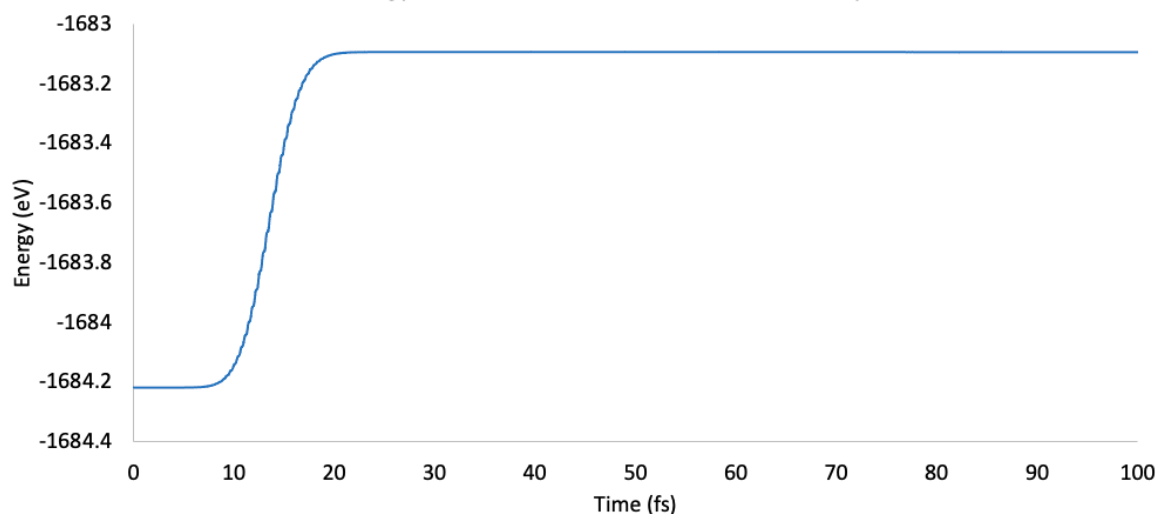


Figure B.26 Energy transfer from the electric field to the system Figure B.2. Transient absorption spectrum of naphthalene with x-polarized probe after excitation of the plasmonic β peak

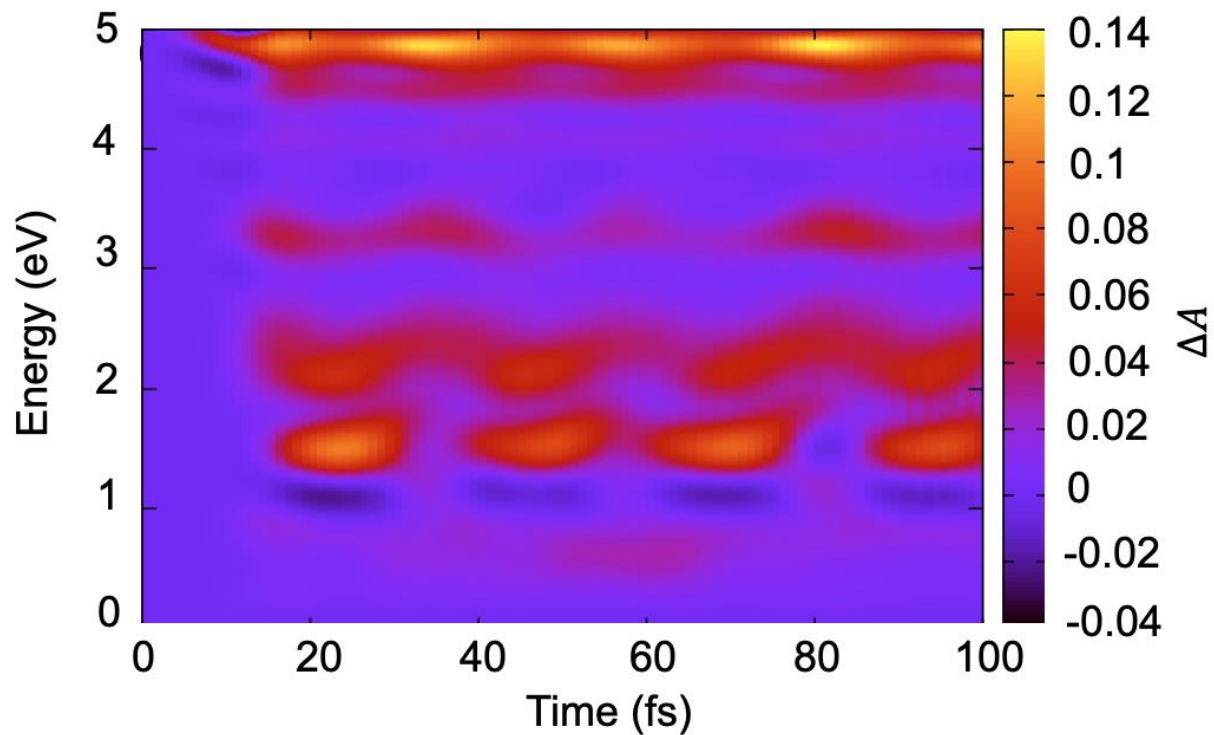
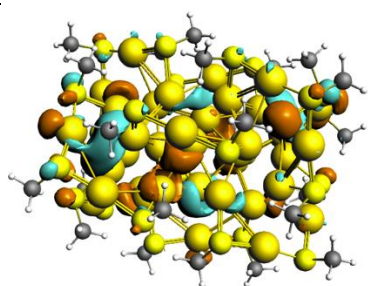
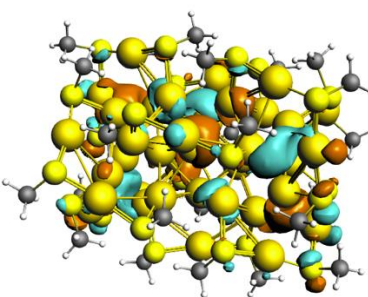
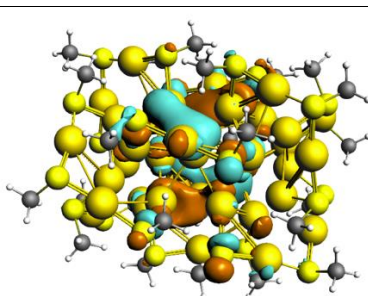
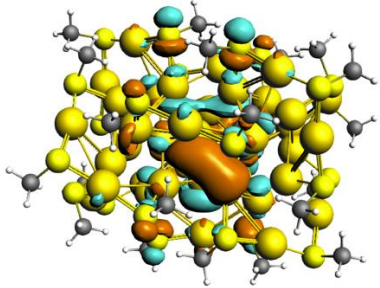
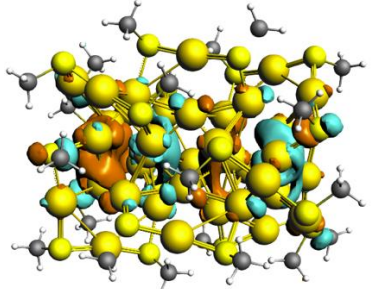
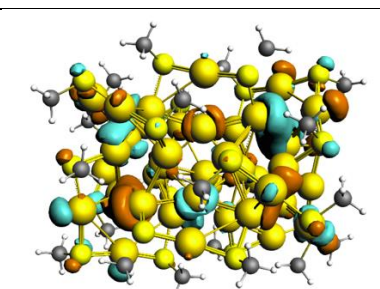
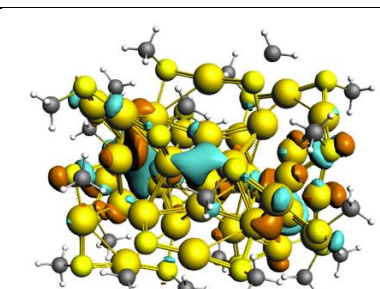
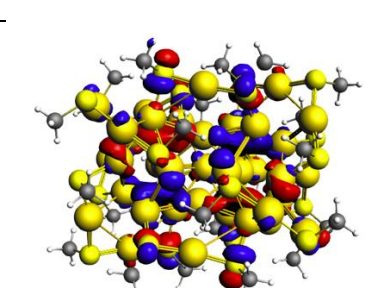


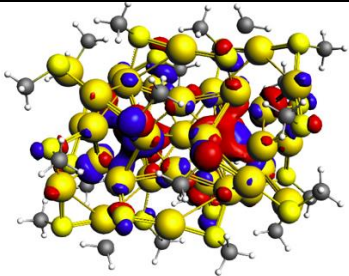
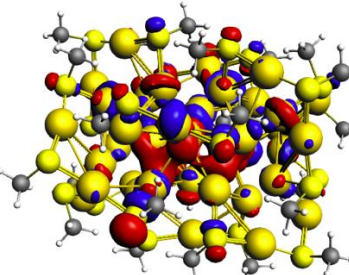
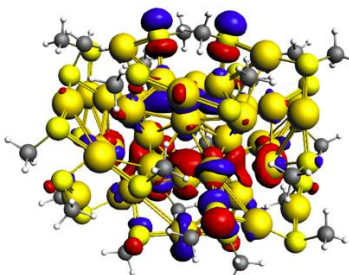
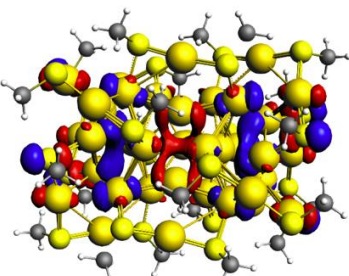
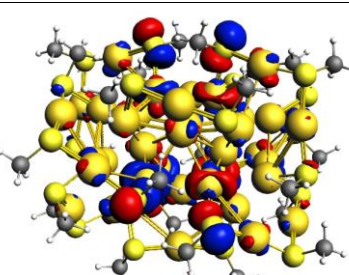
Figure B.27 Transient absorption spectrum of naphthalene with x-polarized probe after excitation of the plasmonic β peak

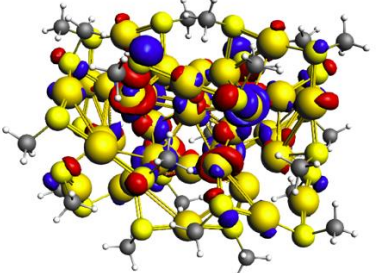
**Appendix C - Supporting Information for “Electronic Excited State
Dynamics of Au₂₅ and Au₃₈ Studied by Simulated Transient
Absorption Spectroscopy”**

Table C.9 Frontier orbitals with their orbital energy and symmetry representation

	Molecular Orbital	Energy (eV)	Orbitals Number
LUMO+6		-2.40	524
LUMO+5		-2.40	523
LUMO+4		-2.96	522

LUMO+3		-2.96	521
LUMO+2		-3.13	520
LUMO+1		-3.30	519
LUMO		-3.30	518
HOMO		-4.22	517

HOMO-1		-4.22	516
HOMO-2		-4.57	515
HOMO-3		-4.58	514
HOMO-4		-4.58	513
HOMO-5		-4.97	512

HOMO-6		-5.02	511
--------	---	-------	-----

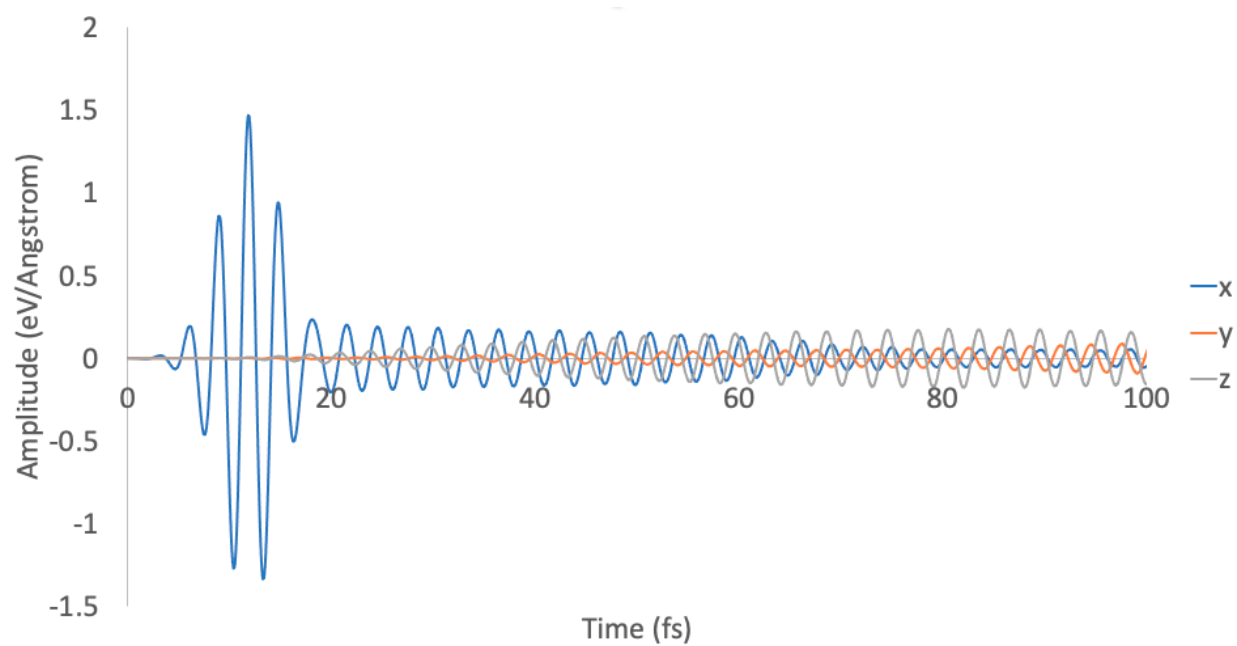


Figure C.28 Dipole fluctuation of Au₂₅ with pump energy of 1.40 eV

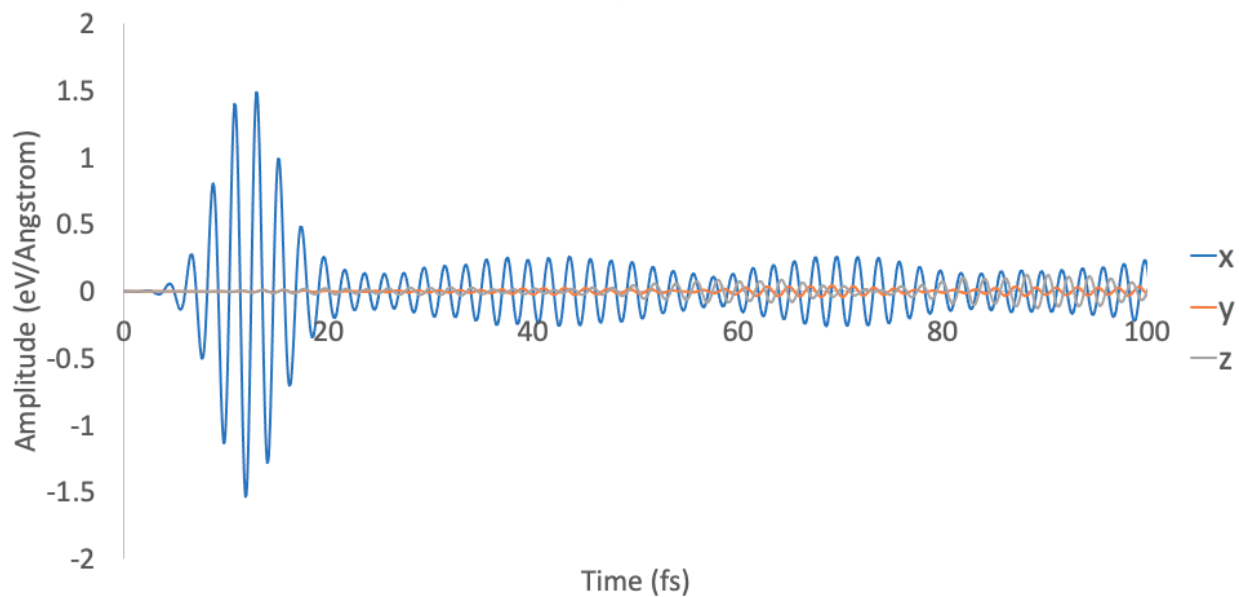


Figure C.29 Dipole fluctuation of Au₂₅ with pump energy of 1.92 eV

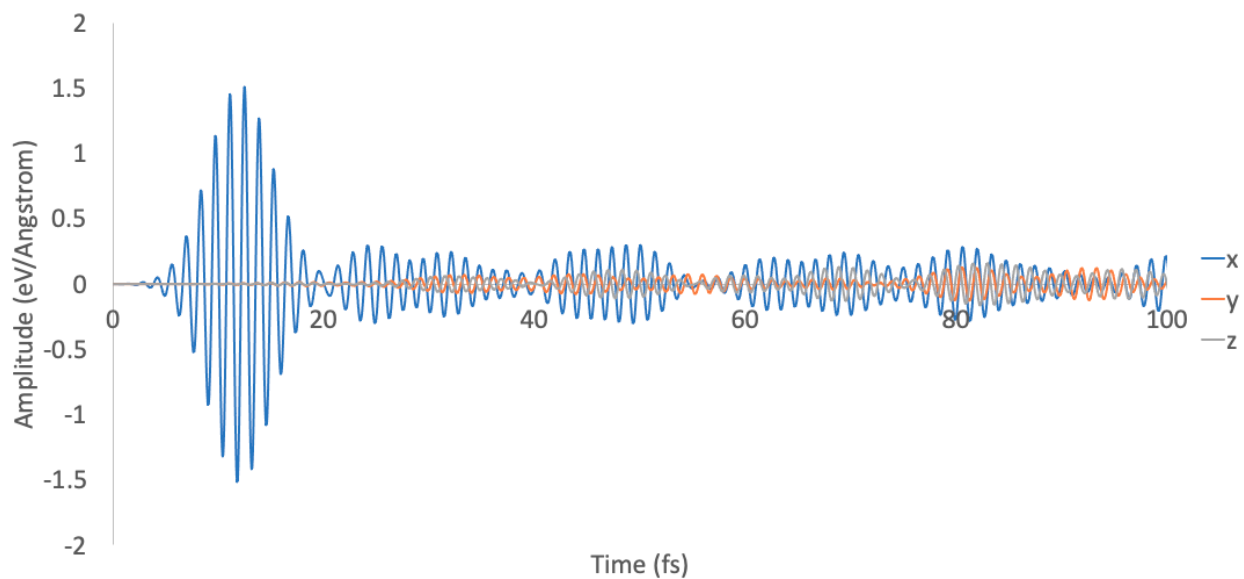


Figure C.30 Dipole fluctuation of Au₂₅ with pump energy of 2.99 eV

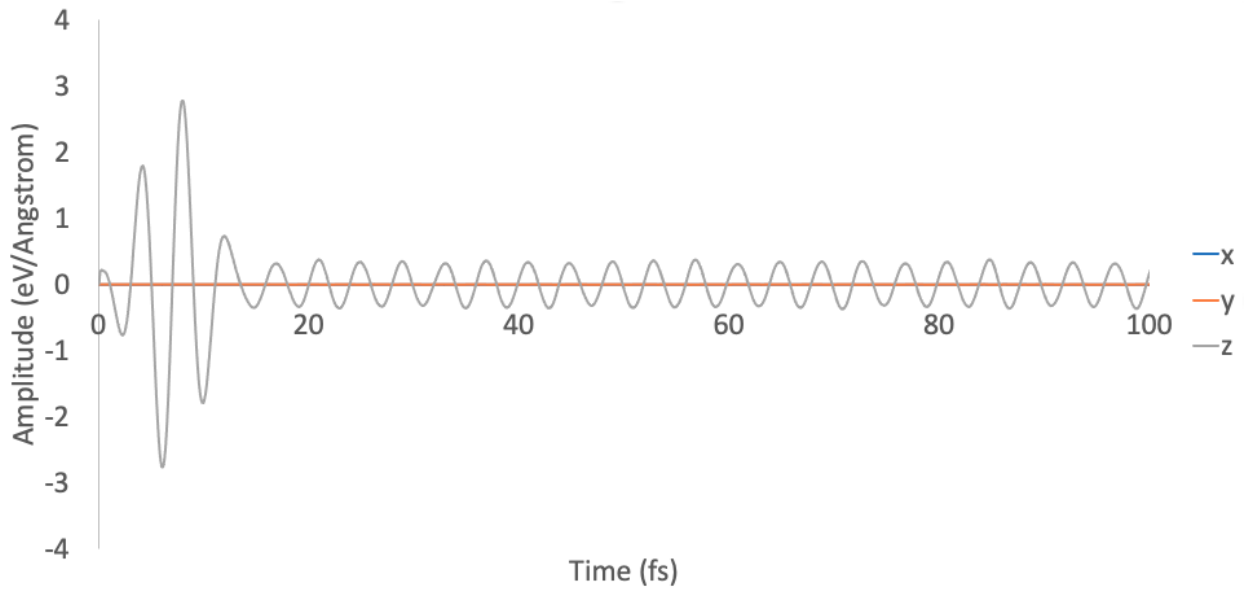


Figure C.31 Dipole fluctuation of Au₃₈ with pump energy of 1.04 eV polarized in z direction

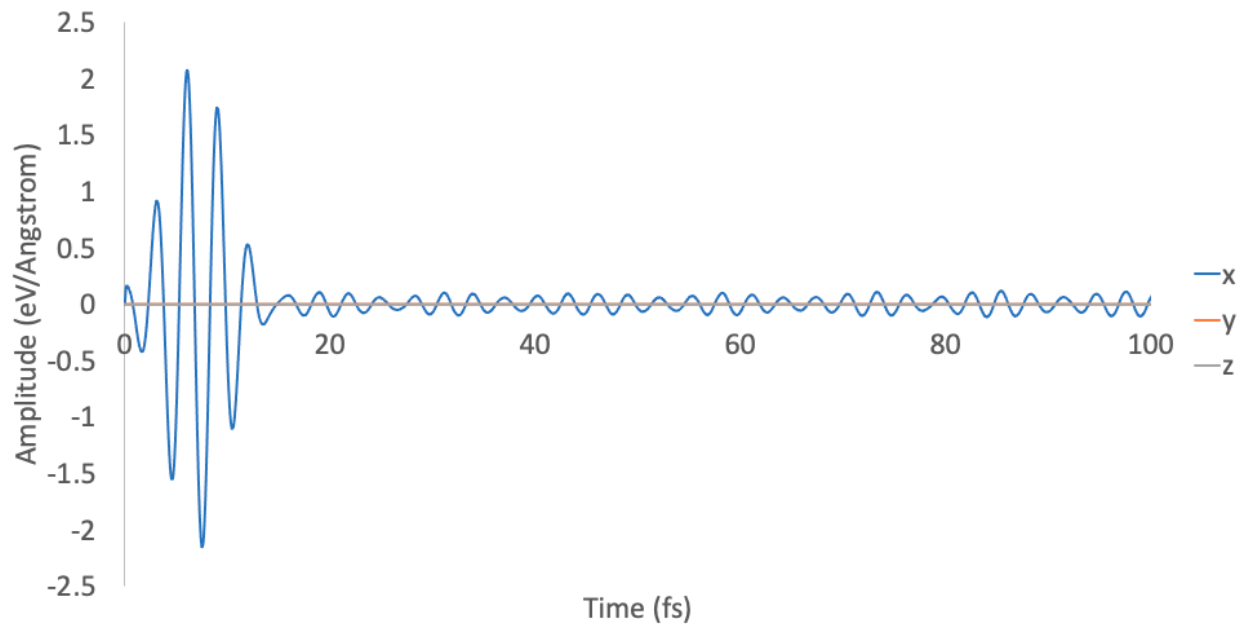


Figure C.32 Dipole fluctuation of Au₃₈ with pump energy of 1.37 eV polarized in x direction

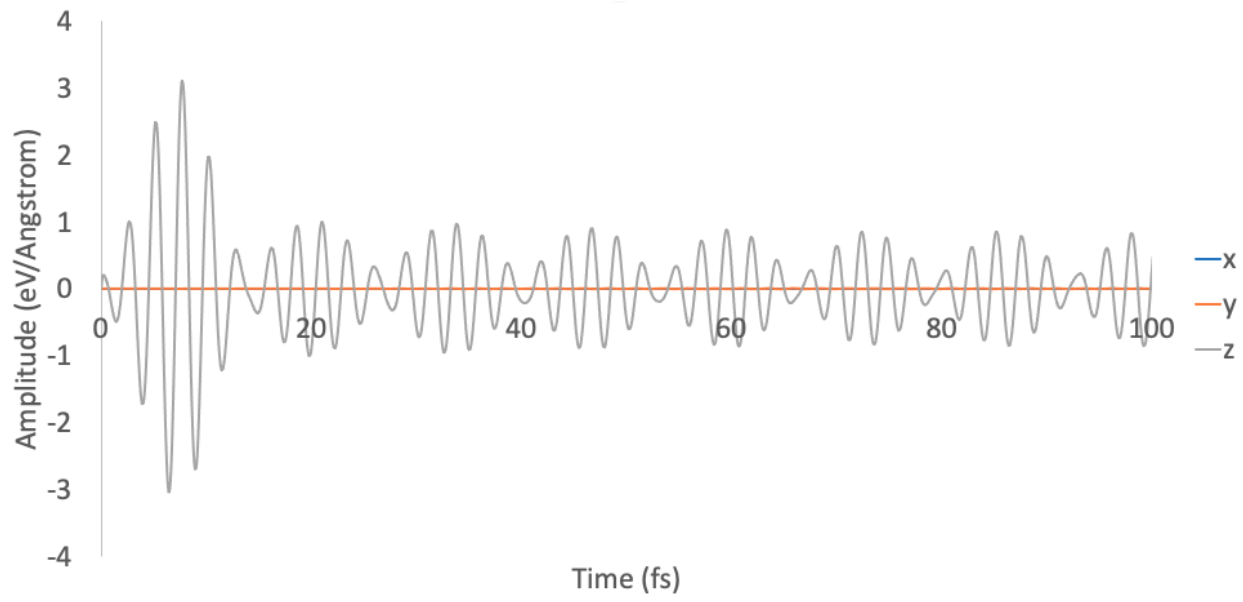


Figure C.33 Dipole fluctuation of Au₃₈ with pump energy of 1.62 eV polarized in z direction